

INFORMATION TO USERS

This manuscript has been reproduced from the microfilm master. UMI films the text directly from the original or copy submitted. Thus, some thesis and dissertation copies are in typewriter face, while others may be from any type of computer printer.

The quality of this reproduction is dependent upon the quality of the copy submitted. Broken or indistinct print, colored or poor quality illustrations and photographs, print bleedthrough, substandard margins, and improper alignment can adversely affect reproduction.

In the unlikely event that the author did not send UMI a complete manuscript and there are missing pages, these will be noted. Also, if unauthorized copyright material had to be removed, a note will indicate the deletion.

Oversize materials (e.g., maps, drawings, charts) are reproduced by sectioning the original, beginning at the upper left-hand corner and continuing from left to right in equal sections with small overlaps.

Photographs included in the original manuscript have been reproduced xerographically in this copy. Higher quality 6" x 9" black and white photographic prints are available for any photographs or illustrations appearing in this copy for an additional charge. Contact UMI directly to order.

**Bell & Howell Information and Learning
300 North Zeeb Road, Ann Arbor, MI 48106-1346 USA**

UMI[®]
800-521-0600

**THE UNIVERSITY OF OKLAHOMA
GRADUATE COLLEGE**

**NUMERICAL STUDY OF SURFACE TENSION AND
GRAVITATIONAL EFFECTS ON MOLD FILLING**

**A DISSERTATION
SUBMITTED TO THE GRADUATE FACULTY**

in partial fulfillment of the requirement for the

degree of

Doctor of Philosophy

By

CHIEN-TE LI

Norman, Oklahoma

2000

UMI Number: 9962963

UMI[®]

UMI Microform 9962963

Copyright 2000 by Bell & Howell Information and Learning Company.

All rights reserved. This microform edition is protected against
unauthorized copying under Title 17, United States Code.

Bell & Howell Information and Learning Company
300 North Zeeb Road
P.O. Box 1346
Ann Arbor, MI 48106-1346

In memory of my late father, Wen-Chuan

© Copyright by Chien-Te Li, 2000


All Right Reserved

**NUMERICAL STUDY OF SURFACE TENSION AND
GRAVITATIONAL EFFECTS ON MOLD FILLING**


**A Dissertation APPROVED FOR
THE SCHOOL OF AEROSPACE AND MECHANICAL ENGINEERING**

By


Dr. F. C. Lai (Chair)


Dr. M. C. Akan


Dr. M. L. Rasmussen


Dr. W. H. Sutton


Dr. L. White

ACKNOWLEDGMENT

I would like to express my sincere gratitude to my advisor, Dr. Feng-Chyuan Lai, for providing me the opportunity to work on this research project in flow injection. I would also like to thank him for his thoughtful guidance and continuous encouragement throughout this study.

Special thanks also go to the members of my dissertation committee, Dr. M. C. Altan, Dr. M. L. Rasmussen, Dr. W. H. Sutton, and Dr. L. White, for their insightful advice, recommendations, and encouragement.

The fruitful discussion with Professor A. N. Hrymak at the McMaster University in Canada and Professor T. -F. Chen at the National Chung-Cheng University in Taiwan is gratefully acknowledged. In addition, the support of supercomputing provided by Silicon Graphics Inc., administrated through Mr. Michael D. Tuttle is also gratefully acknowledged.

This study was made possible through a grant from NASA Marshall Research Center (NAG8-1271). I wish to express my sincere gratitude for their support.

I would like to thank Mrs. Lin Shieh, Han-Chien, president of the Hon-Kao Group, for her continuous encouragement and financial support during this study.

I also would like to thank Mr. Lung-Sheng Shieh, former Vice Speaker of National Assembly of Republic of China, for his encouragement during this study.

In addition, I would like to thank my mother, Chao-Yueh, and my lovely wife, Di-Man, for their understanding and full support during this study.

Lastly, I would like to dedicate this work to my late father, Wen-Chuan, in Pure Land.

TABLE OF CONTENTS

ACKNOWLEDGMENT	iv
TABLE OF CONTENT	v
LIST OF TABLES	ix
LIST OF FIGURES	x
NOMENCLATURE	xvii
ABSTRACT	xx
CHAPTER 1 INTRODUCTION AND LITERATURE REVIEW	1
1.1 Injection Molding	1
1.2 Macroscopic Description of Flow Injection	2
1.2.1 One-Dimensional Models	2
1.2.2 Two-Dimensional Hele-Shaw Flow Models	2
1.3 Microscopic Description of Flow Injection	3
1.3.1 Moving Contact Line	4
1.3.2 Contact Angle	8
1.3.3 Fountain Flow Effect	13
1.4 Objective of Present Study	20
CHAPTER 2 FORMULATION AND NUMERICAL METHOD	30
2.1 Flow Injection through Planar Gaps	30
2.1.1 Governing Equations	30
2.1.2 Boundary Conditions	32

2.1.3	Numerical Method	34
a.	Finite Element Method	34
b.	Taylor-Galerkin Formulation	37
c.	Numerical Integration	39
d.	Free Surface Updating Scheme	41
e.	Estimation of Time Step	42
f.	Contact Line Moving Scheme	43
g.	Boundary Conditions for Surface Tension	43
h.	Automatic Mesh Generation Scheme	46
i.	Mesh Refinement Test	46
2.2	Flow Injection through Center-Gated Disks	47
2.2.1	Governing Equations	47
2.2.2	Boundary Conditions	48
2.2.3	Numerical Method	49
a.	Finite Element Method	49
b.	Boundary Conditions for Surface Tension	51
c.	Automatic Mesh Scheme	53
CHAPTER 3 ISOTHERMAL INJECTION IN PLANAR GAPS		65
3.1	Flow Injection through Vertical Channels	65
3.1.1	Gravitational Effects	65
3.1.2	Effects of Surface Tension	67

3.1.3	Pressure Distribution	68
3.2	Flow Injection through Inclined Channels	70
3.2.1	Gravitational Effects	70
3.2.2	Effects of Surface Tension	72
3.3	Flow Injection through Horizontal Channels	72
3.3.1	Gravitational Effects	72
3.3.2	Effects of Surface Tension	74
3.4	Conclusions	75
CHAPTER 4	ISOTHERMAL FLOW INJECTION IN CENTER-GATED DISKS ...	111
4.1	Flow Injection in Center-Gated Disks with Negligible Surface Tension and Gravitational Effects	112
4.2	Gravitational Effects on Flow Injection through Center-Gated Disks ...	114
4.3	Surface Tension Effects on Flow Injection through Center-Gated Disks	117
4.4	Conclusions	118
CHAPTER 5	NON-ISOTHERMAL FLOW INJECTION THROUGH VERTICAL CHANNELS	136
5.1	Temperature Effects	136
5.2	Gravitational Effects	141
5.3	Effects of Surface Tension	144
5.4	Conclusions	145
CHAPTER 6	CONCLUSIONS	180
REFERENCES	182

APPENDIX A191

LIST OF TABLES

Table 2.1	Comparison of predicted flow front travel distances (Δy) at the full-developed stage (vertical channels)	56
Table 3.1	Time required for the contact line to initiate its first move (vertical channels)	77
Table 3.2	Time required for the contact line to initiate its first move (horizontal channels): (a) upper contact line, (b) bottom contact line	77
Table 5.1	Relative front tip travel distance for various heat transfer conditions at different injection time ($Ca \rightarrow \infty$ and $St = 0$)	147
Table 5.2	Time required for the contact line to initiate its first move: (a) $Pe = 1$, (b) $Pe = 10$, and (c) $Pe = 50$	147
Table 5.3	Relative front tip travel distance under various heat transfer conditions and surface tension and gravitational effects: (a) $Pe = 1$, (b) $Pe = 10$, and (c) $Pe = 50$	148

LIST OF FIGURES

Figure 1.1	Macroscopic overview of molding with microscopic flow profile inserted (Behrens et al., 1987)	22
Figure 1.2	Contact line motion model to describe rolling motion (Mavridis et al., 1988)	23
Figure 1.3	Use of finite-element predictor-corrector method for free surface updating and moving of the contact line (Behrens et al., 1987)	24
Figure 1.4	Schematic representation of the velocity dependence of the experimentally determined contact angle θ , showing static, advancing and receding limits θ_A and θ_R	25
Figure 1.5	Conceptualization of flow field near the contact line (Dussan, 1977)	26
Figure 1.6	Schematics of kinematically consistent flow patterns (A is displaced phase and B is displacing phase): (a) split injection in A and rolling ejection in B, (b) motionless interface pattern with rolling injection in B and rolling ejection in A, and (c) rolling injection in B and split ejection in A (Savelski et al., 1995)	27
Figure 1.7	Flow field for $Ca = 10^{-3}$, slip length = $6 \times 10^{-3} R$, and contact angle = 40° with the insert showing the slipping region (Sheng and Zhou, 1992)	28
Figure 1.8	Deformation and arrangement of three sequential tracer lines show V-shape marks and mushroom-like flow shape (Coyle et al., 1987)	29
Figure 2.1	Flow injection through planar gaps: (a) vertical channels, (b) horizontal and inclined channels ($\theta = 0^\circ, 30^\circ, 45^\circ, \text{ and } 60^\circ$)	57
Figure 2.2	A four-point bilinear element and its interpolation functions	58
Figure 2.3	A nine-point biquadratic element and its interpolation functions	59
Figure 2.4	Viscosity variation of glycerol with temperature effects	60
Figure 2.5	A typical finite element mesh used for flow injection through planar gaps, (a) initial mesh (b) mesh in transition	61
Figure 2.6	Flow injection through center-gated disks	62
Figure 2.7	Construction for second radius of curvature	63

Figure 2.8	A typical finite element mesh used for flow injection through center-gated disks: (a) initial mesh, (b) mesh in transition	64
Figure 3.1	Definition of the front tip travel distance relative to the contact lines (Δy , Δy_1 , and Δy_2): (a) vertical channel, (b) horizontal or inclined channels ($\theta = 0^\circ, 30^\circ, 45^\circ$, and 60°)	78
Figure 3.2	Development of flow front in a vertical channel at various Stokes numbers ($Ca = 1$): (a) $St = 0$, (b) $St = 0.1$, (c) $St = 1$, (d) $St = 2$, and (e) $St = 10$	79
Figure 3.3	Velocity fields for flow injection in a vertical channel at various Stokes numbers ($Ca = 1$): (a) $St = 0$, (b) $St = 0.1$, (c) $St = 1$, (d) $St = 2$, and (e) $St = 10$	80
Figure 3.4	Relative flow front travel distance under various gravitational effects (vertical channels, $Ca = 1$)	81
Figure 3.5	Relationship between the Stokes number and fully developed front Tip travel distance ($Ca = 10$ and $Ca \rightarrow \infty$)	82
Figure 3.6	Fully developed front tip travel distance as a function of the Stokes and capillary numbers	83
Figure 3.7	Pressure contour of a fully developed flow field in vertical flow injection ($St = 0, Ca \rightarrow \infty$, and $\Delta P = 0.5$)	84
Figure 3.8	Comparison of pressure distribution of fully-developed creeping flow and that of flow injection with negligible surface tension and gravitational effects	85
Figure 3.9	Gravitational effects on the pressure distribution along the wall and centerline ($Ca \rightarrow \infty$): wall (- - -) and centerline (—)	86
Figure 3.10	Surface tension effects on the pressure distribution along the wall and centerline ($St = 0$): wall (- - -) and centerline (—)	87
Figure 3.11	Gravitational effects on the development of flow front in a 30° inclined channel ($Ca = 1$): (a) $St = 0.1$, (b) $St = 10$, and (c) $St = 2$	88
Figure 3.12	Gravitational effects on the development of flow front in a 45° inclined channel ($Ca = 1$): (a) $St = 0.1$, (b) $St = 10$, and (c) $St = 2$	89
Figure 3.13	Gravitational effects on the development of flow front in a 60° inclined channel ($Ca = 1$): (a) $St = 0.1$, (b) $St = 10$, and (c) $St = 2$	90

Figure 3.14	Development of flow front for flow injection in various inclined channels at $Ca = 1$ and $St = 2$	91
Figure 3.15	Gravitational effects on the velocity field for a 30° inclined channel: $St = 0.1$, (b) $St = 1$, and (c) $St = 2$	92
Figure 3.16	Gravitational effects on the velocity field for a 45° inclined channel: $St = 0.1$, (b) $St = 1$, and (c) $St = 2$	93
Figure 3.17	Gravitational effects on the velocity field for a 60° inclined channel: $St = 0.1$, (b) $St = 1$, and (c) $St = 2$	94
Figure 3.18	Relative flow front travel distance under various gravitational effects in a 30° inclined channel: (a) $St = 0.1$, (b) $St = 1$, and (c) $St = 2$	95
Figure 3.19	Relative flow front travel distance under various gravitational effects in a 45° inclined channel: (a) $St = 0.1$, (b) $St = 1$, and (c) $St = 2$	96
Figure 3.20	Relative flow front travel distance under various gravitational effects in a 60° inclined channel: (a) $St = 0.1$, (b) $St = 1$, and (c) $St = 2$	97
Figure 3.21	Pressure contour of a fully developed flow field in a 30° inclined channel ($Ca = 10$, $St = 0.1$, and $\Delta P = 0.5$)	98
Figure 3.22	Gravitational effects on the pressure distribution in a 30° inclined channel: upper wall (—) and bottom wall (- - -)	99
Figure 3.23	Gravitational effects on the pressure distribution in a 45° inclined channel: upper wall (—) and bottom wall (- - -)	100
Figure 3.24	Gravitational effects on the pressure distribution in a 60° inclined channel: upper wall (—) and bottom wall (- - -)	101
Figure 3.25	Fully developed front tip travel distance relative to the upper contact lines, Δy_1, and bottom contact line, Δy_2, as a function of the Stokes and capillary number (30° inclined channels)	102
Figure 3.26	Fully developed front tip travel distance relative to the upper contact lines, Δy_1, and bottom contact line, Δy_2, as a function of the Stokes and capillary number (45° inclined channels)	103

Figure 3.27	Fully developed front tip travel distance relative to the upper contact lines, Δy_1 , and bottom contact line, Δy_2 , as a function of the Stokes and capillary number (60° inclined channels)	104
Figure 3.28	Development of flow front for injection through a horizontal channel at various Stokes numbers ($Ca = 1$): (a) $St = 0$, (b) $St = 0.1$, (c) $St = 1$, and (d) $St = 2$	105
Figure 3.29	Velocity fields for flow injection through a horizontal channel at various Stokes numbers ($Ca = 1$): (a) $St = 0$, (b) $St = 0.1$, (c) $St = 1$, and (d) $St = 2$	106
Figure 3.30	Relative flow front travel distance under various gravitational effects (horizontal channels, $Ca = 1$): (a) $St = 0.1$, (b) $St = 1$, and (c) $St = 2$	107
Figure 3.31	Pressure contour of a fully developed flow field in a horizontal channel ($Ca = 10$, $St = 0.1$, and $\Delta P = 0.5$)	108
Figure 3.32	Gravitational effects on the pressure distribution in a horizontal channel: upper wall (—) and bottom wall (- - -)	109
Figure 3.33	Fully developed front tip travel distance relative to the upper contact lines, Δy_1 , and bottom contact line, Δy_2 , as a function of the Stokes and capillary number (horizontal channels)	110
Figure 4.1	Development of flow front for flow injection through center-gated disks with negligible surface tension and gravitational effects	121
Figure 4.2	Velocity fields for flow injection through center-gated disks with negligible surface and gravitational effects: (a) $\tau = 0.557$, (b) $\tau = 1.512$, (c) $\tau = 3.512$, and (d) $\tau = 12.009$	122
Figure 4.3	Relative front tip travel distance for flow injection through center-gated with negligible surface tension and gravitational effects	123
Figure 4.4	Development of contact angles in a center-gated flow injection without surface tension and gravitational effects (a) upper contact angle, (b) bottom contact angle	124
Figure 4.5	Pressure contour for flow injection through center-gated disks with negligible surface tension and gravitational effects ($\Delta P = 0.5$)	125
Figure 4.6	Development of flow front for flow injection through center-gated disks under various gravitational effects ($Ca = 1$): (a) $Bo = 0.1$, (b) $Bo = 1$, (c) $Bo = 5$, and (d) $Bo = 10$	126

Figure 4.7	Velocity fields for flow injection through center-gated disks under various gravitational effects ($Ca = 1$): (a) $Bo = 0.1$, (b) $Bo = 1$, (c) $Bo = 5$, and (d) $Bo = 10$	128
Figure 4.8	Relative front tip travel distance for flow injection through center-gated disks under various gravitational effects ($Ca = 1$)	129
Figure 4.9	Development of moving contact angles for flow injection through center-gated disks under various gravitational effects ($Ca = 1$): (a) $Bo = 0.1$ and $Bo = 10$	130
Figure 4.10	Pressure contours ($\Delta P = 1$) for flow injection through center-gated disks under various gravitational effects ($Ca = 1$): (a) $Bo = 0.1$, (b) $Bo = 1$, $Bo = 5$, and (d) $Bo = 10$	131
Figure 4.11	Development of flow front for flow injection through center-gated disks under various surface tension effects ($Bo = 1$): (a) $Ca = 0.1$, (b) $Ca = 0.2$, (c) $Ca = 1$, (d) $Ca = 2$, and (e) $Ca = 10$	132
Figure 4.12	Relative front tip travel distance for flow injection through center-gated disks under various surface tension effects ($Bo = 1$)	134
Figure 4.13	Development of moving contact angles for flow injection through center-gated disks under various surface tension effects ($Bo = 1$)	135
Figure 5.1	Development of flow front in a vertical channel at various Peclet numbers ($Ca \rightarrow \infty$ and $St = 0$): (a) $Pe = 1$, (b) $Pe = 10$, (c) $Pe = 50$	149
Figure 5.2	Velocity fields for flow injection in a vertical channel at various Peclet numbers ($Ca \rightarrow \infty$ and $St = 0$): (a) $Pe = 1$, (b) $Pe = 10$, and (c) $Pe = 50$	150
Figure 5.3	Thermal effects on the velocity distribution ($Pe = 10$): (a) along the centerline, and (b) cross-channel thickness at various flow locations	151
Figure 5.4	Relative flow front travel distance for various Peclet numbers ($Ca \rightarrow \infty$ and $St = 0$)	152
Figure 5.5	Temperature contours at various injection times ($Pe = 10$, $Ca \rightarrow \infty$ and $St = 0$): (a) $\tau = 4.03$, (b) $\tau = 5.02$, and (c) $\tau = 6.02$ ($\Delta T = 0.1$)	153
Figure 5.6	Viscosity contours at various injection times ($Pe = 10$, $Ca \rightarrow \infty$, and $St = 0$): (a) $\tau = 4.03$, (b) $\tau = 5.02$, and (c) $\tau = 6.02$ ($\Delta \mu = 0.15$)	154

Figure 5.7	Temperature contours for flow injection at various Peclet number ($St = 0$ and $Ca \rightarrow \infty$): (a) $Pe = 10$ (constant viscosity), (b) $Pe = 1$, (c) $Pe = 10$, and (d) $Pe = 50$ ($\Delta T = 0.1$)	155
Figure 5.8	Viscosity contours for flow injection at various Peclet numbers ($St = 0$ and $Ca \rightarrow \infty$): (a) $Pe = 1$, (b) $Pe = 10$, and (c) $Pe = 50$ ($\Delta\mu = 0.15$)	156
Figure 5.9	Pressure contours for flow injection at various Peclet numbers ($St = 0$ and $Ca \rightarrow \infty$): (a) $Pe = 1$ ($P_{max} = 185.33$, $P_{min} = -45.66$, and $\Delta P = 3$), (b) $Pe = 10$ ($P_{max} = 58.66$, $P_{min} = -5.68$ and $\Delta P = 1$), and (c) $Pe = 50$ ($P_{max} = 39.79$, $P_{min} = -3.60$, and $\Delta P = 1$)	157
Figure 5.10	Thermal effects on the pressure distribution along the wall and centerline ($Ca \rightarrow \infty$ and $St = 0$): wall (- - -) and centerline (—)	158
Figure 5.11	Variation of contact angle at various Peclet numbers ($Ca \rightarrow \infty$ and $St = 0$): (a) $Pe = 1$, (b) $Pe = 10$, and (c) $Pe = 50$	159
Figure 5.12	Development of flow front under various gravitational effects ($Ca = 1$): (a) $Pe = 1$, (b) $Pe = 10$, and (c) $Pe = 50$	160
Figure 5.13	Velocity fields for flow injection in a vertical channel under various gravitational effects ($Ca = 1$): (a) $Pe = 1$, (b) $Pe = 10$, and (c) $Pe = 50$..	163
Figure 5.14	Relative flow front travel distance under various gravitational effects ($Ca = 1$): (a) $Pe = 1$, (b) $Pe = 10$, and (c) $Pe = 50$	166
Figure 5.15a	Pressure contours for flow injection under various gravitational effects ($Ca = 1$): $Pe = 1$ ($\Delta P = 5$) ..	167
Figure 5.15b	Pressure contours for flow injection under various gravitational effects ($Ca = 1$): $Pe = 10$ ($\Delta P = 3$)	168
Figure 5.15c	Pressure contours for flow injection under various gravitational effects ($Ca = 1$): $Pe = 50$ ($\Delta P = 2$) ..	169
Figure 5.16	Gravitational effects on the pressure distribution along the wall and centerline for various Peclet numbers ($Ca = 1$): wall (- - -) and centerline (—)	170
Figure 5.17	Temperature contours at various injection times for $St = 1$, $Ca = 1$, and $Pe = 10$ ($\Delta T = 0.1$): (a) $\tau = 4.02$, (b) $\tau = 5.04$, and (c) $\tau = 6.01$	171
Figure 5.18	Viscosity contours at various injection times for $St = 1$, $Ca = 1$, and $Pe = 10$ ($\Delta\mu = 0.15$): (a) $\tau = 4.02$, (b) $\tau = 5.04$, and (c) $\tau = 6.01$..	172

Figure 5.19	Temperature contours under various gravitational effects ($Ca = 1$): (a) $Pe = 1$, (b) $Pe = 10$, and (c) $Pe = 50$ ($\Delta T = 0.1$)	173
Figure 5.20	Viscosity contours under various gravitational effects ($Ca = 1$): (a) $Pe = 1$, (b) $Pe = 10$, and (c) $Pe = 50$ ($\Delta\mu = 0.15$)	176
Figure 5.21	Pressure distribution along the centerline under various surface tension effect ($St = 0$): $Ca = 1$ (—) and $Ca \rightarrow \infty$ (- - -)	179

NOMENCLATURE

Bo	Bonds number, $Bo = Ca \cdot St = \rho g R_0^2 / \gamma$
Ca	capillary number, $\mu U_\infty / \gamma$
d_{n+1}	root mean square truncation error at time τ_{n+1}
f	normal force at the free surface
g	acceleration due to gravity
H	half gap width
K	dimensionless mean surface curvature
\vec{n}	unit outward normal vector
p	pressure
P	dimensionless pressure, $p / (\mu U_\infty / H)$
P_a	dimensionless ambient pressure
Pe	Peclet number, $Pe = Re \cdot Pr = U_\infty H / \alpha$
R_1, R_2	radius of curvature of the free surface
Δr_1	dimensionless front tip travel distance relative to the upper contact line (center-gated disks)
Δr_2	dimensionless front tip travel distance relative to the bottom contact line (center-gated disks)
R_i	radius of center gate disks
Re	Reynolds number, $\rho U_\infty H / \mu$
St_x	x-component of the Stokes number, $\rho g_x H^2 / \mu U_\infty$
St_y	y-component of the Stokes number, $\rho g_y H^2 / \mu U_\infty$

\vec{t}	unit tangent vector
T_i	inlet temperature
T_w	wall temperature
U_∞	average velocity at the entrance
U, u	dimensionless and dimensional velocity in x-direction, $U = u / U_\infty$
V_n	nodal velocity of the free surface at time τ_n
V, v	dimensionless and dimensional velocity in y-direction, $V = v / U_\infty$
X, x	dimensionless and dimensional coordinate in the direction perpendicular to the flow, $X = x / H$
Y, y	dimensionless and dimensional coordinate in the flow direction, $Y = y / H$
Δy	dimensionless relative front tip travel distance (vertical channel)
Δy_1	dimensionless front tip travel distance relative to the upper contact line (horizontal or inclined channel)
Δy_2	dimensionless front tip travel distance relative to the bottom contact line (horizontal or inclined channel)
ϕ	interpolation function for the pressure
γ	surface tension
η	coordinate in the transformed domain
λ	penalty parameter
μ	dynamic viscosity fluid
μ_∞	reference dynamic viscosity of fluid
ρ	density of fluid
θ	inclined angle
τ	dimensionless time, $t / (H / U_\infty)$

- $\Delta\tau_n$ n^{th} time step, $\Delta\tau_n = \tau_{n+1} - \tau_n$
- σ_n normal stress component at the free surface
- σ_t tangential stress component at the free surface
- ξ coordinate in the transformed domain
- ψ interpolation function for the velocities and temperature
- Γ boundary
- Ω computational domain

ABSTRACT

The filling process of injection molding in various planar gaps and center-gated disks are analyzed numerically. Comprehensive mathematical models are developed for flows in planar gaps and center-gated disks. An incompressible Newtonian fluid with creeping velocity is assumed in the present study. Also assumed is that the fluid viscosity is a function of temperature only.

Because the fountain flow effect plays an important role on the molecular orientation, the related effects of gravitational force, surface tension, and non-isothermal conditions on the fountain flow are systematically analyzed for flow injection through various mold geometries and orientations. Additionally, in order to seek a complete and general understanding of the flow fields involved, all the variables presented are non-dimensionalized. The results of negligible surface tension and gravitational effects are compared with previous studies and have well agreement.

The transient development of flow front, required injection pressure in the inlet and velocity and temperature distributions have been obtained for different molding conditions. These results provide the important information for the design of the new molding process, such as the construction of mold, exit gate design, choice of material, heat transfer design and so on.

CHAPTER 1

INTRODUCTION AND LITERATURE REVIEW

1.1 Injection Molding

Injection molding is one of the main manufacturing techniques for producing identical products from the designed mold in polymer processing. The process can be divided into three steps: filling stage, packing stage, and cooling stage. The filling stage is the most important and complex step of the injection molding cycle. Material deformation and orientation that take place during the filling stage have a major effect on the morphology and ultimate properties of the molded part.

Since the pioneering work of Spencer and Gilmore (1951), injection mold filling has been the subject of great interest over the last three decades. Their study has dealt with the modeling of the fluid mechanics in the mold filling process, pressure and temperature variations in the molding cycle, time dependence of the flow front position during the mold filling, and orientation and residual stresses in the molded part. In their study, they considered the problem to be one-dimensional. The actual mold filling process on a macroscopic scale is shown in Fig. 1.1. Fluid is injected from the gate. It fills the mold when it advances to the right. The plot shows the advancing flow front at successive times. The insert of the cross-sectional diagram in Fig. 1.1 shows the fountain flow effect in the transverse plane, which is one of the main interests in the present study.

1.2 Macroscopic Description of Flow Injection

1.2.1 One-Dimensional Models

Ballman and co-workers (1959a, b) reported the first model of non-isothermal mold filling in thin rectangular cavities. They used the power law model to track the fluid velocity in the mold. The effect of molding process conditions on the resulting orientation distribution and its consequence on the physical properties of the mold part were studied. Later, Harry and Parrot (1970) performed a numerical simulation for flow injection in rectangular thin cavities by coupling the energy and momentum equations. The problem was considered as a quasi-stationary flow and the constant injection pressure was imposed. A similar model for the rectangular cavities was also reported by Lord and William (1975) and Thienel and Menges (1978).

For the filling problems of center-gated disk, numerical simulation and experimental results were reported by Kamal and Kenig (1972a, b). Further numerical simulations and experimental studies were presented by Berger and Gogos (1973) and Wu et al. (1974).

Considering the geometric complexity involved in most mold cavities in industry, the one-dimensional model is apparently not capable of producing detailed information about the filling process. Nevertheless, this simple approach allows one to obtain a quick solution and the first estimate of the process.

1.2.2 Two-Dimensional Hele-Shaw Flow Models

Generally speaking, the thickness of most injection molded parts is very small. It allows the simplification of an originally three-dimensional flow injection problem to a

two-dimensional flow progression problem. Based on this idea, Tadmor et al. (1974) developed a method called Flow Analysis Network (FAN) to predict the flow front position and the pressure field during cavity filling. The same model was numerically solved using a finite element/finite difference formulation (Hieber and Shen, 1980; Chiang et al., 1991) and a boundary element formulation (Shen, 1984). The numerical simulation for the advancing flow front, the location of weldlines and the pressure field at various positions within the cavity have a good agreement with the measured data (Hieber et al., 1983). Kuo and Kamal (1976) presented an analytical solution for flow injection in rectangular cavities by solving the Laplace equation for pressure, which was coupled with the energy equation. Good agreement between the analytical results and experimental data were found for the flow front position and pressure distribution.

1.3 Microscopic Description of Flow Injection

Although the Hele-Shaw flow models can effectively describe the overall macroscopic behavior of the flow injection and predict the pressure, flow rate, required filling time, and the position of the leading edge of the fluid. However, it can not provide any insight to the flow pattern in the direction of the part thickness, such as the shape of flow front, velocity, and pressure distributions near the front. For example, it can not provide the detailed information needed for the prediction of molecular orientation for homopolymers or the orientation of fibers for fiber reinforced plastics. It also can not reveal the fountain flow pattern near the free surface as observed by Rose (1961).

In the following sections, some fundamental issues related to flow injection molding are discussed. These include the moving contact line, contact angle, and fountain flow effect. A literature review on these subjects is also provided.

1.3.1 Moving Contact Line

A contact line forms at the intersection of the fluid-fluid interface and solid wall. A fundamental difficulty in the hydrodynamic analysis of dynamic wetting arises when the no-slip boundary condition is applied to the contact line. Since the normal stress difference across the fluid interface varies with R^{-1} (where R is the distance from the contact line), the work done by wall stresses and surface force required to advance the liquid becomes logarithmically infinite (Huh and Scriven, 1971). This singular effect was reported by Moffat (1964) and Bhattacharji and Savic (1965) in the analysis of a steady, creeping flow of liquid with a flat, free surface intersecting a moving solid wall. Their findings seem to contradict the common belief (i.e., no-slip boundary condition) in fluid mechanics. Particularly, Goldstein (1938) stated that the confidence in the no-slip assumption for liquids flowing over the solid surface was based on the direct experimental evidences and which agreed with the macroscopic theories that relied on the assumption. The confidence was reinforced by the analysis of flow over a rough surface, which showed that even the perfect slip was assumed at the submicroscopic length scale, the flow appeared to obey the no-slip boundary condition at the length scale larger than the asperities (Richardson, 1973; Jansons, 1988).

However, Dussan and Davis (1974) emphasized that the unbounded force was a dynamic consequence of the multivalued velocity field at the contact line. They showed

that no-slip boundary condition and the moving contact line are kinematically compatible.

Huh and Scriven (1971) were the first to theoretically deal with the moving contact line and showed the consequence of the stress singularity. In order to remove (mentioned above) the singularity, various slip boundary conditions have been proposed (Huh and Scriven, 1971; Hocking, 1976, 1977; Dussan, 1976; Huh and Mason, 1977; Greenspan, 1978; Lowndes, 1980; Cox, 1986; Durbin, 1988).

Hocking (1977) has successfully analyzed the flow field associated with the displacement of two immiscible fluids through a capillary tube and between two parallel plates by using a slip boundary condition. One of his major contributions was to demonstrate that the flow field containing moving contact lines could be analyzed near the singular points by the method of matched asymptotic expansions (Dussan, 1979; Kafka and Dussan, 1979).

Huh and Mason (1977) proposed a slip boundary condition based on a physical model of the motion of a gas-liquid interface. When the molecules of the liquid rolled onto the contact line, they were not oriented and required a re-orientation time t before attaching the solid surface. During the re-orientation time, they experienced no drag force by the solid surface and they did not slip along the surface afterward. The main criticism of this model came from Dussan (1979). As she pointed out, the model declared that the liquid underwent a rolling motion, but the solution of the problem showed that it was not so. Material points located on the gas-liquid interface never arrived at the moving contact line and the contact line always consisted of the same material points.

More recently, the studies of molecular dynamics of the immiscible liquid/liquid displacement on a smooth solid surface showed that the no-slip boundary condition broke down at a distance of a few molecular diameters away from the moving contact line (Thompson and Robbins, 1989; Koplík et al., 1988).

Although the slip boundary conditions are effective in dealing with the free surface flow problems with moving contact lines, the selection of a slip boundary condition is however never easy. Since a slip condition can remove the singularity mentioned above, it has been widely used for its mathematical convenience, but not for its physical correctness. The approach itself has some serious weak points (Shikhmurzaev, 1994, 1996, 1997) which include: (i) it replaces the actual rolling motion of the liquid by the sliding motion, and qualitatively changes the characteristics of the liquid flow; (ii) the velocity-dependence of the dynamic contact angle cannot be obtained using this approach and it must be prescribed instead.

Yarnold (1938) was the first to use the term rolling motion to describe his observation that dust particles sprinkled on top of a mercury drop sliding down an inclined plane advanced at a velocity that was considerably greater than that of the drop as a whole. The motion of liquid along the interface toward the moving contact line has been confirmed by following the movement of dye marks placed in the liquids (Dussan and Davis, 1974; Dussan, 1977) and by direct measurement with LDV (Mues, 1989). Later, the rolling motion was modeled in the numerical simulation of fountain flow by Behrens et al. (1987) and Mavridis et al. (1988).

In order to describe the actual rolling motion of the liquid, Mavridis et al. (1988) illustrated the rolling motion processes as shown in Fig. 1.2. In the beginning, free

surface ABCD is perpendicular to the wall at time t_0 . As the flow advances (at time t_1), the liquid particles in the free surface ABCD roll toward the solid wall and the contact angle increases. In their numerical algorithm, the position of the contact line remains fixed until when the contact angle becomes 180° . Afterward, a fixed contact line position is replaced by the 180° contact angle condition, and the contact line is allowed to move.

Kistler (1984) reported that the Galerkin finite element method allows the computation of macroscopic flow solutions without imposing the slip boundary condition on the dynamic contact line. Since the method was based on a weak form of the governing equation, one could manage the discretization to satisfy both the kinematic condition of interface and the condition of impervious solid surface at the contact line. Behrens et al. (1987) and Mavridis et al. (1988) took the advantage of this approach and applied the no-slip boundary condition in their numerical models.

Instead of prescribing a 180° dynamic contact angle as the boundary condition, Behrens (1983) and Behrens et al. (1987) determined the contact line movement using the projected shape functions. For a given free surface mesh at t_n , they calculated the velocities of each node along the free surface at the same instant, then moved the free surface nodes to their new location at t_{n+1} as shown in Fig. 1.3. If the projected free surface did not intersect the boundary wall at more than one location, they concluded that the contact line did not move within this time step. But, if the projected free surface intersected the boundary wall at another location, this point of intersection became the new contact line. This model has successfully described the “rolling” motion of the fluid as reported earlier by Yarnold (1938) and Dussan and Davis (1974). In this method, the

size of the time step is controlled by some prescribed conditions and is calculated through a predictor-corrector numerical procedure. This method was later adopted by Friedrichs and Guceri (1993). It has also been adopted in the present study. To numerically simulate the advancement of free surface and the movement of contact line from t_n to t_{n+1} , one needs to move the nodes on the free surface to their new positions. The procedure to relocate the free surface nodes is schematically presented in Fig. 1.3.

1.3.2 Contact Angle

The contact angle between the fluid-fluid interface and solid wall plays an important role in the solution of any wetting problem. It is given as a boundary condition to determine the shear stress on the solid wall and the surface force on the free surface. It leads to the determination of the interface shape. The dependence of the dynamic contact angle on the capillary number (Ca) has been reported by many investigators (Elliott and Riddiford, 1967; Hansen and Toong, 1971a; Hoffman, 1975; Jiang et al., 1979; Ngan and Dussan, 1989; Dussan et al., 1991; and Shikhmurzaev, 1994, 1996, and 1997).

Elliott and Riddiford (1967) measured the angle at which the wall appeared to make with the interface at the solid-fluid-fluid intersection (i.e., contact line). They assumed that the angle measured was equal to that at a close range to the wall. Their experimental results showed that advancing contact angle was independent of the interfacial velocity at small capillary numbers. Above a certain critical capillary number (1 mm/min in their experiment), the advancing contact angle at first increased linearly with Ca . But at a higher capillary number, the rate of change diminished until it finally reached a limiting value. They also showed that the upper limiting value for the

advancing contact angle was 180° in the case of a two-liquid system. However, they found that it was difficult to correlate the advancing contact angle with any particular velocity in their experiment.

A direct (photographic) measurement of the contact angle characterizing interfaces in motion in a capillary tube was reported by Rose and Heins (1962). The axial distance between the apex of the meniscus and the contact line was measured. They assumed that the interface was a sector of a sphere and the angle formed between the interface and the capillary tube would be the contact angle.

Based on the hydrodynamic analysis, Hansen and Toong (1971a) were the first to point out that the fluid-fluid interface might be severely deformed by the viscous forces in the vicinity of the solid-fluid-fluid intersection, even in the case of a small capillary number. The measured contact angle in the capillary tube was probably not its actual contact angle and it could not be accurately measured using low-magnification optical techniques. Instead of measuring the contact angle with protractor, they reported their findings in terms of an apparent contact angle (Hansen and Toong, 1971a, b) given by the following equation:

$$\theta_{App} = \cos^{-1} \left\{ \frac{-2H/a}{1 + (H/a)^2} \right\} \quad (1.1)$$

where a is the radius of capillary and H is the distance between the meniscus apex and the plane containing the contact line.

For a low capillary number, they found that the interface between a heavy paraffin oil and air was a spherical sector. For a high capillary number, for example $Ca = 2.12$, they reported deviations from a spherical shape. They also reported that the classical laws of fluid motion and interface behavior were not applicable for the range

which was smaller than 10^{-5} cm from the contact line. Since molecular interaction might be dominant in this range, it precluded the use of continuum concepts. Their theory predicted a 13° difference between the contact angle obtained from (Eq. 1.1) and that evaluated at a distance of 10^{-5} cm from the moving contact line at a capillary number of 2×10^{-3} .

In the study of the shape of an advancing interface in a liquid-gas system, Hoffman (1975) found that the apparent contact angle could be correlated as a function of the capillary number with a shift factor $f(\theta_s)$ when the interfacial and viscous forces were the dominant factors controlling the system. If the interfacial forces between a solid and a liquid did not change when the flow occurred, the shift factor could be determined solely by the static contact angle between the liquid and solid wall. He also reported that the shift factor $f(\theta_s)$ could be determined using the apparent contact angle θ_{App} instead of θ_s . Hoffman's experiments (1975) covered a wide range of capillary numbers ($4 \times 10^{-5} < Ca < 36$), allowing the contact angle to vary from a few degrees to approximately 180° . The resulting correlation was compared with the data of Hansen and Toong (1971a) and Rose and Heins (1962). A good agreement was found. Based on the experimental data presented by Hoffman (1975), Jiang et al., (1979) presented an explicit expression of Hoffman's correlation. They found that the data were best fitted by the following curve:

$$\frac{\cos\theta_s - \cos\theta_{App}}{\cos\theta_s + 1} = \tanh(4.96Ca^{0.702}) \quad (1.2)$$

Voinov (1976) did not consider the region of stress singularity immediate in the vicinity of the contact line. He prescribed an angle θ_m at the distance h_m from the contact line, which was on the order of molecular dimension. He proposed a profile equation for the interface at a location close to but not right at the contact line. He balanced the local capillary pressure with the normal stresses directly calculating from Moffat's (1964) solution which acted on a straight wedge with the local slope $\theta(r)$. The approximate result for contact angle $\theta < 135^\circ$, given by

$$\theta^3 - \theta_m^3 = 9Ca \ln(h / h_m) \quad (1.3)$$

When θ_m approaches zero, Voinov's results reduces to the well-known power law proposed by Tanner (1979) for small capillary numbers.

$$\theta_d \sim Ca^{1/3} \quad (1.4)$$

The power law was directly derived from hydrodynamics theory without assuming a prewet surface by Tanner (1979). It has been verified by the experiments of de Gennes (1985). For this reason, equation (1.4) was referred as Hoffman-Voinov-Tanner law by Kistler (1993). Later, the approach of Voinov (1976) was also adopted by Boender et al. (1991).

To remove the singularity in stress at the moving contact line, Huh and Scriven (1971) and Dussan (1979) suggested that the force singularity was non-integrable if the contact angle was less than 180° . Later, Pisman and Nir (1982) pointed out that this singularity could be relaxed as the dynamic contact angle approached 180° in the immediate vicinity of the moving contact line. The no-slip boundary condition and 180° dynamic contact angle were applied to the mold filling related problems by Blake (1987), Coyle et al. (1987), and Mavridis et al. (1988).

Although the concept of the apparent contact angle has been well received, it is not the true dynamic contact angle after all. It is also not a material property of the system. Ngan and Dussan (1982, 1984) were the first to present the size effect on the apparent contact angle from their experimental results.

Based on the earlier findings reported by Hocking and Rivers (1982) and Cox (1986), Ngan and Dussan (1989) introduced the parameter θ_r , defined to be the contact angle at some distance from the contact line, for which the interface was located within the intermediate region. They used θ_r as a boundary condition to predict the size effect they had observed earlier in experiments.

This model was improved by Dussan et al. (1991). The interface shape at low capillary numbers was given by:

$$\theta \sim g^{-1}\left(g(\omega_0) + Ca \ln(r/a)\right) + f_0(r/a; \omega_0; R_T/a) - \omega_0 \quad (1.5)$$

$$g(x) = \int_0^x \frac{y - \sin(y) \cos(y)}{2 \sin(y)} dy \quad (1.6)$$

where θ is the local slope of the interface with respect to the solid wall, r is the distance from the contact line to the point on the interface, which is located at the intermediate region where viscous effect and surface tension are both important, a is the capillary length $\sqrt{\sigma/\rho g}$, and g^{-1} is the inverse function of g . A good agreement between the predictions from this model and the experimental results was found (Dussan et al., 1991). The experimental data of Marsh (1992), Marsh et al. (1993), and Chen et al. (1995) have shown that this model accurately predicts the interface shape within 300 μm from the contact line for $Ca < 0.1$. However, ω_0 shown in Eq. (1.5) depends on the material properties of the system, and which must be determined experimentally. ω_0 plays a

similar role of the dynamic contact angle. Apparently, It would be difficult to apply this model in the numerical simulation without the value of ω_0 from experiment.

In the numerical simulation of the mold filling process, the condition of 180° dynamic contact angle is commonly used for fluid with high viscosity and negligible surface tension (Coyle et al., 1987; Mavridis et al., 1988). From the numerical results presented by Behrens et al. (1987), in which only no-slip boundary condition was applied to the solid wall, the dynamic contact angle was found to be close to 180° . In a review of contact angles by Blake (1993), he concluded that the contact angle was in a certain range of values, even for the static contact angle (Fig. 1.4). In addition, the flow direction (advancing or receding) plays an important role to determine the value of the dynamic contact angle. This conclusion has prompted the use of Behrens's free surface updating and contact line moving schemes in the present study.

1.3.3 Fountain Flow Effect

Rose (1961) introduced "fountain effect" to describe the advancing fluid particles from the central region decelerate as they approach the slower moving interface region, and which requires a finite outward component of velocity as they roll over towards the advancing interface. Correspondingly, a "reverse fountain effect" has been observed in the receding fluid ahead of the interface as the fluid particles are displaced from the wall region and move towards the centerline. As such, the fluid particles accelerate centrally ahead of the advancing interface.

Based on the experimental observation, Rose concluded that the tangential velocity was zero at the boundary of each phase forming the interfacial region. The

capillary pressure at each point in the interface region would have some constant value and the moving interface would have a constant curvature throughout. However, it was later found that Rose's argument was not completely valid. The flow field with fountain effect and reverse fountain effect is shown in Fig. 1.5, which also reveals the presence of two vortices near the receding interface.

More recently, Savelski et al. (1995) experimentally studied the flow patterns associated with the steady movement of immiscible fluids. Their experimental results showed that there were three types of flow patterns in the vicinity of a moving contact line, depending on the ratio of viscosity of the advancing fluid to that of receding fluid. One was observed by Rose (1961). The other two flow patterns both had rolling motion and split-injection (or split-ejection) streamlines are shown in Fig. 1.6. Based on the slip model proposed by Huh and Mason (1977) and the assumption of dynamic contact angle being equal to static contact angle, Sheng and Zhou (1992) presented their numerical results of the dynamics of immiscible-fluid displacement in a capillary tube. Their results showed that the shape of the interface and the macroscopic immiscible-fluid behavior were determined by the slip length and pre-set dynamic contact angle. The macroscopic flow pattern with the microscopic details in the slipping region is shown in Fig. 1.7.

Tadmor (1974) presented a semi-quantitative model to estimate the effect of fountain flow on molecular orientation by assuming the flow as a planar stagnation flow. The flow was considered fully developed before the fluid particle moved into a region within one gap width (or one diameter for tube in axisymmetric case) from the front. Based on approximation, the centerline velocity would decrease linearly from the

maximum value to the average one. Since Tadmor assumed a constant elongation rate, it can be calculated to give

$$\begin{aligned} d_{11} &= (U_{\max} - U_{\text{avg}}) / 2H \\ &= 0.25U_{\text{avg}} / H && \text{(planar flow)} && (1.7a) \end{aligned}$$

$$= 0.5U_{\text{avg}} / H \quad \text{(axisymmetric flow)} \quad (1.7b)$$

Behrens et al. (1987) and Mavridis et al. (1988) compared Eq. (1.7) with their finite element results. They found that it did provide a reasonable approximation after adjustment of some numerical coefficients.

Schmidt (1974) found that for a thin-wall molding, colored pellets introduced along the centerline came out at the surface in contact with the mold walls in a reverse order of that they were introduced. The lines of tracers were deformed into a series of characteristic “V” shape marks.

To numerically simulate the fountain flow effect, a finite difference method combined with the marker and cell (MAC) scheme was used by Huang (1978) to keep track of the front progression in a fixed frame of reference. The same numerical technique was employed in the studies of Gogos et al. (1986), Lafleur and Kamal (1986), Kamal and Lafleur (1986), and Kamal et al. (1986, 1988).

By finite element simulations, Wang et al. (1978, 1979) and Mavridis et al. (1986a) presented a steady-state results of the flow front in a parallel channel. Mavridis et al. (1986b) put some tracer fluid elements in the core region to investigate the deformation and orientation of their path, and to reveal the fountain effect in the flow front. The “V” shape marks formed near the wall were illustrated as a “rolling” type

motion which fell far behind the advancing front. Later, the tracer technique was adopted by Coyle et al. (1987) to obtain a more comprehensive picture on the formation of “V” shape marks. A mushroom-like flow front was formed when the V-shaped marks were swept backward parallel to the walls as shown in Fig. 1.8.

A boundary element method with tracer-in-domain technique was applied to simulate the fountain flow by Jin (1993). The moving boundary nodes were relocated at each time step. In this approach, only the boundary values are involved in the calculation. If any boundary element was stretched longer than a critical length, one additional node was inserted between the two boundary nodes to form two new elements to replace the old one. Similar results to the earlier studies were reported and which were in close agreement with the visualization results shown by Schmidt (1974).

The mechanism of the fountain flow was investigated by Beris (1987). He showed that the deformation of “V” shape marks in the front region was independent of the constitutive equations, and it was only determined by the flow continuity and the viscous force.

The first theoretical approach to determine the flow field inside a tube was reported by Bhattacharji and Savic (1965). The flat interface with no shear and no-slip boundary condition was assumed. The analytical solution was presented in terms of streamfunction. The model developed by Bhattacharji and Savic (1965) was later adopted by Castro and Macosko (1982), Lekakou and Richardson (1986), and Gong (1994) in their studies of the reaction injection mold-filling process. The model of Bhattacharji and Savic (1965) has been reported to have a singularity in stresses at the contact line by Huh and Scriven (1971). Various slip boundary conditions have been

proposed to replace the no-slip one. The alternative boundary conditions were proposed by Huh and Mason (1977), Hocking and Rivers (1982), Cox (1986) and many others.

Behrens (1983) and Behrens et al. (1987) studied the transient fountain flow in a tube and a planar gap by using Galerkin finite element method. They considered an isothermal, incompressible Newtonian fluid with a low Reynolds number (i.e., creeping flow). Since the understanding of true dynamic contact angle was limited, no-slip boundary was applied to the wall instead of using a specified contact angle. The relative distance between the front tip and the contact line in the flow direction (Δy) was calculated. They showed that, for axisymmetric flows, the fully developed relative front tip travel distance Δy was 0.865 when using a fixed frame of reference and it was 0.82 when using a moving frame of reference. A good agreement was found between the numerical prediction and their experimental results.

A similar finite element method was employed by Mavridis et al. (1988) to solve the full Navier-Stokes equations to predict the transient flow front shape. The only exception was that a 180° contact angle boundary condition was employed in the latter study. However a good agreement with the experimental results of Behrens (1983) and Behrens et al. (1987) was achieved by combining the free surface deformation method of Khesghi and Scriven (1984) and Keunings (1986) with a predictor-corrector scheme for the case of negligible surface tension and gravitational effects. Fauchon et al. (1991) presented a numerical simulation for fountain flow, flow in a 90° bent, and jet in a sudden expansion. The fountain flow numerical results were compared with those of Behrens et al. (1987) and Mavridis et al. (1988).

The study of transient fountain flow for viscoelastic fluids was reported by Sato and Richardson (1995) using a finite element method and a finite volume method. The contour plots of pressure, normal stress, and shear stress for Oldroyd-B fluids with different operating conditions were presented for a flow domain of up to approximately sixteen times of the gap width. The reported fully-developed front tip travel distance was between 0.92 and 0.98.

Some of the models discussed earlier have been applied to reaction injection molding (RIM) simulations. In the filling process of the reaction injection molding, the fluid contains chemical species undergoing temperature-dependent reaction and thus has a temperature-dependent viscosity. From the engineering point of view, it is most important to know how a melt front advancing in a thick rectangular mold cavity and how the viscosity affects the flow advancement in the cavity. The model of Bhattacharji and Savic (1965) was adopted by Castro and Macosko (1982) in a study of the injection molding in rectangular thick cavities. The assumptions that they made include a flat flow front, uniform mixture properties such as viscosity in the fountain flow region, and a quasi-steady condition with respect to the momentum balance at the flow front. They found that the fountain flow effect significantly influenced the temperature and conversion behavior in the mold. The numerical solution was found in good agreement with their experimental results.

Lekakou and Richardson (1986) adopted the same model of Castro and Macosko (1982) but employed a finite difference/control volume method in their numerical study. The time dependent term was retained in their analysis. Their model was reported to reproduce the results of previous studies.

A numerical model similar to that of Lekakou and Richardson (1986) was employed by Perrett et al. (1993) without the assumption of a flat front and a parabolic flow region behind the front. Neglecting the surface tension and gravitational effects, the predicted front shape in a thin mold was approximately semi-circular. They compared their results with those of the flat front model (Lekakou and Richardson, 1986) and experimental results of Castro and Macosko (1982). The macroscopic pressure, temperature, and conversion profiles were shown very little sensitive to the front shape. In the force balance analysis, they reported that the curved front shape provided a better result than the flat one.

The Petrov-Galerkin finite element method was applied to the reaction injection molding problem by Anturkar (1994, 1995). The predicted results were compared with those obtained by the conventional Galerkin finite element method and the reported experimental data of Castro and Macosko (1982). The results showed that the Petrov-Galerkin finite element formulation was more stable and accurate than the conventional (Galerkin) formulation, particularly when convection is dominant.

Lee (1997) solved the non-isothermal, power-law non-Newtonian flow injection using finite element method. In the numerical simulation, the streamline Upwind/Petrov-Galerkin technique proposed by Brooks and Hughes (1982) was employed. The fully-developed relative front tip travel distance Δy was reported to be 50% higher than the results of Behrens et al. (1987). His simulation also found that the shapes of free surface became flatter as the melt front advanced and Δy approached unity (i.e., approximately a semicircle).

1.4 Objective of Present Study

The motivation of the present study has stemmed from a recent investigation on the feasibility of producing high-performance composite materials under microgravity environment. It has been speculated that the special spreading and wetting characteristics of resin in space may lead to the production of super-strength composite materials using resin transfer molding (RTM) process. To evaluate this technical plausibility, it is important to have a complete understanding of gravitation, surface tension, and heat transfer effects on the development of the flow front.

For impregnation of a fibrous pre-form, these factors can significantly influence the fluid behavior. Particularly, surface tension may become the dominant factor in microgravity environment. Since the phenomena involved are very complicated, it has been decided to first investigate the flow injection process in the absence of fibrous pre-form. Thus, the present study is the first step toward a comprehensive modeling of the fiber impregnation process.

It should be mentioned that the previous studies on injection molding have all neglected the surface tension and gravitational effects except one study by Coyle et al. (1987). However, these effects on injection molding were considered only for a very limited case in a vertical channel ($St = 33$ and $Ca = 5$). As such, the related flow details and their general trends were not fully disclosed. Therefore, it is also the objective of the present study to supplement the literature with a complete study of the effects of surface tension and gravitation on flow injection.

To this end, the present study has covered a wide range of the governing parameters. For flow injection in planar gaps, channels at various inclined angles ($\theta =$

0° , 30° , 45° , 60° , and 90°) have been studied. The parametric ranges considered are $1 \leq Pe \leq 50$, $0 \leq St \leq 10$, and $1 \leq Ca \leq \infty$. For flow injection through center-gated disks, the parametric ranges are $0 \leq Bo$ ($Bo = St \cdot Ca$) ≤ 10 and $Ca = 0.1, 0.2, 1, 2, 10$, and ∞ .

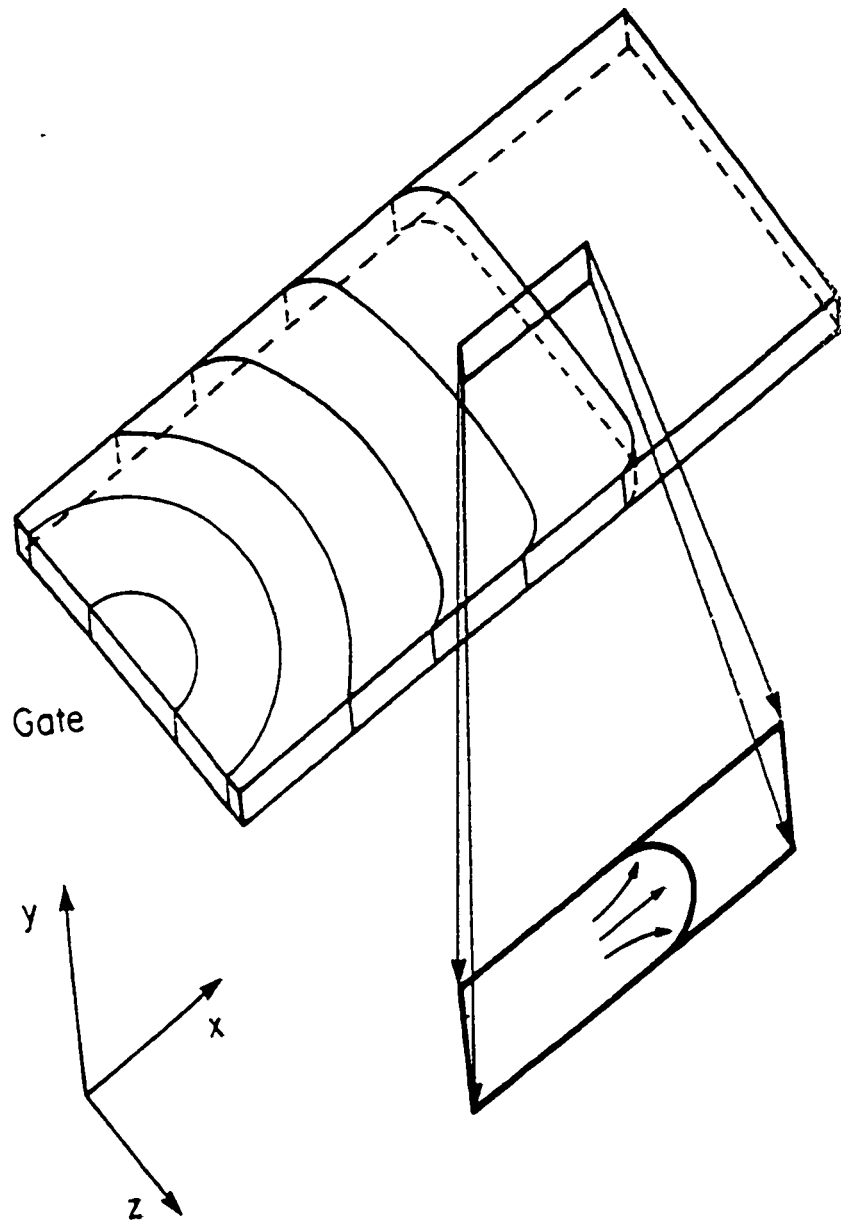


Figure 1.1 Macroscopic overview of molding with microscopic flow profile inserted (Behrens et al., 1987)

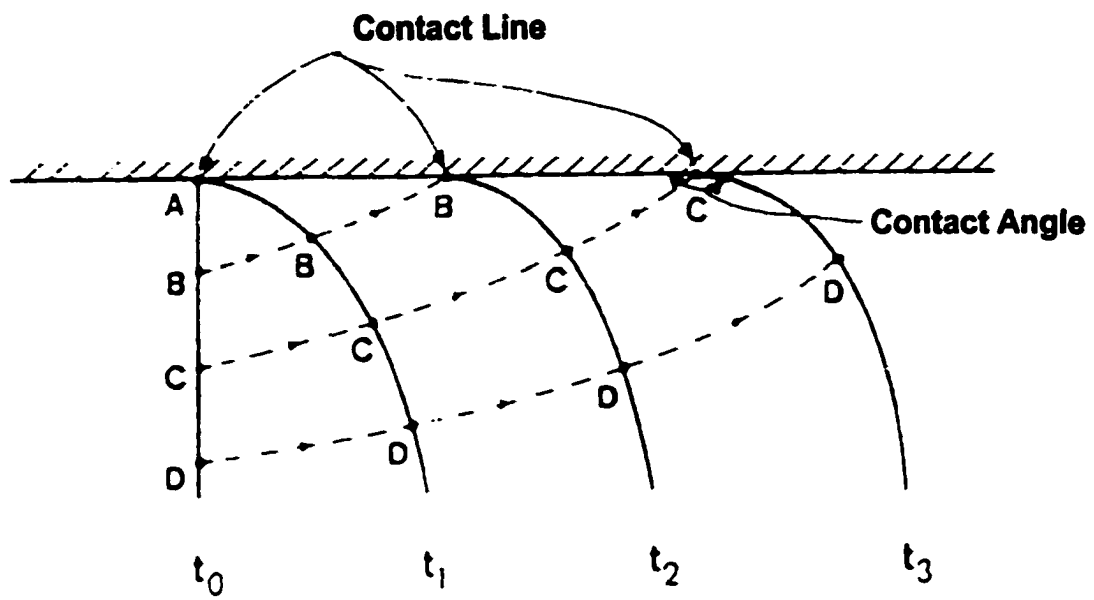
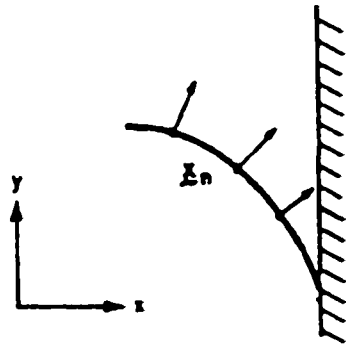


Figure 1.2 Contact line motion model to describe rolling motion (Mavridis et al., 1988).

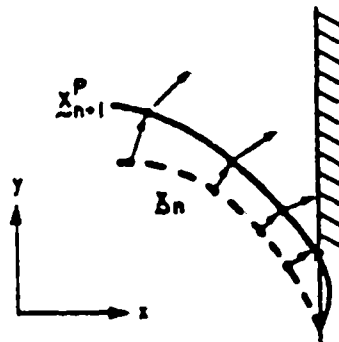
1. Initial Surface



$$\xi_n \text{ given}$$

$$y_n = f(\xi_n)$$

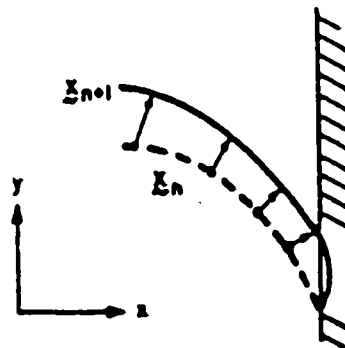
2. Predicted Surface



$$\xi_{n+1}^P = \xi_n + \Delta t_n \left[v_n + \frac{\Delta t_n}{2\Delta t_{n-1}} (v_n - v_{n-1}) \right]$$

$$y_{n+1}^P = f(\xi_{n+1}^P)$$

3. Corrected Surface



$$\xi_{n+1} = \xi_n + \frac{\Delta t_n}{2} (v_n + v_{n+1}^P)$$

Figure 1.3 Use of finite-element predictor-corrector method for free surface updating and moving of the contact line (Behrens et al., 1987).

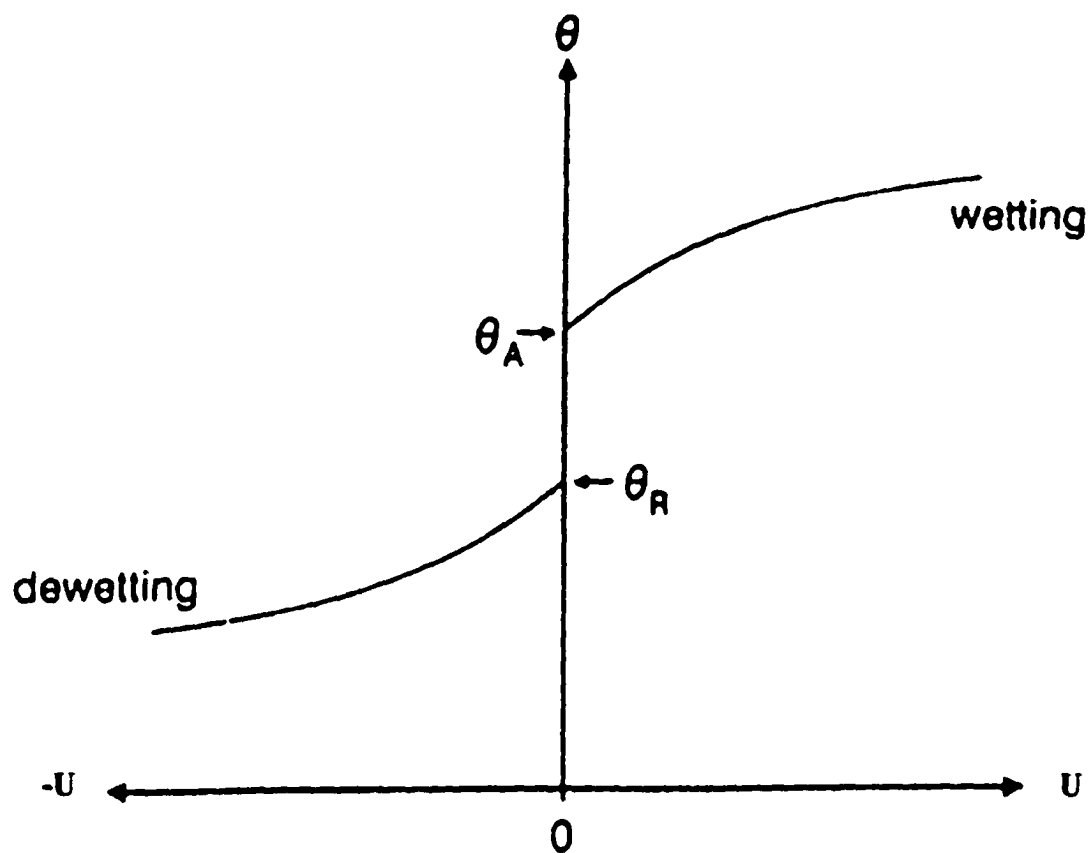


Figure 1.4 Schematic representation of the velocity dependence of the experimentally determined contact angle θ , showing static, advancing and receding limits θ_A and θ_R (Blake, 1993).

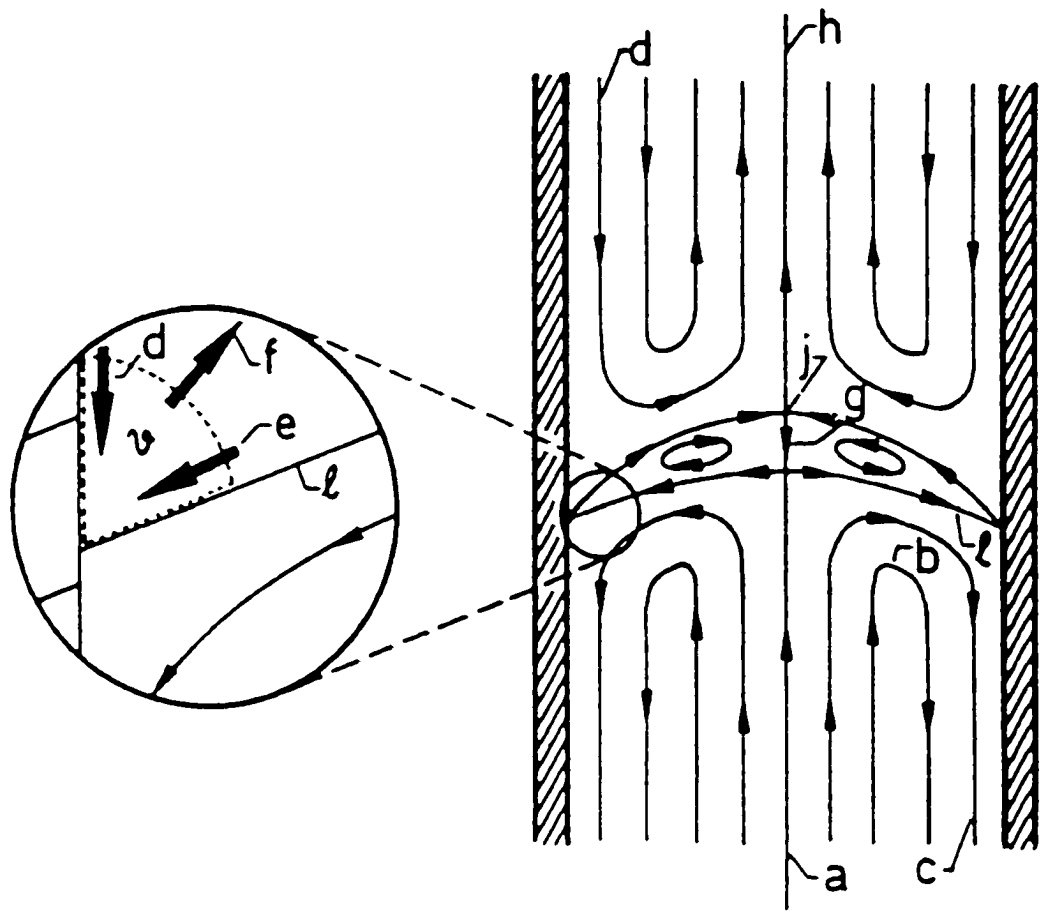


Figure 1.5 Conceptualization of flow field near the contact line (Dussan, 1977)

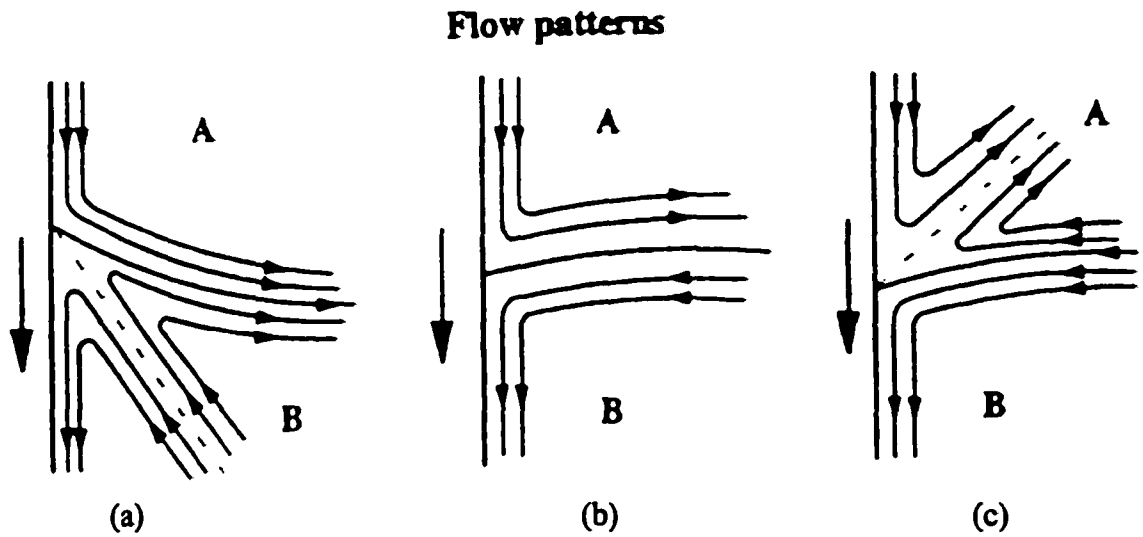


Figure 1.6 Schematics of kinematically consistent flow patterns (A is displaced phase and B is displacing phase): (a) split injection in A and rolling ejection in B, (b) motionless interface pattern with rolling injection in B and rolling ejection in A, and (c) rolling injection in B and split ejection in A (Savelski et al., 1995).

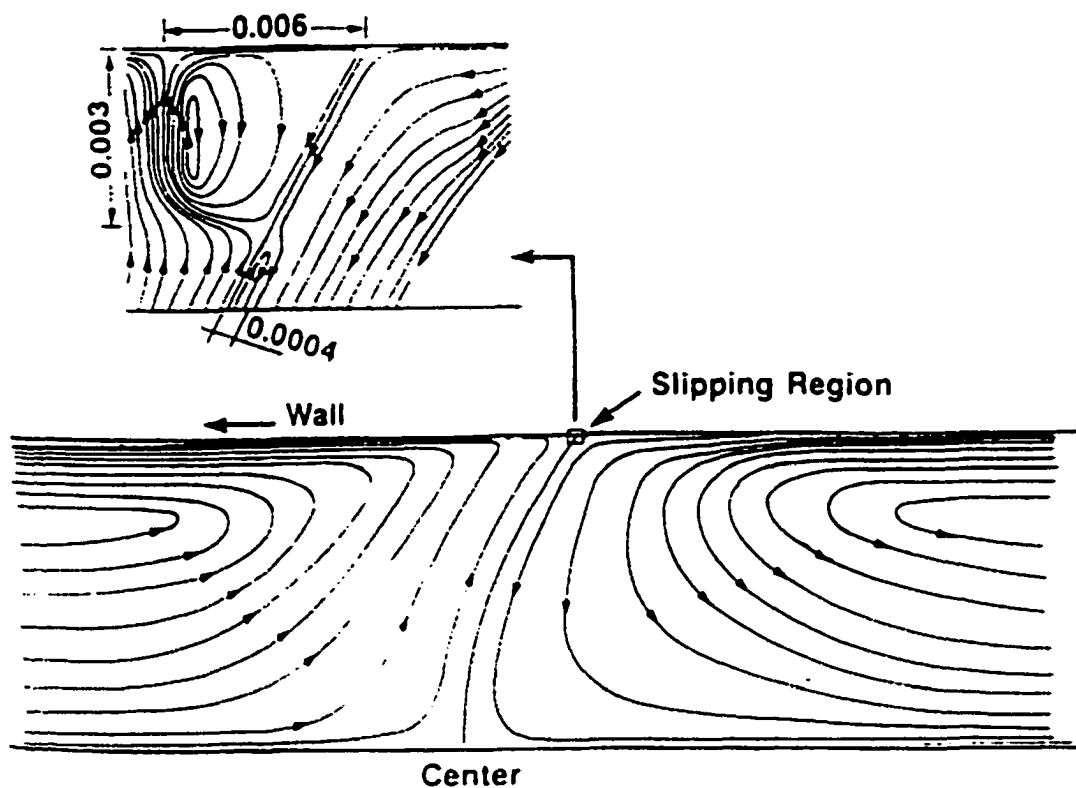


Figure 1.7 Flow field for $Ca = 10^{-3}$, slip length = $6 \times 10^{-3} R$, and contact angle = 40° with the insert showing the slipping region (Sheng and Zhou, 1992).

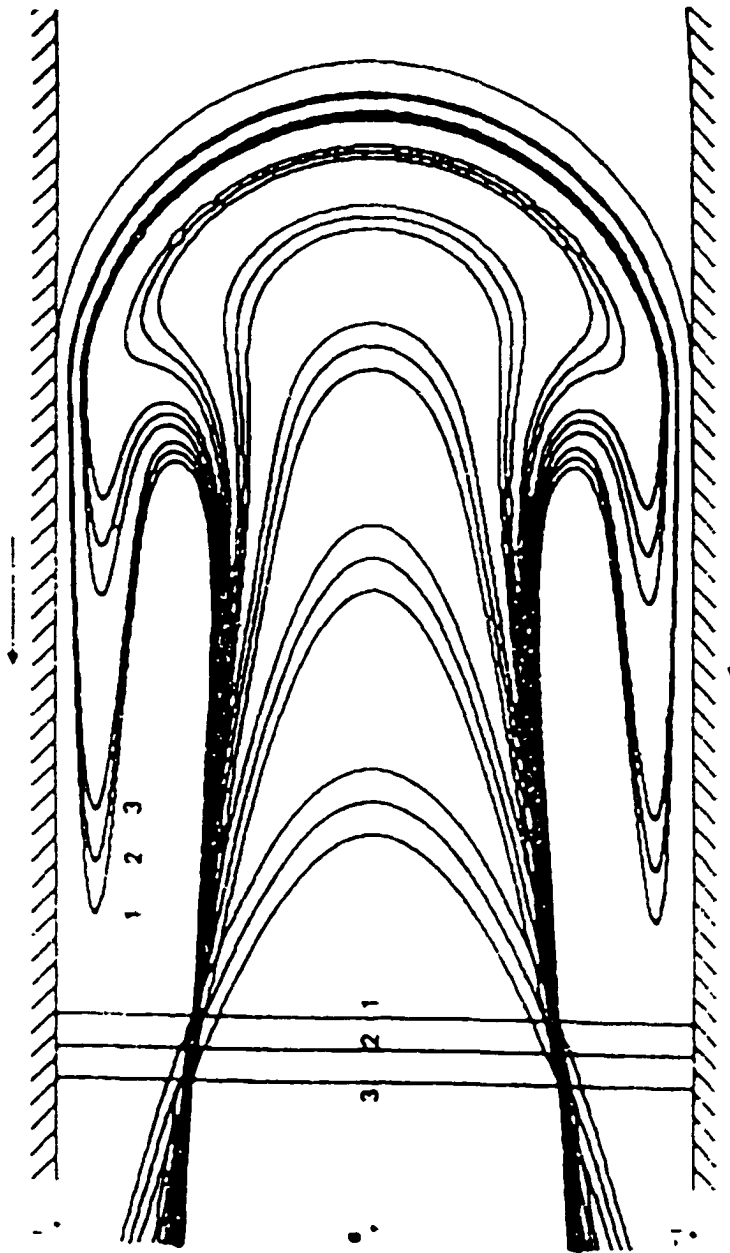


Figure 1.8 Deformation and arrangement of three sequential tracer lines show V-shape marks and mushroom-like flow shape (Coyle et al., 1987).

CHAPTER 2

FORMULATION AND NUMERICAL METHOD

2.1 Flow Injection through Planar Gaps

2.1.1 Governing Equations

The filling process in flow injection molding through planar gaps can be modeled as a transient flow front advancing between two parallel plates (Fig. 2.1). The geometries considered include vertical channels (with the gravitational force acting against the flow direction), horizontal channels, and inclined channels (with an inclined angle $\theta = 30^\circ$, 45° , 60°). For an incompressible Newtonian fluid, the continuity and momentum equations are given as follows:

Continuity Equation:

$$\frac{\partial u}{\partial x} + \frac{\partial v}{\partial y} = 0, \quad (2.1a)$$

Momentum Equations:

$$\rho \left(\frac{\partial u}{\partial t} + u \cdot \frac{\partial u}{\partial x} + v \cdot \frac{\partial u}{\partial y} \right) = -\frac{\partial p}{\partial x} + \frac{\partial}{\partial x} \left(2\mu \frac{\partial u}{\partial x} \right) + \frac{\partial}{\partial y} \left(\mu \left(\frac{\partial u}{\partial y} + \frac{\partial v}{\partial x} \right) \right) - \rho g_x, \quad (2.1b)$$

$$\rho \left(\frac{\partial v}{\partial t} + u \cdot \frac{\partial v}{\partial x} + v \cdot \frac{\partial v}{\partial y} \right) = -\frac{\partial p}{\partial y} + \frac{\partial}{\partial x} \left(\mu \left(\frac{\partial u}{\partial y} + \frac{\partial v}{\partial x} \right) \right) + \frac{\partial}{\partial y} \left(2\mu \frac{\partial v}{\partial y} \right) - \rho g_y. \quad (2.1c)$$

If temperature effects on the flow field are considered, then energy equation must be included and solved simultaneously with the previous two equations. To simplify the problem, it is assumed that the viscosity of the fluid is dependent on the fluid temperature, while other properties (such as density, heat capacity, conductivity and

surface tension) remain constant in this study. For a non-isothermal, incompressible Newtonian fluid, the energy equation is given as:

$$\rho c_p \left(\frac{\partial T}{\partial t} + u \cdot \frac{\partial T}{\partial x} + v \cdot \frac{\partial T}{\partial y} \right) = k \cdot \left(\frac{\partial^2 T}{\partial x^2} + \frac{\partial^2 T}{\partial y^2} \right) \quad (2.1d)$$

where c_p and k are the specific heat capacity and thermal conductivity of the fluid, respectively. The variables are normalized using the average entry velocity U_∞ , half gap width H and reference viscosity μ_∞ . For pressure and time, they are non-dimensionalized using $\mu_\infty U_\infty / H$ and H / U_∞ . The governing equations in the dimensionless form are given below.

$$\frac{\partial U}{\partial X} + \frac{\partial V}{\partial Y} = 0, \quad (2.2a)$$

$$\text{Re} \left(\frac{\partial U}{\partial \tau} + U \cdot \frac{\partial U}{\partial X} + V \cdot \frac{\partial U}{\partial Y} \right) = -\frac{\partial P}{\partial X} + \frac{\partial}{\partial X} \left(2 \frac{\mu}{\mu_\infty} \frac{\partial U}{\partial X} \right) + \frac{\partial}{\partial Y} \left(\frac{\mu}{\mu_\infty} \left(\frac{\partial U}{\partial Y} + \frac{\partial V}{\partial X} \right) \right) - \text{St}_x, \quad (2.2b)$$

$$\text{Re} \left(\frac{\partial V}{\partial \tau} + U \cdot \frac{\partial V}{\partial X} + V \cdot \frac{\partial V}{\partial Y} \right) = -\frac{\partial P}{\partial Y} + \frac{\partial}{\partial X} \left(\frac{\mu}{\mu_\infty} \left(\frac{\partial U}{\partial Y} + \frac{\partial V}{\partial X} \right) \right) + \frac{\partial}{\partial Y} \left(2 \frac{\mu}{\mu_\infty} \frac{\partial V}{\partial Y} \right) - \text{St}_y, \quad (2.2c)$$

$$\text{Pe} \left(\frac{\partial T}{\partial \tau} + U \cdot \frac{\partial T}{\partial X} + V \cdot \frac{\partial T}{\partial Y} \right) = \frac{\partial^2 T}{\partial X^2} + \frac{\partial^2 T}{\partial Y^2}. \quad (2.2d)$$

where Re is the Reynolds number, $\rho U_\infty H / \mu_\infty$. The body force terms in x and y direction are expressed in terms of the Stoke numbers, $\text{St}_x = \rho g_x H^2 / \mu_\infty U_\infty$ and $\text{St}_y = \rho g_y H^2 / \mu_\infty U_\infty$, which are defined as the ratio of gravitational forces to viscous forces. Pe is the Peclet number ($\text{Pe} = U_\infty H / \alpha = \text{Re} \cdot \text{Pr}$), which measures the relative magnitude of thermal

energy carried by the flow to heat transfer by conduction.

Since the injection velocity is usually small, the flow is assumed to be quasi-steady in this study. The time dependent term and inertial terms are neglected due to the assumption of $Re \ll 1$. Thus, the original transient problem is now reduced to a series of quasi-steady processes. Consequently, the momentum equations are simplified to give

$$\frac{\partial P}{\partial X} - \frac{\partial}{\partial X} \left(2 \frac{\mu}{\mu_{\infty}} \frac{\partial U}{\partial X} \right) - \frac{\partial}{\partial Y} \left(\frac{\mu}{\mu_{\infty}} \left(\frac{\partial U}{\partial Y} + \frac{\partial V}{\partial X} \right) \right) + St_x = 0, \quad (2.3a)$$

$$\frac{\partial P}{\partial Y} - \frac{\partial}{\partial X} \left(\frac{\mu}{\mu_{\infty}} \left(\frac{\partial U}{\partial Y} + \frac{\partial V}{\partial X} \right) \right) - \frac{\partial}{\partial Y} \left(2 \frac{\mu}{\mu_{\infty}} \frac{\partial V}{\partial Y} \right) + St_y = 0. \quad (2.3b)$$

If the order of magnitude of the Peclet number is much less than unity, then energy equation can be further simplified to Eq. (2.3c). Otherwise, the whole energy equation, Eq. (2.2d) will be solved simultaneously with the continuity and momentum equations.

$$\frac{\partial^2 T}{\partial X^2} + \frac{\partial^2 T}{\partial Y^2} = 0. \quad (2.3c)$$

2.1.2 Boundary Conditions

For vertical channels (i.e., the inclined angle is 90°), the governing equations are solved using only half of the channel due to the symmetry of the problem. For all other cases, the equations are solved using the entire channel. In the present study, the fluid is assumed to be injected into the channel with a constant flow rate and a fully developed velocity profile. The appropriate boundary conditions for the problem are

- At the inlet,

$$U = 0, \quad V = V(X), \quad T = T_i. \quad (2.4a)$$

- Along the channel walls ($X = \pm 1$),

$$U = 0, \quad V = 0, \quad T = T_w. \quad (2.4b)$$

- Along the free surface, the normal force component is proportional to the local curvature of the free surface and the surface tension. In addition, the tangential force component vanishes and heat transfer from the flow front to the ambient air is assumed negligible,

$$\sigma_t = 0, \quad \sigma_n = \frac{K}{Ca} + P_a, \quad k \frac{\partial T}{\partial X_n} = 0. \quad (2.4c)$$

where σ_t and σ_n are the dimensionless stresses in the tangential and normal direction, respectively. K is the dimensionless mean surface curvature and P_a is the ambient pressure. $Ca (= \mu U_\infty / \gamma)$ is the capillary number defined as the ratio of viscous force to surface tension. Accordingly, a small capillary number implies a large surface tension. When the capillary number approaches infinity, the surface tension effect becomes insignificant.

For vertical channels, the boundary condition at the wall ($X = -1$), Eq. (2.4b), is replaced by the symmetrical condition at the centerline ($X = 0$), i.e.,

- Along the centerline,

$$U = 0, \quad \frac{\partial V}{\partial X} = 0, \quad \frac{\partial T}{\partial X} = 0. \quad (2.4d)$$

2.1.3 Numerical Method

a. Finite Element Method

Since the flow domain is continuously deformed and expands for flow injection problems, it is felt that finite element method is best suit for this kind of problems. In the finite element method, the unknown velocities and pressures are approximated using following expressions,

$$U \approx \sum_{i=1}^N \psi_i(\xi, \eta) U_i(\tau), \quad (2.5a)$$

$$V \approx \sum_{i=1}^N \psi_i(\xi, \eta) V_i(\tau), \quad (2.5b)$$

$$P \approx \sum_{j=1}^M \phi_j(\xi, \eta) P_j(t), \quad (2.5c)$$

where U_i , V_i , P_j are the nodal velocities and pressure at a given time step, respectively; ψ_i and ϕ_j are the interpolation functions of velocity and pressure, N and M are the number of nodes used in the approximation of velocities and pressure at each element. In the present study, a nine-point quadrilateral element was used for the calculation of the velocity field and a four-point bilinear element for the pressure field. ξ and η are the coordinates in the isoparametric domain. A four-point bilinear element and a nine-point biquadratic element and their relative interpolation functions are expressed in Fig. 2.2 and Fig. 2.3.

The transformation between the physical and isoparametric domain is given below.

$$X = \sum_{i=1}^N \psi_i(\xi, \eta) X_i(\tau), \quad (2.6a)$$

$$Y = \sum_{i=1}^N \psi_i(\xi, \eta) Y_i(\tau), \quad (2.6b)$$

where $-1 \leq \xi \leq 1$ and $-1 \leq \eta \leq 1$.

With the adoption of the Galerkin criterion and the selection of the weighting function $w_i(x, y) = \psi_i(x, y)$ in Eq. (2.5), one can derive the following system of equations from Eq. (2.3).

$$\int_{\Omega} \left[2 \frac{\partial \psi_i}{\partial X} \frac{\mu}{\mu_{\infty}} \frac{\partial U}{\partial X} + \frac{\partial \psi_i}{\partial Y} \frac{\mu}{\mu_{\infty}} \left(\frac{\partial U}{\partial Y} + \frac{\partial V}{\partial X} \right) - \frac{\partial \psi_i}{\partial X} P \right] d\Omega = - \int_{\Omega} \psi_i St_x d\Omega + \int_{\Gamma} \psi_i T_x d\Gamma, \quad (2.7a)$$

$$\int_{\Omega} \left[\frac{\partial \psi_i}{\partial X} \frac{\mu}{\mu_{\infty}} \left(\frac{\partial U}{\partial Y} + \frac{\partial V}{\partial X} \right) + 2 \frac{\partial \psi_i}{\partial Y} \frac{\mu}{\mu_{\infty}} \frac{\partial V}{\partial Y} - \frac{\partial \psi_i}{\partial Y} P \right] d\Omega = - \int_{\Omega} \psi_i St_y d\Omega + \int_{\Gamma} \psi_i T_y d\Gamma, \quad (2.7b)$$

$$\int_{\Omega} \psi_i \left(\frac{\partial U}{\partial X} + \frac{\partial V}{\partial Y} \right) d\Omega = 0, \quad (2.7c)$$

$$\text{where } T_x = \left(2 \frac{\mu}{\mu_{\infty}} \frac{\partial U}{\partial X} - P \right) \cdot n_x + \frac{\mu}{\mu_{\infty}} \left(\frac{\partial U}{\partial Y} + \frac{\partial V}{\partial X} \right) \cdot n_y, \quad (2.7d)$$

$$T_y = \frac{\mu}{\mu_{\infty}} \left(\frac{\partial U}{\partial Y} + \frac{\partial V}{\partial X} \right) \cdot n_x + \left(2 \frac{\mu}{\mu_{\infty}} \frac{\partial V}{\partial Y} - P \right) \cdot n_y. \quad (2.7e)$$

Express velocities and pressure in terms of their interpolation functions, one obtains

$$\begin{bmatrix} 2\mathbf{K}_{11} + \mathbf{K}_{22} & \mathbf{K}_{21} & -\mathbf{Q}_1 \\ \mathbf{K}_{12} & \mathbf{K}_{11} + 2\mathbf{K}_{22} & -\mathbf{Q}_2 \\ -\mathbf{Q}_1^T & -\mathbf{Q}_2^T & \mathbf{0} \end{bmatrix} \begin{bmatrix} \mathbf{U} \\ \mathbf{V} \\ \mathbf{P} \end{bmatrix} = \begin{bmatrix} \mathbf{F}_x \\ \mathbf{F}_y \\ \mathbf{0} \end{bmatrix}, \quad (2.8)$$

$$\text{where } K_{ij} = \int_{\Omega} \frac{\partial \psi}{\partial X_i} \frac{\mu}{\mu_{\infty}} \frac{\partial \psi^T}{\partial X_j} d\Omega, \quad (2.9a)$$

$$Q_i = \int_{\Omega} \frac{\partial \psi}{\partial X_i} \phi^T d\Omega, \quad (2.9b)$$

$$F_x = - \int_{\Omega} \psi St_x d\Omega + \int_{\Gamma} \psi T_x d\Gamma, \quad (2.9c)$$

$$F_y = - \int_{\Omega} \psi St_y d\Omega + \int_{\Gamma} \psi T_y d\Gamma. \quad (2.9d)$$

For isothermal condition ($\mu/\mu_{\infty} = 1$) and Eq. (2.9a) can be simplified further. Otherwise, the temperature effect on the fluid viscosity should be considered in Eq. (2.9a). In this study, the variation of fluid viscosity with temperature is assumed to be an inverse linear function as shown in Eq. (2.10) below.

$$\mu = \frac{1}{(A + B \cdot T)} \quad (2.10)$$

where A and B are the coefficients of correlation. In this expression, temperature is in °C and viscosity in Pa · s .

Most polymeric resins experience a phase change (specifically solidification) when exposed to a large temperature variation. To avoid further complication from phase change, glycerol has been chosen as the sample fluid in the present study. Although this dose not represent the actual process, it is expected that the results obtained should at least provide us a qualitative assessment of the process variables.

The viscosity of glycerol is correlated with temperature using available data in the literature. The correlation was performed using TableCurve 2D (Jandel Scientific,

Window v2.03) and the coefficients were found to be $A = -2.3595155$ and $B = 0.15342883$. The variation of viscosity of glycerol with temperature is plotted in Fig. 2.4.

b. Taylor-Galerkin Formulation

For small Peclet numbers, the conventional Galerkin finite element formulation can be applied to the convection-diffusion problems and provide reasonable results. However, for convection dominant problems (i.e., problems with large Peclet numbers), spurious oscillations may arise and completely obscure the true result. To avoid the numerical oscillations mentioned above, Taylor-Galerkin formulation has been applied to the energy equation in this study. Taylor-Galerkin method was first introduced by Donea (1984) for various time marching schemes. Later Donea et al. (1984) and Zienkiewicz et al. (1984, 1985) extended this method to the solution of advection-diffusion problems. Consider the dimensionless energy equation,

$$Pe\left(\frac{\partial T}{\partial \tau} + U \cdot \frac{\partial T}{\partial X} + V \cdot \frac{\partial T}{\partial Y}\right) = \frac{\partial^2 T}{\partial X^2} + \frac{\partial^2 T}{\partial Y^2}. \quad (2.11)$$

Using the forward Taylor series expansion, one has

$$\frac{T_{n+1} - T_n}{\Delta \tau} = T'_n + \frac{\Delta \tau}{2} T''_n + O(\Delta \tau)^2, \quad (2.12)$$

where T'_n is the first derivative of temperature with respect to time at the n^{th} time step.

From Eq. (2.11), one can obtain the following expressions.

$$Pe T'_n = -Pe\left(U_n \frac{\partial T_n}{\partial X} + V_n \frac{\partial T_n}{\partial Y}\right) + \frac{\partial^2 T_n}{\partial X^2} + \frac{\partial^2 T_n}{\partial Y^2}, \quad (2.13)$$

$$\text{Pe}T_n' = -\text{Pe}(U_n \frac{\partial T_n'}{\partial X} + V_n \frac{\partial T_n'}{\partial Y}) + \frac{\partial^2 T_n'}{\partial X^2} + \frac{\partial^2 T_n'}{\partial Y^2}, \quad (2.14)$$

Eq. (2.14) is resulted from taking further differentiation with respect to time to Eq. (2.13).

The variation of velocity within the time step is assumed negligible. Since the time step is chosen to be very small, it is not likely to have a drastic change in velocity. Substitute Eqs. (2.13) and (2.14) into Eq. (2.12) and neglect the higher order terms, one yields

$$\begin{aligned} \text{Pe}(\frac{T_{n+1} - T_n}{\Delta\tau}) &= \text{Pe}(T_n' + \frac{\Delta\tau}{2} T_n'') \\ &= -\text{Pe}(U_n \frac{\partial T_n'}{\partial X} + V_n \frac{\partial T_n'}{\partial Y}) + \nabla^2 T_n' - \frac{\Delta\tau}{2} \text{Pe}(U_n \frac{\partial T_n'}{\partial X} + V_n \frac{\partial T_n'}{\partial Y}) + \frac{\Delta\tau}{2} \nabla^2 T_n' \\ &= -\text{Pe}(U_n \frac{\partial T_n'}{\partial X} + V_n \frac{\partial T_n'}{\partial Y}) + \nabla^2 T_n' + \frac{\Delta\tau}{2} \text{Pe} U_n \frac{\partial}{\partial X} ((U_n \frac{\partial T_n'}{\partial X} + V_n \frac{\partial T_n'}{\partial Y}) - \nabla^2 T_n') \\ &\quad + \frac{\Delta\tau}{2} \text{Pe} V_n \frac{\partial}{\partial Y} ((U_n \frac{\partial T_n'}{\partial X} + V_n \frac{\partial T_n'}{\partial Y}) - \nabla^2 T_n') + \frac{\Delta\tau}{2} \nabla^2 T_n', \end{aligned} \quad (2.15)$$

which can be further simplified to give

$$\begin{aligned} \text{Pe}(\frac{T_{n+1} - T_n}{\Delta\tau}) &= -\text{Pe}(U_n \frac{\partial T_n'}{\partial X} + V_n \frac{\partial T_n'}{\partial Y}) + \nabla^2 T_n' + \frac{\Delta\tau}{2} \text{Pe} U_n \frac{\partial}{\partial X} (U_n \frac{\partial T_n'}{\partial X} + V_n \frac{\partial T_n'}{\partial Y}) \\ &\quad + \frac{\Delta\tau}{2} \text{Pe} V_n \frac{\partial}{\partial Y} (U_n \frac{\partial T_n'}{\partial X} + V_n \frac{\partial T_n'}{\partial Y}) + \frac{\Delta\tau}{2} \nabla^2 (\frac{T_{n+1} - T_n}{\Delta\tau}). \end{aligned} \quad (2.16)$$

In Eq. (2.16), the higher order terms are neglected and the last term with T_n' in

Eq. (2.15) is approximated by $(T_{n+1} - T_n)/\Delta\tau$ to avoid third-order derivatives. Collecting

the coefficients of T_{n+1} and T_n , the final equation can be written as

$$\frac{\text{Pe}}{\Delta\tau} T_{n+1} - \frac{1}{2} \nabla^2 T_{n+1}$$

$$\begin{aligned}
&= \frac{\text{Pe}}{\Delta\tau} T_n + \frac{1}{2} \nabla^2 T_n - \text{Pe} \left(U_n \frac{\partial T_n}{\partial X} + V_n \frac{\partial T_n}{\partial Y} \right) + \frac{\text{Pe} \Delta\tau}{2} U_n \frac{\partial}{\partial X} \left(U_n \frac{\partial T_n}{\partial X} + V_n \frac{\partial T_n}{\partial Y} \right) \\
&\quad + \frac{\text{Pe} \Delta\tau}{2} V_n \frac{\partial}{\partial Y} \left(U_n \frac{\partial T_n}{\partial X} + V_n \frac{\partial T_n}{\partial Y} \right). \tag{2.17}
\end{aligned}$$

The conventional Galerkin finite element formulation is applied to Eq. (2.17). A nine-point biquadratic element is used for the calculation of temperature distribution.

The unknown temperatures are approximated using in the following expression,

$$T \approx \sum_{i=1}^N \psi_i(\xi, \eta) T_i(\tau), \tag{2.18}$$

With the integration by parts on the higher order terms, the fully discretised Galerkin equations can be written as

$$\left(\frac{\mathbf{M}}{\Delta\tau} + \frac{\mathbf{K}}{2} \right) \mathbf{T}_{n+1} = \left(\frac{\mathbf{M}}{\Delta\tau} - \frac{\mathbf{K}}{2} - \text{Pe}(\mathbf{A} + \mathbf{S}) \right) \mathbf{T}_n, \tag{2.19}$$

where $\mathbf{M} = \text{Pe} \int_{\Omega} \psi \psi^T d\Omega,$ (2.20a)

$$\mathbf{K} = \int_{\Omega} \left(\frac{\partial \psi}{\partial X} \frac{\partial \psi^T}{\partial X} + \frac{\partial \psi}{\partial Y} \frac{\partial \psi^T}{\partial Y} \right) d\Omega, \tag{2.20b}$$

$$\mathbf{A} = \int_{\Omega} \psi \left(U_n \frac{\partial \psi^T}{\partial X} + V_n \frac{\partial \psi^T}{\partial Y} \right) d\Omega, \tag{2.20c}$$

$$\mathbf{S} = \frac{\Delta\tau}{2} \int_{\Omega} \left(U_n^2 \frac{\partial \psi}{\partial X} \frac{\partial \psi^T}{\partial X} + U_n V_n \frac{\partial \psi}{\partial X} \frac{\partial \psi^T}{\partial Y} + V_n U_n \frac{\partial \psi}{\partial Y} \frac{\partial \psi^T}{\partial X} + V_n^2 \frac{\partial \psi}{\partial Y} \frac{\partial \psi^T}{\partial Y} \right) d\Omega. \tag{2.20d}$$

c. Numerical Integration

Since all the calculations are performed on the computational (isoparametric)

domain, it is necessary to establish the Jacobian matrix first in order to facilitate the numerical integration. The transformation between the derivatives of the interpolation

function $(\frac{\partial \psi_i}{\partial \xi}, \frac{\partial \psi_i}{\partial \eta})$ and derivatives of coordinates $(\frac{\partial \psi_i}{\partial X}, \frac{\partial \psi_i}{\partial Y})$ is established using the

chain rule.

$$\frac{\partial \psi_i}{\partial \xi} = \frac{\partial \psi_i}{\partial X} \frac{\partial X}{\partial \xi} + \frac{\partial \psi_i}{\partial Y} \frac{\partial Y}{\partial \xi}, \quad (2.21a)$$

$$\frac{\partial \psi_i}{\partial \eta} = \frac{\partial \psi_i}{\partial X} \frac{\partial X}{\partial \eta} + \frac{\partial \psi_i}{\partial Y} \frac{\partial Y}{\partial \eta}, \quad (2.21b)$$

or in the matrix form

$$\begin{bmatrix} \frac{\partial \psi_i}{\partial \xi} \\ \frac{\partial \psi_i}{\partial \eta} \end{bmatrix} = \begin{bmatrix} \frac{\partial X}{\partial \xi} & \frac{\partial Y}{\partial \xi} \\ \frac{\partial X}{\partial \eta} & \frac{\partial Y}{\partial \eta} \end{bmatrix} \begin{bmatrix} \frac{\partial \psi_i}{\partial X} \\ \frac{\partial \psi_i}{\partial Y} \end{bmatrix}. \quad (2.22)$$

The required derivatives $\frac{\partial \psi_i}{\partial X}$ and $\frac{\partial \psi_i}{\partial Y}$ in Eq. (2.9) are obtained out by matrix inversion,

$$\begin{bmatrix} \frac{\partial \psi_i}{\partial X} \\ \frac{\partial \psi_i}{\partial Y} \end{bmatrix} = \mathbf{J}^{-1} \begin{bmatrix} \frac{\partial \psi_i}{\partial \xi} \\ \frac{\partial \psi_i}{\partial \eta} \end{bmatrix}, \quad (2.23)$$

where \mathbf{J} is the Jacobian matrix and is defined as

$$\mathbf{J} = \begin{bmatrix} \frac{\partial X}{\partial \xi} & \frac{\partial Y}{\partial \xi} \\ \frac{\partial X}{\partial \eta} & \frac{\partial Y}{\partial \eta} \end{bmatrix}. \quad (2.24)$$

Three points Gauss-quadrature (3×3) is used to perform the numerical integration for the velocity field and two points Gauss-quadrature (2×2) is used for the pressure. The

differential area $d\Omega (=dX \cdot dY)$ in Eq. (2.9) is replaced by an equivalent part in the ξ, η coordinates,

$$dX \cdot dY = \det(\mathbf{J}) d\xi \cdot d\eta. \quad (2.25)$$

d. Free Surface Updating Scheme

To accurately predict the location of the flow front, a second-order predictor-corrector scheme (namely, the Adams-Bashforth predictor and the trapezoid-rule corrector) developed by Gresho et al. (1979) has been employed in the present study.

The predictor scheme is applied first to predict the new location of the free surface nodes at each time step.

$$X_{n+1}^p = X^n + \frac{\Delta\tau_n}{2} \left[\left(2 + \frac{\Delta\tau_n}{\Delta\tau_{n-1}} \right) V_n - \frac{\Delta\tau_n}{\Delta\tau_{n-1}} V_{n-1} \right], \quad (2.26)$$

where $\Delta\tau_n$ is the n^{th} time step ($\Delta\tau_n = \tau_{n+1} - \tau_n$),

V_n, V_{n-1} are the velocities at time τ_n and τ_{n-1} (given),

X^n is the location of the free surface nodes at time τ_n ,

X_{n+1}^p is the predicted location of the free surface nodes at time τ_{n+1} .

Note that at least two velocity values are needed to apply the above scheme.

Given X_{n+1}^p , the velocity V_{n+1}^p at time τ_{n+1} can be predicted and the location of the actual free surface nodes is determined by the corrector step,

$$X^{n+1} = X^n + \frac{\Delta\tau_n}{2} (V_n + V_{n+1}^p). \quad (2.27)$$

e. Estimation of Time Step

The use of Adams-Bashforth predictor and trapezoid-rule corrector leads to a truncation error of $O(\Delta\tau^3)$ and a pre-set error tolerance to control the time step. To estimate the truncation error, Taylor series expansion is applied to the predictor and corrector scheme (Gresho et al., 1979). The predictor truncation error is given by

$$X_{n+1}^p - X(\tau_{n+1}) = -\frac{1}{12} \left(2 + 3 \frac{\Delta\tau_{n-1}}{\Delta\tau_n} \right) (\Delta\tau)^3 \ddot{X}_n + O(\Delta\tau^4), \quad (2.28)$$

where as the corrector truncation error is

$$d_{n+1} = X_{n+1} - X(\tau_{n+1}) = \frac{1}{12} (\Delta\tau)^3 \ddot{X}_n + O(\Delta\tau^4), \quad (2.29)$$

where d_{n+1} is the local time truncation error of the actual solution. Combine Eqs. (2.28) and (2.29), the actual truncation error d_{n+1} can be obtained after some manipulations.

$$d_{n+1} = \frac{X_{n+1} - X_{n+1}^p}{3 \left(1 + \frac{\Delta\tau_{n-1}}{\Delta\tau_n} \right)} + O(\Delta\tau^4). \quad (2.30)$$

As the actual truncation error is obtained from Eq. (2.30), Eq. (2.29) is used to estimate the next time step as shown below,

$$\frac{|d_{n+2}|}{|d_{n+1}|} = \left(\frac{\Delta\tau_{n+1}}{\Delta\tau_n} \right)^3 \cdot \frac{|\ddot{X}_{n+1}|}{|\ddot{X}_n|}. \quad (2.31)$$

Since $\ddot{X}_{n+1} = \ddot{X}_n + O(\Delta\tau)$, $\Delta\tau_{n+1}$ is determined by setting $d_{n+2} = \varepsilon$ and neglecting the higher order terms. Thus, one obtains

$$\Delta\tau_{n+1} = \Delta\tau_n \left(\varepsilon / |d_{n+1}| \right)^{1/3}, \quad (2.32)$$

where $|d_{n+1}|$ is the root mean square truncation error at time τ_{n+1} . In this study, ε is set to be 0.001 for the calculation of the next time step.

f. Contact Line Moving Scheme

A major difficulty encountered in free-surface flow problems is the determination of the movement of the contact line. As discussed in the Chapter 1, the boundary condition of specified contact angle (180°) used by Mavridis et al. (1988) is only appropriate when surface tension is absent. The criterion to determine the movement of contact line described by Behrens et al. (1987) is more general and has been adopted in the present study. As the free surface nodes is moved from τ_n to τ_{n+1} , the new projected surface is determined by the new free surface nodes instantaneously. The movement of the contact line is determined as follows. If the contact line does not intersect the boundary wall at more than one location, it is assumed that the contact line does not move in this time step. If it intersects the boundary wall at another location, the contact line is assumed to move to that new location. With this approach, the no-slip boundary condition is still imposed on the boundary wall.

g. Boundary Conditions for Surface Tension

When surface tension is present at the free surface (in a planar gap), the normal force is given by

$$\mathbf{f} = -\frac{\gamma}{R}\bar{\mathbf{n}}, \quad (2.33)$$

where γ is the surface tension, R is the radius of curvature of the free surface, and $\bar{\mathbf{n}}$ is the unit outward normal vector from the fluid. R is positive if the origin of the circle which prescribes the free surface is located within the fluid. Along the free surface, the unit tangential vector $\bar{\mathbf{t}}$ is expressed as

$$\bar{\mathbf{t}} = \frac{\partial \mathbf{r}}{\partial s} = \dot{\mathbf{r}}, \quad (2.34)$$

$$\dot{\bar{\mathbf{t}}} = \frac{\partial^2 \mathbf{r}}{\partial s^2} = -\frac{1}{R} \bar{\mathbf{n}}. \quad (2.35)$$

Substitute Eqs. (2.34) and (2.35) into Eq. (2.33), one can rewrite the normal force as

$$\mathbf{f} = \gamma \ddot{\mathbf{r}} = \gamma \frac{\partial^2 \mathbf{r}}{\partial s^2}, \quad (2.36)$$

or in the dimensionless form

$$\mathbf{f} = \frac{1}{Ca_\infty} \frac{\partial^2 \mathbf{R}}{\partial s^2}.$$

(2.36b)

The normal force at the flow front is integrated over the free surface to give

$$\begin{aligned} F_i &= \int_{\Gamma} \psi_i \mathbf{f} \cdot d\Gamma \\ &= \int_{s_1}^{s_2} \psi_i \frac{1}{Ca_\infty} \frac{\partial^2 \mathbf{R}}{\partial s^2} \cdot ds \\ &= \frac{1}{Ca_\infty} \int_{s_1}^{s_2} \psi_i \frac{\partial^2 \mathbf{R}}{\partial s^2} \cdot ds \end{aligned} \quad (2.37)$$

Integrating by parts, one can cast Eq. (2.37) into the following form,

$$\begin{aligned} F_i &= \frac{1}{Ca_\infty} \left(\psi_i \frac{d\mathbf{R}}{ds} \right)_{s_1}^{s_2} - \frac{1}{Ca_\infty} \int_{s_1}^{s_2} \frac{\partial \mathbf{R}}{\partial s} \cdot \frac{\partial \psi_i}{\partial s} ds \\ &= \frac{1}{Ca_\infty} \left((\psi_i \bar{\mathbf{t}})_{s_2} - (\psi_i \bar{\mathbf{t}})_{s_1} - \int_{s_1}^{s_2} \bar{\mathbf{t}} \frac{\partial \psi_i}{\partial s} ds \right) \end{aligned} \quad (2.38)$$

Equation (2.38) shows that the effect of surface tension has three contributing terms, the first two terms represent the contact line effect and the last term represents the effect over the free surface.

When surface tension is included in the problem formulation, ripples on the free surface are frequently observed in the numerical solutions. Since these ripples are not physically present, they are believed to be induced by numerical instability. To overcome this numerical instability, an implicit treatment of the surface tension term (i.e., the last term in Eq. (2.38)) recommended by Slikkerveer et al. (1996) has been employed. To obtain the implicit expression for the surface tension term, one needs to know the surface tension at the next time step. Taylor series expansion has been used in the derivation of the implicit surface tension term as shown below.

$$\left[-\int_{\bar{r}} \frac{\partial \psi_i}{\partial s} ds \right]_{\tau+\Delta\tau} = \left[-\int_{\bar{r}} \frac{\partial \psi_i}{\partial s} ds \right]_{\tau} - \left[\frac{d}{d\tau} \int_{\bar{r}} \frac{\partial \psi_i}{\partial s} ds \right]_{\tau} \Delta\tau + O(\Delta\tau)^2. \quad (2.39)$$

Since the tracking algorithm for the free surface is linear (Eq. (2.27)), only the first two terms are needed. In the present study, the change of surface tension at the contact line is neglected. The time dependent term in Eq. (2.39) can be rewritten as an integral along a reference curve L in the reference element which is independent of time. This can be expressed as follows,

$$-\left[\frac{d}{d\tau} \int_{\bar{r}} \frac{d\psi_i}{ds} ds \right]_{\tau} \Delta\tau = -\Delta\tau \int_{\bar{r}} \frac{d\bar{t}}{d\tau} \left[\frac{d\psi_i}{dL} \right] dL. \quad (2.40)$$

For the change in the tangential vector with time, it has been derived by Slikkerveer et al. (1996) and is given by

$$\frac{d\bar{t}}{d\tau} = \left(\frac{du}{ds} \cdot \bar{n} \right) \bar{n}. \quad (2.41)$$

Substitute Eq. (2.41) into Eq. (2.40), one obtains

$$-\Delta\tau\int_L\frac{d\bar{t}}{d\tau}\frac{d\psi_i}{dL}dL = -\Delta\tau\int_L\left[\left(\frac{du}{ds}\cdot\bar{n}\right)\bar{n}\right]\frac{\partial\psi_i}{\partial L}dL. \quad (2.42)$$

By applying this implicit treatment for the surface tension term, ripples on the free surface can be successfully removed.

h. Automatic Mesh Generation Scheme

Since the fluid domain is continuously deformed and advanced, an automatic grid generation scheme is required for the numerical solutions. As the flow front advances, the grid generation scheme is used to re-create the mesh for calculations in the next time step. This is realized by solving the following Laplace equations (Eq. (2.43)) with the new location of the flow front as the boundary condition.

$$\left(\frac{\partial^2}{\partial\xi^2} + \frac{\partial^2}{\partial\eta^2}\right)X(\xi, \eta) = 0, \quad (2.43a)$$

$$\left(\frac{\partial^2}{\partial\xi^2} + \frac{\partial^2}{\partial\eta^2}\right)Y(\xi, \eta) = 0. \quad (2.43b)$$

i. Mesh Refinement Test

Three finite element meshes, 8×8 , 10×10 , and 12×10 , have been used for the mesh refinement test. With the absence of the gravitational and surface tension effects, the predicted relative front tip travel distance shows an improvement of 2.5% when the mesh is refined from 8×8 to 10×10 . However, only 0.3% of improvement is observed when the mesh is further refined from 10×10 to 12×10 . In addition, the mesh with

12×10 elements provides the best result when compared with the previous studies (Table 2.1). Thus, it is chosen for the present study (Fig. 2.5).

2.2 Flow Injection through Center-Gated Disks

2.2.1 Governing Equations

The filling process in center-gated disks can be modeled as an axisymmetric transient flow front advancing radially between two parallel disks (Fig. 2.6). The gap between the two disks is considered to be very thin and has the same order of magnitude as the injection hole. Since the creeping motion is assumed for the present study (i.e., $Re \ll 1$), the time dependent term and inertial terms are neglected. As a result, the continuity and momentum equations are simplified to give:

Continuity Equation:

$$\frac{1}{r} \frac{\partial}{\partial r}(ru) + \frac{\partial w}{\partial z} = 0, \quad (2.44a)$$

Momentum equations:

$$-\frac{\partial p}{\partial r} + \mu \left(\frac{\partial}{\partial r} \left(\frac{1}{r} \frac{\partial}{\partial r}(ru) \right) + \frac{\partial^2 u}{\partial z^2} \right) = 0, \quad (2.44b)$$

$$-\frac{\partial p}{\partial z} + \mu \left(\frac{1}{r} \frac{\partial}{\partial r} \left(r \frac{\partial w}{\partial r} \right) + \frac{\partial^2 w}{\partial z^2} \right) - \rho g_z = 0. \quad (2.44c)$$

The variables are normalized using the average entry velocity U_∞ , radius of the injection hole R_i and viscosity μ . Pressure p is non-dimensionalized by $\mu U_\infty / R_i$ and time t is non-dimensionalized by R_i / U_∞ . The resulting dimensionless governing equations are given by

$$\frac{1}{R} \frac{\partial}{\partial R} (RU) + \frac{\partial W}{\partial Z} = 0, \quad (2.45a)$$

$$-\frac{\partial P}{\partial R} + \left(\frac{\partial}{\partial R} \left(\frac{1}{R} \frac{\partial}{\partial R} (RU) \right) + \frac{\partial^2 U}{\partial Z^2} \right) = 0, \quad (2.45b)$$

$$-\frac{\partial P}{\partial Z} + \left(\frac{1}{R} \frac{\partial}{\partial R} \left(R \frac{\partial W}{\partial R} \right) + \frac{\partial^2 W}{\partial Z^2} \right) - St_z = 0. \quad (2.45c)$$

Substitute Eq. (2.45a) into Eqs. (2.45b) and (2.45c), momentum equations can be rewritten in the traction form.

$$\frac{1}{R} \frac{\partial}{\partial R} \left(R \left(-P + 2 \frac{\partial U}{\partial R} \right) \right) + \frac{1}{R} \left(-P + 2 \frac{U}{R} \right) + \frac{\partial}{\partial Z} \left(\frac{\partial U}{\partial Z} + \frac{\partial W}{\partial R} \right) = 0, \quad (2.45d)$$

$$\frac{1}{R} \frac{\partial}{\partial R} \left(R \left(\frac{\partial U}{\partial Z} + \frac{\partial W}{\partial R} \right) \right) + \frac{\partial}{\partial Z} \left(-P + 2 \frac{\partial W}{\partial Z} \right) - St_z = 0. \quad (2.45e)$$

where $St_z (= \rho g_z R^2 / \mu U_\infty)$ is the Stokes number, which is defined as the ratio of gravitational force to viscous force in z direction.

2.2.2 Boundary Conditions

For flow injection through center-gated disks, the governing equations are solved using only half of the physical domain since the problem is axisymmetrical. The appropriate boundary conditions for the problem are:

- At the inlet,

$$U = 0, \quad W = W(R). \quad (2.46a)$$

- Along the solid walls,

$$U = 0, \quad W = 0. \quad (2.46b)$$

- Along the centerline of the injection hole ($R = 0$),

$$\frac{\partial W}{\partial R} = 0, \quad U = 0. \quad (2.46c)$$

- Along the free surface, the normal force component is proportional to the local curvature of the free surface and the surface tension. In addition, the tangential force component vanishes and the heat transfer from flow front to the ambient air is negligible,

$$\sigma_t = 0, \quad \sigma_n = \frac{1}{Ca} \left(\frac{1}{R_1} + \frac{1}{R_2} \right) + P_a, \quad (2.46d)$$

where σ_t and σ_n are the dimensionless stresses in the tangential and normal direction respectively. R_1 and R_2 are the dimensionless radius of curvature of the front surface, and P_a is the ambient pressure. $Ca (= \mu U_\infty / \gamma)$ is the capillary number defined as the ratio of viscous force to surface tension.

2.2.3 Numerical Method

a. Finite Element Method

To simulate the filling process in center-gated disks, Galerkin finite element method is adopted here for its flexibility and superiority in handling domains with irregular shape. Following the same procedure discussed in section 2.1.3, the fully discretized Galerkin equations can be obtained.

$$\int_{\Omega} \left(\frac{\partial \phi_i}{\partial R} (RU) + \frac{\partial \phi_i}{\partial Z} (RW) \right) d\Omega = 0, \quad (2.47a)$$

$$\int_{\Omega} \left(\frac{\partial \psi_i}{\partial R} \left(R(-P + 2 \frac{\partial U}{\partial R}) \right) + \psi_i \left(-P + 2 \frac{U}{R} \right) + \frac{\partial \psi_i}{\partial Z} \left(R \left(\frac{\partial U}{\partial Z} + \frac{\partial W}{\partial R} \right) \right) \right) d\Omega = \int_{\Gamma} \psi_i RT_r d\Gamma, \quad (2.47b)$$

$$\int_{\Omega} \left(\frac{\partial \psi_i}{\partial R} \left(R \left(\frac{\partial U}{\partial Z} + \frac{\partial W}{\partial R} \right) \right) + \frac{\partial \psi_i}{\partial Z} \left(R(-P + 2 \frac{\partial W}{\partial Z}) \right) \right) d\Omega = - \int_{\Omega} \psi_i R St_z d\Omega + \int_{\Gamma} \psi_i RT_z d\Gamma, \quad (2.47c)$$

$$\text{where } T_r = (-P + 2 \frac{\partial U}{\partial R}) n_r + \left(\frac{\partial U}{\partial Z} + \frac{\partial W}{\partial R} \right) n_z, \quad (2.47d)$$

$$T_z = \left(\frac{\partial U}{\partial Z} + \frac{\partial W}{\partial R} \right) n_r + (-P + 2 \frac{\partial W}{\partial Z}) n_z. \quad (2.47e)$$

Express velocities and pressure in terms of their interpolation functions, one obtains the following equation in the matrix form.

$$\begin{bmatrix} 2\mathbf{K}_{11} + \mathbf{K}_{22} + 2\mathbf{C} & \mathbf{K}_{21} & -\mathbf{Q}_1 \\ \mathbf{K}_{12} & \mathbf{K}_{11} + 2\mathbf{K}_{22} & -\mathbf{Q}_2 \\ -\mathbf{Q}_1^T & -\mathbf{Q}_2^T & \mathbf{0} \end{bmatrix} \begin{bmatrix} \mathbf{U} \\ \mathbf{W} \\ \mathbf{P} \end{bmatrix} = \begin{bmatrix} \mathbf{F}_r \\ \mathbf{F}_z \\ \mathbf{0} \end{bmatrix}, \quad (2.48)$$

$$\text{where } \mathbf{K}_{ij} = \int_{\Omega} R \frac{\partial \psi}{\partial X_i} \frac{\partial \psi^T}{\partial X_j} d\Omega, \quad (2.49a)$$

$$\mathbf{C} = \int_{\Omega} \psi \frac{\psi^T}{R} d\Omega \quad (2.49b)$$

$$\mathbf{Q}_1 = \int_{\Omega} \frac{\partial}{\partial R} (R\psi) \phi^T d\Omega \quad (2.49c)$$

$$\mathbf{Q}_2 = \int_{\Omega} R \frac{\partial \psi}{\partial Z} \phi^T d\Omega, \quad (2.49d)$$

$$F_r = \int_{\Gamma} \psi R T_r d\Gamma, \quad (2.49e)$$

$$F_z = -\int_{\Omega} \psi R St_z d\Omega + \int_{\Gamma} \psi R T_z d\Gamma. \quad (2.49f)$$

The estimation of time step, free surface updating scheme, and contact line moving scheme are the same as those described in section 2.1.

b. Boundary Conditions for Surface Tension

For flow injection through center-gated disks, the normal force has two contributing radii of curvature along the free surface. The normal force is expressed by

$$f = -\left(\frac{l}{R_1} + \frac{l}{R_2}\right)\gamma\bar{n}, \quad (2.50)$$

where γ is the fluid surface tension. R_1 is given by Eq. (2.35) and R_2 can be found directly from the geometric construction (Fig. 2.7) and is given by.

$$\frac{l}{R_2} = \frac{n_r}{r}. \quad (2.51)$$

With the aid of Eqs. (2.34)-(2.36), one can non-dimensionalize the normal force to give

$$\hat{f} = \frac{l}{Ca} \left(\frac{\partial^2 R}{\partial s^2} - \frac{n_r}{R} \bar{n} \right). \quad (2.52)$$

Since only isothermal condition is considered for the present case, the normal force at the flow front can be integrated directly over the free surface to give

$$\begin{aligned} F_i &= \int_{\Gamma} \psi_i R f \cdot d\Gamma \\ &= \int_{s_1}^{s_2} \frac{\psi_i R}{Ca} \frac{\partial^2 R}{\partial s^2} d\Gamma - \int_{s_1}^{s_2} \frac{l}{Ca} \psi_i n_r \bar{n} d\Gamma. \end{aligned} \quad (2.53)$$

Integrating by parts, one can cast Eq. (2.53) into the following form,

$$\begin{aligned}
F_i &= \frac{1}{Ca} \left(\psi_i R \frac{dR}{ds} \right)_{s_1}^{s_2} - \frac{1}{Ca} \int_{s_1}^{s_2} \frac{\partial R}{\partial s} \cdot \frac{\partial}{\partial s} (\psi_i R) ds - \frac{1}{Ca} \int_{s_1}^{s_2} \psi_i n_r \bar{n} ds \\
&= \frac{1}{Ca} \left((\psi_i R \bar{t})_{s_2} - (\psi_i R \bar{t})_{s_1} - \int_{s_1}^{s_2} \bar{t} \left(R \frac{\partial \psi_i}{\partial s} + \psi_i \frac{\partial R}{\partial s} \right) ds - \int_{s_1}^{s_2} \psi_i n_r \bar{n} ds \right). \quad (2.54)
\end{aligned}$$

Equation (2.54) shows that the effect of surface tension has four contributing terms. The first two terms represent the contact line effect and the last two terms represent the effect over the free surface. To overcome the numerical instability induced by surface tension, an implicit treatment of the surface tension terms (i.e., the last terms in Eq. (2.54)) recommended by Slikkerveer et al. (1996) has been adopted. To obtain the implicit expression for the surface tension terms, one needs to know the surface tension at the next time step. By Taylor series expansion, the implicit surface tension terms can be obtained as follows,

$$\begin{aligned}
\left[\int_{\Gamma} \left(\bar{t} \left(R \frac{\partial \psi_i}{\partial s} + \psi_i \frac{\partial R}{\partial s} \right) + \psi_i n_r \bar{n} \right) ds \right]_{\tau+\Delta\tau} &= \left[\int_{\Gamma} \left(\bar{t} \left(R \frac{\partial \psi_i}{\partial s} + \psi_i \frac{\partial R}{\partial s} \right) + \psi_i n_r \bar{n} \right) ds \right]_{\tau} \\
&\quad - \left[\frac{d}{d\tau} \int_{\Gamma} \left(\bar{t} \left(R \frac{\partial \psi_i}{\partial s} + \psi_i \frac{\partial R}{\partial s} \right) + \psi_i n_r \bar{n} \right) ds \right]_{\tau} \Delta\tau + O(\Delta\tau)^2. \quad (2.55)
\end{aligned}$$

Since the algorithm used to track the free surface is linear (Eq. (2.27)), only the first two terms are needed. In our numerical approach, the change of surface tension at the contact line is neglected. Following the procedure discussed in previous section, the time dependent term in Eq. (2.55) can be written as

$$- \left[\frac{d}{d\tau} \int_{\Gamma} \left(\bar{t} \left(R \frac{\partial \psi_i}{\partial s} + \psi_i \frac{\partial R}{\partial s} \right) + \psi_i n_r \bar{n} \right) ds \right]_{\tau} \Delta\tau$$

$$= -\Delta\tau \int_r \frac{d\bar{t}}{d\tau} \left(R \frac{\partial\psi_i}{\partial s} + \psi_i \frac{\partial R}{\partial s} \right) ds - \Delta\tau \int_r \bar{t} \left(\frac{dR}{d\tau} \frac{\partial\psi_i}{\partial s} + \psi_i \frac{d(\frac{\partial R}{\partial s})}{d\tau} \right) ds - \Delta\tau \int_r \frac{d\bar{n}}{d\tau} \psi_i n_r ds \quad (2.56)$$

For the change in the tangential vector with time, it has been derived by Slikkerveer et al. (1996) and is given by

$$\frac{d\bar{t}}{d\tau} = \left(\frac{du}{ds} \cdot \bar{n} \right) \bar{n}. \quad (2.57)$$

For the change in the normal vector with time, it has been derived and documented in Appendix A. It is expressed in the following equation.

$$\frac{d\bar{n}}{d\tau} = - \left(\frac{du}{ds} \cdot \bar{n} \right) \bar{t}. \quad (2.58)$$

Substitute Eqs. (2.57) and (2.58) into Eq. (2.56), the implicit surface tension term in the Eq. (2.56) now can be expressed as follows

$$\begin{aligned} & -\Delta\tau \int_r \frac{d\bar{t}}{d\tau} \left(R \frac{\partial\psi_i}{\partial s} + \psi_i \frac{\partial R}{\partial s} \right) ds - \Delta\tau \int_r \bar{t} \left(\frac{dR}{d\tau} \frac{\partial\psi_i}{\partial s} + \psi_i \frac{d(\frac{\partial R}{\partial s})}{d\tau} \right) ds - \Delta\tau \int_r \frac{d\bar{n}}{d\tau} \psi_i n_r ds \\ & = -\Delta\tau \int_r \left(\frac{dU}{d\tau} \cdot \bar{n} \right) \bar{n} \left(R \frac{\partial\psi_i}{\partial s} + \psi_i \frac{\partial R}{\partial s} \right) ds - \Delta\tau \int_r \bar{t} \left(U \frac{\partial\psi_i}{\partial s} + \psi_i \frac{dU}{ds} \right) ds \\ & \quad + \int_r \left(\frac{dU}{ds} \cdot \bar{n} \right) \bar{t} \psi_i n_r ds \end{aligned} \quad (2.59)$$

By applying the implicit treatment for the surface tension above, one can successfully remove ripples on the free surface.

c. Automatic Mesh Scheme

As the flow front advances, an automatic grid generation scheme is required to

recreate the mesh for the calculations in the next time step. The automatic grid generation scheme introduced by George (1991) and Heinrich and Pepper (1999) is realized by solving the following Laplace equations (2.60a, b) with the new location of the flow front as the boundary condition.

$$\xi_{RR} + \xi_{ZZ} = 0, \quad (2.60a)$$

$$\eta_{RR} + \eta_{ZZ} = 0. \quad (2.60b)$$

Once the solutions of Eq. (2.60) are known, one can find $R(\xi, \eta)$ and $Z(\xi, \eta)$ through the inverse process. Using the chain rule, one obtains

$$dR = \frac{\partial R}{\partial \xi} d\xi + \frac{\partial R}{\partial \eta} d\eta = \frac{\partial R}{\partial \xi} \left(\frac{\partial \xi}{\partial R} dR + \frac{\partial \xi}{\partial Z} dZ \right) + \frac{\partial R}{\partial \eta} \left(\frac{\partial \eta}{\partial R} dR + \frac{\partial \eta}{\partial Z} dZ \right), \quad (2.61a)$$

$$dZ = \frac{\partial Z}{\partial \xi} d\xi + \frac{\partial Z}{\partial \eta} d\eta = \frac{\partial Z}{\partial \xi} \left(\frac{\partial \xi}{\partial R} dR + \frac{\partial \xi}{\partial Z} dZ \right) + \frac{\partial Z}{\partial \eta} \left(\frac{\partial \eta}{\partial R} dR + \frac{\partial \eta}{\partial Z} dZ \right). \quad (2.61b)$$

Note that product of these derivatives yields the following relations

$$\underbrace{\begin{bmatrix} \frac{\partial R}{\partial \xi} & \frac{\partial R}{\partial \eta} \\ \frac{\partial Z}{\partial \xi} & \frac{\partial Z}{\partial \eta} \end{bmatrix}}_{\equiv M} \begin{bmatrix} \frac{\partial \xi}{\partial R} & \frac{\partial \xi}{\partial Z} \\ \frac{\partial \eta}{\partial R} & \frac{\partial \eta}{\partial Z} \end{bmatrix} = \begin{bmatrix} 1 & 0 \\ 0 & 1 \end{bmatrix}, \quad (2.62a)$$

or

$$\begin{bmatrix} \frac{\partial \xi}{\partial R} & \frac{\partial \xi}{\partial Z} \\ \frac{\partial \eta}{\partial R} & \frac{\partial \eta}{\partial Z} \end{bmatrix} = \frac{1}{J} \underbrace{\begin{bmatrix} \frac{\partial Z}{\partial \eta} & -\frac{\partial R}{\partial \eta} \\ -\frac{\partial Z}{\partial \xi} & \frac{\partial R}{\partial \xi} \end{bmatrix}}_{\equiv M^{adj}}. \quad (2.62b)$$

where J is the Jacobian, which is similar to that defined in Eq. (2.24) except that X and Y are now replaced by R and Z . From Eq. (2.62), one can obtain the expressions of the second derivative for ξ and η . Given $\partial\xi/\partial R = (1/J)(\partial Z/\partial\eta)$, one has

$$\frac{\partial^2\xi}{\partial R^2} = \frac{\partial}{\partial\xi}\left(\frac{1}{J}\frac{\partial Z}{\partial\eta}\right)\frac{\partial\xi}{\partial R} + \frac{\partial}{\partial\eta}\left(\frac{1}{J}\frac{\partial Z}{\partial\eta}\right)\frac{\partial\eta}{\partial R}, \quad (2.63a)$$

or

$$\frac{\partial^2\xi}{\partial R^2} = \frac{\partial}{\partial\xi}\left(\frac{1}{J}\frac{\partial Z}{\partial\eta}\right)\frac{1}{J}\frac{\partial Z}{\partial\eta} - \frac{\partial}{\partial\eta}\left(\frac{1}{J}\frac{\partial Z}{\partial\eta}\right)\frac{1}{J}\frac{\partial Z}{\partial\xi}. \quad (2.63b)$$

Carrying out the derivatives in Eq. (2.63b) one yields

$$\frac{\partial^2\xi}{\partial R^2} = \frac{1}{J^2}\left(\frac{\partial Z}{\partial\eta}\frac{\partial^2 Z}{\partial\eta\partial\xi} - \frac{\partial Z}{\partial\xi}\frac{\partial^2 Z}{\partial\eta^2}\right) + \frac{1}{J^3}\left(-\frac{\partial J}{\partial\xi}\left(\frac{\partial Z}{\partial\eta}\right)^2 + \frac{\partial J}{\partial\eta}\frac{\partial Z}{\partial\eta}\frac{\partial Z}{\partial\xi}\right). \quad (2.64)$$

Similar expressions for $\partial^2\xi/\partial Z^2$, $\partial^2\eta/\partial R^2$, and $\partial^2\eta/\partial Z^2$ can be obtained with the aid of Eq. (2.62). Given Eq. (2.60) and the values of $\partial J/\partial\xi$ and $\partial J/\partial\eta$ in terms of R and Z , one can show that R and Z satisfy the following system

$$g_{11}\frac{\partial^2 R}{\partial\xi^2} + g_{22}\frac{\partial^2 R}{\partial\eta^2} - 2g_{12}\frac{\partial^2 R}{\partial\xi\partial\eta} = 0, \quad (2.65a)$$

$$g_{11}\frac{\partial^2 Z}{\partial\xi^2} + g_{22}\frac{\partial^2 Z}{\partial\eta^2} - 2g_{12}\frac{\partial^2 Z}{\partial\xi\partial\eta} = 0, \quad (2.65b)$$

$$\text{where } g_{11} = R_\eta^2 + Z_\eta^2, \quad (2.65c)$$

$$g_{22} = R_\xi^2 + Z_\xi^2, \quad (2.65d)$$

$$g_{12} = R_\xi R_\eta + Z_\xi Z_\eta. \quad (2.65e)$$

A typical mesh used for flow injection through in center-gated disks is shown in Fig. 2.8.

Table 2.1: Comparison of predicted flow front travel distances (Δy) at the full-developed stage (vertical channels)

Investigators	Frame of Reference	Δy
Wang et al. (1978)	Moving--steady	1.04
Wang et al. (1979)	Moving--steady	0.84
Mavridis et al. (1986a)	Moving--steady	0.90
Behrens et al. (1987)	Moving--steady	0.94
Behrens et al. (1987)	fixed--transient	0.91
Shin and Lee (1995)	fixed--transient	0.933
present study (1998)	fixed--transient	0.930

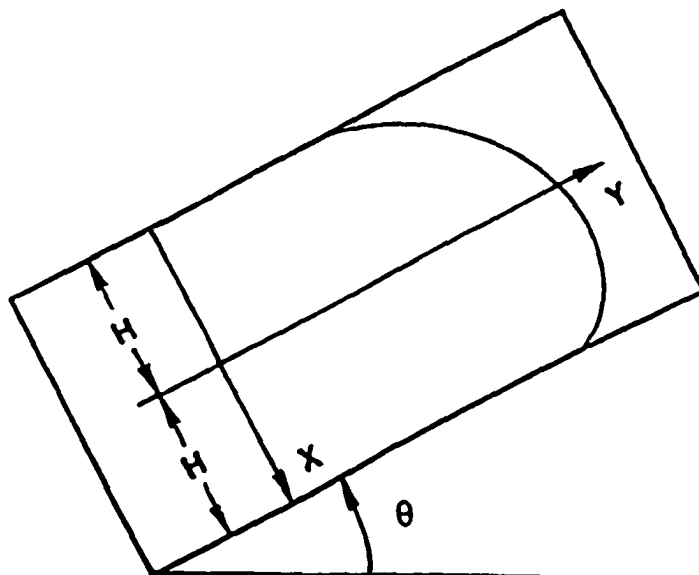
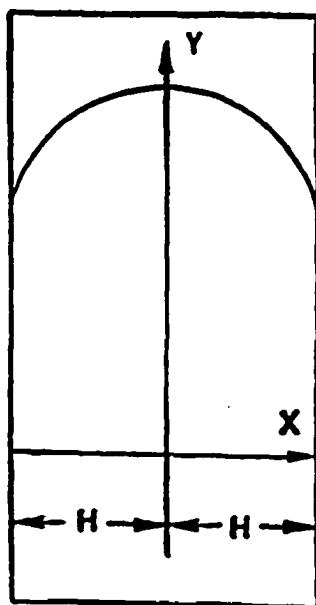
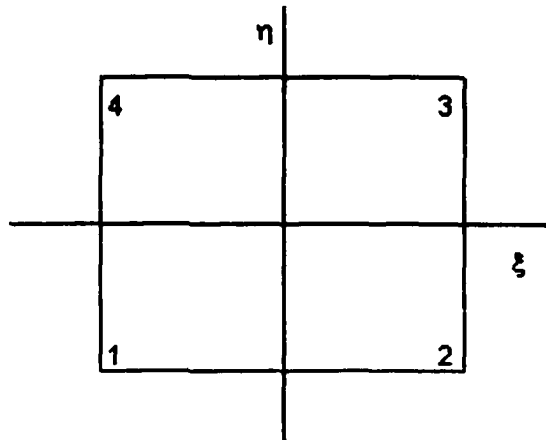


Figure 2.1 Flow injection through planar gaps: (a) vertical channels, (b) horizontal and inclined channels ($\theta = 0^\circ, 30^\circ, 45^\circ,$ and 60°).

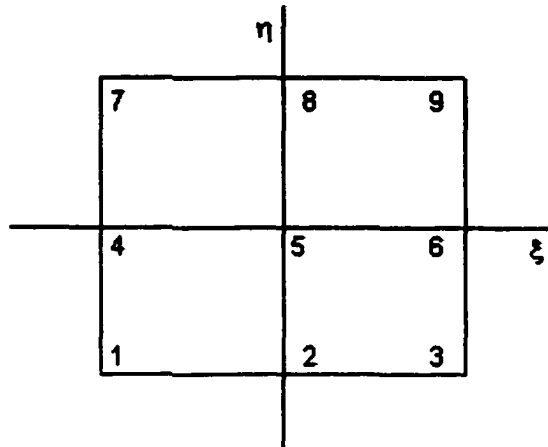


$$p \approx \sum_{j=1}^M \phi_j(\xi, \eta) p_j(t)$$

where $\phi_1 = L_1^{(x)} L_1^{(y)}$ $\phi_2 = L_2^{(x)} L_1^{(y)}$

$\phi_3 = L_2^{(x)} L_2^{(y)}$ $\phi_4 = L_1^{(x)} L_2^{(y)}$

Figure 2.2 A four-point bilinear element and its interpolation functions.



$$U \approx \sum_{i=1}^9 \psi_i(\xi, \eta) U_i(\tau)$$

$$V \approx \sum_{i=1}^9 \psi_i(\xi, \eta) V_i(\tau)$$

where

$$\psi_1 = L_1^{(x)} L_1^{(y)}$$

$$\psi_2 = L_2^{(x)} L_1^{(y)}$$

$$\psi_3 = L_3^{(x)} L_1^{(y)}$$

$$\psi_4 = L_1^{(x)} L_2^{(y)}$$

$$\psi_5 = L_2^{(x)} L_2^{(y)}$$

$$\psi_6 = L_3^{(x)} L_2^{(y)}$$

$$\psi_7 = L_1^{(x)} L_3^{(y)}$$

$$\psi_8 = L_2^{(x)} L_3^{(y)}$$

$$\psi_9 = L_3^{(x)} L_3^{(y)}$$

and

$$L_1^{(x)} = \xi(\xi - 1)/2$$

$$L_2^{(x)} = 1 - \xi^2$$

$$L_3^{(x)} = \xi(\xi + 1)/2$$

$$L_1^{(y)} = \eta(\eta - 1)/2$$

$$L_2^{(y)} = 1 - \eta^2$$

$$L_3^{(y)} = \eta(\eta + 1)/2$$

Figure 2.3 A nine-point biquadratic element and its interpolation functions.

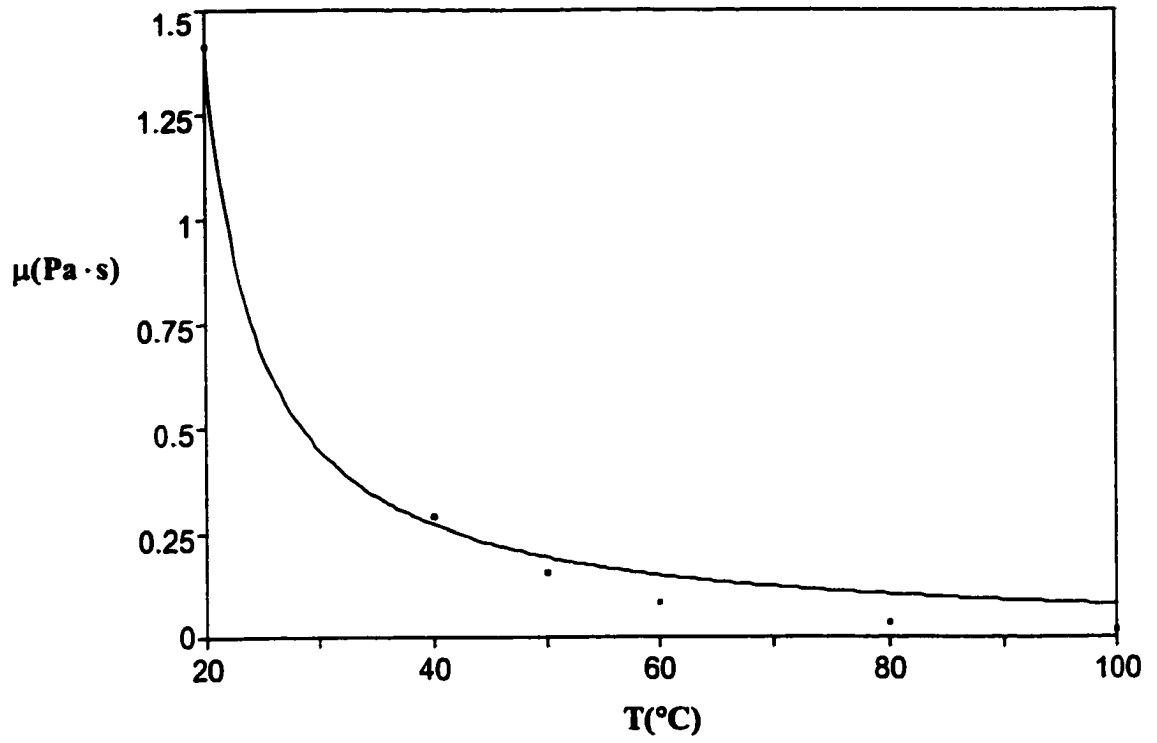
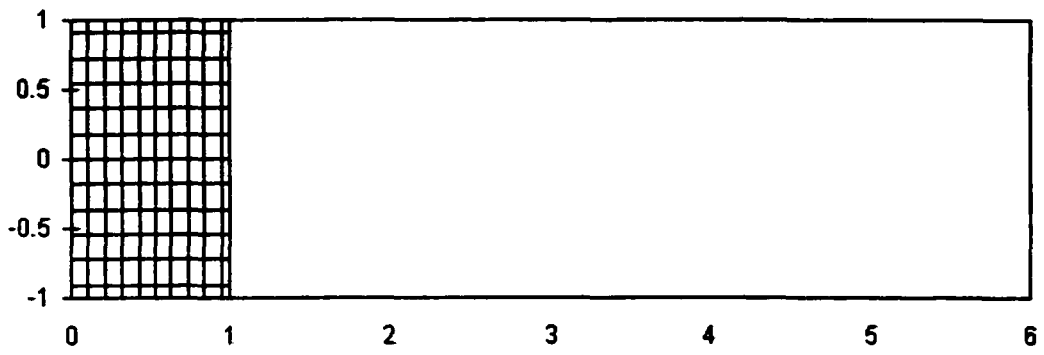
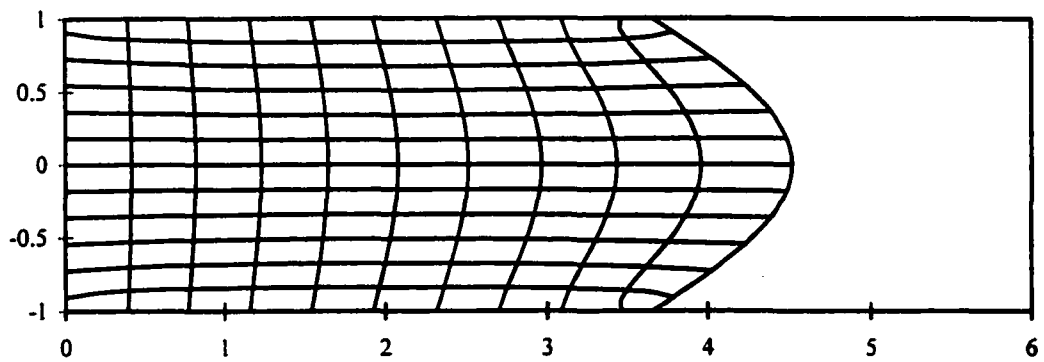


Figure 2.4 Viscosity variation of glycerol with temperature effects.



(a)



(b)

Figure 2.5 A typical finite element mesh used for flow injection through planar gaps, (a) initial mesh, (b) mesh in transition..

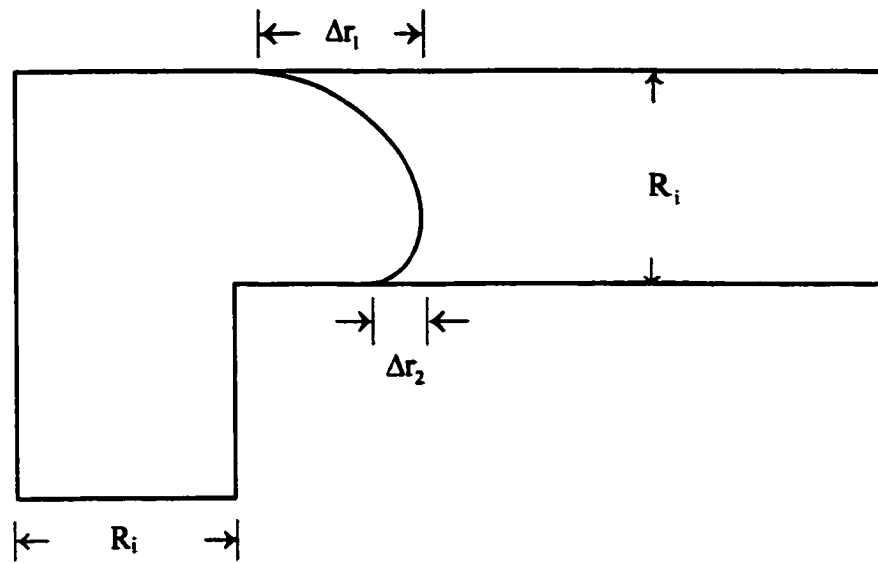


Figure 2.6 Flow injection through center-gated disks

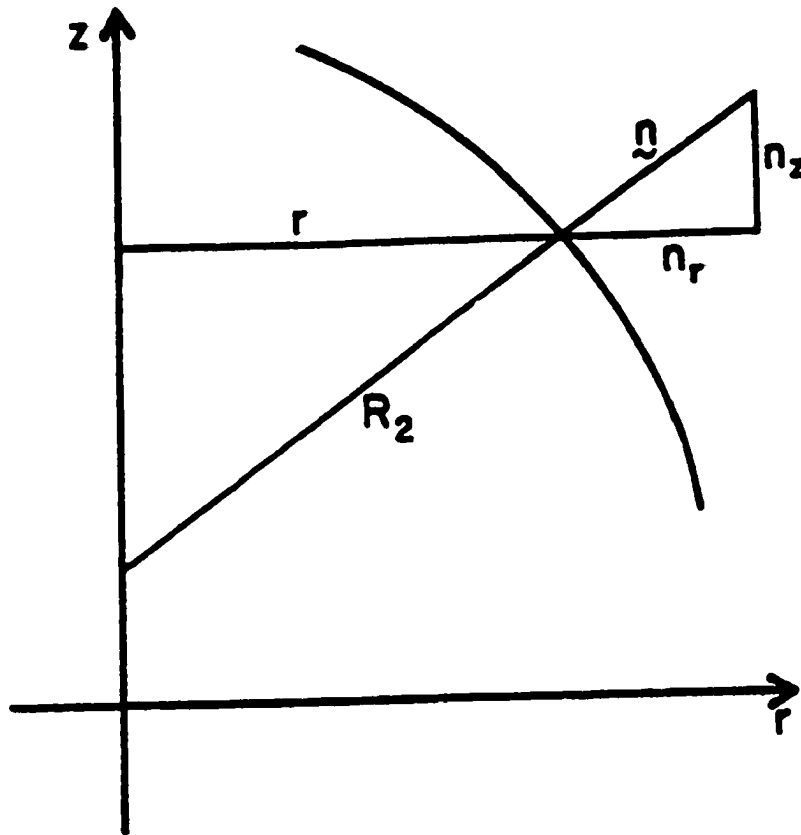
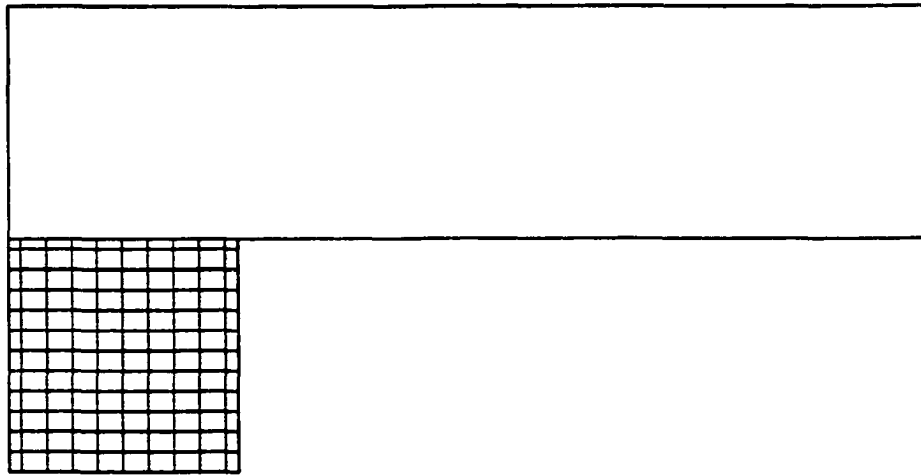
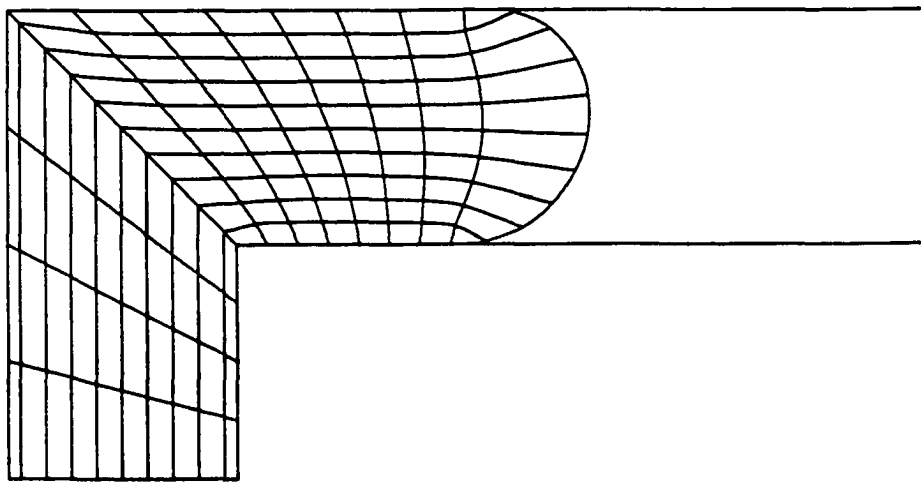


Figure 2.7 Construction for second radius of curvature (Behrens, 1983).



(a)



(b)

Figure 2.8 A typical finite element mesh used for flow injection through center-gated disks: (a) initial mesh, (b) mesh in transition.

CHAPTER 3

ISOTHERMAL INJECTION IN PLANAR GAPS

Flow injection between two parallel plates has been numerically studied using the finite element method described in the previous chapter. The advancement of the flow front, its shape and velocity distribution are obtained. To validate the numerical code, the results obtained are compared with the data available in the literature for the special case of negligible gravitational and surface tension effects. The asymptotic (fully developed) values of the front tip travel distance relative to the contact lines (Δy) are listed in Table 2.1 for comparison. The definition of Δy for various channel orientations is shown in Fig. 2.1. As shown, the present result agrees very well with the results obtained from the previous studies.

3.1 Flow Injection through Vertical Channels

3.1.1 Gravitational Effects

For flow injection through a vertical channel, the gravitational force is acting opposite to the flow direction. Its effects on the development of the flow front at a given capillary number ($Ca = 1$) are shown in Fig. 3.2. The first curve represents the front shape at the time when the contact lines begin to move. Since the time step is controlled by the pre-set error criterion (Eq. (2.32)), its value is different in each case. As a result, it is difficult to present the flow front profiles at the exactly same time frame. The flow front profiles presented in Fig. 3.2 are roughly at the same time frame and thus they are intended for qualitative discussion only. It is clear to see that the gravitational effect has

significantly shortened the front tip travel distance. The initial front tip travel distance (when the contact line initiates its first move) decreases from 0.805 to 0.490 as the Stokes number increases from 0 to 10. As a result, the flow front becomes flattened when the gravitational force increases. This is understood since the gravitational force is acting opposite to the flow direction. The velocity fields under various gravitational effects are shown in Fig. 3.3. From the figure, the fountain flow pattern near the flow front can be clearly observed. The gravitational force flattens the flow front and minimizes the fountain flow region. As the Stokes number increases, the fountain flow region although becomes more confined, its effect can still be felt at the flow front. Also observed is that the flow at the upstream region (close to the inlet) has attained a fully developed (parabolic) velocity profile.

The advancement of flow front under various gravitational effects is shown in Fig. 3.4. As the gravitational force increases, the asymptotic value of the front tip travel distances decreases. It decreases from 0.964 to 0.559 as the Stokes number increases from 0 to 10 ($Ca = 1$). At the same time, it is observed that the gravitational effect also reduces the time needed for the first move of the contact line. The time is calculated to be 0.631 for $St = 0$ and is decreased to 0.385 for $St = 10$. Since the gravitational effect flattens the flow front, the contact line is forced to move earlier. Figure 3.4 also shows that it would be faster for the flow to become fully developed when the Stokes number is higher. A similar situation is also observed for other capillary numbers ($Ca = 2, 5, 10$ and ∞).

The gravitational effects on the fully developed front tip travel distance is shown in Fig. 3.5 for capillary number fixed at $Ca = 10$ and ∞ . It shows that the gravitational

force has a dramatic effect on the front tip travel distance when the Stokes number is greater than 0.1. For Stokes numbers less than 0.1, the effect of gravitation becomes insignificant. Based on this observation, one can conclude that the gravitational effects on fountain flow are negligible under microgravity environment.

3.1.2 Effects of Surface Tension

The effect of surface tension on flow injection can be cross-examined from Fig. 3.6. For a negligible gravitational force ($St = 0$), the asymptotic value of the front tip travel distance decreases from 0.965 to 0.929 as the capillary number increases from 1 to ∞ (the limiting case of no surface tension effect). It clearly shows that the effect of surface tension is to expand the fountain flow region and increase the front tip travel distance. From the present study, it shows that the effect of surface tension on the relative front tip travel distance is insignificant for capillary number greater than 10. It becomes important only when the capillary number is less than 10. A similar situation is also observed for other Stokes numbers ($St = 0.1, 1, 2, \text{ and } 10$).

Although the surface tension does not have a significant influence over the final profile of the flow front for capillary number greater than 10, it does affect the contact line moving time. For fluids with a larger surface tension (i.e., a smaller capillary number), a longer time is required for the contact line to initiate its first move because of a higher potential energy on their free surfaces. This surface energy can withstand larger shear stresses acting on the free surface and thus can move the free surface further downstream before the contact line begins to move. For a given flow rate, their contact lines will move later than those with a smaller surface tension. The time required for the

contact line to initiate its first move is listed in Table 3.1 for various capillary and Stokes numbers. For a fixed Stokes number, the waiting time decreases with the capillary number. Similarly, it also decreases with the Stokes number when the capillary number is fixed.

From Fig. 3.5, it is also noticed that the effect of surface tension on the front tip travel distance is limited if the capillary number is greater than 10. This change on the relative front tip travel distance is less than 1% for all Stokes numbers considered ($St = 0, 0.1, 1, 2, \text{ and } 10$).

3.1.3 Pressure Distribution

The pressure contour in a flow field with a negligible gravitational effects is shown in Fig. 3.7. It shows that the pressure gradient is constant in the upstream region but becomes more complicated near the fountain flow region, particularly in the vicinity of the moving contact lines. The pressure distribution can be cross-examined from Fig. 3.8. In the upstream region, the pressures along the channel wall and the centerline are exactly the same. The deviation appears only in the fountain flow region.

To get a better insight to the phenomenon observed, consider a creeping flow in a vertical channel (y is treated as flow direction and x is perpendicular to the flow direction.). When the flow becomes fully developed, the momentum equations are simplified to give:

$$\frac{\partial p}{\partial x} = 0 \quad (3.1a)$$

$$-\frac{\partial p}{\partial y} + \mu \frac{\partial^2 v}{\partial x^2} - \rho g_y = 0 \quad (3.1b)$$

Momentum equations (3.1) can be non-dimensionalized using the half channel width (H), average velocity (U_∞), and fluid viscosity (μ) to give:

$$\frac{\partial P}{\partial X} = 0 \quad (3.2a)$$

$$\frac{\partial^2 V}{\partial X^2} = \frac{\partial P}{\partial Y} + St_y \quad (3.2b)$$

With the boundary conditions: $V = 0$ for $X = \pm 1$. Where P is the dimensionless pressure and $St_y (= \rho g_y H^2 / \mu U_\infty)$ is the body force term in y direction due to gravitational effect. Since $\partial P / \partial X = 0$, the pressure is uniform in the direction perpendicular to the flow and is a function of Y only. Thus $\partial P / \partial Y = \text{constant}$ (Eq. 3.2b) and the velocity distribution of the flow can be found to be:

$$V = \frac{-1}{2} \left(\frac{dP}{dY} + St_y \right) (1 - X^2) \quad (3.3)$$

The fully developed velocity distribution of the creeping flow is known as

$$V = \frac{3}{2} (1 - X^2) \quad (3.4)$$

Substituting Eq. (3.4) into Eq. (3.3), and thus

$$\frac{dP}{dY} = -(St_y + 3) \quad (3.5)$$

For negligible gravitational effects ($St_y = 0$), the pressure gradient ($\partial P / \partial Y$) of the fully developed creeping flow is thus equal to -3 . This result is compared with the pressure distributions of the flow injection along the vertical channel wall and centerline and is plotted in Fig. 3.8. Figure 3.8 shows that the pressure gradient for the injection flow in the upstream region is exactly the same as that of the fully developed creeping flow.

For negligible surface tension ($Ca \rightarrow \infty$), the effects of the gravitational force on the pressure distribution along the channel wall and centerline are plotted in Fig. 3.9. Figure 3.9 shows that the pressure gradient increases as the Stokes number increases. Similar results are observed for other surface tension conditions ($Ca = 1, 2, 5, \text{ and } 10$). Surface tension effect on the pressure distribution is shown in Fig. 3.10 for negligible gravitational effect. It shows that the pressure gradients of various capillary number have the same value, except the fountain flow region. Due to the surface tension effect, the pressure distribution shifts upward as surface tension increases. Similar results are observed for other Stokes numbers ($St = 0.1, 1, 2, \text{ and } 10$).

3.2 Flow Injection through Inclined Channels

3.2.1 Gravitational Effects

For flow injection through inclined channels ($30^\circ, 45^\circ, \text{ and } 60^\circ$), the gravitational force is acting both parallelly and perpendicularly to the flow direction. The normal component of the gravitational force destroys the symmetric flow structure which is featured in flow injection through vertical channels. In addition, the flow is sagging toward the bottom wall when it advances. Figures 3.11 to 3.13 show the gravitational effect on the development of flow front for various inclined channels ($30^\circ, 45^\circ, 60^\circ$) at a given capillary number ($Ca = 1$). For a given inclined angle, the sagging of fluid becomes more serious as the gravitational effect (St) increases. As a result, the flow front profile becomes more asymmetric and the front tip is observed to shift downward. On the other hand, the development of flow front approaches that of the symmetric one when the inclined angle increases. The difference between the front tip travel distance relative

to the upper contact line, Δy_1 , and that relative to the bottom contact line, Δy_2 , becomes small, which is evident from Fig. 3.14. Figures 3.15 to 3.17 show the gravitational effects on the velocity fields for various inclined channels (30° , 45° , 60°) at a given capillary number ($Ca = 1$). Again, as the inclined angle decreases, the lower fountain flow region expands as more gravitational force acting perpendicular to the flow direction increases. At the same time, more rolling motion is observed on the lower channel as the inclined angle decreases.

The effects of gravitational force on the advancement of flow front for various inclined angles are shown in Figs. 3.18 to 3.20. For a given inclined angle, the front tip travel distance relative to the upper contact line, Δy_1 , increases with the Stokes number while its travel distance relative to the bottom contact line, Δy_2 , decreases. As the inclined angle increases, the asymptotic value of Δy_1 decreases and that of Δy_2 increases. It is clear that these two values converge as the inclined angle approaches 90° (i.e., vertical channels) and the flow field becomes symmetric.

For a given inclined angle (30°) with $Ca = 10$ and $St = 0.1$, the pressure distribution is shown in Fig. 3.21. It shows that the pressure gradient is constant in the upstream region. Similar results are also observed in other inclined channels. The gravitational effects on the pressure distribution along the upper and bottom wall for various inclined channels are shown in Figs. 3.22 to 3.24. As the gravitational effect increases, the pressure gradient increases. It also increases the pressure difference between the upper and bottom wall at the same flow front travel distance. For a fixed capillary number and Stokes number, pressure gradient increases with the inclined angle because there are more gravitational forces acting against the flow.

3.2.2 Effects of Surface Tension

The effect of surface tension can be examined from Figs. 3.25 to 3.27. For a given inclined angle (30°) and a weak gravitational effect ($St = 0.1$), the asymptotic value of Δy_1 decreases from 0.966 to 0.965 and Δy_2 decreases from 0.870 to 0.862 as the capillary number increases from 10 to ∞ . The change is less than 1%. Thus, one can conclude that the surface tension effects on the asymptotic values of Δy_1 and Δy_2 are insignificant for the capillary numbers greater than 10. On the other hand, if the capillary number is less than 10, the effect of surface tension on Δy_1 and Δy_2 becomes more important, which is evident from Fig. 3.25. As the capillary number decreases from ∞ to 1 (i.e., surface tension increases), the values of Δy_2 and Δy_1 increase. For larger gravitational effects ($St = 1$ and 2), the value of Δy_2 increases but the value of Δy_1 decreases as surface tension increases. However, the results of inclined channels at 45° and 60° (Figs. 3.26 and 3.27) show that the values of Δy_2 and Δy_1 both increase with the surface tension for a given gravitational force.

3.3 Flow Injection through Horizontal Channels

3.3.1 Gravitational Effects

For flow injection through a horizontal channel, the gravitational force is acting perpendicular to the flow direction. This gravitational effect destroys the symmetric nature which is featured in flow injection through vertical channels. In addition, the flow is sagging toward the bottom wall as it advances. With an increase in the gravitational force, the sagging of fluid becomes more serious. Figure 3.28 shows the gravitational effect on the development of flow front at a given capillary number ($Ca = 1$). The case of

$St = 0$ is included for comparison. As the gravitational force increases, the flow profile becomes more asymmetric. Also observed is the downward shifting of the front tip location. The velocity fields under various gravitational effects are shown in Fig. 3.29. It is clear that the gravitational force has further modified the flow velocity distribution as compared with those in inclined channels. When the Stokes number increases, the fountain flow region at the upper channel is compressed while it is expanded at the lower channel. More rolling motion of fluid is observed in the lower channel.

Figure 3.30 shows the advancement of flow front under various gravitational effects ($Ca = 1$). Because of the sagging of fluid, the asymptotic value of Δy_1 increases with the Stokes number while the asymptotic value of Δy_2 decreases. For a weak gravitational force ($St = 0.1$), the front tip is positioned close to the centerline of the channel when the flow reaches the fully developed stage. With an increase in the gravitational force ($St = 1$ and 2), the sagging of fluid becomes critical. Since the upper contact line moves relatively slower than the bottom contact line, Δy_1 initially increases with time. It continues for some time before it approaches the asymptotic value.

With weak surface tension and gravitational effects ($Ca = 10$ and $St = 0.1$), the pressure contour in the fully developed flow field is shown in Fig. 3.31. Although the pressure gradient is also a constant (except in the fountain flow region), the pressure distribution is not uniform across the channel height. This can be cross-examined from Fig. 3.32 for pressure distribution along both the upper and bottom walls. Despite that the gravitational force is acting perpendicular to the flow direction, it does not affect the pressure gradient in the upstream region. The pressure gradient ($\partial P / \partial X$) is still -3 in the upstream region, which is the same as the fully developed creeping channel flow.

3.3.2 Effects of Surface Tension

The effect of surface tension on the horizontal channel flow can be examined from Fig. 3.33. For a weak gravitational force ($St = 0.1$), the asymptotic value of Δy_1 decreases from 1.00 to 0.974 while the asymptotic value of Δy_2 decreases from 0.923 to 0.853 as the capillary number increases from 1 to ∞ . It shows that the effect of surface tension is to hold and strengthen the free surface and thus it increases the values of Δy_1 and Δy_2 . However, for an increased gravitational force ($St = 2$ or 3), flow is sagging toward the bottom wall and the upper contact line is more difficult to move forward. For a given gravitational force, surface tension helps the upper contact line to move faster and thus reduces Δy_1 . On the other hand, surface tension is holding the free surface close to the bottom channel and which leads to an increase in Δy_2 . Actually, both changes in Δy_1 and Δy_2 are only about 2% as the capillary number increases from 10 to ∞ . One can thus conclude that the surface tension effect on the front tip travel distance is insignificant in horizontal injection molding if the capillary number is greater than 10.

Although the effect of surface tension on the relative front tip travel distance is insignificant for capillary numbers greater than 10, its effect on the waiting time for the contact lines to initiate their first move is quite obvious. The time required for the contact lines to begin their first move is listed in Table 3.2 for various capillary and Stokes numbers. For the bottom contact line, the waiting time decreases with the capillary number and Stokes number. However, for the upper contact line, the waiting time decreases with the capillary number when the Stokes number is less than or equal to unity, but increases with the capillary number if the Stokes number is greater than unity. In all cases, the waiting time increases as the Stokes number increases.

3.4 Conclusion

The effects of gravitational force and surface tension on flow injection through various channel inclinations (0° , 30° , 45° , 60° , 90°) are analyzed using the Galerkin finite element method. The present study not only confirms the results of the previous studies (i.e., for the case when the surface tension and gravitational effects are both negligible), but also brings out the new evidences of the gravitational and surface tension effects on injection molding.

For vertical channels, gravitational force flattens the flow front and reduces the fountain flow region. It also shortens the time required for the contact line to initiate its first move and the total time to reach a fully developed stage. With negligible surface tension and gravitational effects, the pressure gradient of the upstream flow has the same value as that of a fully developed creeping flow. As the gravitational force increases, the absolute value of the pressure gradient increases as indicated by Eq. (3.5).

The effect of surface tension is to expand the fountain flow region. With a large surface tension, the front tip travel distance increases. Although surface tension also has an influence over the waiting time for the first move of the contact line, its effect is insignificant for $Ca > 10$. The effect of surface tension on the front tip travel distance become important only when the capillary number is less than 10. Also, their effect on the pressure distribution is limited for $Ca < 1$.

For horizontal channels, the effect of the gravitational force is drastic, especially for $St \geq 0.1$. It has not only destroyed the symmetric nature of the flow field, but also greatly modified the fountain flow region, velocity, and pressure distribution. Due to the sagging of fluid, the gravitational effect leads to non-uniform impregnation, a condition

which is not preferred in resin transfer molding processes. The effect of surface tension leads to an increase in the value of Δy_2 . However, the value of Δy_1 increases with surface tension at $St = 0.1$ but decreases with surface tension when $St = 1$ and 2 . Although the effect of surface tension on the front tip travel distance is insignificant for $Ca > 10$, but its effects on the waiting time is quite obvious.

For inclined channels, the gravitational effects on the development of the flow front, velocity field, pressure distribution and the front tip travel distance are in between the two limiting cases of vertical and horizontal channels. As the inclined angle increases, the flow field becomes more symmetrical and the difference between Δy_1 and Δy_2 reduces. The effect of surface tension on the asymptotic value of front tip travel distance becomes more important as the capillary number becomes less than 10 .

A further increase in the gravitational force leads to the retreat of the upper contact line and the solution becomes more difficult. For resin transfer molding processes, it can be concluded that the presence of gravity results in non-uniform impregnation and will adversely affect the part quality.

Table 3.1: Time required for the contact line to initiate its first move (vertical channels)

St \ Ca	1	2	5	10	∞
0	0.631	0.462	0.296	0.285	0.240
0.1	0.595	0.429	0.296	0.285	0.240
1	0.529	0.396	0.285	0.276	0.236
2	0.495	0.362	0.285	0.269	0.229
10	0.385	0.296	0.240	0.229	0.196

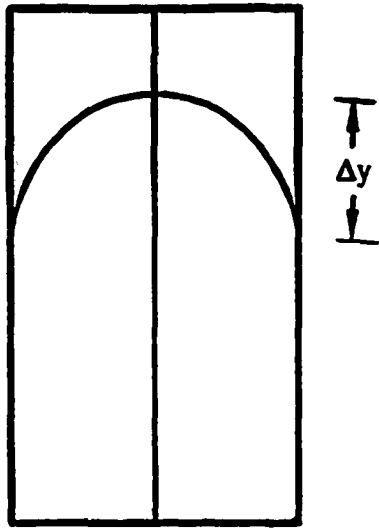
Table 3.2: Time required for the contact line to initiate its first move (horizontal channels): (a) upper contact line, (b) bottom contact line.

St \ Ca	1	2	5	10	∞
0.1	0.629	0.462	0.329	0.296	0.262
1	1.001	0.995	0.878	0.429	0.345
2	1.382	1.494	1.529	1.544	1.564

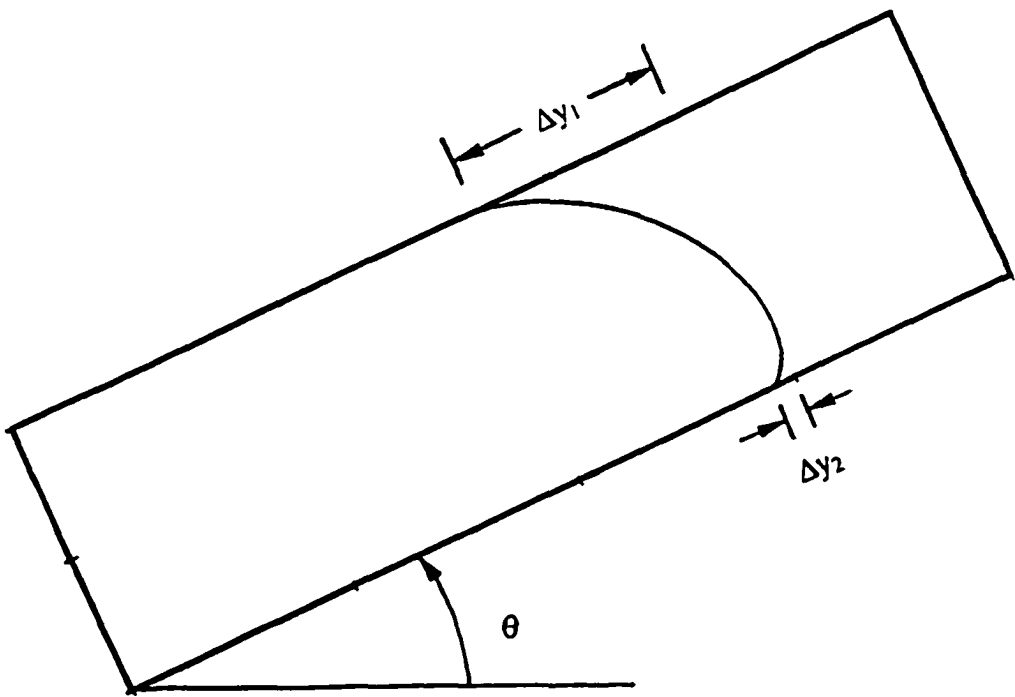
(a)

St \ Ca	1	2	5	10	∞
0.1	0.562	0.429	0.296	0.276	0.240
1	0.396	0.329	0.241	0.224	0.196
2	0.329	0.262	0.196	0.187	0.152

(b)



(a)



(b)

Figure 3.1 Definition of the front tip travel distance relative to the contact lines (Δy , Δy_1 , and Δy_2): (a) vertical channel, (b) horizontal or inclined channels ($\theta = 0^\circ, 30^\circ, 45^\circ$, and 60°).

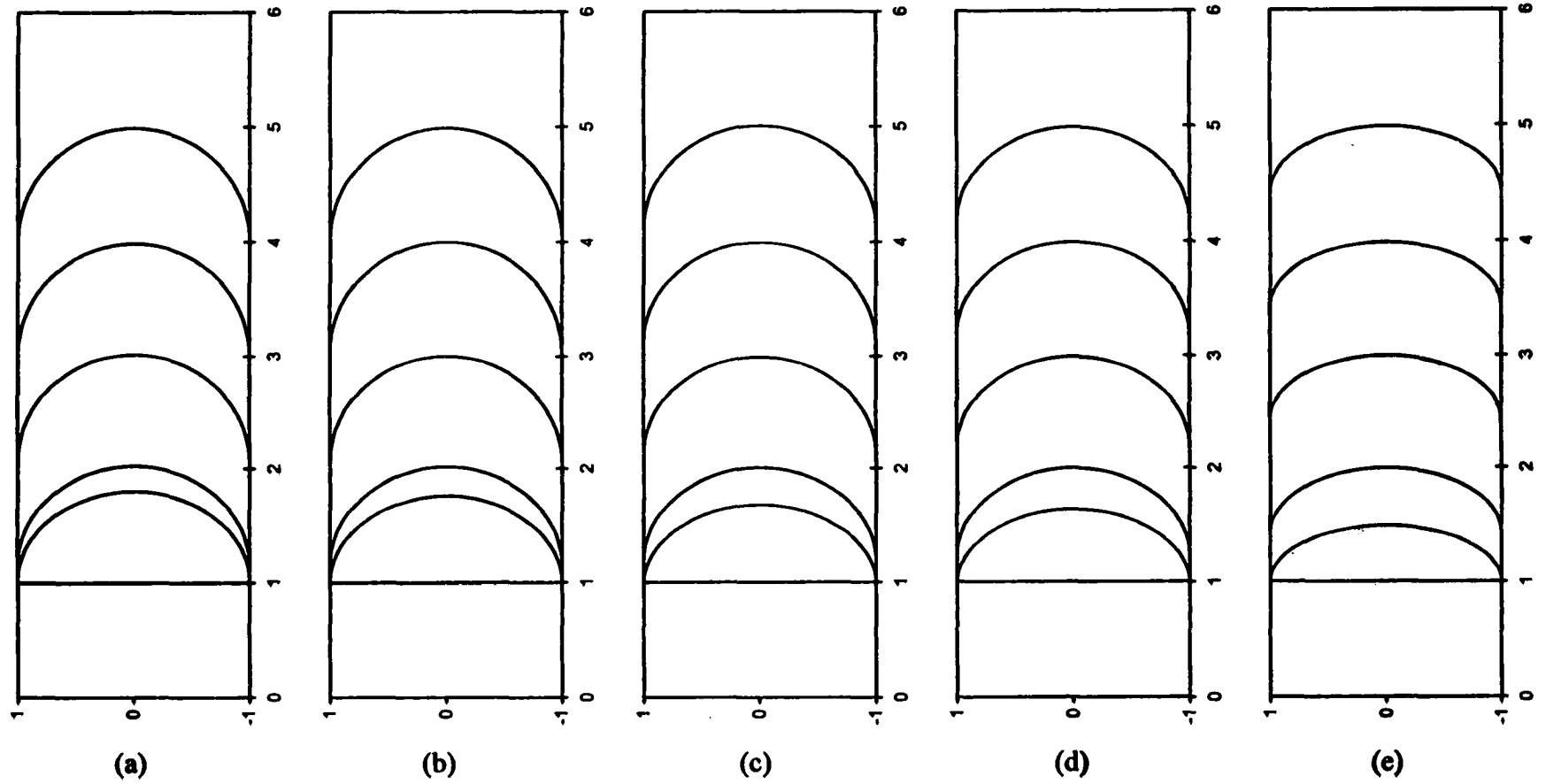


Figure 3.2 Development of flow front in a vertical channel at various Stokes numbers ($Ca = 1$): (a) $St = 0$, (b) $St = 0.1$, (c) $St = 1$, (d) $St = 2$, and (e) $St = 10$.

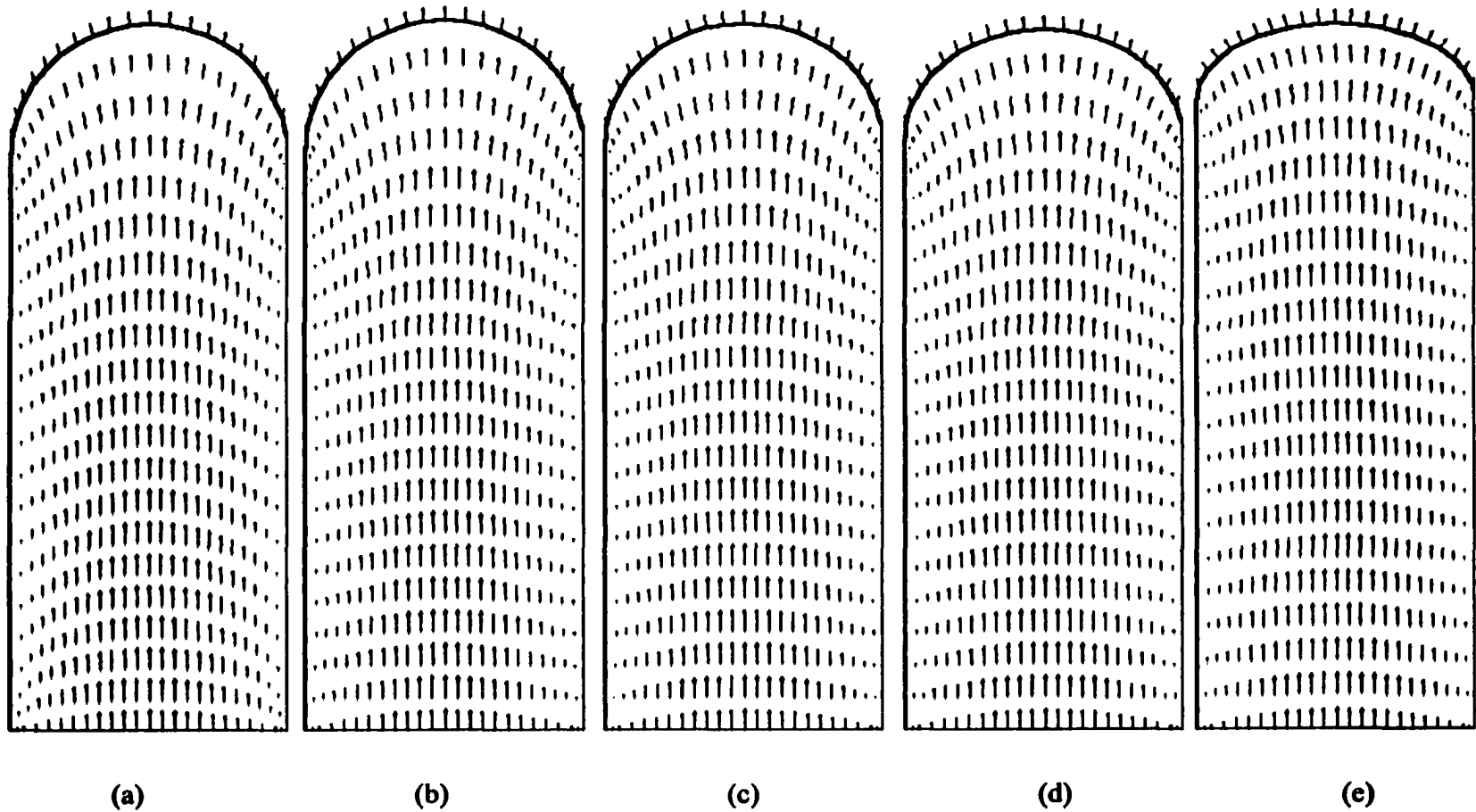


Figure 3.3 Velocity fields for flow injection in a vertical channel at various Stokes numbers ($Ca = 1$): (a) $St = 0$, (b) $St = 0.1$, (c) $St = 1$, (d) $St = 2$, and (e) $St = 10$.

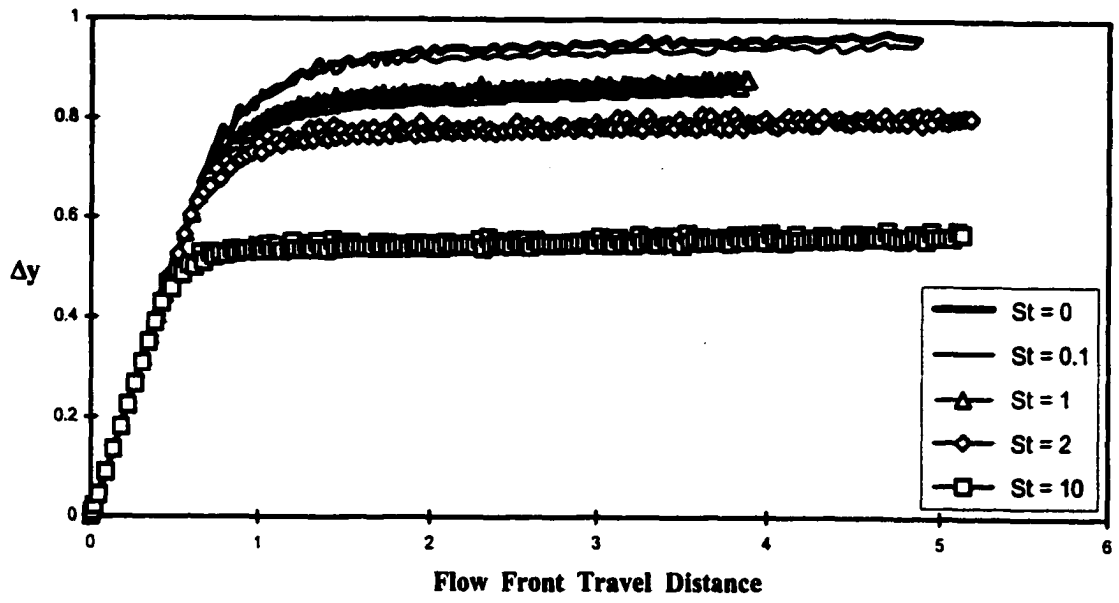


Figure 3.4 Relative flow front travel distance under various gravitational effects (vertical channels, $Ca = 1$).

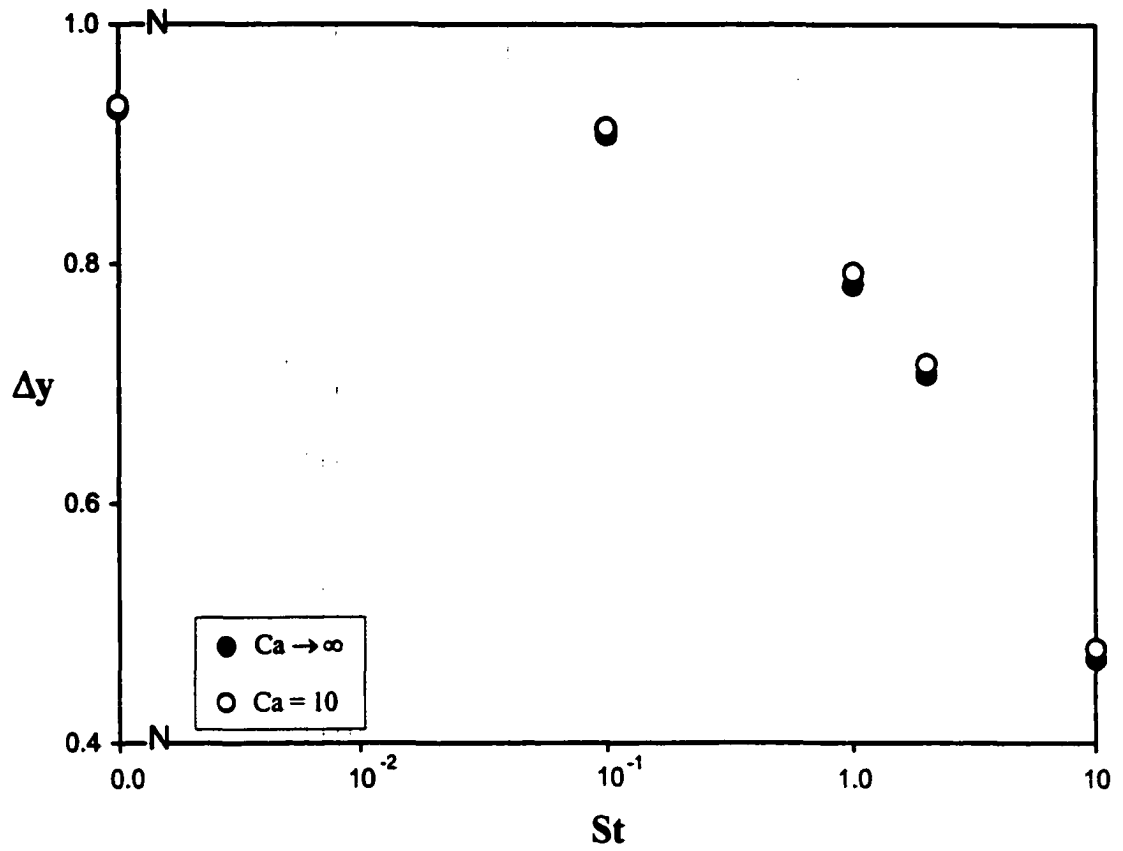


Figure 3.5 Relationship between the Stokes number and fully developed front tip travel distance ($Ca = 10$ and $Ca \rightarrow \infty$).

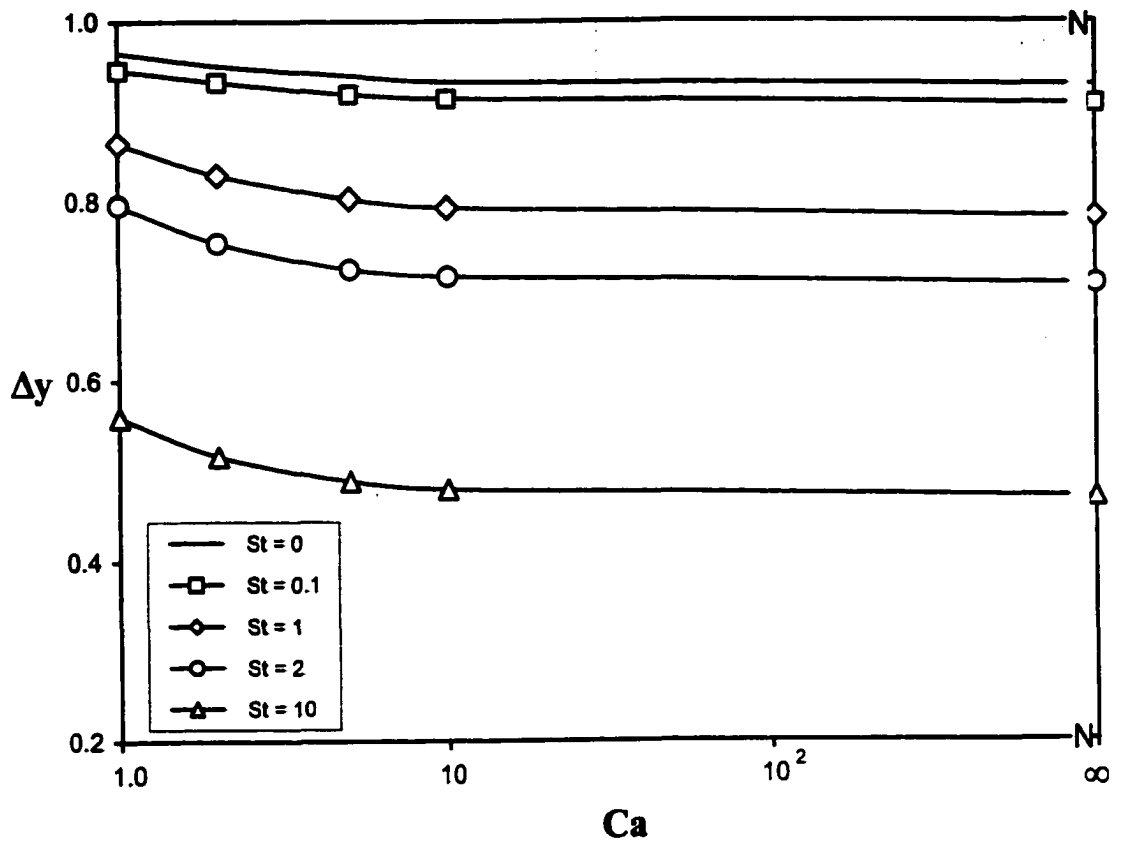


Figure 3.6 Fully developed front tip travel distance as a function of the Stokes and capillary numbers.

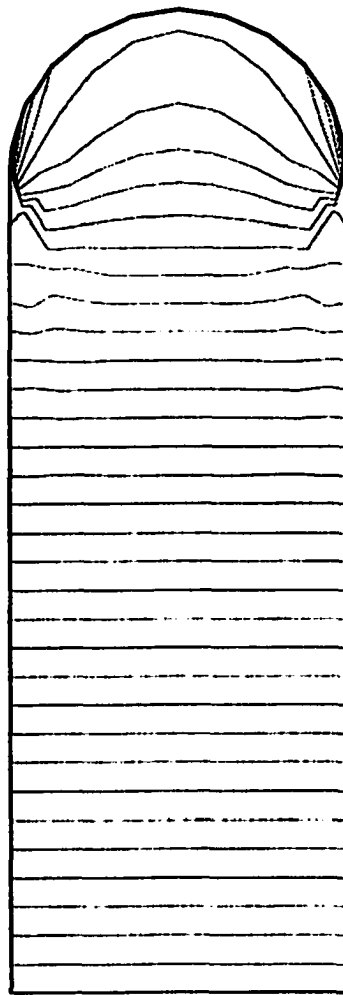


Figure 3.7 Pressure contour of a fully developed flow field in vertical flow injection ($St = 0, Ca \rightarrow \infty$, and $\Delta P = 0.5$).

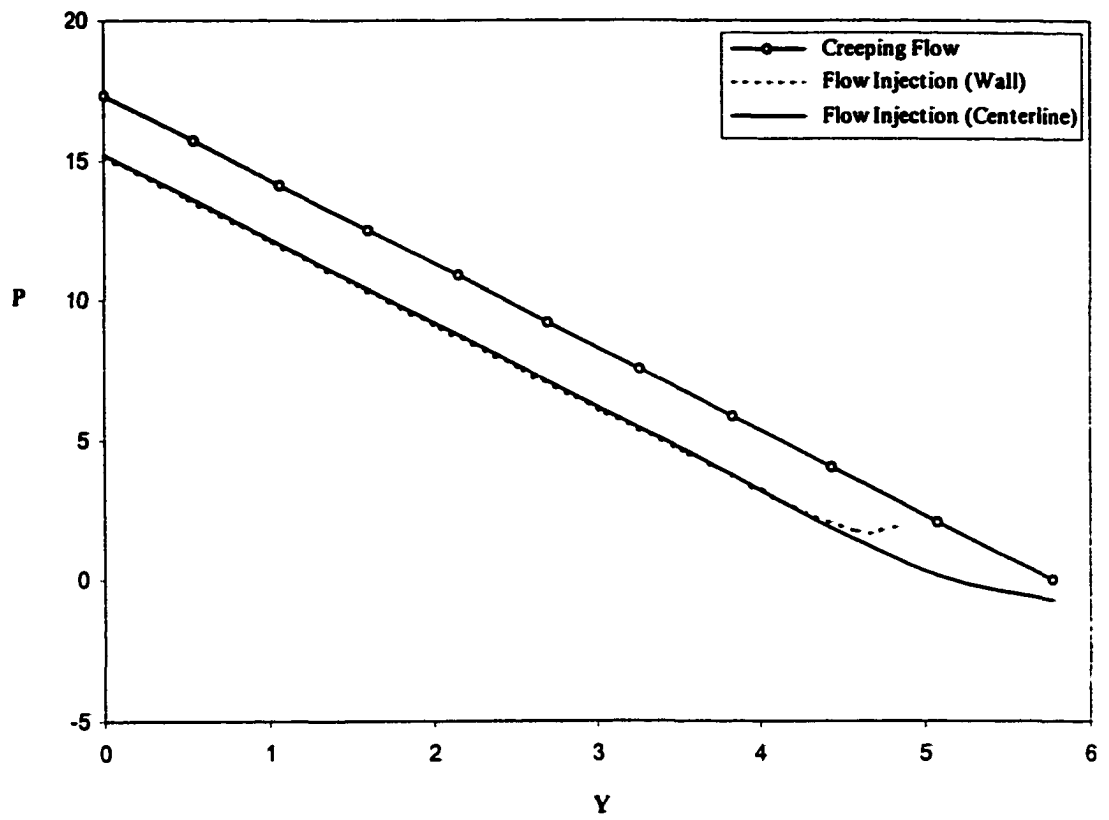


Figure 3.8 Comparison of pressure distribution of fully-developed creeping flow and that of flow injection with negligible surface tension and gravitational effects.

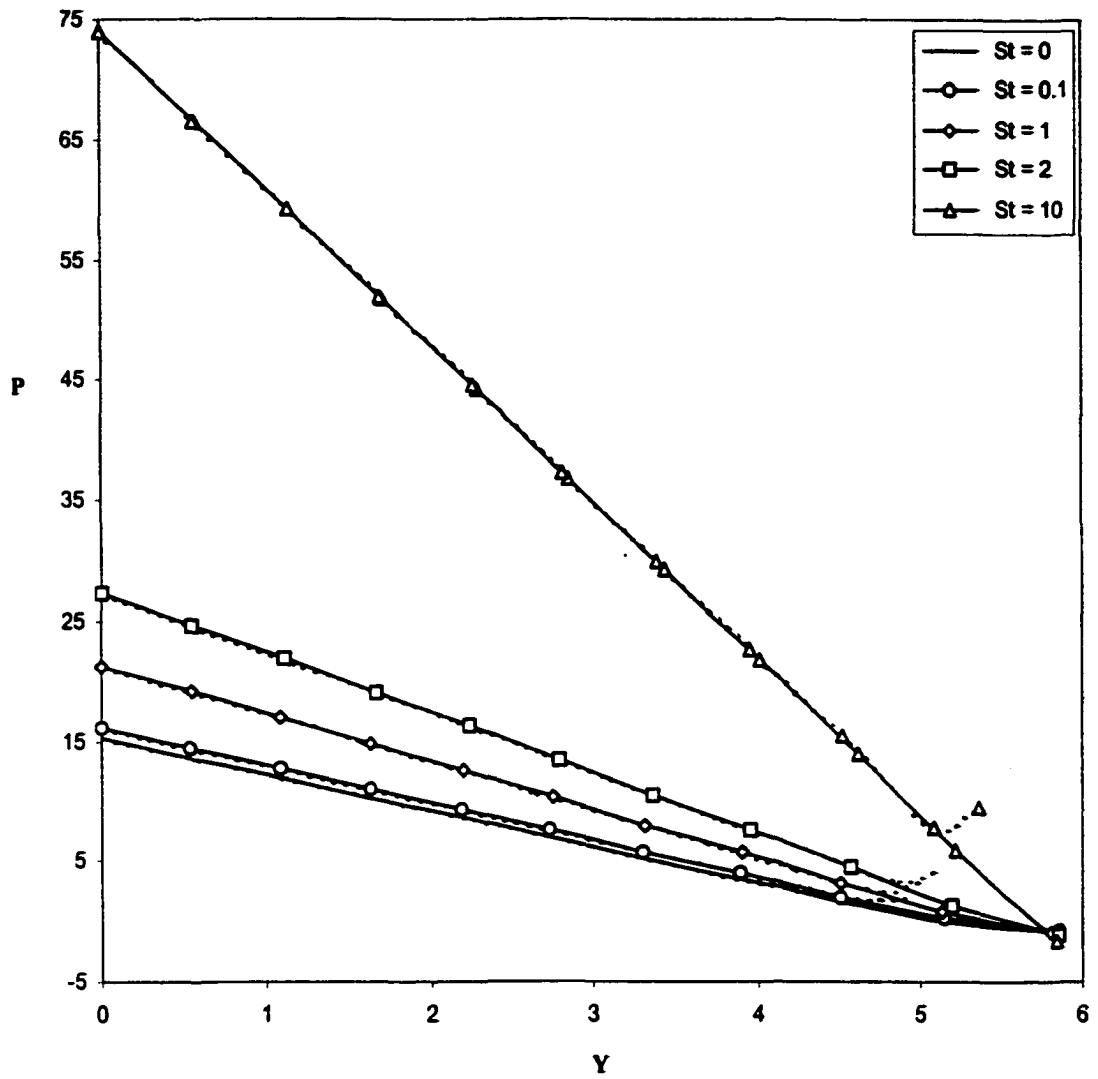


Figure 3.9 Gravitational effects on the pressure distribution along the wall and centerline ($Ca \rightarrow \infty$): wall (- - -) and centerline (—).

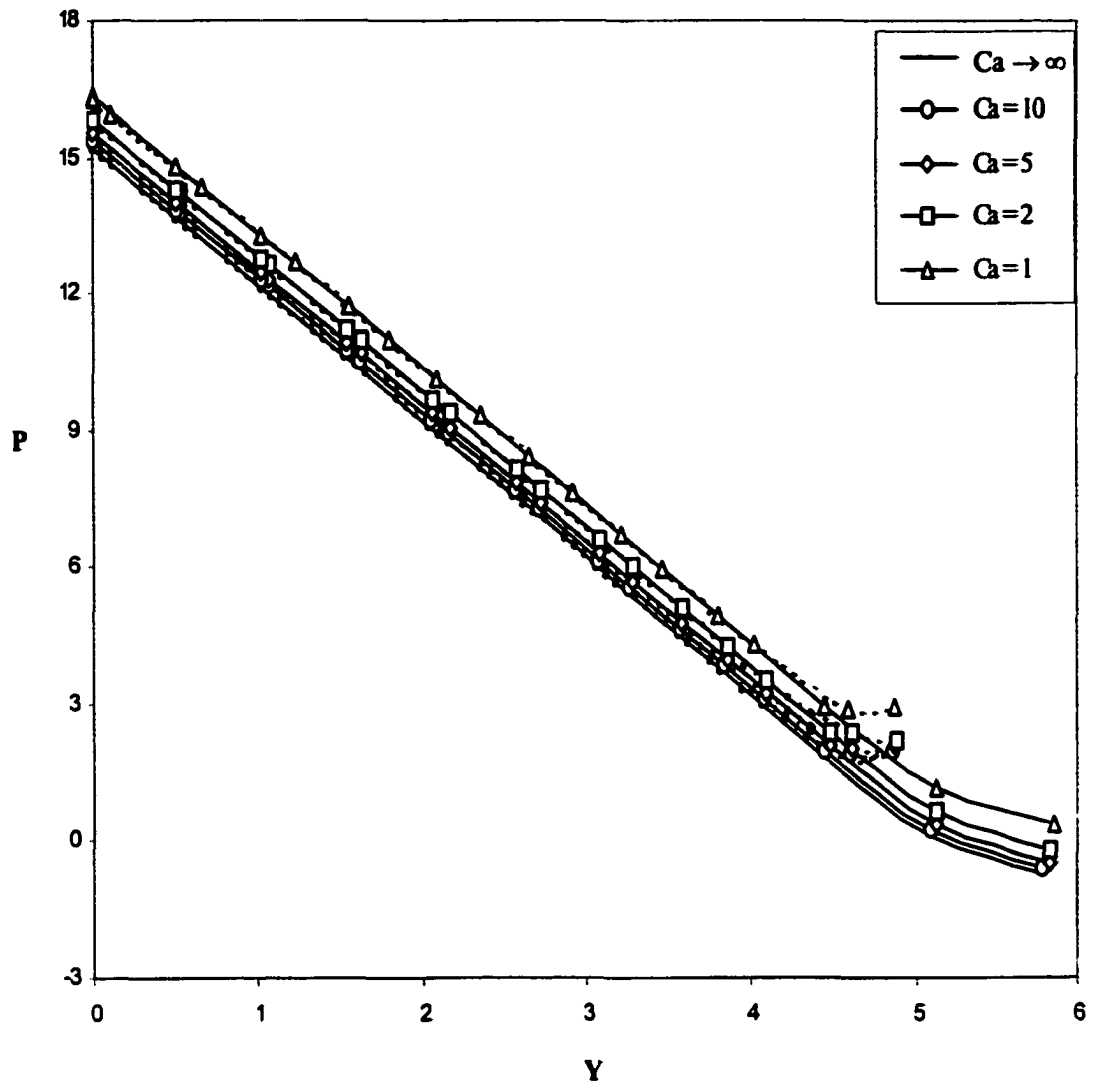


Figure 3.10 Surface tension effects on the pressure distribution along the wall and centerline ($St = 0$): wall (---) and centerline (—).

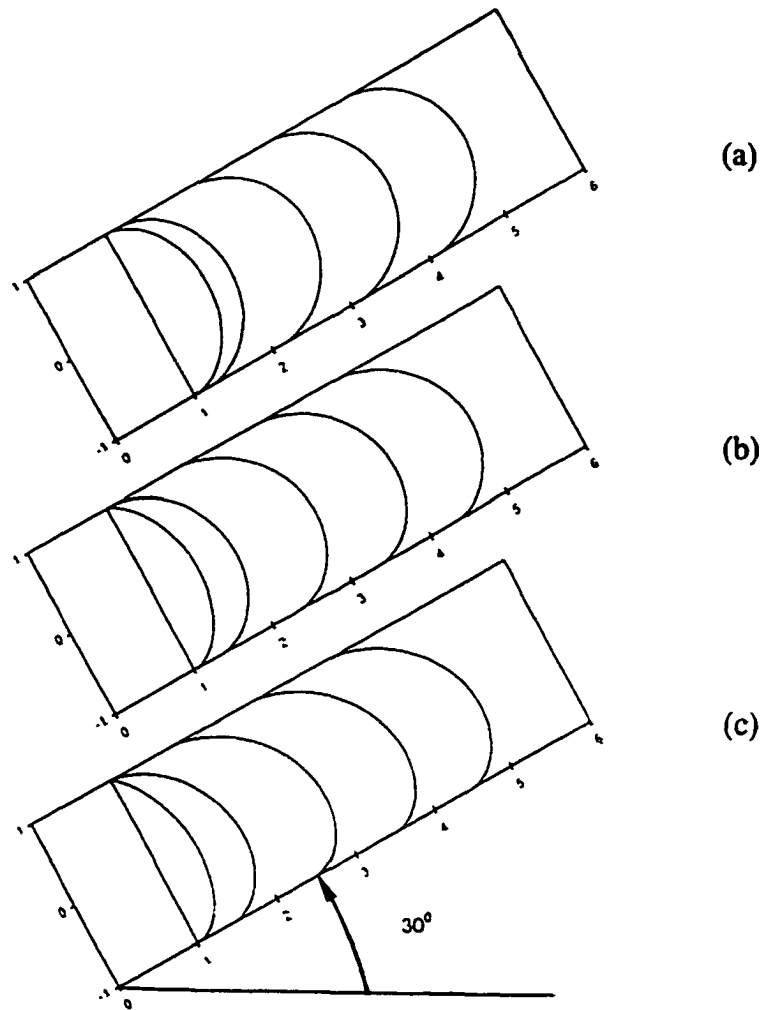


Figure 3.11 Gravitational effects on the development of flow front in a 30° inclined channel ($Ca = 1$): (a) $St = 0.1$, (b) $St = 1$, and (c) $St = 2$.

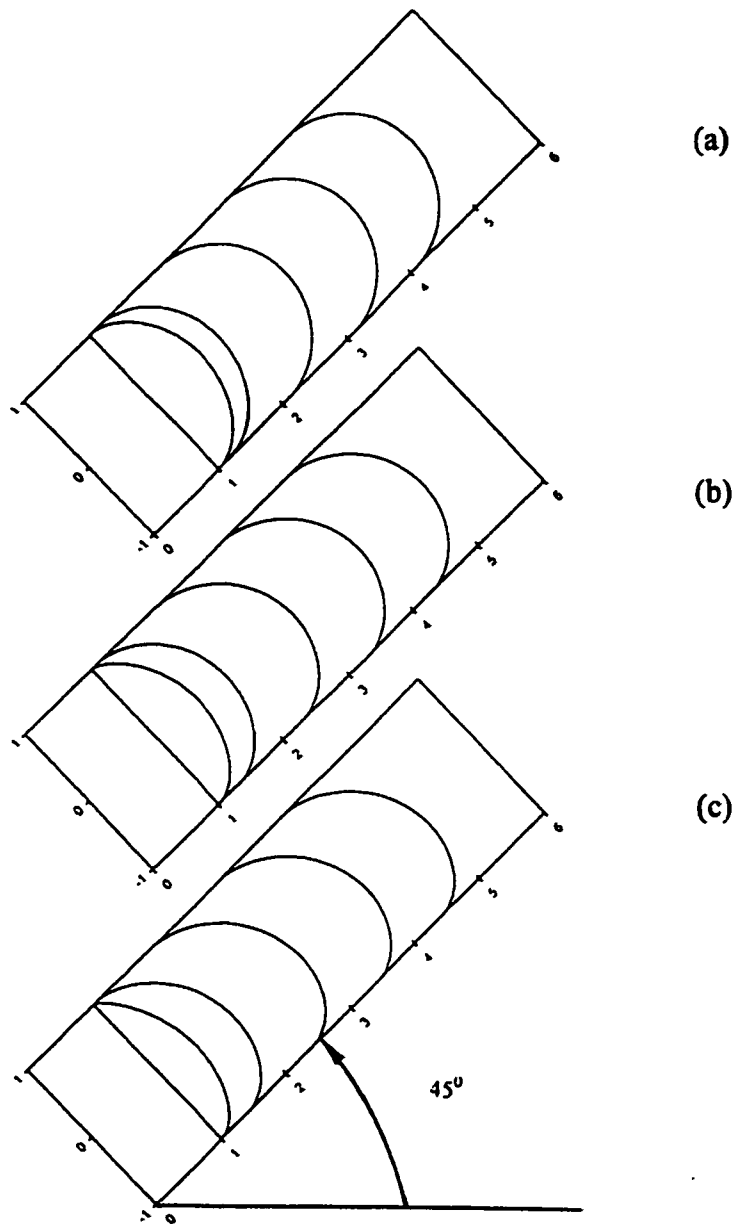


Figure 3.12 Gravitational effects on the development of flow front in a 45° inclined channel ($Ca = 1$): (a) $St = 0.1$, (b) $St = 1$, and (c) $St = 2$.

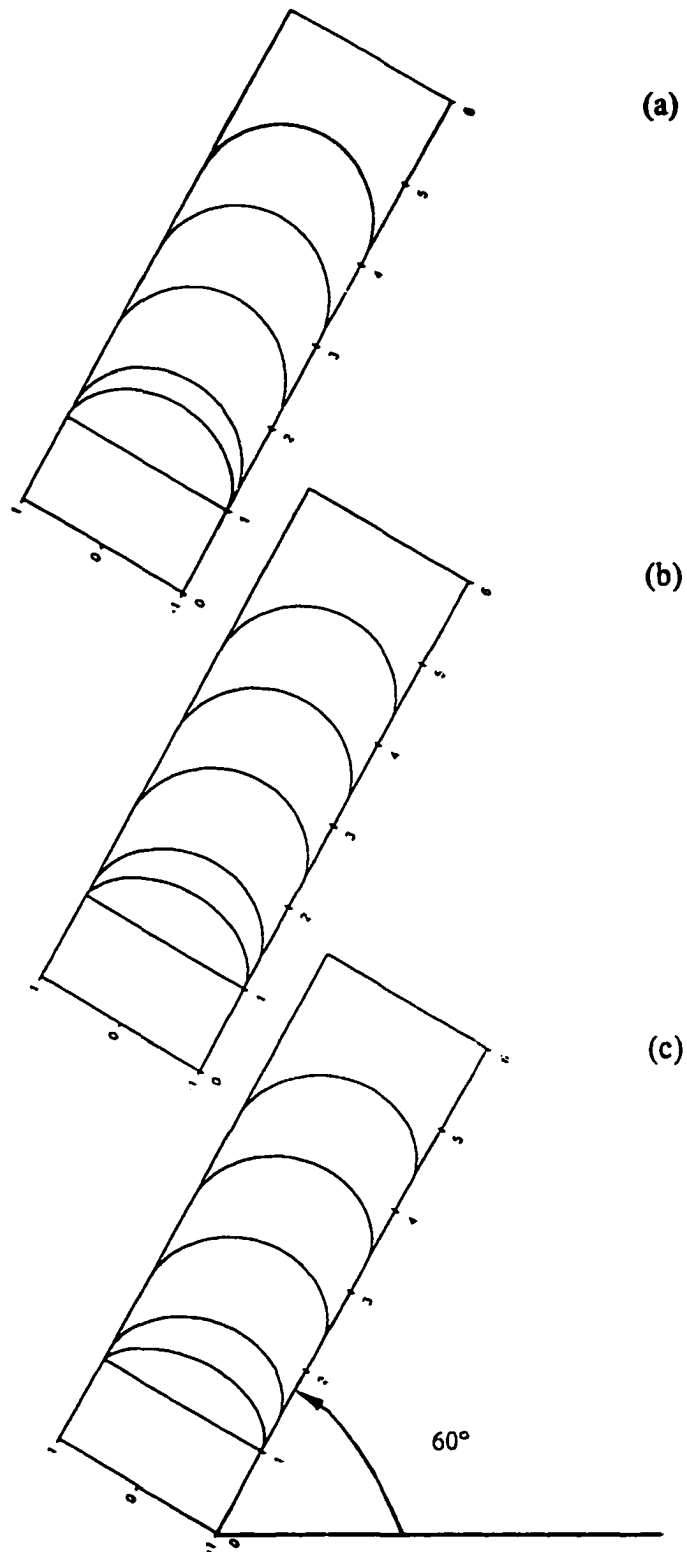


Figure 3.13 Gravitational effects on the development of flow front in a 60° inclined channel ($Ca = 1$): (a) $St = 0.1$, (b) $St = 1$, and (c) $St = 2$.

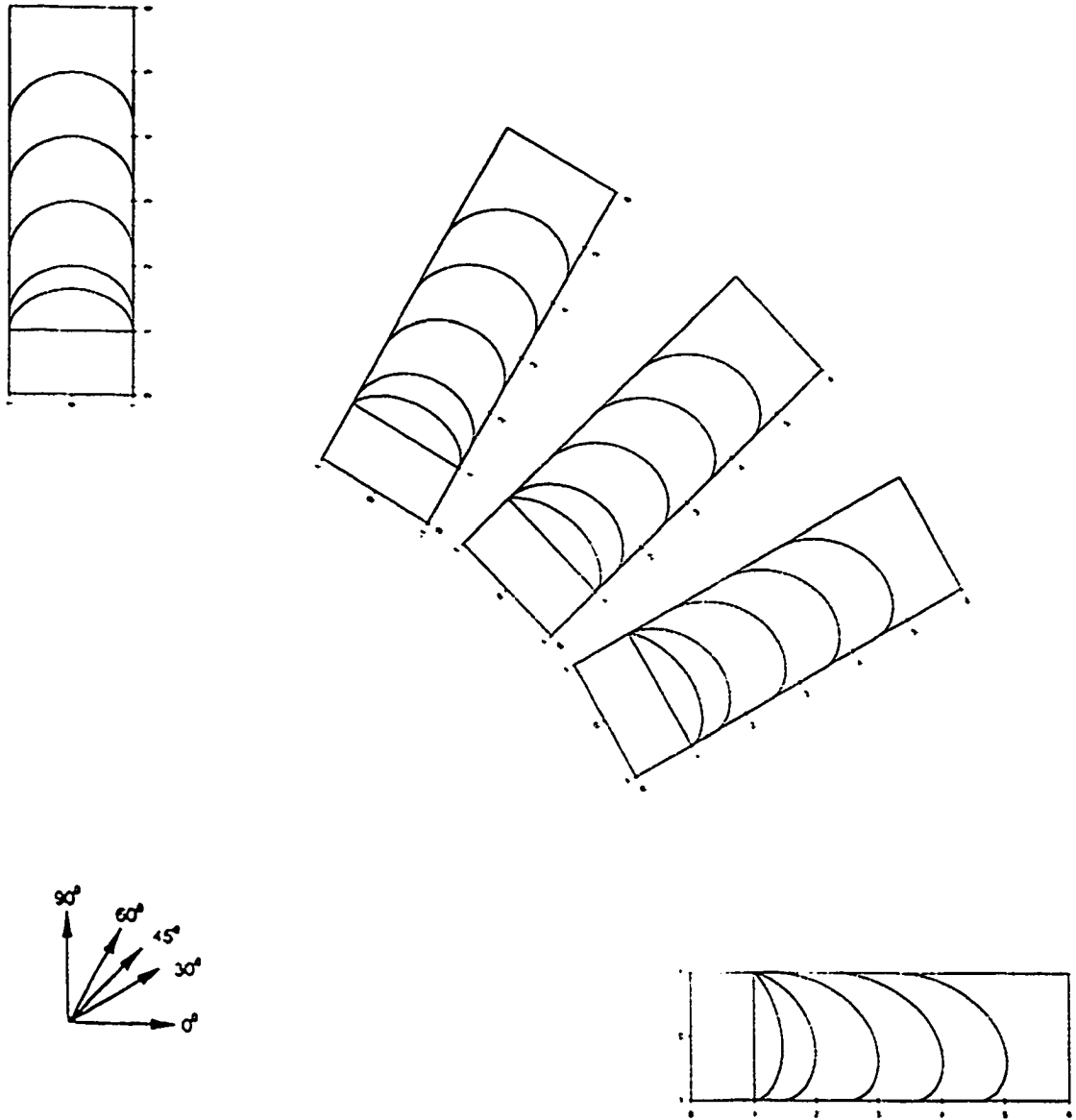


Figure 3.14 Development of flow front for flow injection in various inclined channels at $Ca = 1$ and $St = 2$.

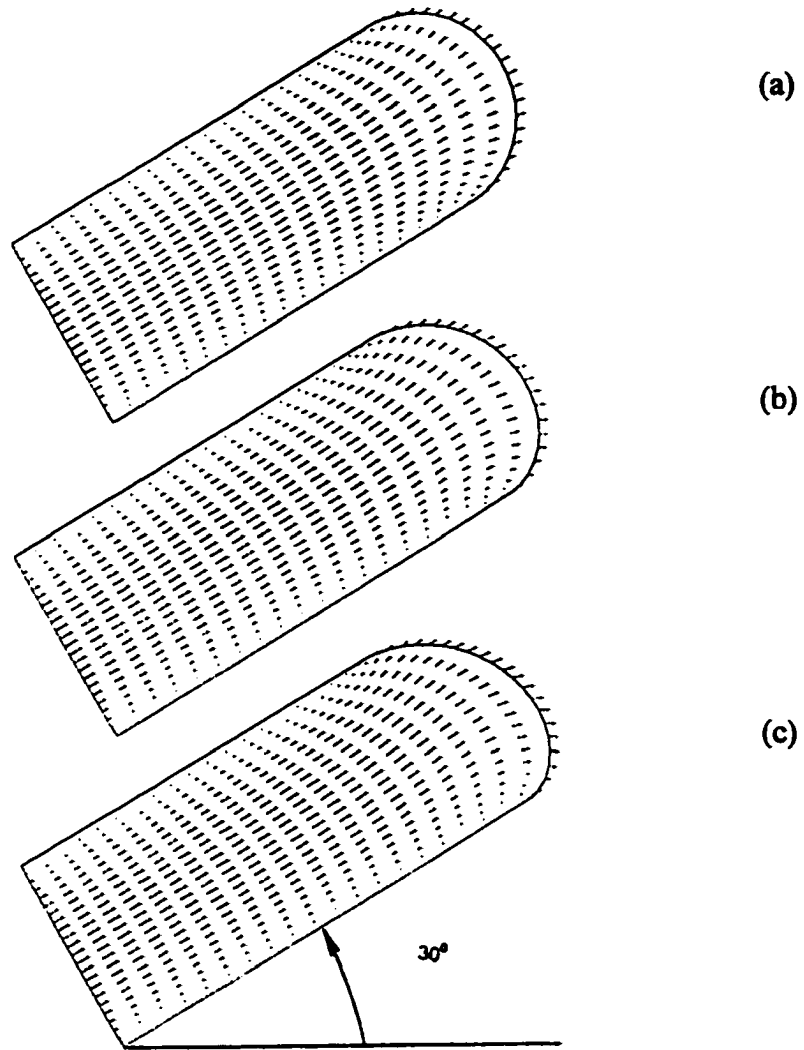


Figure 3.15 Gravitational effects on the velocity field for a 30° inclined channel: (a) $St = 0.1$, (b) $St = 1$, and (c) $St = 2$.

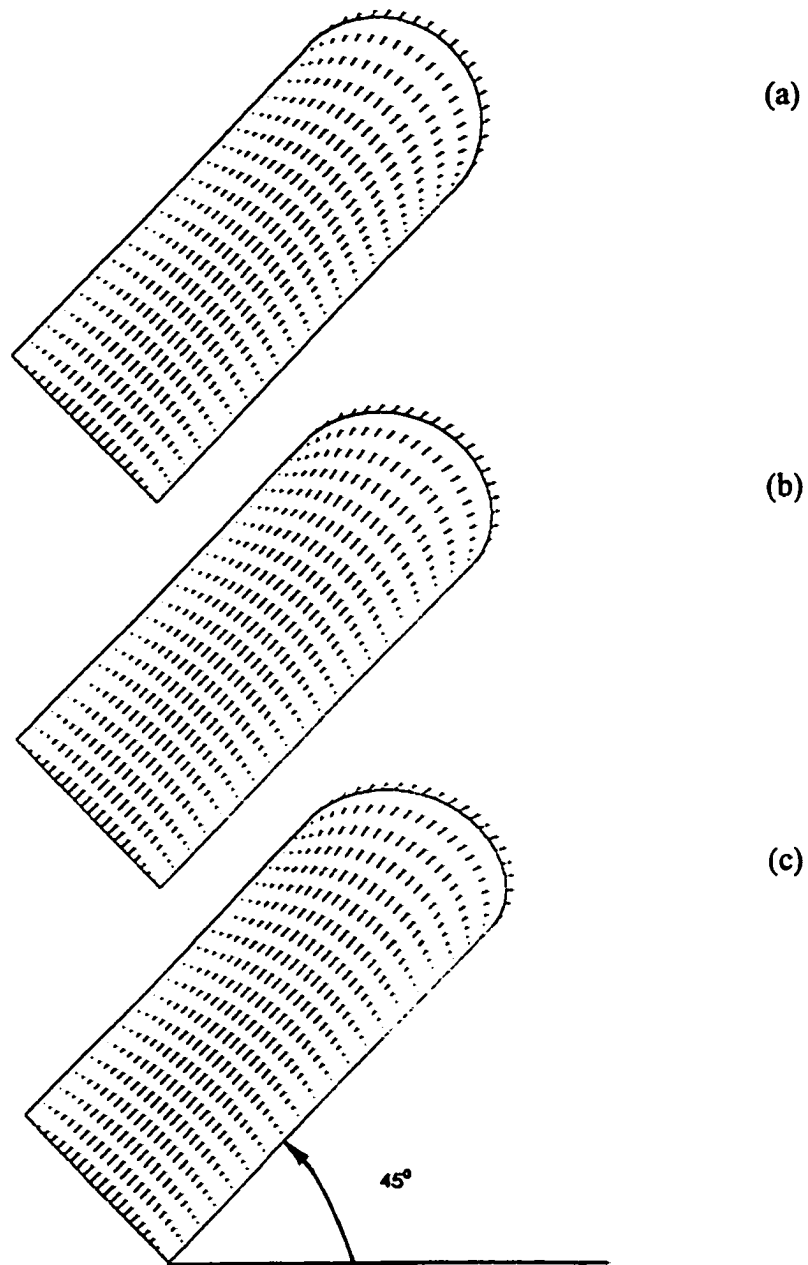


Figure 3.16 Gravitational effects on the velocity field for a 45° inclined channel: (a) $St = 0.1$, (b) $St = 1$, and (c) $St = 2$.

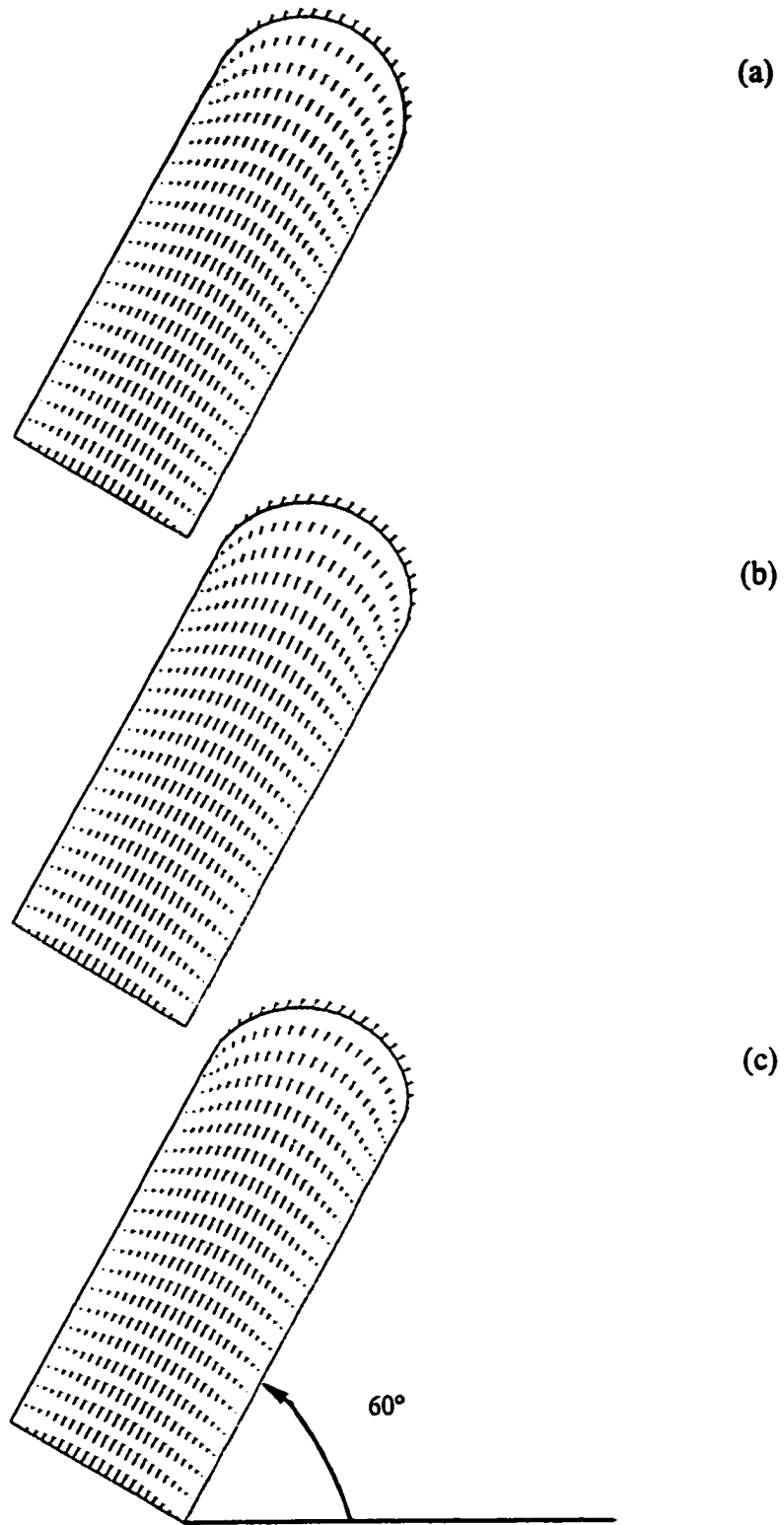
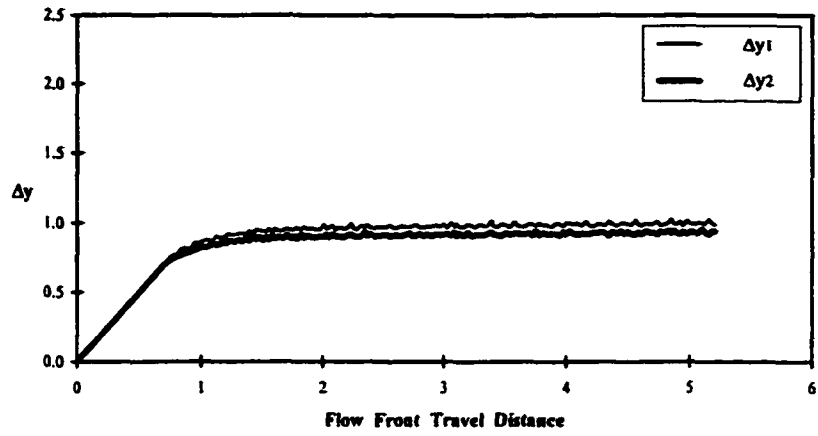
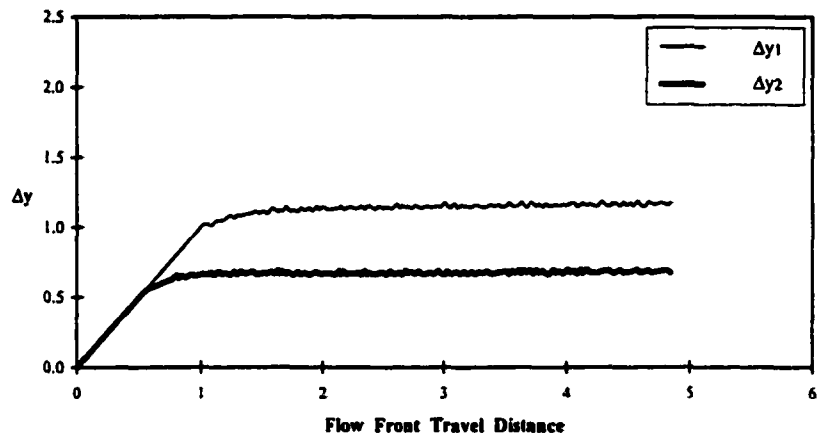


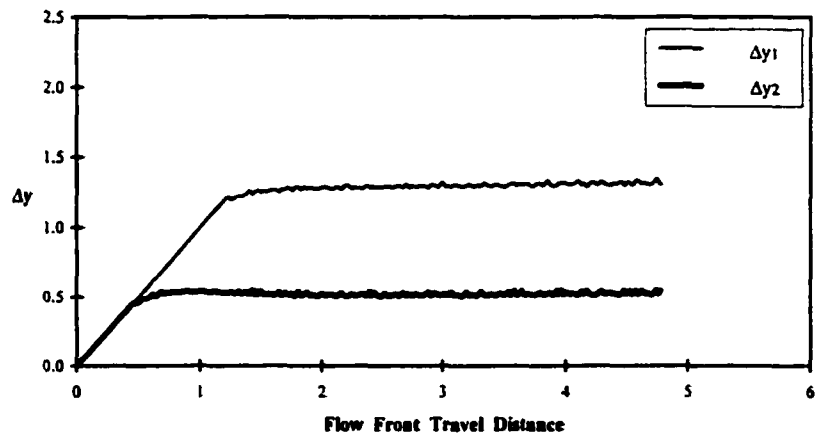
Figure 3.17 Gravitational effects on the velocity field for a 60° inclined channel: (a) $St = 0.1$, (b) $St = 1$, and (c) $St = 2$.



(a)

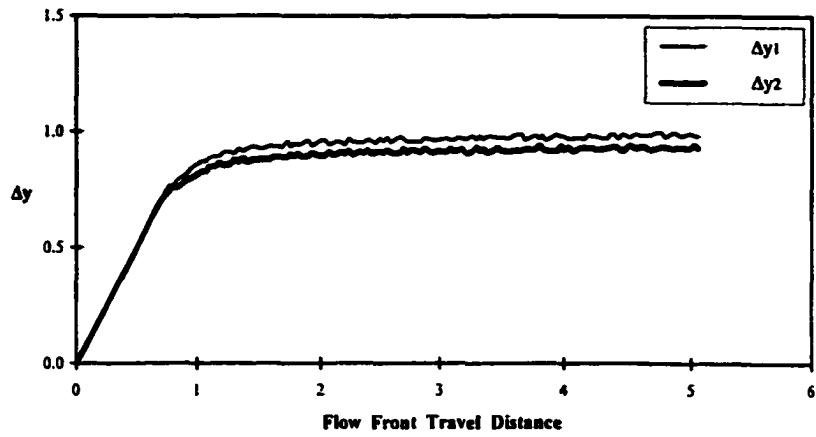


(b)

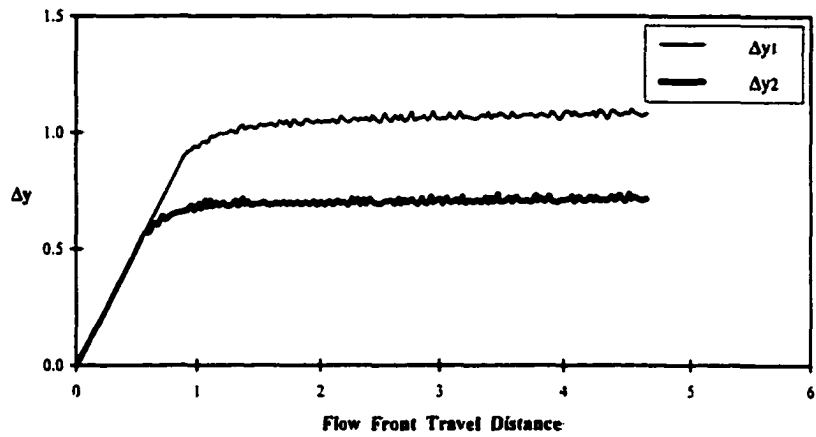


(c)

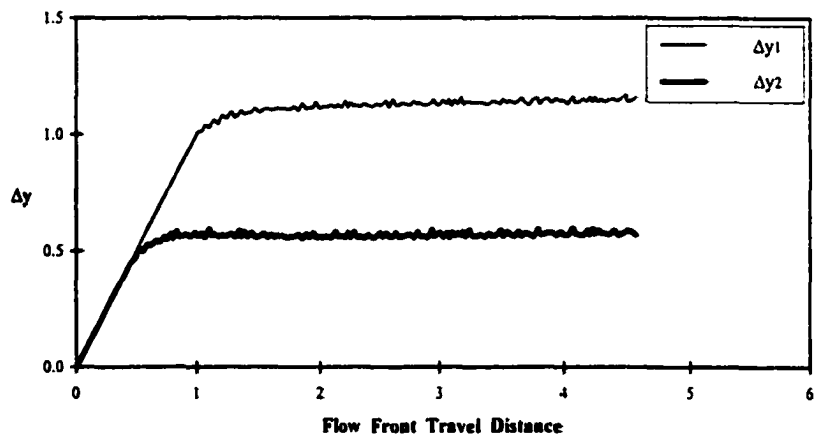
Figure 3.18 Relative flow front travel distance under various gravitational effects in a 30° inclined channel: (a) $St = 0.1$, (b) $St = 1$, and (c) $St = 2$.



(a)

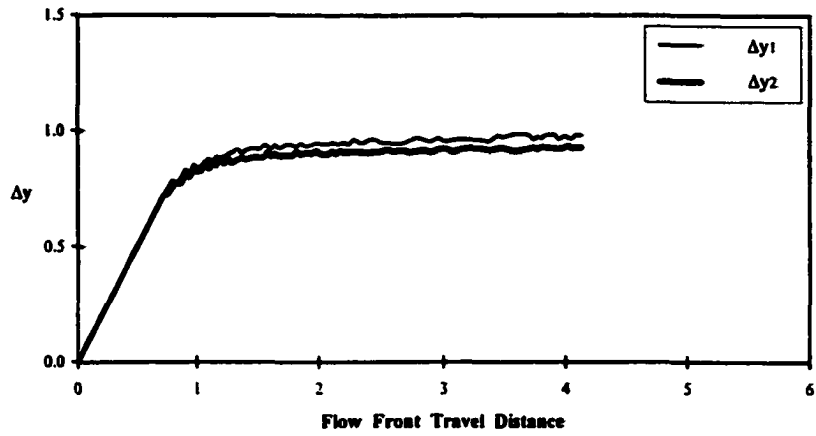


(b)

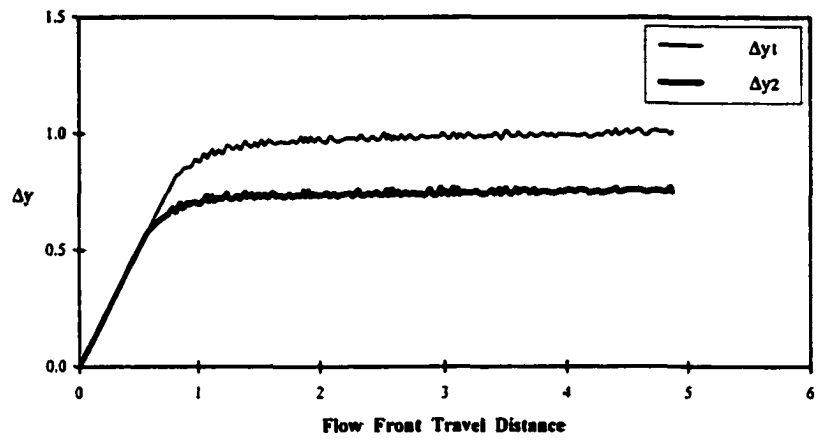


(c)

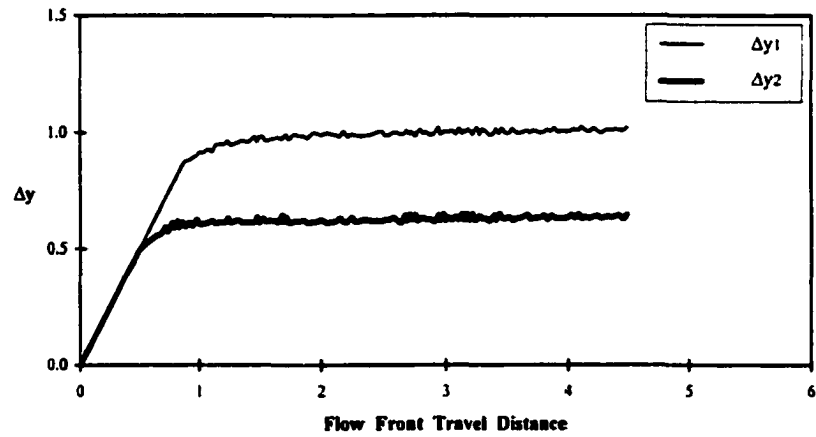
Figure 3.19 Relative flow front travel distance under various gravitational effects in a 45° inclined channel: (a) $St = 0.1$, (b) $St = 1$, and (c) $St = 2$.



(a)



(b)



(c)

Figure 3.20 Relative flow front travel distance under various gravitational effects in a 60° inclined channel: (a) $St = 0.1$, (b) $St = 1$, and (c) $St = 2$.

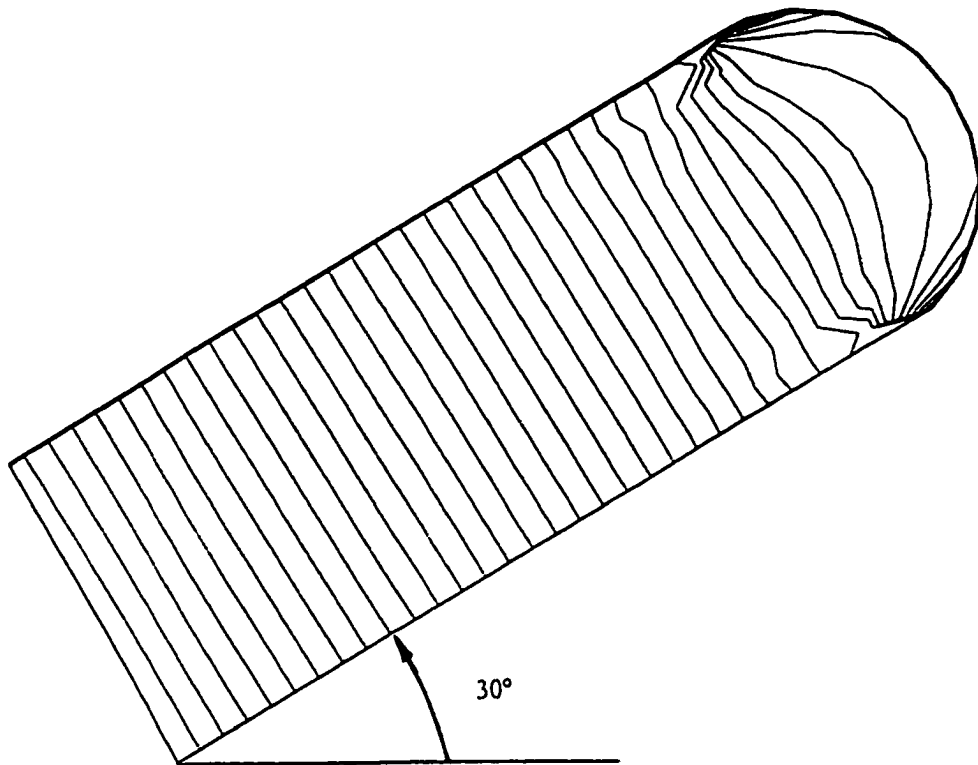


Figure 3.21 Pressure contour of a fully developed flow field in a 30° inclined channel (Ca = 10, St = 0.1, and $\Delta P = 0.5$).

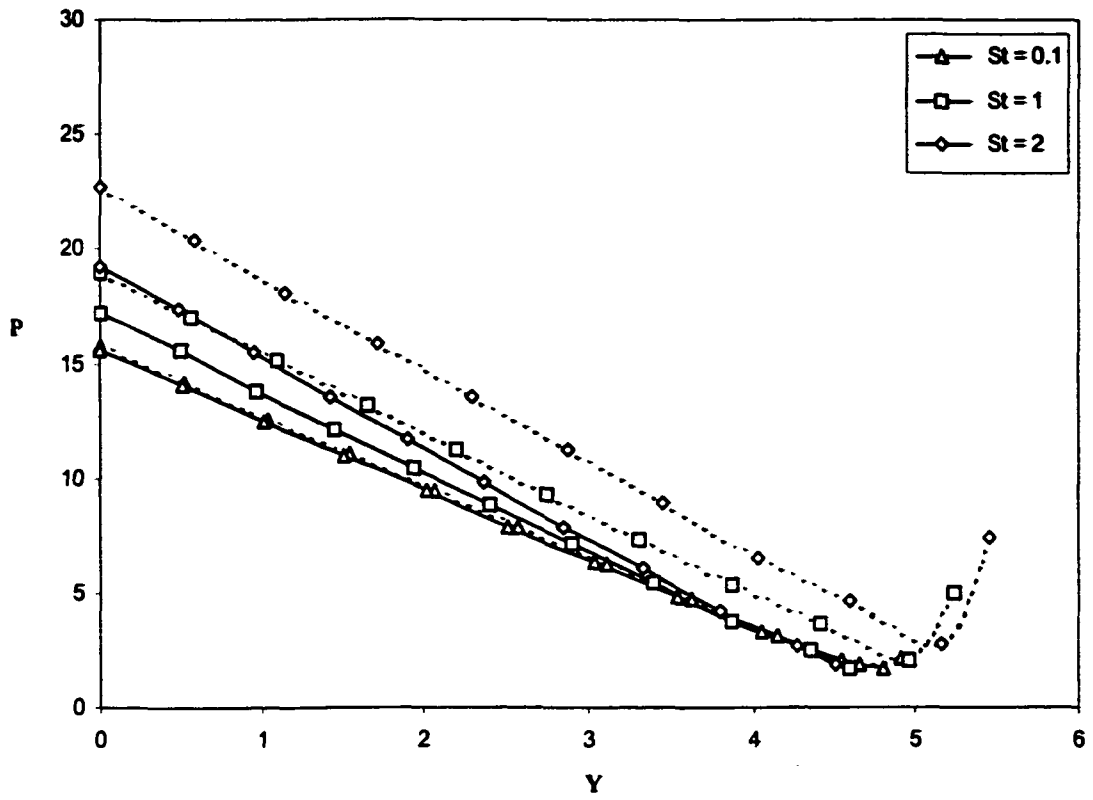


Figure 3.22 Gravitational effects on the pressure distribution in a 30° inclined channel: upper wall (—) and bottom wall (- - -).

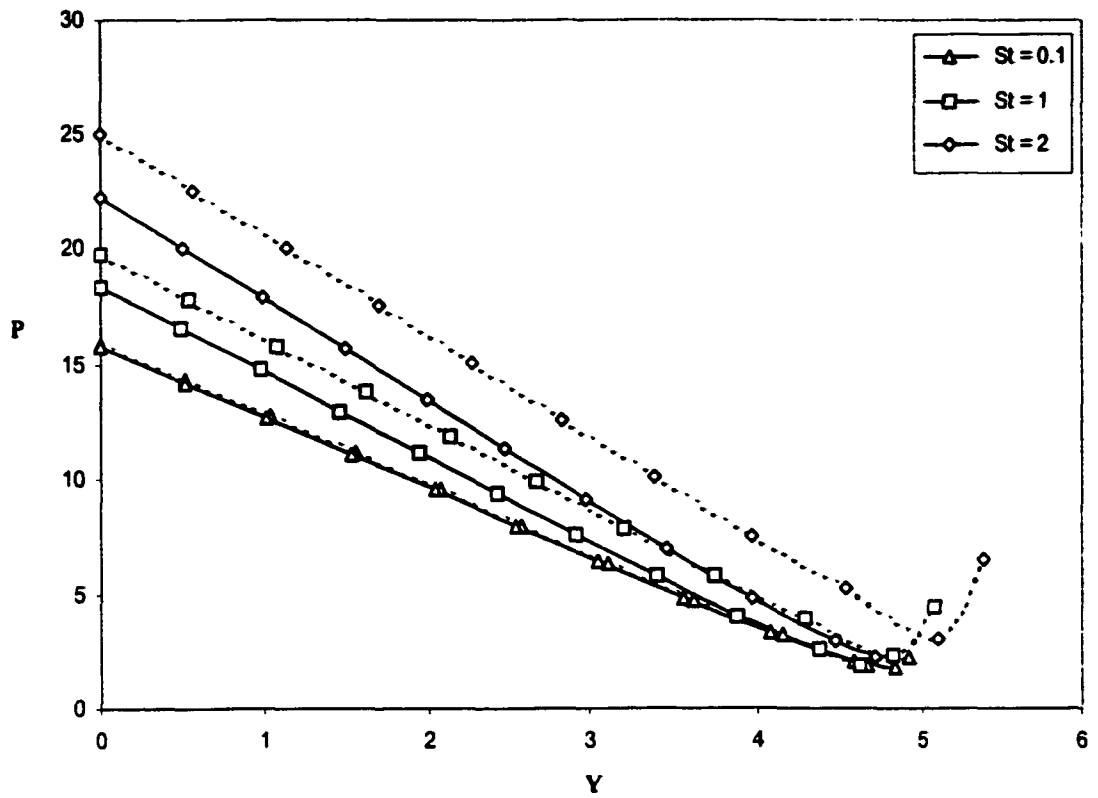


Figure 3.23 Gravitational effects on the pressure distribution in a 45° inclined channel: upper wall (—) and bottom wall (- - -).

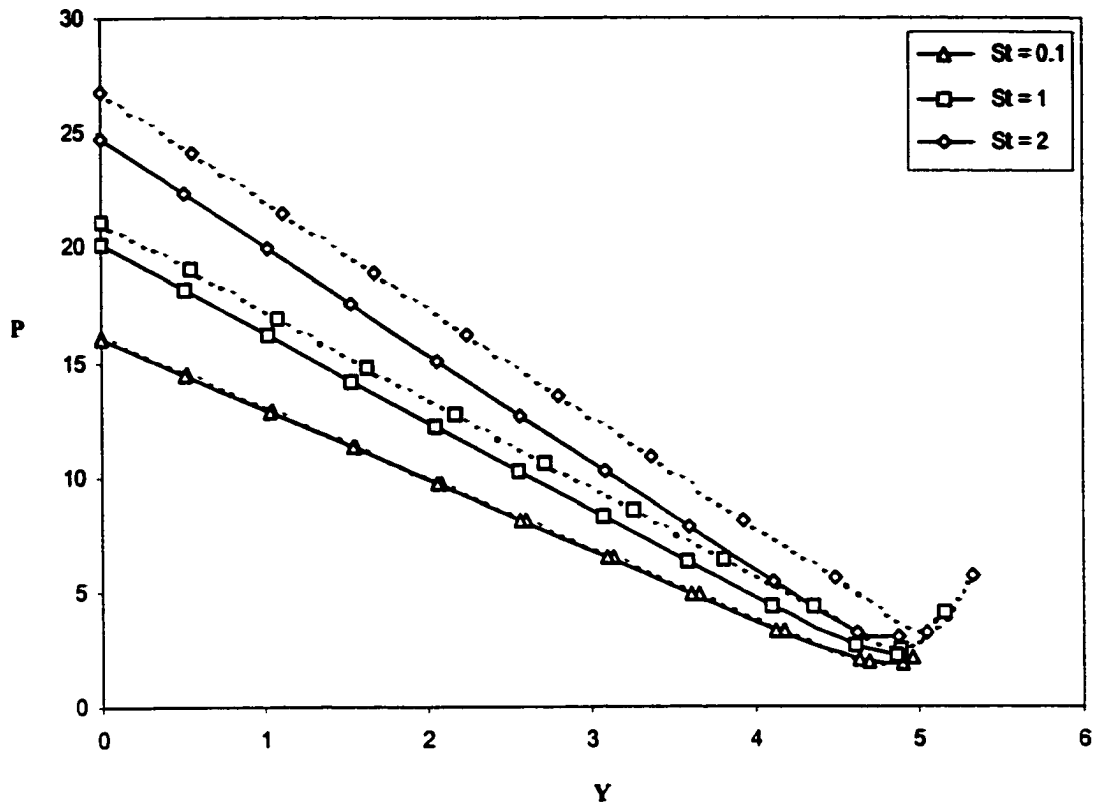


Figure 3.24 Gravitational effects on the pressure distribution in a 60° inclined channel: upper wall (—) and bottom wall (- - -).

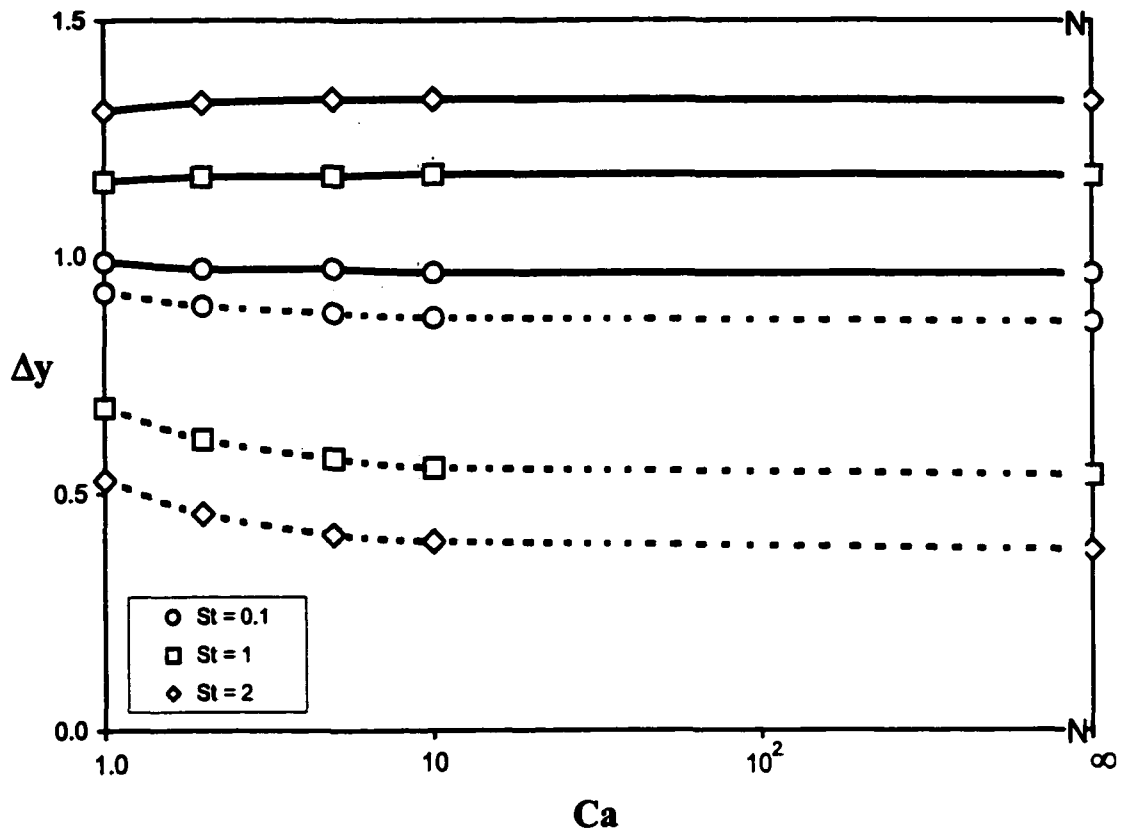


Figure 3.25 Fully developed front tip travel distance relative to the upper contact lines, Δy_1 , and bottom contact line, Δy_2 , as a function of the Stokes and capillary number (30° inclined channels).

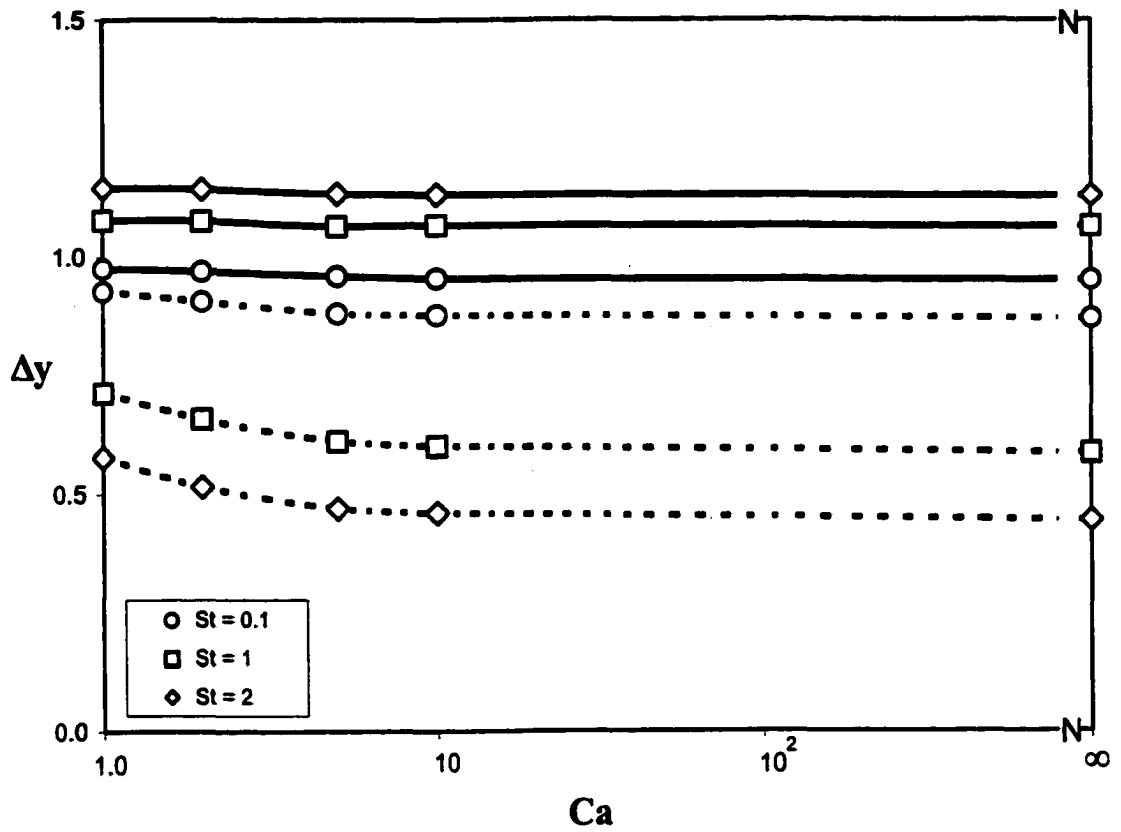


Figure 3.26 Fully developed front tip travel distance relative to the upper contact lines, Δy_1 , and bottom contact line, Δy_2 , as a function of the Stokes and capillary number (45° inclined channels).

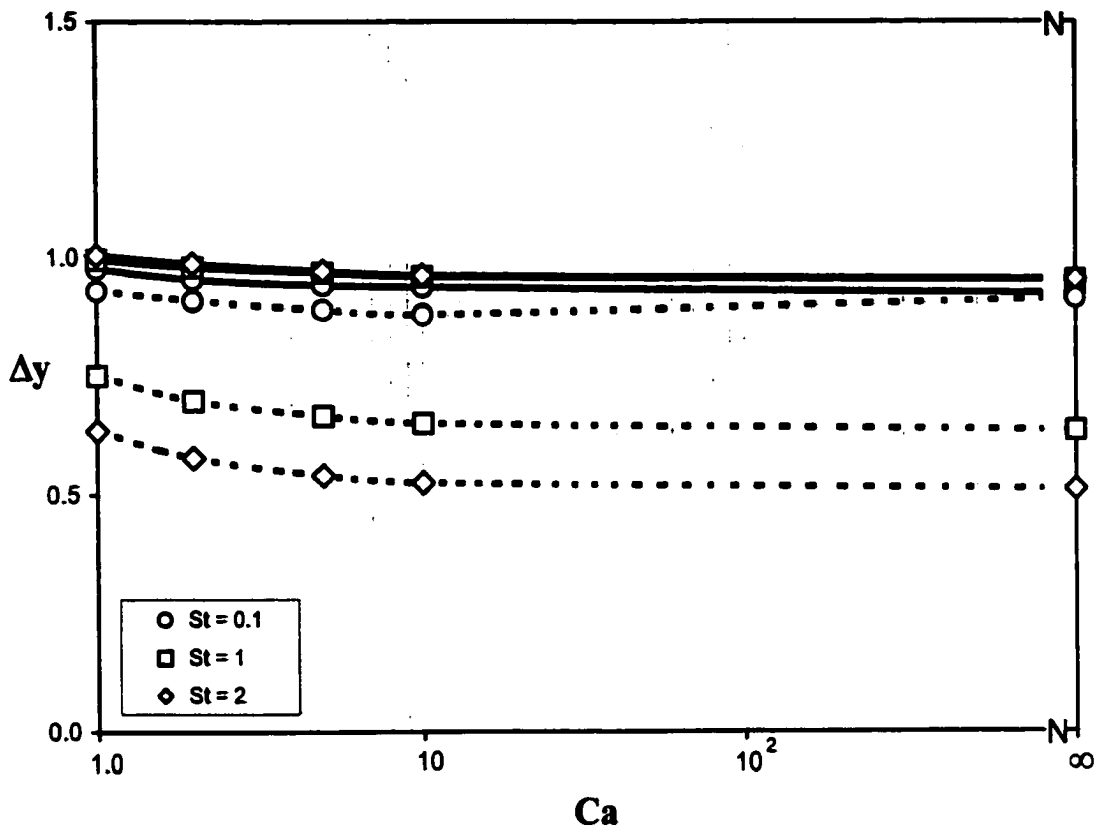
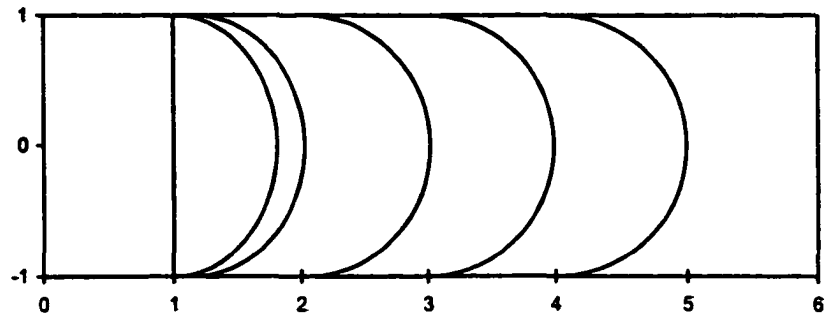
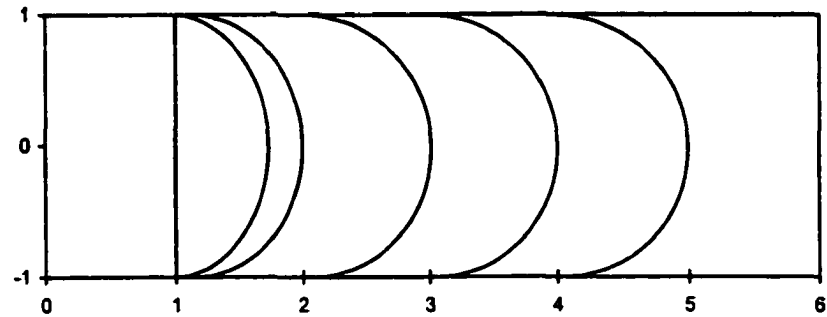


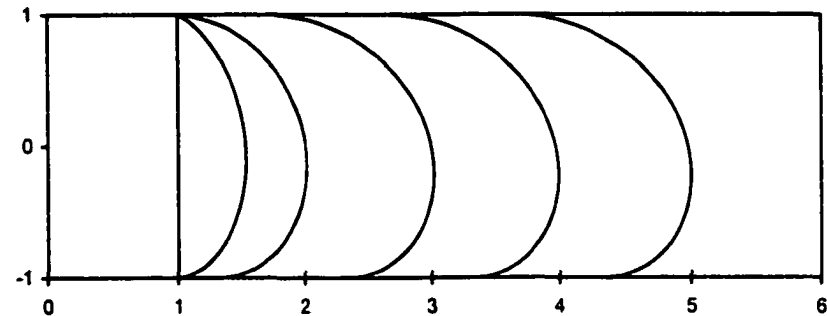
Figure 3.27 Fully developed front tip travel distance relative to the upper contact lines, Δy_1 , and bottom contact line, Δy_2 , as a function of the Stokes and capillary number (60° inclined channels).



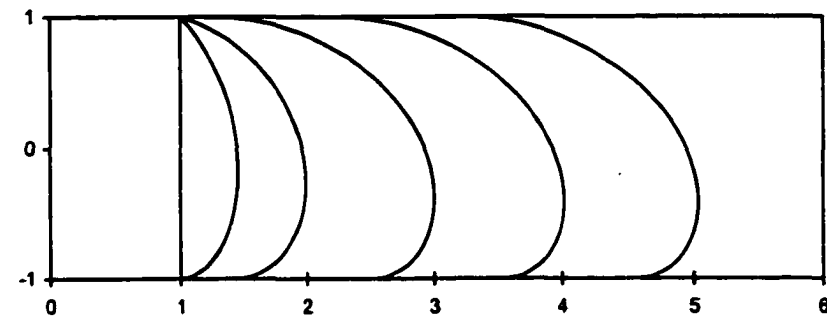
(a)



(b)

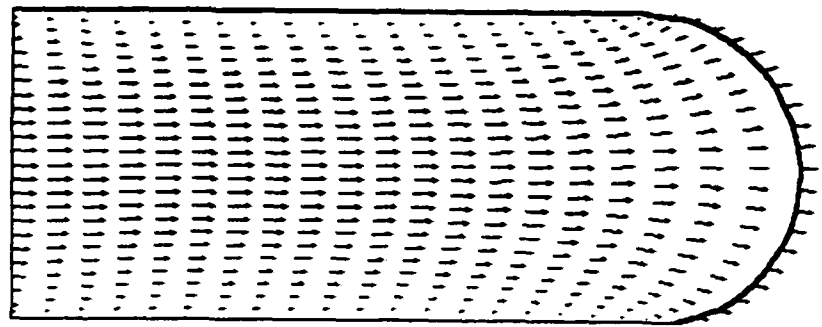


(c)

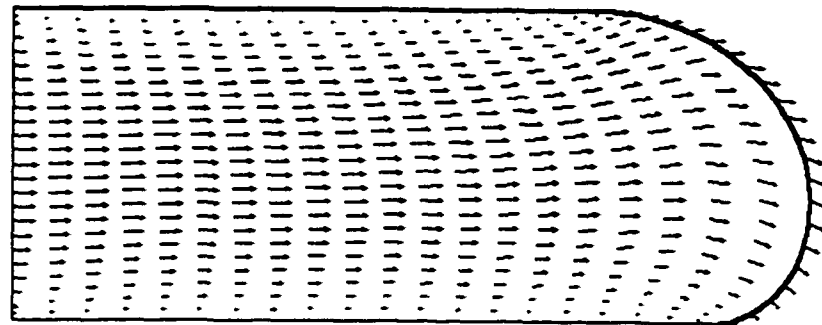


(d)

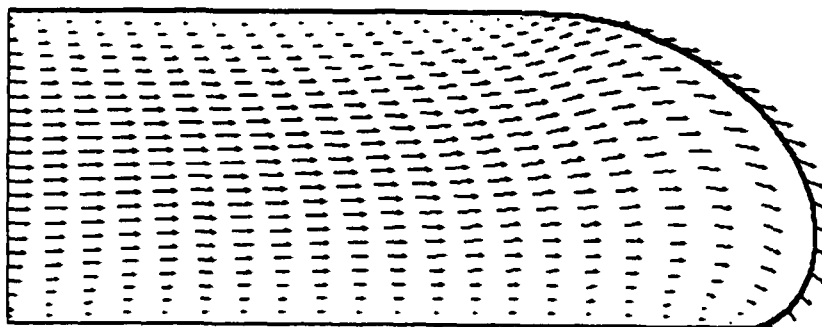
Figure 3.28 Development of flow front for injection through a horizontal channel at various Stokes numbers ($Ca = 1$): (a) $St = 0$, (b) $St = 0.1$, (c) $St = 1$, and (d) $St = 2$.



(a)

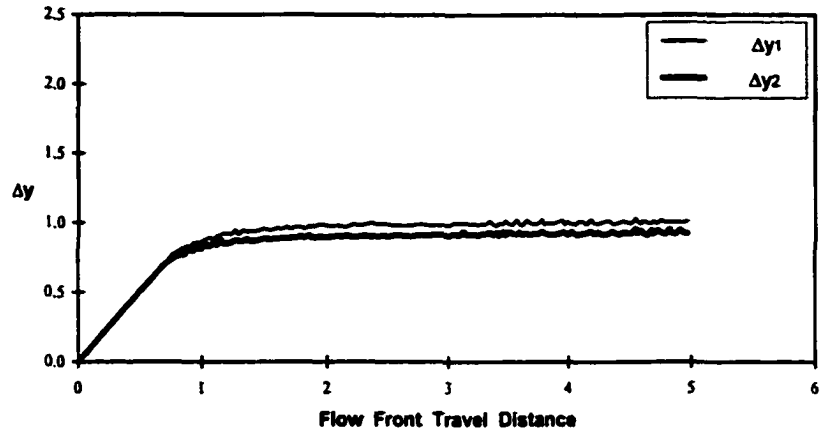


(b)

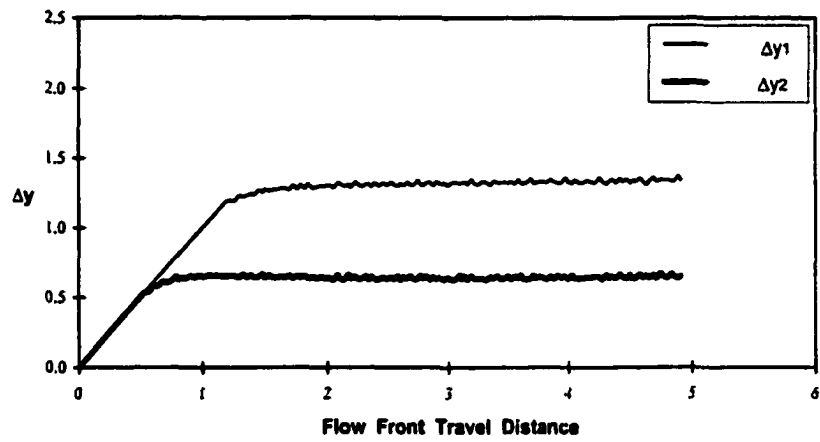


(c)

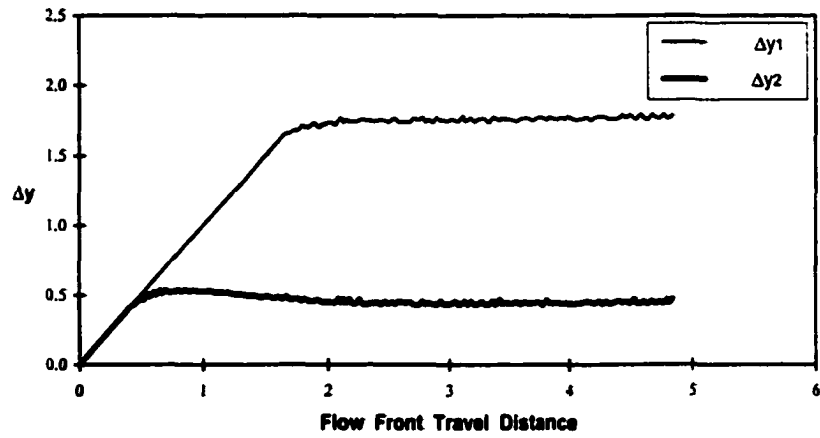
Figure 3.29 Velocity fields for flow injection through a horizontal channel at various Stokes numbers ($Ca = 1$): (a) $St = 0$, (b) $St = 0.1$, (c) $St = 1$, and (d) $St = 2$.



(a)



(b)



(c)

Figure 3.30 Relative flow front travel distance under various gravitational effects (horizontal channels, $Ca = 1$): (a) $St = 0.1$, (b) $St = 1$, and (c) $St = 2$.

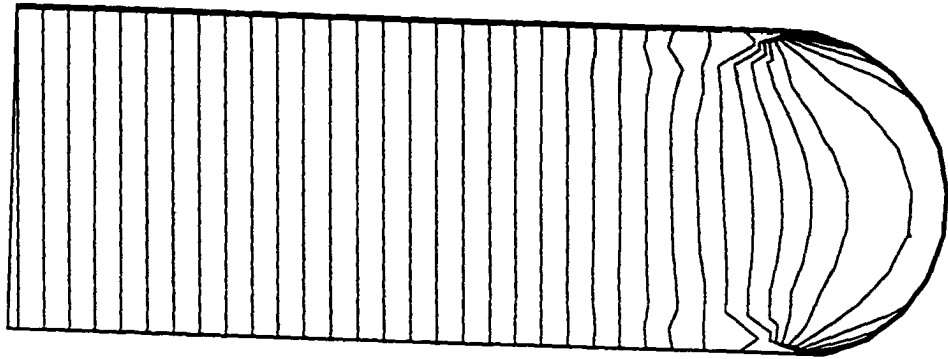


Figure 3.31 Pressure contour of a fully developed flow field in a horizontal channel ($Ca = 10$, $St = 0.1$, and $\Delta P = 0.5$).

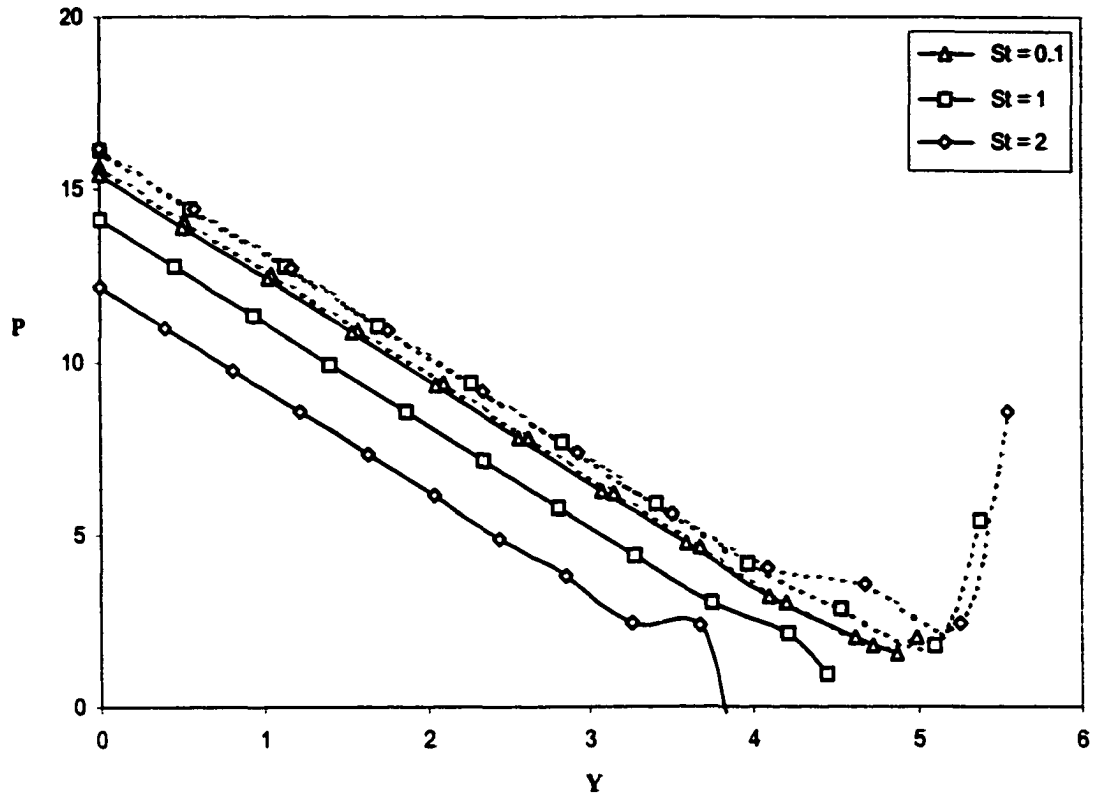


Figure 3.32 Gravitational effects on the pressure distribution in a horizontal channel: upper wall (—) and bottom wall (- - -).

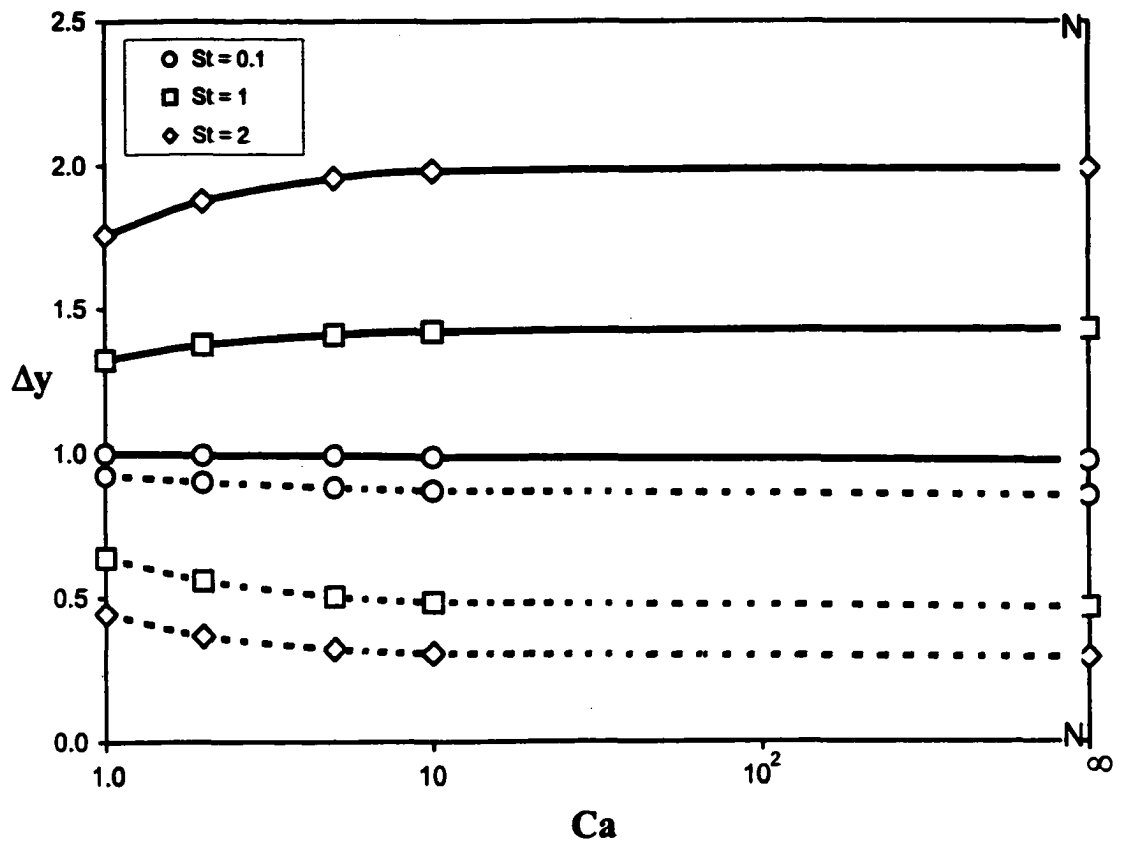


Figure 3.33 Fully developed front tip travel distance relative to the upper contact lines, Δy_1 , and bottom contact line, Δy_2 , as a function of the Stokes and capillary number (horizontal channels).

CHAPTER 4

ISOTHERMAL FLOW INJECTION IN CENTER-GATED DISKS

For flow injection through center-gated disks, the cross-section area of the flow passage increases and the average flow velocity decreases when the flow advances radially. As a result, the flow inside a center-gated disk never reaches the fully developed stage. A comprehensive three-dimensional mathematical model is developed to simulate the filling stage of the injection molding process in the center-gated disk under isothermal condition. Since the flow is axisymmetric, only half of the domain is used in the numerical simulation. The left boundary of Fig. 2.6 represents the axis of a center-gated disk. The flow is assumed to be quasi-steady in this study. A combination of Galerkin finite element method and predictor-corrector scheme are employed to evaluate the surface tension and gravitational effect on the transient flow front shape, velocity distribution, pressure distribution, and advancement of the flow front.

The results of this study have covered a wide range of the governing parameters (i.e., $0 < Bo < 10$, and $Ca = 0.1, 0.2, 1, 2, 10$, and ∞). All parameters, such as capillary number (Ca), Stokes number (St), and Bond number ($Bo = St \cdot Ca$), are defined based on the characteristic velocity U_{∞} , the radius of the injection hole R , and the viscosity of the fluid μ . The definitions of the front tip travel distance relative to the contact lines are given in Fig. 2.6.

4.1 Flow Injection in Center-Gated Disks with Negligible Surface Tension and Gravitational Effects

For flow injection through center-gated disks with negligible surface tension and gravitational effect ($St = 0$ and $Ca \rightarrow \infty$), the initial flow front shape is assumed to be flat and perpendicular to the axis (Fig. 2.8a). In the numerical simulation, the fluid initially takes up the space the depth of one hole radius below the injections hole and the initial velocity distribution is assumed to be fully developed. A mesh that consists of 120 elements and 525 nodes is employed in this study (Fig. 2.8b). The total number of unknowns (U , V , and P) is 1193. The development of the flow front, as the fluid advances in the center-gated disks, is shown in Fig. 4.1. The first solid line in Fig. 4.1 is the initial front position. The first dash line shows the flow front position when the front tip just touches the upper wall and the second one represents the flow front position when the bottom contact line begins to move. Before the front tip reaches the top disk, the flow front advances upward along the centerline, but the bottom contact line does not move at all. As the front tip touches the top wall, it becomes the upper contact line and moves radially outward along the top wall. During this period of time, the bottom contact line remains still on the lower wall. This stationary nature of the bottom contact line is simply a consequence of relative high level viscous effect in the fluid since Reynolds number is much less than one. As times increases, the bottom contact line begins to move (at $\tau = 4.568$). The upper contact line is initially moving faster than the bottom contact line. Finally, the values of front tip travel distances Δr_1 and Δr_2 (relative to upper and bottom contact lines respectively) converge and the flow profile becomes symmetric downstream.

The velocity distribution at various injection times is shown in Fig. 4.2. From the figure, the fountain flow pattern can be clearly observed near the flow front. As soon as the front tip reaches the upper disk, its velocity is assigned zero immediately to satisfy the no-slip boundary condition on the top wall. Actually, the velocity of the front tip is calculated to be 0.93 when it hits the upper wall. It is expected that some oscillations (flow transients) may occur after the front tip hits the upper wall. This situation, although interesting, was not investigated further due to the limitation of the numerical code. The flow then turns and spreads radially outward after it reaches the top wall. It acts like a three-dimensional round jet impinging the upper disk at right angle and spreading radially outward in all directions. The center of the upper disk acts like a stagnation point. The velocity distribution along the axis decreases gradually from 2 to 0. As the flow direction turns radial, more motion takes place at upper half gap in the earlier stage. This explains why the upper contact line is moving fast in the beginning of spreading. Since the flow rate is fixed, the average velocity of the flow front decreases gradually when the flow advances radially outward. As a result, the fountain flow effect is more clearly observed in the early stage. When the flow advances, its effect diminishes gradually, but can still be felt at the flow front.

The relative front tip travel distance during the injection process can be examined from Fig. 4.3. Both Δr_1 and Δr_2 are calculated after the front tip reaches the upper wall. As the flow advances, Δr_1 decreases immediately and Δr_2 increases almost linearly before the bottom contact line begins to move. When the bottom contact line begins to move, the value of Δr_2 decreases immediately. The sharp change in the curve indicates the time when the bottom contact line begins to move. At the meantime, the value of Δr_1

begins to increase. Thereafter, the difference between Δr_1 and Δr_2 continues to decrease as the flow advances. It eventually becomes zero if the injection time is long enough.

From the previous studies, we know that the moving contact angle is 180° when the surface tension and gravitational effects are negligible. The moving contact angle of the present case is shown in Fig. 4.4. It shows that the upper contact angle is about 171.5° when the flow front reaches the upper wall. Afterward, it increases with some oscillations and approaches 180° . The oscillation becomes weak when the flow moves further downstream. On the other hand, the bottom contact line does not move until the contact angle is increased approximately up to 180° . The asymptotic values of both upper and bottom contact angles are 180° . It also shows that the oscillation of the upper contact angle is weaker than the bottom one in the final stage

The pressure field in the center-gated flow injection is shown in Fig. 4.5. The pressure contour is plotted with an increment of 0.5 dimensionless pressure ($\mu U_\infty / H$). From the figure, it is observed that pressure decreases almost linearly in the upstream region flow entry and in the downstream region except close to turning corners and flow front. Since the flow direction changes, the pressure drop is large near the bottom wall. It is also observed that there are pressure jumps along the axis and the bottom wall (i.e., close to the turning points).

4.2 Gravitational Effects on Flow Injection through Center-Gated Disks

For flow injection through center-gated disks, the gravitational force is acting perpendicular to the flow direction in the downstream while it is acting against to the flow direction close to the injection hole. Figure 4.6 shows the gravitational effects on

the development of flow front at a given capillary number ($Ca = 1$). Since each time step is controlled by the pre-set error criterion (Eq. 2.32), its value is different for each case. The flow front profiles presented in Fig. 4.6 are not at the same time frame and they are intended for reference only. The flow front profiles shown in Fig. 4.6 are plotted approximately every dimensionless time except the first curve which is about 0.5 dimensionless time. The first dash curve shows the flow front position at the time when the front tip reaches the top disk. The second one represents the flow front position at the time when the bottom contact line begins to move. Clearly, the gravitational force has significantly modified the shape of flow front. As the gravitational force increases, the front tip is compressed and becomes flattened before it hits the top wall. During the radial spreading, the front tip position is shifting downward as the flow advances. The time required for the flow front to reach the upper wall increases from $\tau = 0.729$ to $\tau = 1.1292$ when the Bond number ($Bo = Ca \cdot St$) increases from 0.1 to 10. However, the time required for the bottom contact line to begin its move decreases from $\tau = 2.51$ to $\tau = 1.28$ for the range of Bond number. If the gravitational force keeps increasing, the bottom contact line will begin to move before the flow front reaches the upper wall. In addition, the flow will sag forward the bottom wall downstream.

The velocity fields under various gravitational effects are shown in Fig. 4.7. For a given capillary number (i.e., a fixed surface tension effect), if the gravitational force increases (correspondingly, the Bond number increases), the fountain flow region near the upper disk is compressed while it is expanded at the lower disk. More rolling motion of fluid is observed near the lower disk, same as the one observed in the horizontal channel case. If the gravitational force increases further, more external pressure pumping

power is required to overcome the gravitational force. Otherwise, the flow front won't be able to reach the upper wall and the fluid will not fill the disk gap completely.

For a fixed capillary number ($Ca = 1$), the relative front tip travel distance under various gravitational effects (in terms of the Bond number) are shown in Fig. 4.8. Due to the sagging of the fluid, gravitational effects increase the time required for the flow front to reach the upper wall but shorten the time required for the bottom contact line to begin its move. Results shows that the front tip travel distances, Δr_2 and Δr_1 display the same trend as that of the special case with negligible surface tension and gravitational effects ($Bo = 0$). The difference between Δr_2 and Δr_1 decreases as the gravitational force increases. The case with negligible surface tension and gravitational effects is also included in Fig. 4.8 for comparison. For a weak gravitational force, the value of $(\Delta r_2 - \Delta r_1)$ approaches an asymptotic value in this study. For higher gravitational effect ($Bo \geq 5$), the value of $(\Delta r_2 - \Delta r_1)$ decreases as the flow advances.

The effect of gravitational force on the moving contact angle is shown in Fig. 4.9. When the front tip reaches the upper wall, the upper moving contact angle increases from 172.39° to 179.3° if the gravitational effects increase from $Bo = 0.1$ to $Bo = 10$. On the other hand, the bottom moving contact angle reduces from 179.8° to 177.2° when the bottom contact line begins to move. Figure 4.9 also shows that the oscillation of the upper contact angle reduces as the gravitational effects increase while it becomes more serious for the bottom contact angle. Since the velocity of the flow front reduces as the flow advances, the local capillary number decreases and bottom contact angle reduces. This result is consistent with the conclusion of the Shikhmurzaev (1994).

The pressure contours of the flow field in center-gated disks under various gravitational effects are shown in Fig. 4.10. The increment of the pressure contours is one dimensionless pressure in each case. For flow injection under a strong gravitational force, it requires a higher injection pressure at the entry. The entry pressure varies from 23.53 to 35.32 dimensionless pressure if the Bond number increases from 0.1 to 10. The pressure gradient along the center axis is almost linear except the region close to the top wall. Results obtained also indicate that there are pressure jumps near two turning points. For a weak gravitational condition ($Bo = 0.1$), the flow front is positioned almost right at the center of the two disks. The pressure contours in the downstream region (away from the front tip) is similar to that in the horizontal channel. As the gravitational force increases, the contour in the downstream region inclined further to the bottom wall. The lowest pressure is located at the upper contact line.

4.3 Surface Tension Effects on Flow Injection through Center-Gated Disks

The surface tension effect on the development of flow front is shown in Figure 4.11. As before, the first dash curve shows the flow front position when the front tip reaches the upper wall. The second one represents the flow front position at the time when the bottom contact line begins to move. For a given Bond number ($Bo = 1$), the time required for the bottom contact line to begin its move reduces from $\tau = 3.342$ to $\tau = 1.781$ dimensionless time when the capillary number reduces from 10 to 0.1. However, the time required for the flow front to reach the upper wall reduces from $\tau = 0.778$ to $\tau = 0.727$ over the same range of the capillary number. Although surface

tension may have some influence over the flow front shape in the early filling stage, its effect on the final shape is insignificant.

The effect of surface tension on flow injection through center-gated disks can be cross-examined from Fig. 4.12. Results shows that the advancement of the front tip travel distance relative to upper and bottom contact line, Δr_1 and Δr_2 , has the same trend as that of the special case ($St = 0$ and $Ca \rightarrow \infty$). For a given Bond number ($Bo = 1$), the difference between Δr_2 and Δr_1 increases as the capillary number increases in the early filling stage. However, they all approach the same asymptotic value in the final stage. Figure 4.12 also shows that a fluid with a smaller capillary number can reach the upper wall faster and the time required for the bottom contact line to begin its move is shorter.

The effect of surface tension on the moving contact angle is shown in Fig. 4.13. For a given Bond number ($Bo = 1$), a larger capillary number results in a larger oscillation on the upper moving contact angle, but its effect on the asymptotic value of both moving contact angles (upper and bottom moving contact angles) is insignificant.

4.4 Conclusions

The effects of gravitational force and surface tension on flow injection through a center-gated disk are analyzed numerically using a Galerkin finite element method. In order to predict the flow front shape, a comprehensive three-dimensional mathematical model is developed for flow injection in the center-gated disks. The transient flow shape and flow fields in the center-gated gap are obtained first for flows with negligible surface tension and gravitational effects. Then, the advancement of flow front, pressure

distribution, moving contact angle, and flow fields are compared with those subject to various surface tension and gravitational effects.

With negligible gravitation and surface tension, flow front will reach the upper wall and then spread radially while bottom contact line still sticks on the wall. It is due to the high level of viscous effect ($Re \ll 1$). During this process, injection flow acts as a three dimensional stagnation flow impinges on the upper wall at right angle to it and flow away radially in all directions. The center of the upper wall acts as a stagnation point. When the flow front reaches the upper wall, it becomes the upper contact line. Results obtained shows that the upper contact line moves faster than bottom contact line in the earlier stage and most flow fluid is distributed on the upper half gap. When the bottom contact line begins to move, the values of the front tip travel distance relative to upper and bottom contact line, Δr_1 and Δr_2 , approach to each other. Finally, the flow front shape is symmetrical between gap and both upper moving contact angle and bottom moving contact angle are 180° .

If the gravitational effects are considered, the gravitational force can significantly modify the flow front shape. As the gravitational force increases, the front tip is compressed and becomes flattened before it reaches the top wall. The front tip position is also moving downward as flow advances. For each case, the flow turns and spreads radially after it reaches the upper disk. It acts as a three-dimensional stagnation flow impinges on the upper disk which we observed in without gravitational and surface tension case. It also shows that the upper contact line is moving faster than the bottom contact line in the earlier stage. The difference between the upper and bottom contact line travel distance (absolute value) increases. The time required for the flow front to

reach the upper wall increases if the Bond number (Bo) increases. However, the time required for the bottom contact line to begin its move is shortened. If the gravitational effects keep increasing, the bottom contact line begins to move before the flow front reaches the upper wall. Finally, the flow is sagging in the bottom half. The gravitational force has also greatly modified the velocity field. If gravitational effect increases, the flow is sagging in the bottom half. The fountain flow region at the upper gap is compressed while it is expanded at the bottom half as the flow advances. Since the average front velocity reduces as the flow advances, the fountain flow effect is most noticeable in the early stage of spreading. When the flow advances, its effect diminishes gradually, but can still be felt at the flow front. More motion is at upper half gap in the earlier stage. It explains the reason why the upper contact line is moving fast in the beginning.

For a given Bo number, the result shows that a fluid with a smaller capillary number reaches the upper wall faster and the time required for the bottom contact line to begin to move shortens. It also leads the flow approaching symmetrical between the gap. The difference between the movement of the upper and bottom contact lines approaches the same value.

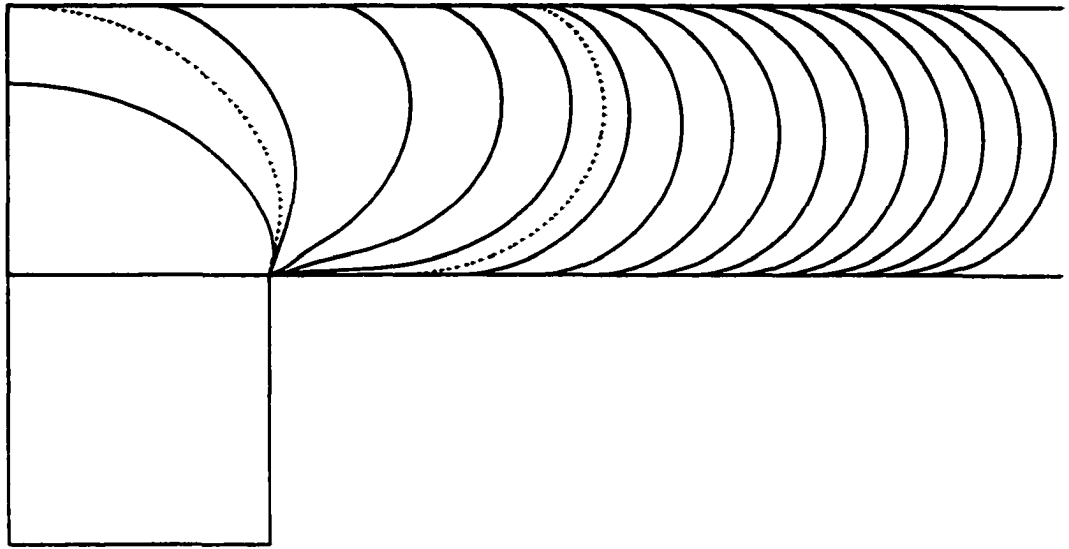


Figure 4.1 Development of flow front for flow injection through center-gated disks with negligible surface tension and gravitational effects.

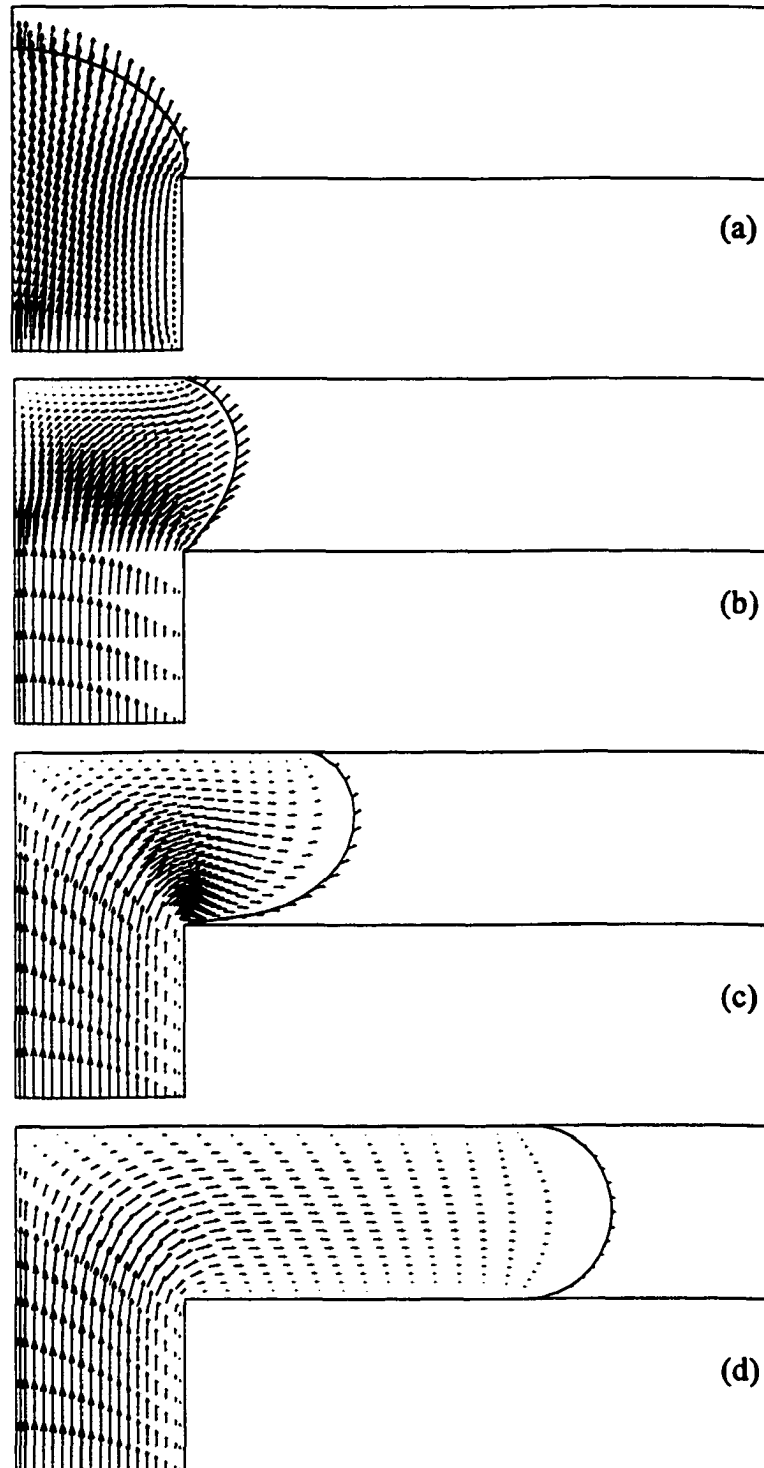


Figure 4.2 Velocity fields for flow injection through center-gated disks with negligible surface and gravitational effects: (a) $\tau = 0.557$, (b) $\tau = 1.512$, (c) $\tau = 3.512$, and (d) $\tau = 12.009$.

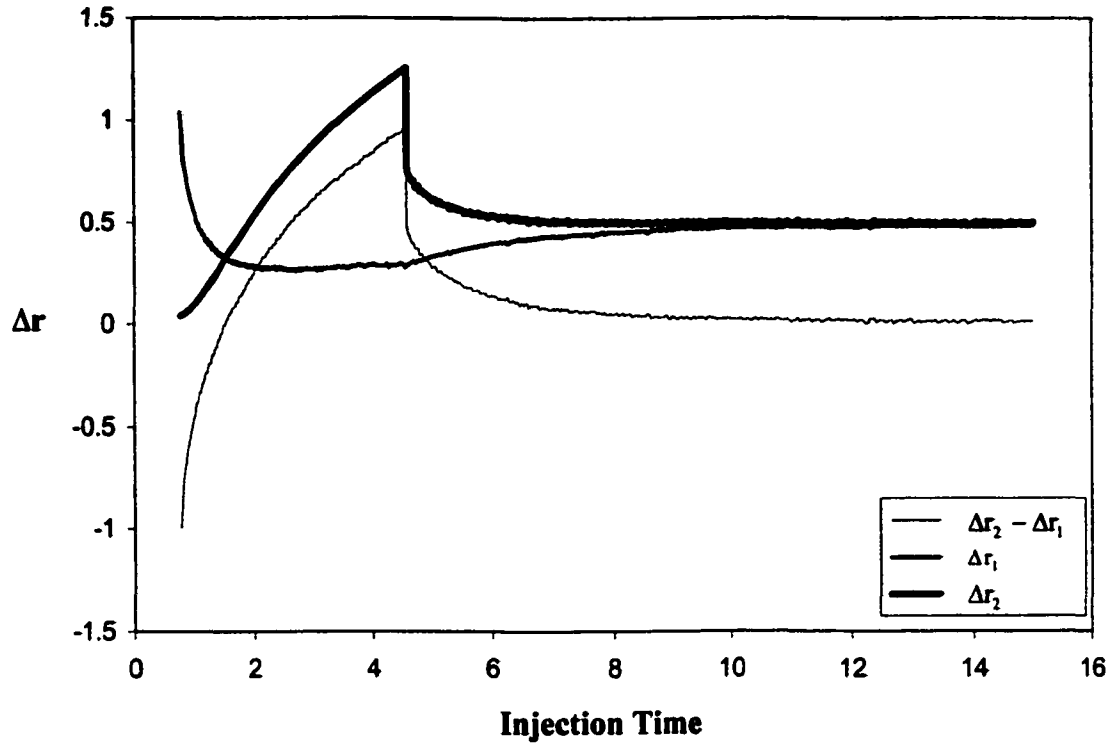
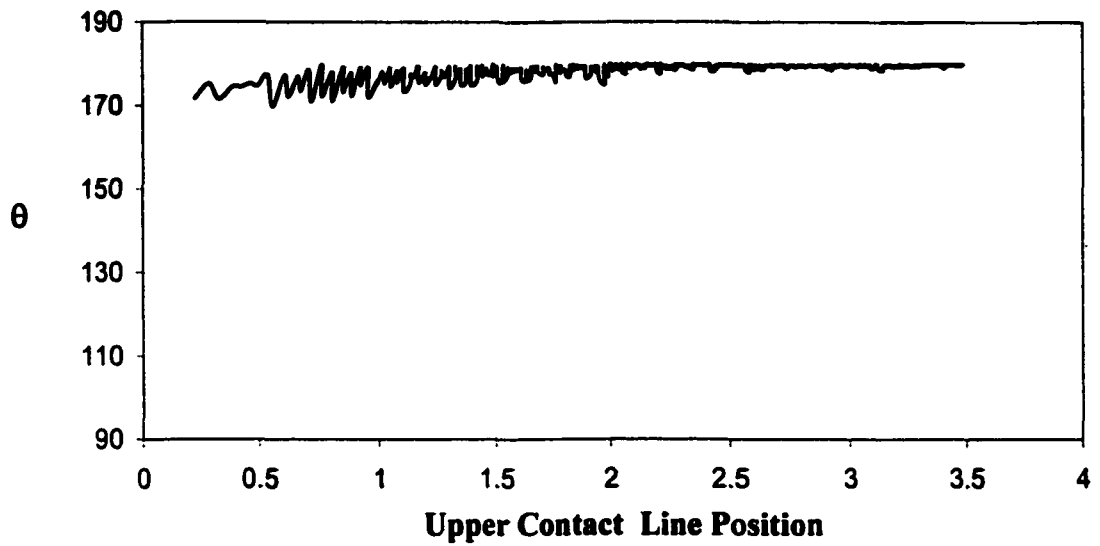
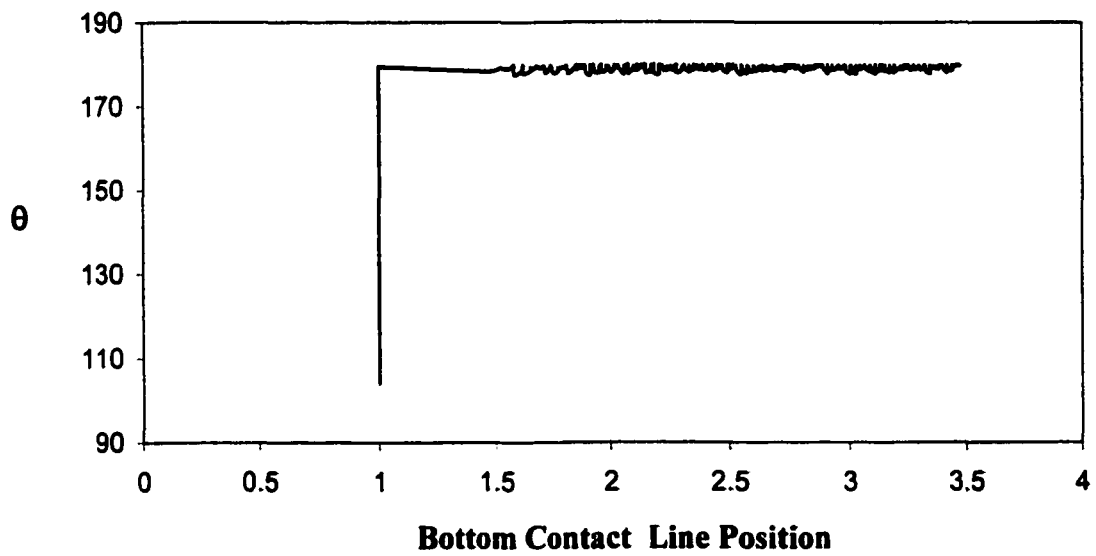


Figure 4.3 Relative front tip travel distance for flow injection through center-gated with negligible surface tension and gravitational effects.



(a)



(b)

Figure 4.4 Development of contact angles in a center-gated flow injection without surface tension and gravitational effects (a) upper contact angle, (b) bottom contact angle.

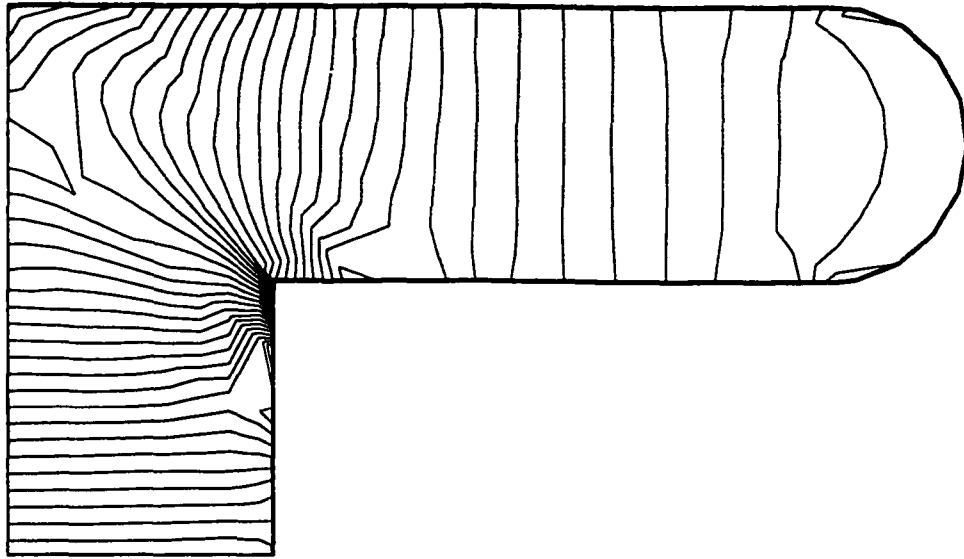
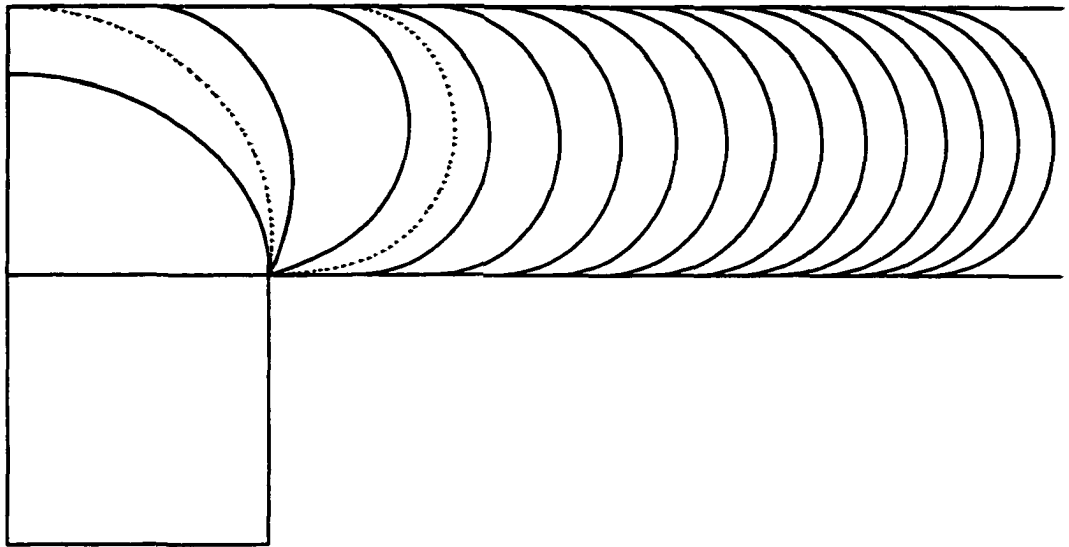
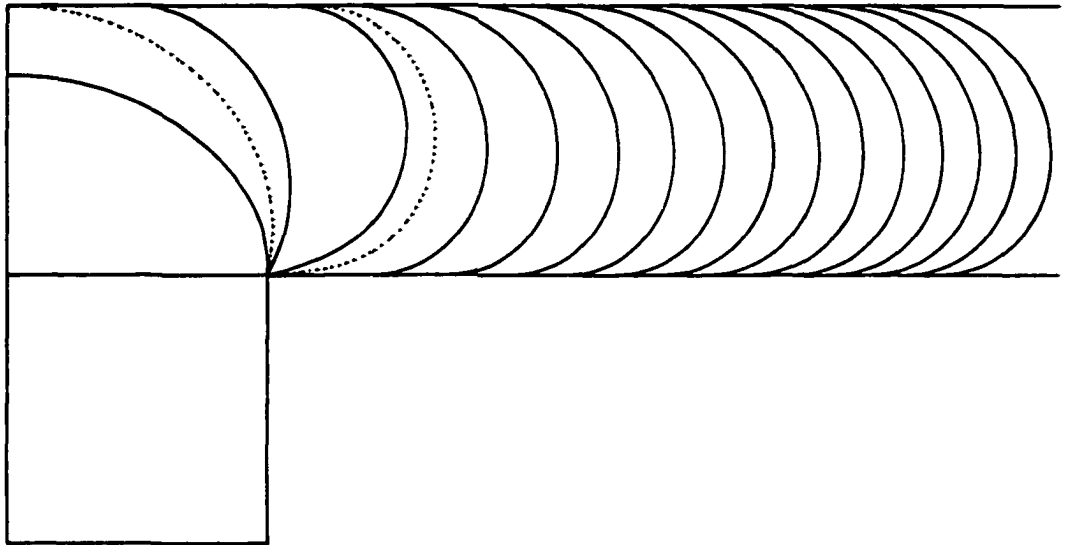


Figure 4.5 Pressure contour for flow injection through center-gated disks with negligible surface tension and gravitational effects ($\Delta P = 0.5$).

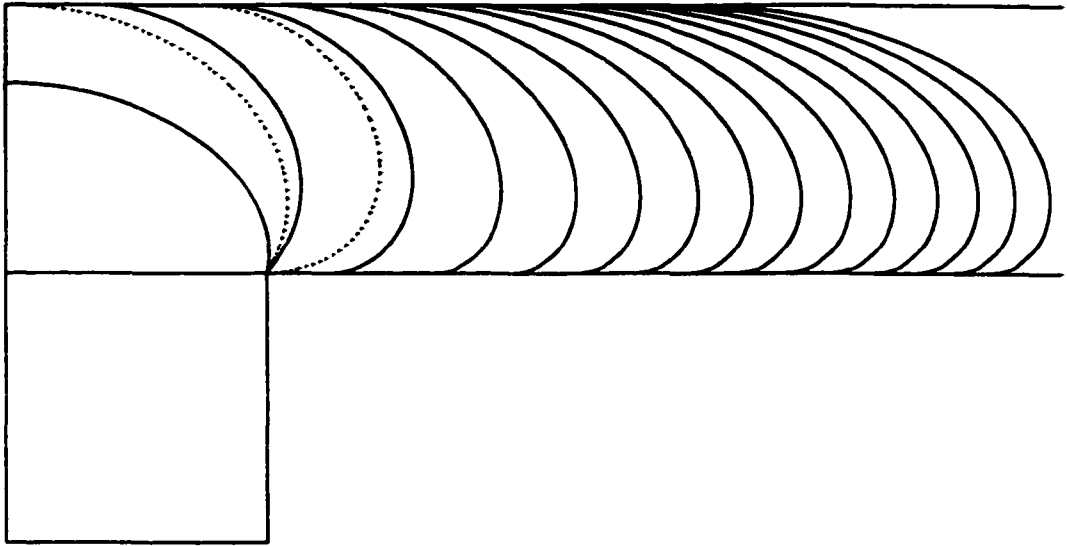


(a)

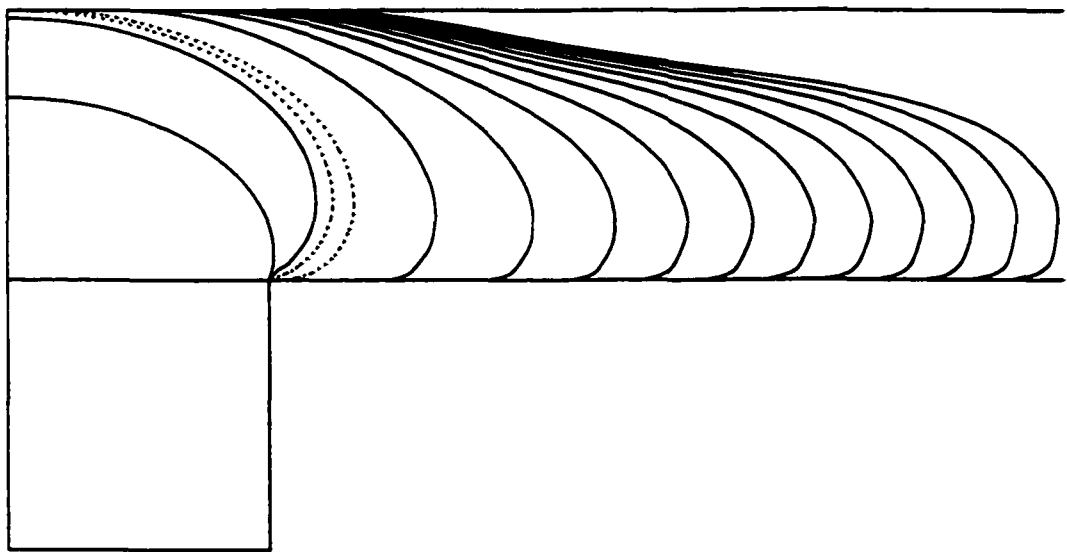


(b)

Figure 4.6 Development of flow front for flow injection through center-gated disks under various gravitational effects ($Ca = 1$): (a) $Bo = 0.1$, (b) $Bo = 1$, (c) $Bo = 5$, and (d) $Bo = 10$.



(c)



(d)

Figure 4.6 Continued

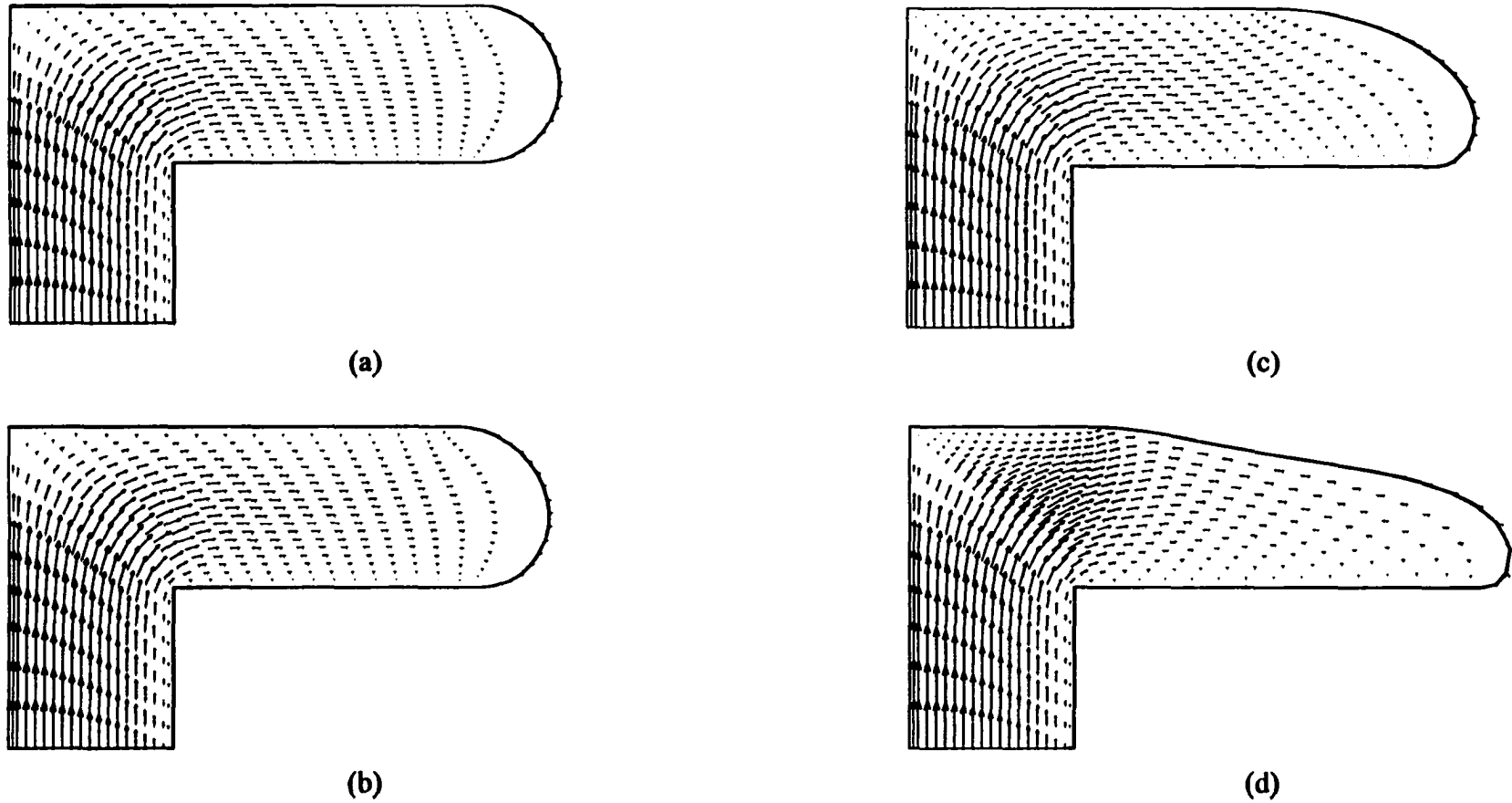


Figure 4.7 Velocity fields for flow injection through center-gated disks under various gravitational effects ($Ca = 1$): (a) $Bo = 0.1$, (b) $Bo = 1$, (c) $Bo = 5$, and (d) $Bo = 10$.

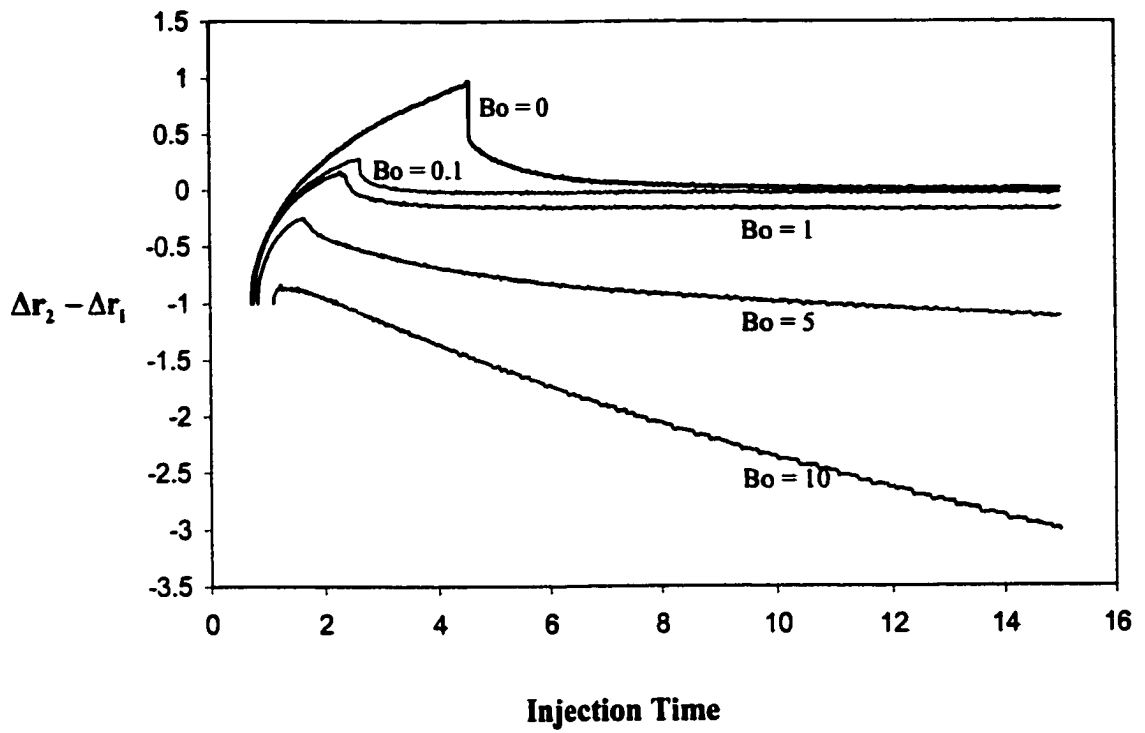


Figure 4.8 Relative front tip travel distance for flow injection through center-gated disks under various gravitational effects ($Ca = 1$).

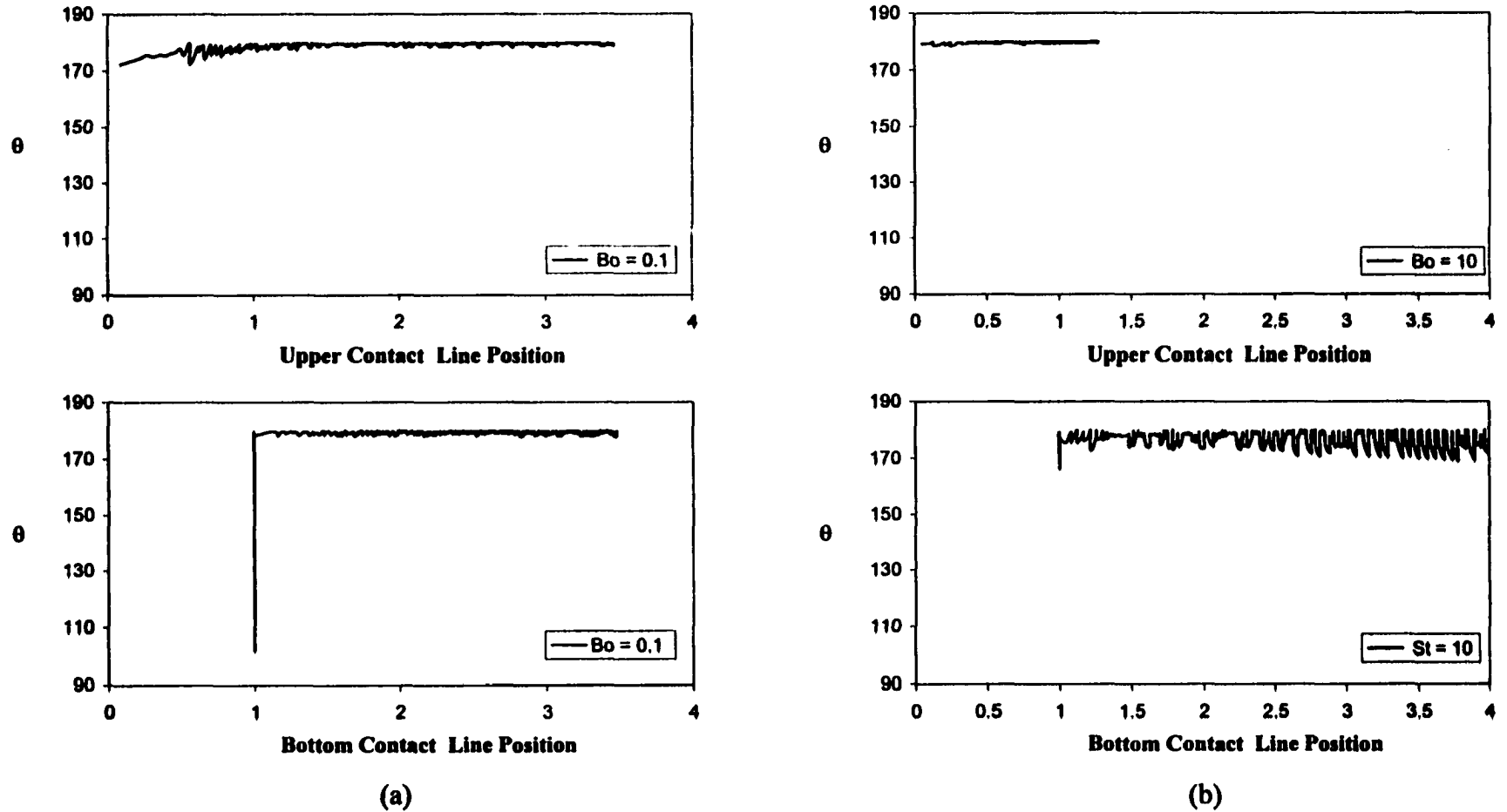


Figure 4.9 Development of moving contact angles for flow injection through center-gated disks under various gravitational effects ($Ca = 1$): (a) $Bo = 0.1$ and (b) $Bo = 10$.

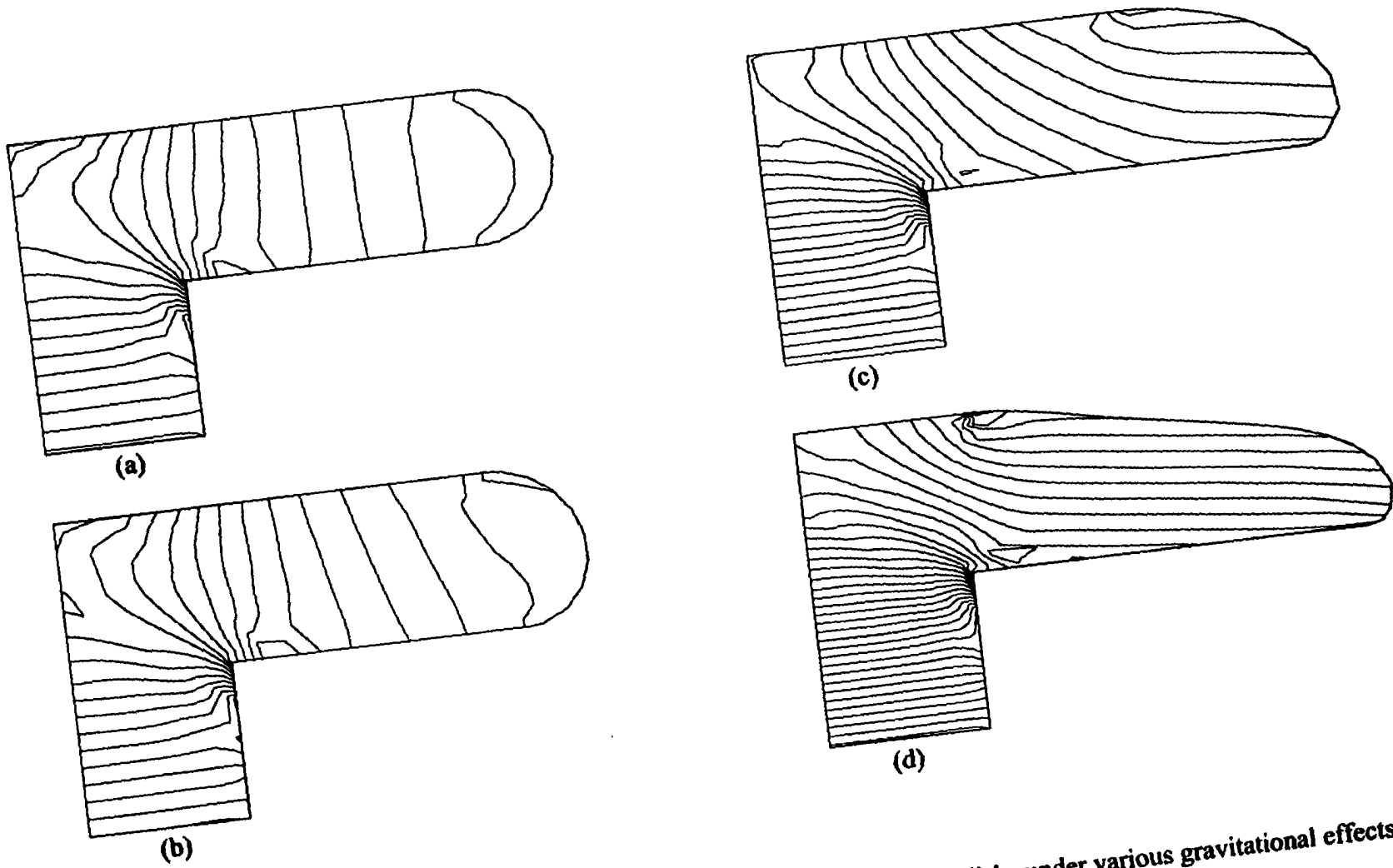
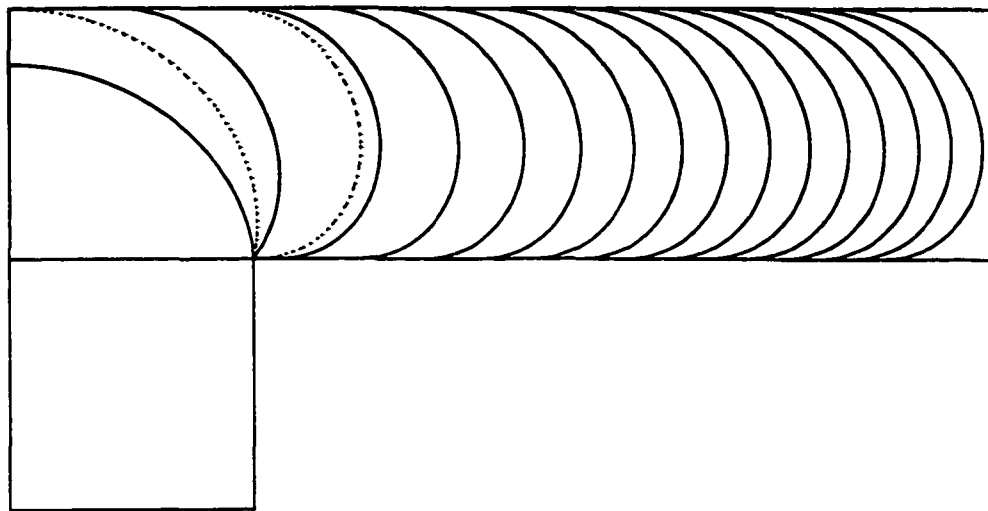
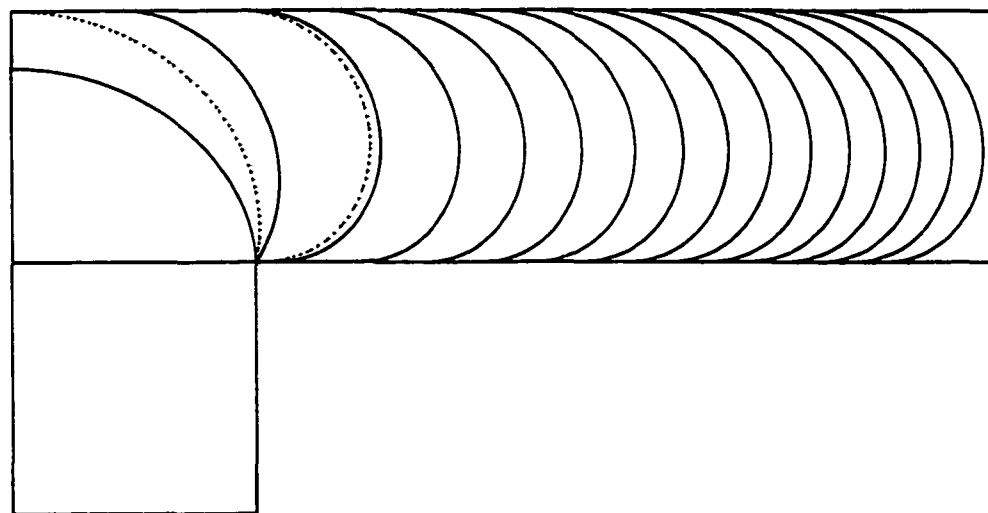


Figure 4.10 Pressure contours ($\Delta P = 1$) for flow injection through center-gated disks under various gravitational effects ($Ca = 1$): (a) $Bo = 0.1$, (b) $Bo = 1$, (c) $Bo = 5$, and (d) $Bo = 10$.

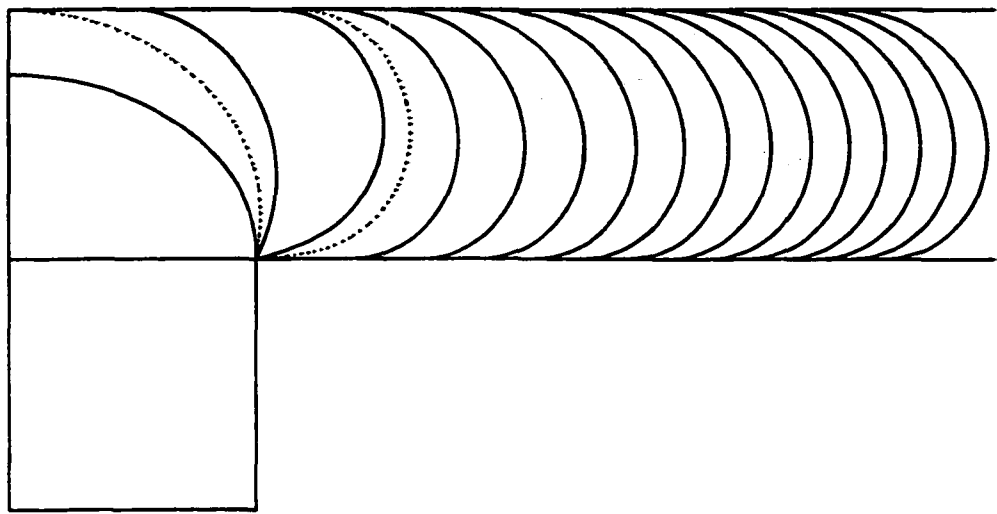


(a)

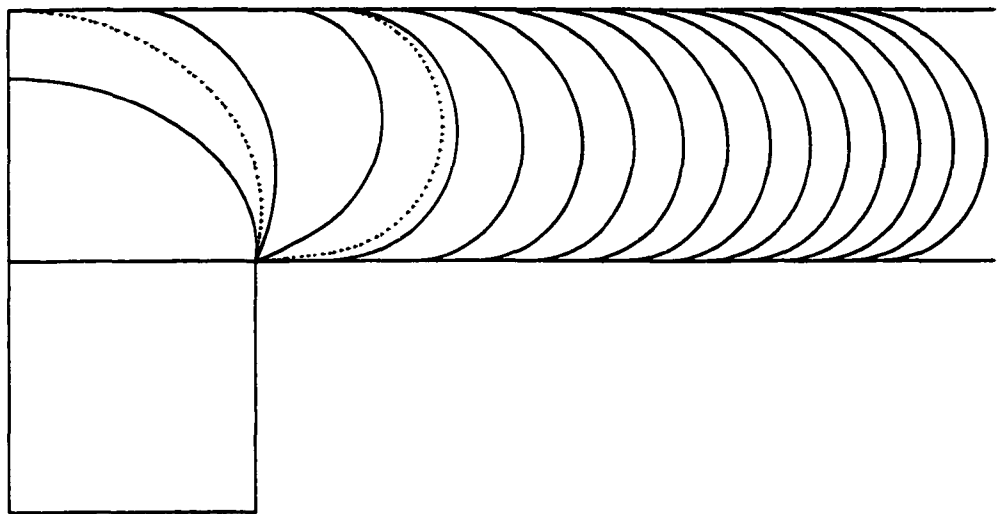


(b)

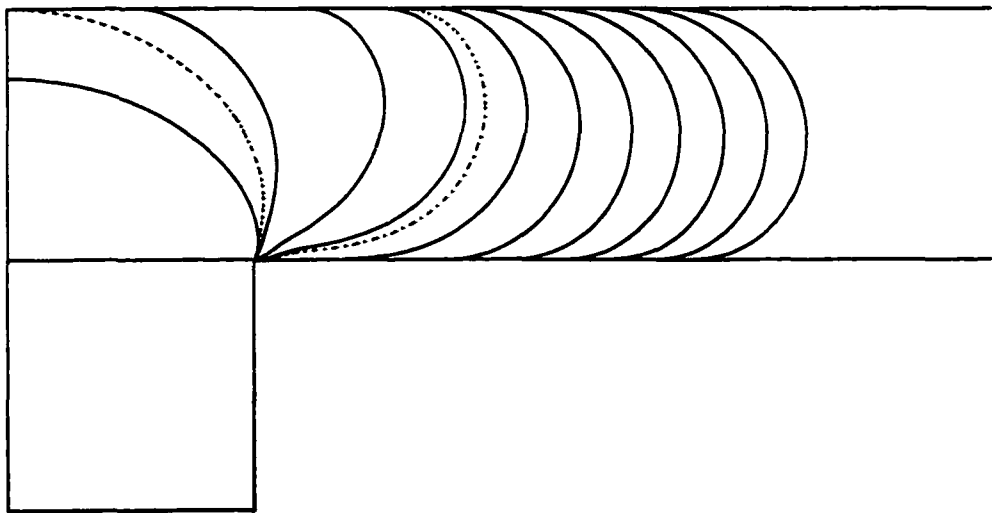
Figure 4.11 Development of flow front for flow injection through center-gated disks under various surface tension effects ($Bo = 1$): (a) $Ca = 0.1$, (b) $Ca = 0.2$, (c) $Ca = 1$, (d) $Ca = 2$, and (e) $Ca = 10$.



(c)



(d)



(e)

Figure 4.11 Continued

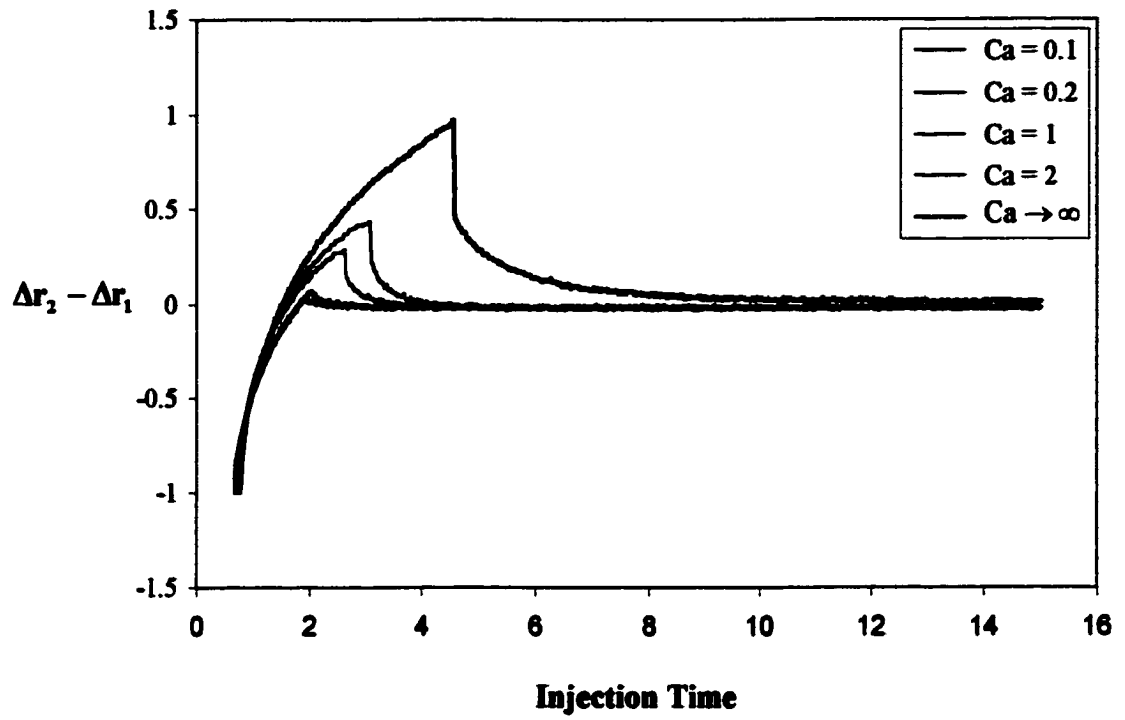


Figure 4.12 Relative front tip travel distance for flow injection through center-gated disks under various surface tension effects ($Bo = 1$).

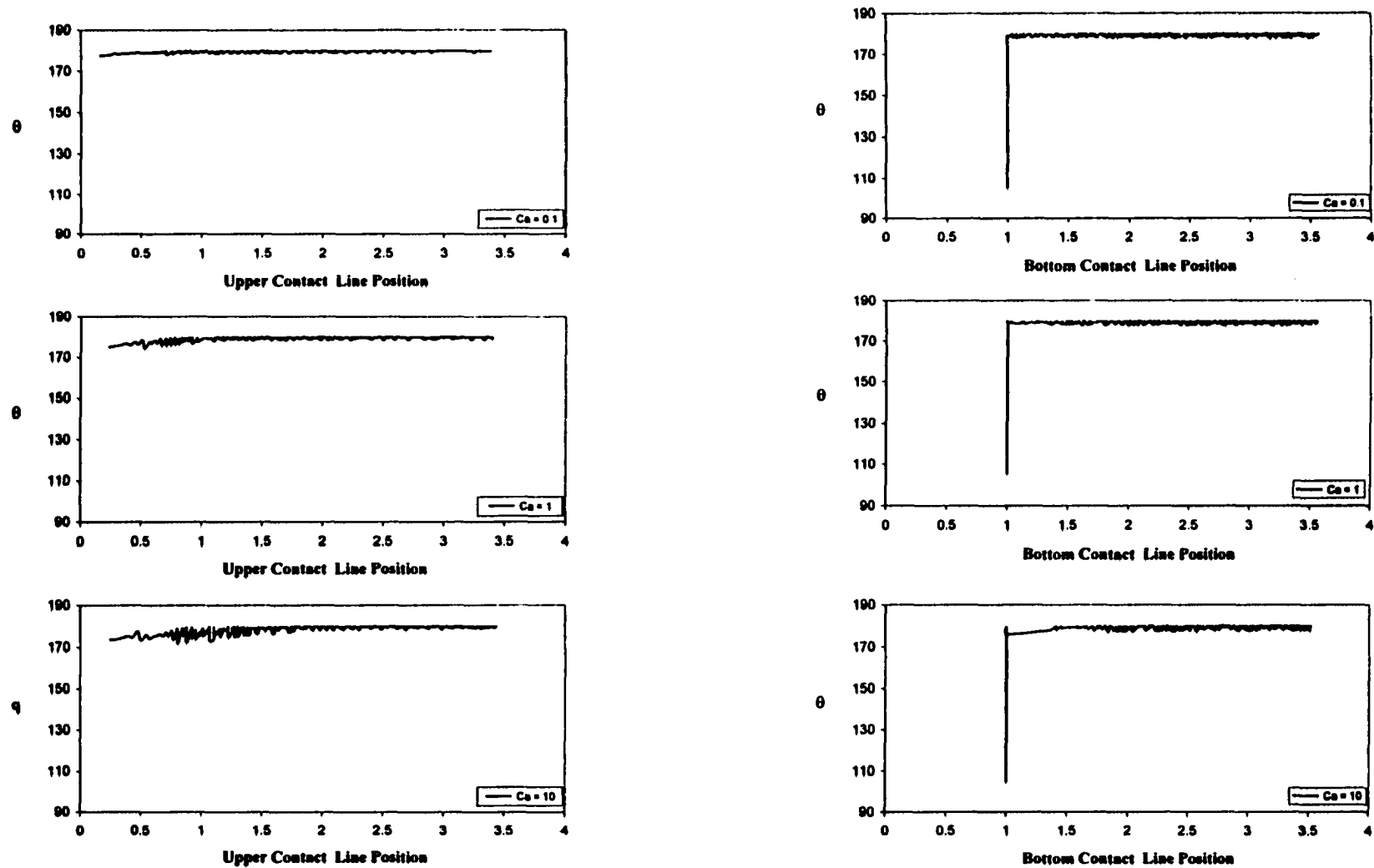


Figure 4.13 Development of moving contact angles for flow injection through center-gated disks under various surface tension effects ($Bo = 1$).

CHAPTER 5

NON-ISOTHERMAL FLOW INJECTION THROUGH VERTICAL CHANNELS

In the injection molding process, the polymer melt at an elevated temperature is injected into a stationary mold. Thus, the flow is non-isothermal and has a transient free surface. In this chapter, the thermal effects on flow injection between two parallel vertical are analyzed using Taylor-Galerkin finite element method. The effects of heat transfer on the advancement of the flow front, transient front shape, velocity, and pressure distributions are carefully investigated. To correlate the results, the temperature and viscosity distributions at various Peclet numbers ($Pe = Re \cdot Pr$) are closely examined. To assess the thermal effects on flow injection through vertical channels, the results obtained here for various Peclet numbers are compared with those reported in Chapter 3 for the isothermal case.

The present study have covered a wide range of the governing parameters (i.e., $1 \leq Pe \leq 50$, $0 \leq St \leq 10$, and $Ca = 1$ and ∞).

5.1 Thermal Effects

In the present study, it is assumed that fluid at a higher temperature is injected to a vertical channel, in which the channel walls are maintained at lower temperature. For computational purpose, glycerol is taken to be the fluid in consideration. The correlation of its viscosity with temperature has been presented in Chapter 2. The inlet fluid temperature and wall temperature are fixed at 100°C and 20°C, respectively.

For flow injection through vertical channels, non-uniform temperature in fluid

affects the velocity and pressure distributions in the flow fields through the change of fluid's viscosity. Its effects on the development of the flow front are shown in Fig. 5.1 when the surface tension and gravitational effects are negligible ($Ca \rightarrow \infty$ and $St = 0$). As explained earlier, the time step used for the present study is controlled by the pre-set error criterion (Eq. (2.32)), thus its value is different in each case (i.e., variable time step). As a result, it is only possible to present the flow profiles at the approximately same times. From Fig. 5.1, it is clear to see the added heat transfer effects have extended the front tip travel distance as the Peclet number increases. The initial front tip travel distance (when the contact line initiates its first move) increases from 0.806 to 0.912 as the Peclet number increases from 1 to 50. Also, the relative front tip travel distance (Δy) increases with the Peclet number at any given injection time. Actually, the result shows that Δy does not reach an asymptotic value during the filling process considered in the present study (i.e., 6 dimensionless time) as one has observed in the isothermal case. Since the Peclet number represents the relative magnitude of heat transfer by convection to that by conduction, a flow with a higher Peclet number will carry more heat in the flow direction, which leads to a sharper temperature gradient at the wall. As a result, the fluid viscosity near the wall is higher than that at the centerline. For a higher Peclet number, the added thermal effect increases the axial velocity along centerline and thus increases Δy .

The corresponding velocity fields under various Peclet numbers are shown in Fig. 5.2. From the figure, it is clear to see that the velocity vectors in the flow front region always direct themselves from the centerline towards the wall. This indicates that fluid in the central region rolls out towards the wall due to the fountain flow effect. The

fountain flow pattern can be clearly observed near the flow front region. As the Peclet number increases, the fountain flow region is expanded further downstream and its effect becomes more obvious.

The added thermal effects on the velocity distribution along the centerline are shown in Fig. 5.3a. From the figure, it is obvious that the thermal effects have dramatically modified the velocity distribution. For isothermal flow injection, the upstream velocity distribution along the centerline remains at 1.5, the fully developed value. It decreases gradually toward the flow front due to the fountain flow effect. However, for the non-isothermal case, the axial velocity along the centerline increases significantly upstream but decreases sharply near the flow front. As will be revealed later, this is due to a smaller viscosity that the fluid experiences along the centerline as compared with that near the flow front.

The thermal effects on the axial velocity distribution across the channel width are shown in Fig. 5.3b for various locations. It shows that the axial velocity has a maximum value at the centerline region and a minimum at the wall. Further downstream, the axial velocity decreases in the centerline region but increases near the wall, especially at the flow front. Since the thermal effects increase the axial velocity along the centerline, it extends the relative front tip travel distance Δy (Fig. 5.4).

The advancement of flow front for various Peclet numbers can be cross-examined from Fig. 5.4. The result of the isothermal case is also included for comparison. Since the flow with a larger Peclet number carries more heat in the flow direction, it reduces the fluid viscosity and increases the axial velocity along the centerline. As the result, the front tip travel distance increases with the Peclet number during the filling process. From

the figure, it is clear that the flow with a larger Peclet number will require a longer waiting time to initiate its first move. The relative front tip travel distance keeps increasing with time for the non-isothermal flows whereas it reaches an asymptotic value for the isothermal flow after certain time (Chapter 3). The relative front tip travel distance for various Peclet numbers at selected times are also listed in Table 5.1 for reference. The fluctuation of Δy is observed for all cases and becomes large when the Peclet number increases. This is believed to be caused by the contact line moving scheme and can be reduced by refining the elements. A similar situation is also observed for flows under other surface tension and gravitational conditions ($0 \leq St \leq 10$ and $Ca = 1$ and ∞).

To better understand the variation of flow field with time, the temperature and viscosity distributions at various times are shown in Figs. 5.5 and 5.6. All the data presented in Figs. 5.5 and 5.6 have been normalized by the reference temperature and reference viscosity. As time increases, the fluid temperature decreases and viscosity increases for any given point in the centerline region. From Fig. 5.5, fountain flow effects can be clearly observed since the fluid with a higher temperature (along the centerline) rolls out towards the wall. As a result, the fluid viscosity is the smallest along the axial direction at the fountain flow region and it increases rapidly as the fluid moves closer to the wall (Fig. 5.6).

The temperature and viscosity distributions for various Peclet numbers are shown in Figs. 5.7 and 5.8. The case with constant viscosity is also included for comparison (Fig. 5.7). Again, the data presented in Figs. 5.7 and 5.8 are normalized by the reference temperature and reference viscosity. A higher temperature gradient and thus a higher

viscosity gradient are found near the wall in the entrance region due to thermal boundary condition imposed. For a larger Peclet number ($Pe = 50$), the temperature along the centerline and near the front tip remains close to the inlet temperature. Accordingly, the fluid viscosity is also close to that of the inlet fluid. With the decrease of temperature, viscosity increases rapidly near the wall. When the Peclet number is small (e.g., $Pe = 1$), the temperature gradient is mostly confined to the upstream region. The fluid temperature at the front tip and along the centerline is considerably lower and as such the viscosity there is higher. Since the viscosity is a function of temperature, a non-uniform temperature distribution leads to a non-uniform viscosity distribution in the flow field, with the smallest value in the core region. As a result, the axial velocity increases in the core region, and which in turn further extends the relative front tip travel distance Δy (Fig. 5.4). The thermal plume is also extended further downstream (comparing Fig. 5.7 (a) and (c)).

Figure 5.9 shows the pressure distribution for various Peclet number. In the entrance region, the pressure profiles have been greatly modified by the presence of a large temperature (and thus, viscosity) gradient. Recall that a uniform pressure profile was observed in the isothermal case. A high pressure gradient occurs at the regions near the wall and the contact line. It is understood that this high pressure gradient has resulted from a high viscosity gradient occurring at these regions (Fig. 5.8), which in turn is due to the presence of a high temperature gradient (Fig. 5.7). The pressure gradient becomes almost constant one channel width downstream of the inlet, but becomes more complicated near the flow front, especially in the region close to the contact line. With an increase in the Peclet number, a smaller injection pressure is required in the inlet.

After 5 dimensionless injection time from the start of injection, the maximum inlet pressure has increased from 39.39 to 185.33 as the Peclet number decreases from 50 to 1. The pressure distributions along the centerline and the wall are shown in Fig. 5.10. The results from the isothermal case are also included for comparison. From the figure, it is observed that the absolute pressure gradient increases as the Peclet number decreases. In addition, as the Peclet number increases, the pressure gradient along the wall approaches that of the centerline constant and both become constant in the front region.

The variation of contact angle for various Peclet numbers is shown in Fig. 5.11. After the contact line begins to move, some fluctuation is observed in the earlier stage for $Pe = 50$. After several time steps, the contact angles become more stable and approach 180° . From these figures, one can conclude that the thermal effect on the variation of contact angle is rather limited.

5.2 Gravitational Effects

For flow injection through a vertical channel, the gravitational force is acting opposite to the flow direction. Figure 5.12 shows the development of the flow front for a given capillary number ($Ca = 1$) and various gravitational forces. It is clear to see that a large gravitational force greatly shortens the front tip travel distance. For $Pe = 10$, the initial front tip travel distance (when the contact line initiates its first move) decreases from 0.904 to 0.636 when the Stokes number increases from 0 to 10. As a result, the flow front becomes flattened when the gravitational force increases. Similar situation is observed for $Pe = 1$ and 50.

The velocity distributions under various gravitational forces are shown in Fig.

5.13. From the figure, the fountain flow effects can be clearly observed near the flow front. It is easy to see that gravitational force flattens the flow front and compresses the fountain flow region. As the gravitational force increases, the fountain flow region becomes more confined, and its effect is more obvious near the flow front. With an increase in the Peclet number, the rolling motion of the fluid at the flow front can be clearly observed (i.e., the change of the vector angle).

The relative flow front travel distance under various gravitational effects is shown in Fig. 5.14 for a given capillary number ($Ca = 1$). For all Peclet numbers considered, the instantaneous front tip travel distance decreases as the gravitational force increases. A large gravitational force (i.e., a high Stokes number) generally reduces the time required for the contact line to initiate its first move. For $Pe = 10$, this waiting time is calculated to be 0.708 at $St = 0$ and it reduces to 0.502 at $St = 10$. The times required for the contact line to initiate its first move under various surface tension and gravitational effects are listed in Table 5.2. From the table, it is clearly observed that the gravitational force shortens the waiting time for the contact line to begin its first move. Since the gravitational force compresses and flattens the flow front, the contact line is forced to move earlier. The relative front tip travel distances under various surface tension and gravitational effects are listed in Table 5.3 for some selected times. From the table, it is observed that the gravitational force has a more significant impact on the relative flow front tip travel distance when the Peclet number is large. For $Pe = 1$, Δy decreases from 0.995 to 0.905 as the Stokes number increases from 0 to 10. At the same time, it decreases from 1.086 to 0.746 when the Stokes number increases from 0 to 10. Since the flow with a higher Peclet number has a higher temperature and a lower

viscosity on the flow front. The gravitational force is able to compress the front region further. The thermal effects on the relative front tip travel distance can be cross-examined from Table 5.3 for various gravitational effects. The results show that the relative flow front tip travel distance increases with the Peclet number if the gravitational effect is small (e.g., $0 \leq St \leq 1$). On the other hand, the relative flow front tip travel distance decreases with the Peclet number when the gravitational effect is significant ($St = 10$).

The gravitational effects on the pressure distribution is shown in Fig. 5.15 for $Ca = 1$. As observed earlier, a high pressure gradient occurs at the entrance region near the wall due to the presence of a higher temperature gradient. There also exists a complicated pressure gradient in the vicinity of the contact line. The pressure gradient becomes nearly constant about one channel width downstream from the inlet. From the figure, it is clearly observed that gravitational effect significantly increases the inlet injection pressure and pressure distribution close to the contact line. For $Pe = 1$, the maximum pressure (which is the required pressure at the inlet for flow injection) has increased from 186.50 to 250.60 as the Stokes number increases from 0 to 10. A similar trend is observed for $Pe = 10$ and 50. From the pressure contours, it is clearly observed that a smaller injection pressure is required when the Peclet number is large. The pressure distributions along the wall and centerline are presented in Fig. 5.16 for cross-examination. As the gravitational effect increases, the pressure distribution between the wall and centerline (at the same distance along the flow direction) decreases. For a given gravitational force, as the Peclet number increases, the required injection pressure decreases and pressure gradient approaches constant.

Figures 5.17 and 5.18 show the transient temperature and viscosity distributions under at a given set of flow condition ($St = 1$, $Ca = 1$ and $Pe = 10$). As time increases, the temperature decreases (and thus viscosity increases) at any given point in the centerline and flow front region. It can be attributed to fountain flow effect that more heat is delivered to the wall. The temperature and viscosity distributions under various gravitational forces are shown in Figs. 5.19 and 5.20. From these figures, it may first appear that the temperature profiles are all identical at a given Peclet number. However, a closer examination on these temperature profiles reveals that there is a difference in the temperature gradient near the wall in the entrance region. A similar situation can be found in the flow front region. Accordingly, differences in the viscosity gradient can be found in these two region, although they may not be as obvious. As a result of these differences, the pressure gradient varies significantly with the Stokes number.

5.3 Effects of Surface Tension

The effect of surface tension on the relative front tip travel distance is listed in Table 5.3. For a given gravitational force ($St = 1$), the relative front tip travel distance (Δy) increases as the capillary number decreases (i.e., the surface tension effect increases) at the selected injection time frame. The results also show that this effect is enhanced when the Peclet number increases. For $Pe = 1$, Δy increases from 0.909 to 0.921 as the capillary number decreases from ∞ to 1. For $Pe = 50$, it increases from 0.916 to 0.966 for the same range of the capillary number. It shows that Δy is further extended more by the surface tension when the Peclet number increases. A similar result is observed for $St = 0$ and $St = 10$. From this observation, one may conclude that the surface tension effect

expands the fountain flow region and enhances the fountain flow effect.

Although the surface tension does not have a significant influence on the velocity field, its effect on the waiting time (the time required for the contact line to initiate its first move) is obvious and can be verified from Table 5.2. As the surface tension effect increases (i.e., the capillary number decreases), a longer waiting time is required. This potential energy can resist more shear stresses acting on the free surface and flow front can move further before the contact line begins to move.

The surface tension effect on the pressure distribution along the centerline is shown in Fig. 5.21 for $St = 0$. It shows that surface tension increases the pressure distribution along the centerline for a fixed Peclet number. For $Pe = 1$, the inlet pressure along the centerline increases from 174.08 to 177.70 when the capillary number decreases from ∞ to 1. For $Pe = 50$, the inlet pressure along the centerline increases from 32.12 to 33.44 for the same range of the capillary number. It shows that the surface tension effect on the required injection pressure is reduced as the Peclet number increases.

5.4 Conclusions

The effects of the gravitation and surface tension on the non-isothermal flow injection through a vertical channel is analyzed numerically using the Taylor-Galerkin finite element method. A predictor-corrector scheme is employed to update the free surface at each time step. The development of the flow front, instantaneous velocity, pressure, temperature, and viscosity are obtained. The fountain flow effect under various gravitational force, surface tension and heat transfer conditions are compared.

For a given surface tension , results obtained show that the gravitational force has a significantly impact on the development of flow front and the relative front tip travel distance (Δy). As the gravitational force increases, the time required for the contact line to begin its first move is shortened and the fountain flow region is compressed. As a result, the required injection pressure increases. This is understood because the gravitational force is acting in a direction opposite to the flow direction.

For a given gravitational force, the relative front tip travel distance increases with the surface tension because of the presence of a higher potential energy on the free surface. This surface energy can withstand a larger deformation of the free surface and thus increases Δy . It also expands the fountain flow region as the surface tension increases.

The results also show that the added temperature effect significantly changes the fountain pattern and the required injection pressure. As the Peclet number increases, the temperature along the centerline and near the front tip increases while the viscosity decreases in these regions. For a small gravitational force ($0 \leq St \leq 1$), the fountain flow region is further expanded by convection and Δy increases with the Peclet number. For a larger gravitational force ($St = 10$), the fountain flow region is compressed further and Δy decreases as the Peclet number increases. This is due to a sharp reduction in the viscosity along the flow front and a weaker viscous force to balance the gravitational force. The required dimensionless injection pressure increases from 46.13 to 191.96 as the Peclet number decreases from 50 to 1 ($\Delta\tau \approx 5$, $St = 1$, and $Ca \rightarrow \infty$). At the same time, the added thermal effect enhances the surface tension effect on the development of flow front and the relative front tip travel distance Δy .

Table 5.1 Relative front tip travel distance for various Peclet numbers at different injection times ($Ca \rightarrow \infty$ and $St = 0$).

Δy				
Time	isothermal flow	non-isothermal flow		
		Pe = 1	Pe = 10	Pe = 50
$\tau \approx 4.0$	0.930	0.950	0.955	1.005
$\tau \approx 5.0$	0.930	0.976	0.996	1.048
$\tau \approx 6.0$	0.930	1.009	1.013	1.075

Table 5.2 Time required for the first movement of contact line: (a) $Pe = 1$, (b) $Pe = 10$, and (c) $Pe = 50$.

Ca \ St	0	1	10
	1	0.663	0.642
∞	0.638	0.618	0.498

(a)

Ca \ St	0	1	10
	1	0.707	0.661
∞	0.704	0.670	0.483

(b)

Ca \ St	0	1	10
	1	0.726	0.681
∞	0.727	0.661	0.454

(c)

Table 5.3 Relative front tip travel distance under various surface tension and gravitational effects: (a) $Pe = 1$, (b) $Pe = 10$, and (c) $Pe = 50$.

Time	$\Delta\tau \approx 4.0$		$\Delta\tau \approx 5.0$		$\Delta\tau \approx 6.0$	
Ca \ St	1	∞	1	∞	1	∞
0	0.931	0.927	0.960	0.960	0.995	0.990
1	0.921	0.909	0.946	0.946	0.985	0.981
10	0.828	0.820	0.868	0.856	0.905	0.901

(a)

Time	$\Delta\tau \approx 4.0$		$\Delta\tau \approx 5.0$		$\Delta\tau \approx 6.0$	
Ca \ St	1	∞	1	∞	1	∞
0	0.989	0.966	1.016	0.996	1.042	1.031
1	0.930	0.902	0.972	0.936	0.994	0.971
10	0.723	0.683	0.759	0.729	0.801	0.771

(b)

Time	$\Delta\tau \approx 4.0$		$\Delta\tau \approx 5.0$		$\Delta\tau \approx 6.0$	
Ca \ St	1	∞	1	∞	1	∞
0	1.038	1.005	1.071	1.048	1.086	1.075
1	0.966	0.916	0.984	0.938	1.022	0.985
10	0.696	0.638	0.719	0.674	0.746	0.708

(c)

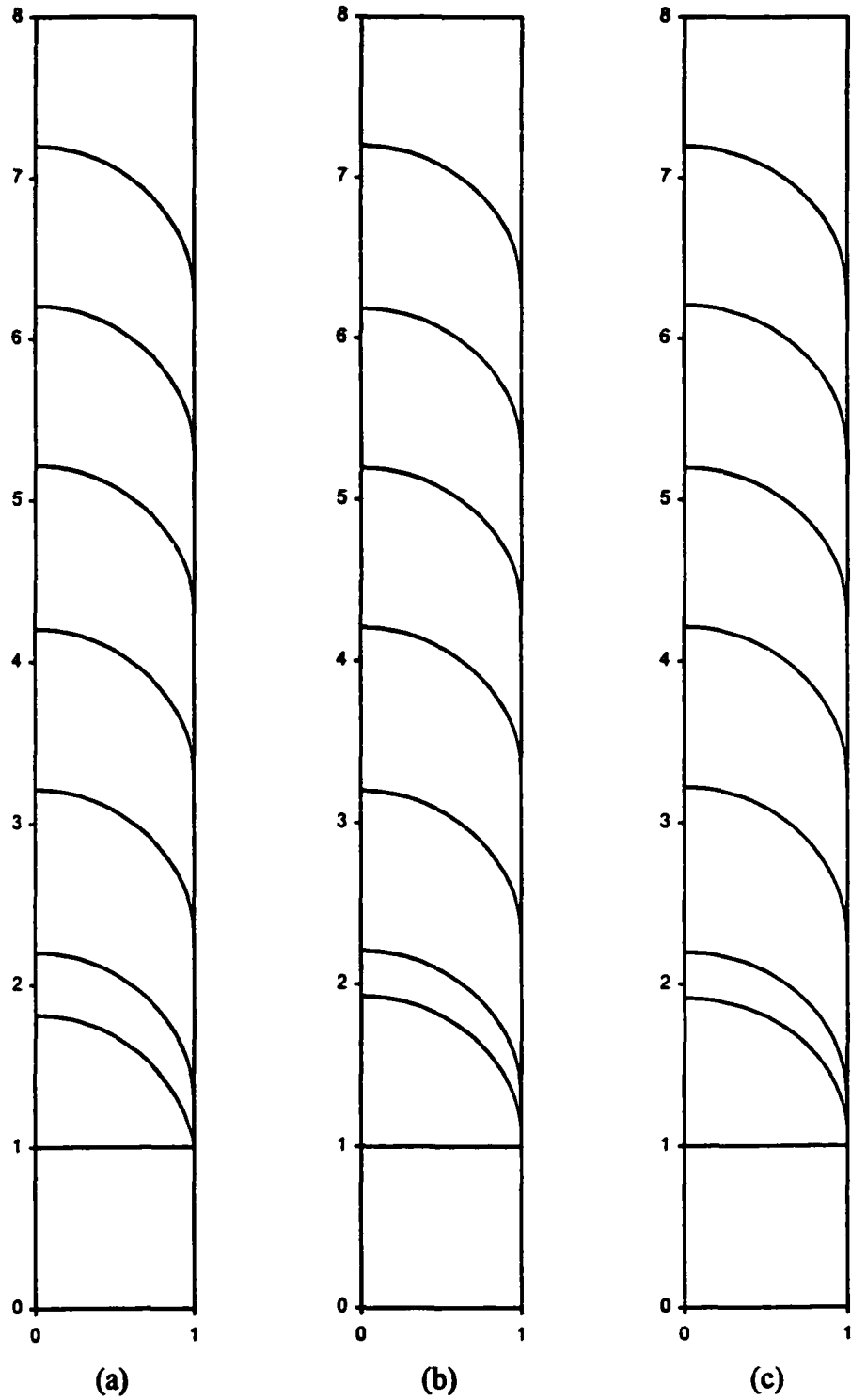


Figure 5.1 Development of flow front in a vertical channel at various Peclet numbers ($Ca \rightarrow \infty$ and $St = 0$): (a) $Pe = 1$, (b) $Pe = 10$, (c) $Pe = 50$.

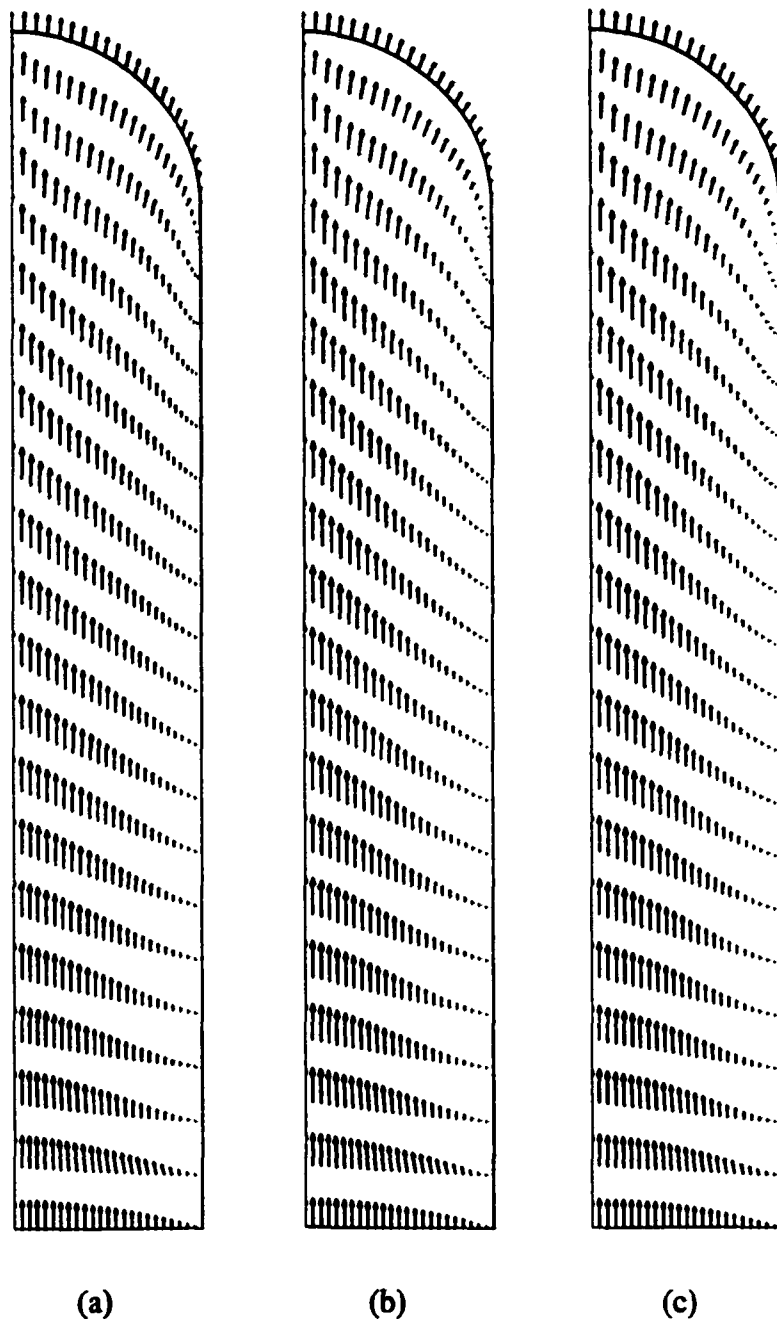


Figure 5.2 Velocity fields for flow injection in a vertical channel at various Peclet numbers ($Ca \rightarrow \infty$ and $St = 0$): (a) $Pe = 1$, (b) $Pe = 10$, and (c) $Pe = 50$.

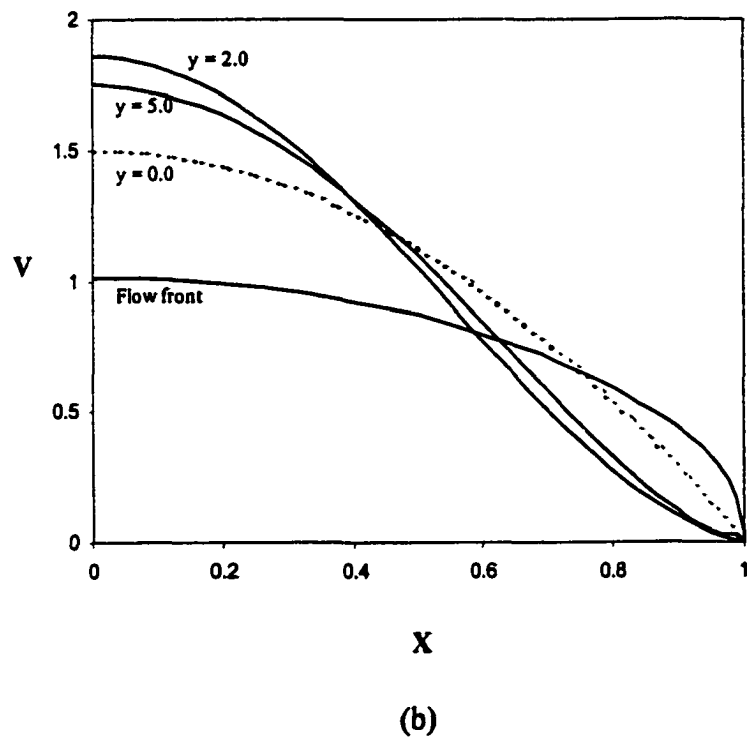
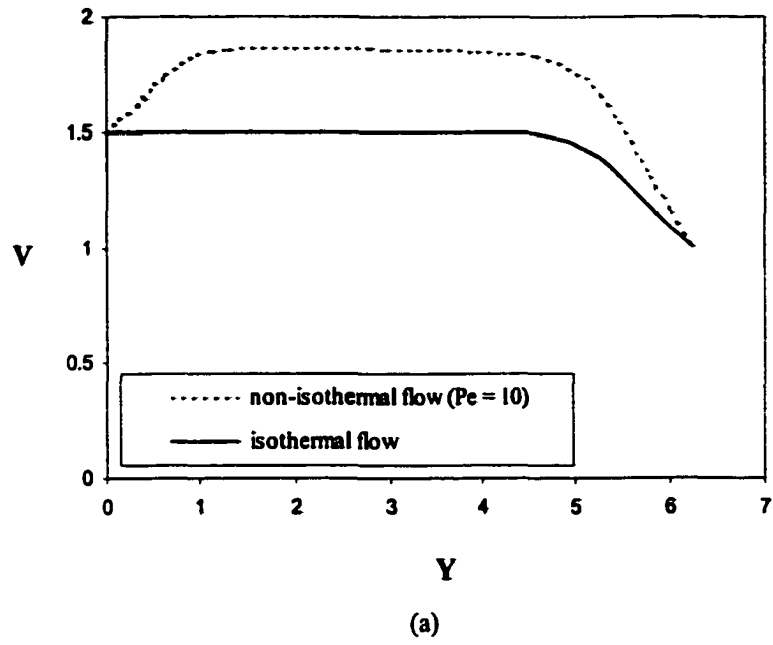


Figure 5.3 Thermal effects on the velocity distribution ($Pe = 10$): (a) along the centerline, and (b) across the channel width at various locations.

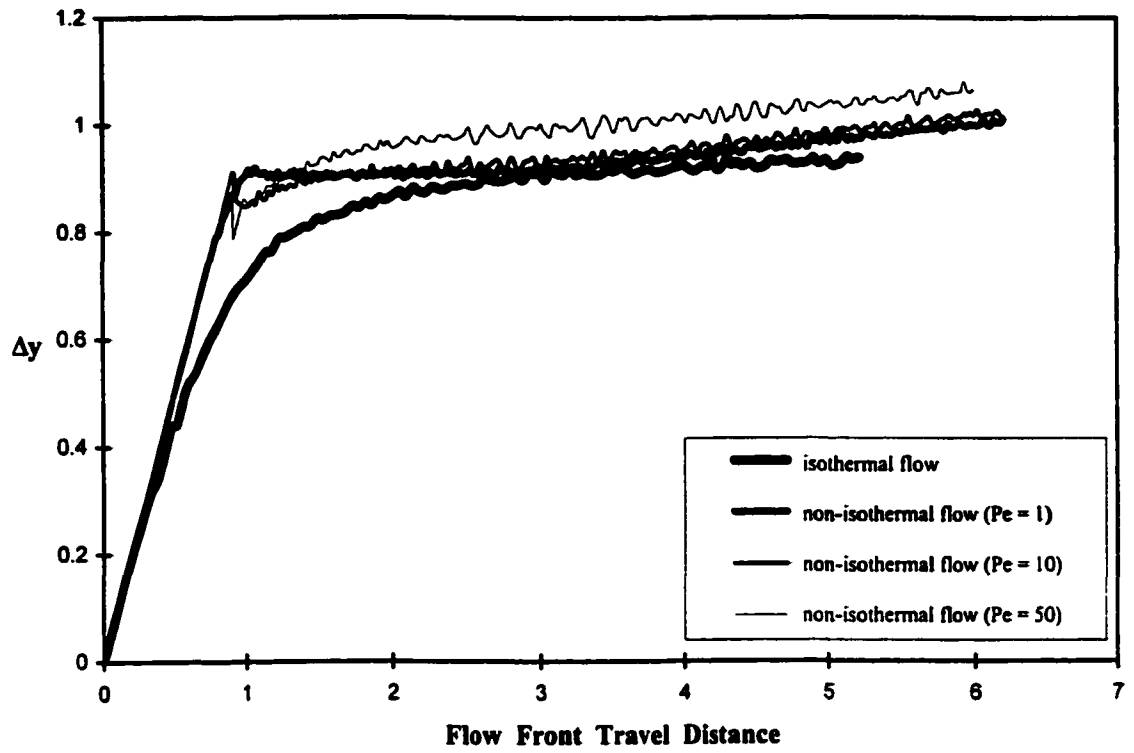


Figure 5.4 Relative flow front travel distance for various Peclet numbers ($Ca \rightarrow \infty$ and $St = 0$).

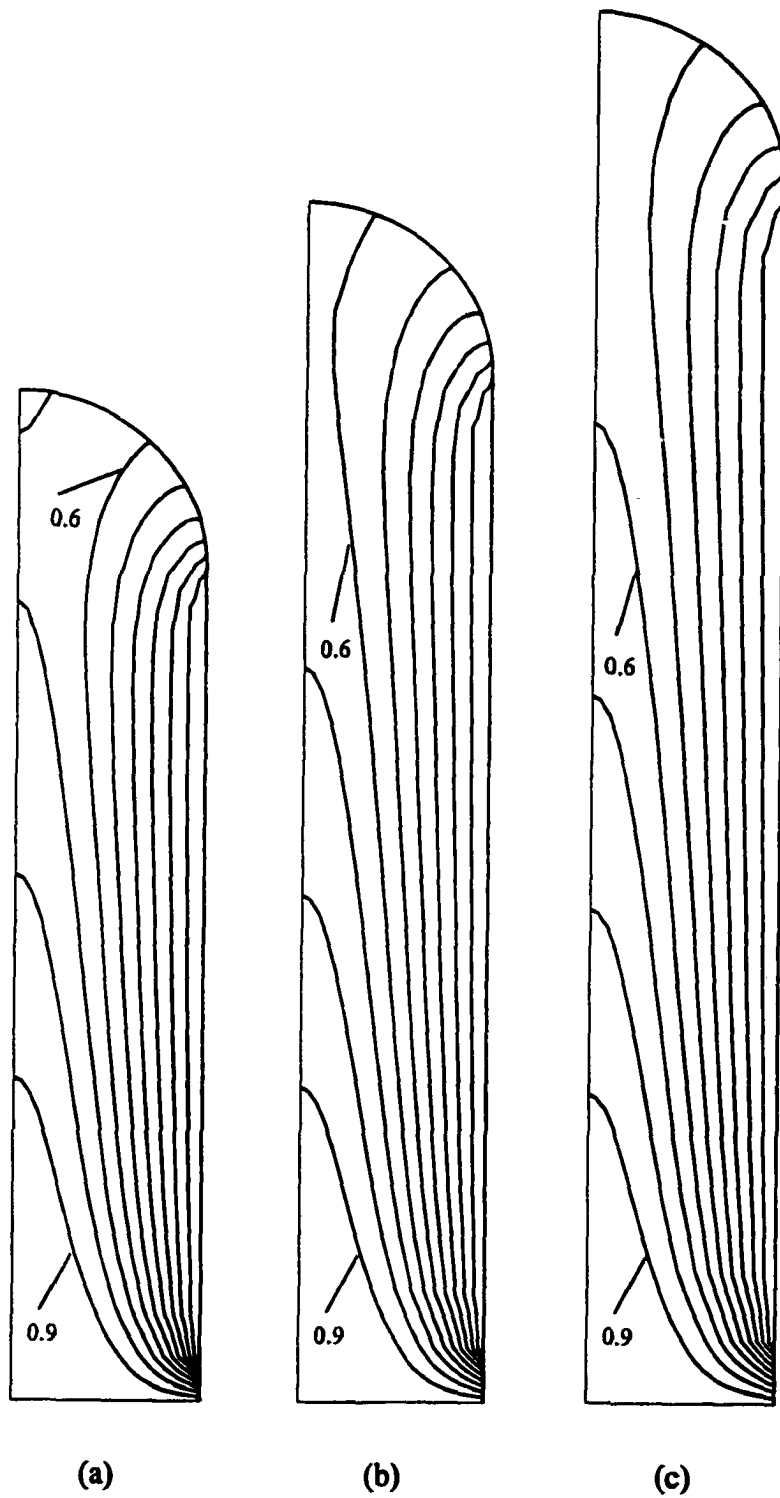


Figure 5.5 Temperature contours at various injection times ($Pe = 10$, $Ca \rightarrow \infty$, and $St = 0$): (a) $\tau = 4.03$, (b) $\tau = 5.02$, and (c) $\tau = 6.02$ ($\Delta T = 0.1$).

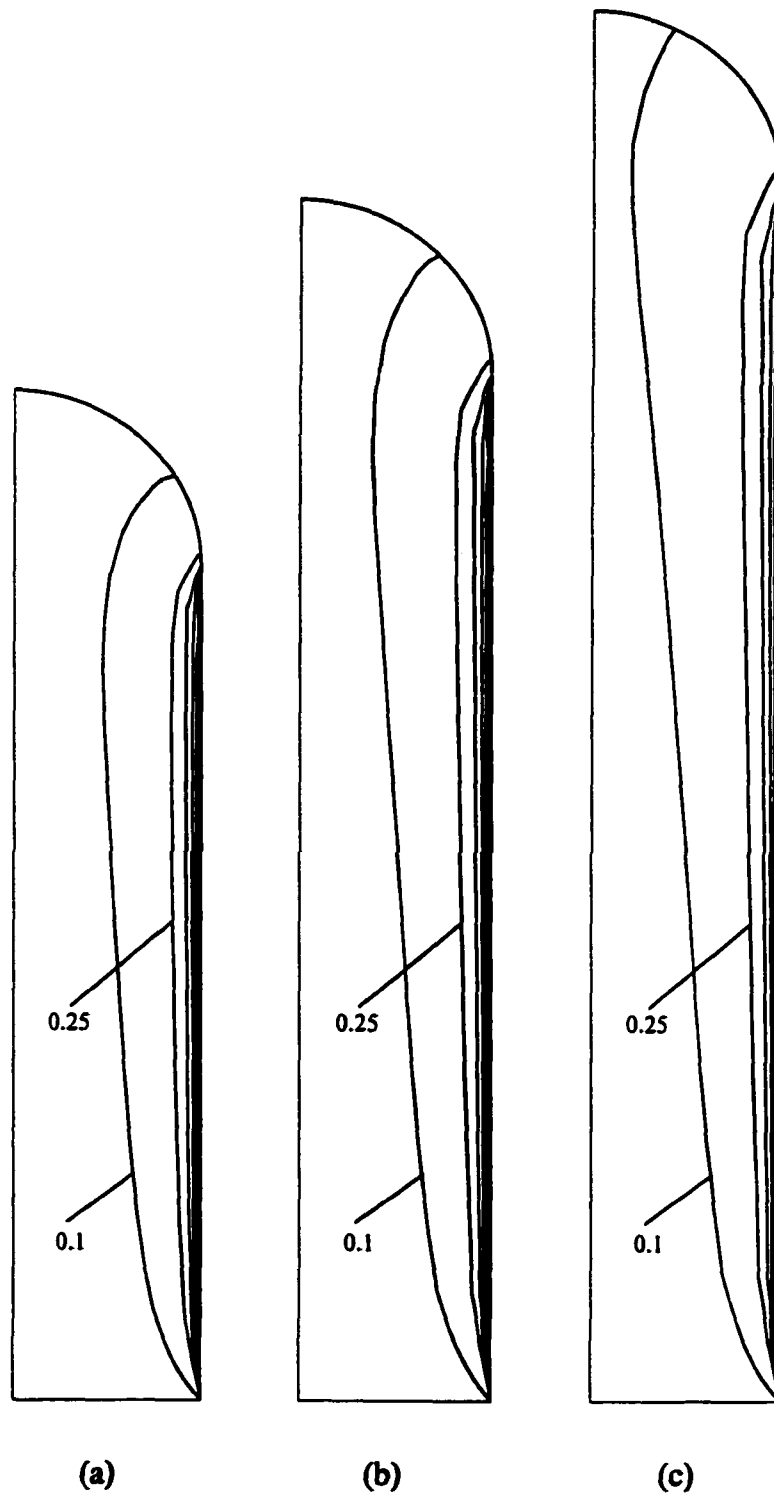


Figure 5.6 Viscosity contours at various injection times ($Pe = 10$, $Ca \rightarrow \infty$, and $St = 0$): (a) $\tau = 4.03$, (b) $\tau = 5.02$, and (c) $\tau = 6.02$ ($\Delta\mu = 0.15$).

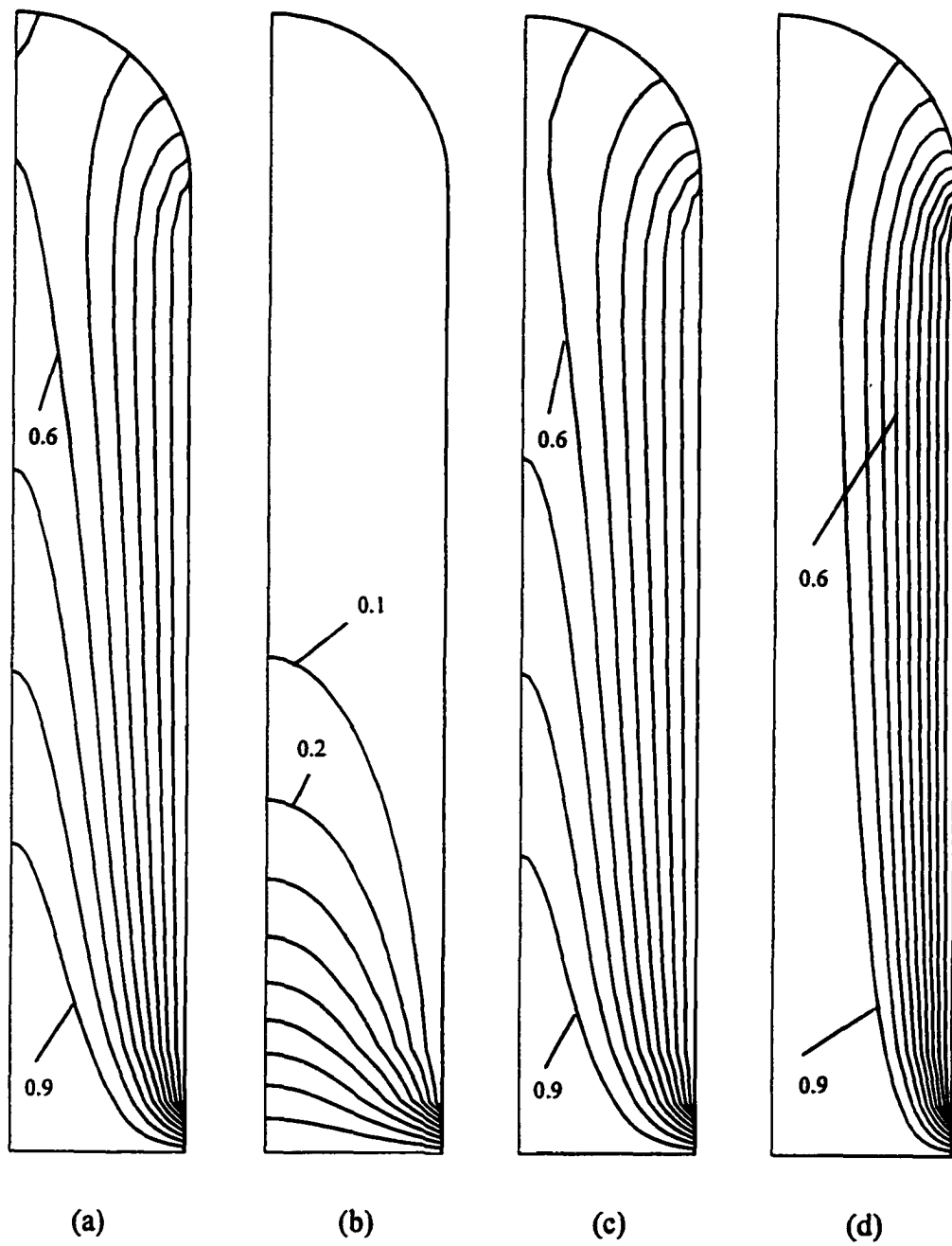


Figure 5.7 Temperature contours for flow injection at various Peclet number ($St = 0$ and $Ca \rightarrow \infty$): (a) $Pe = 10$ (constant viscosity), (b) $Pe = 1$, (c) $Pe = 10$, and (d) $Pe = 50$ ($\Delta T = 0.1$).

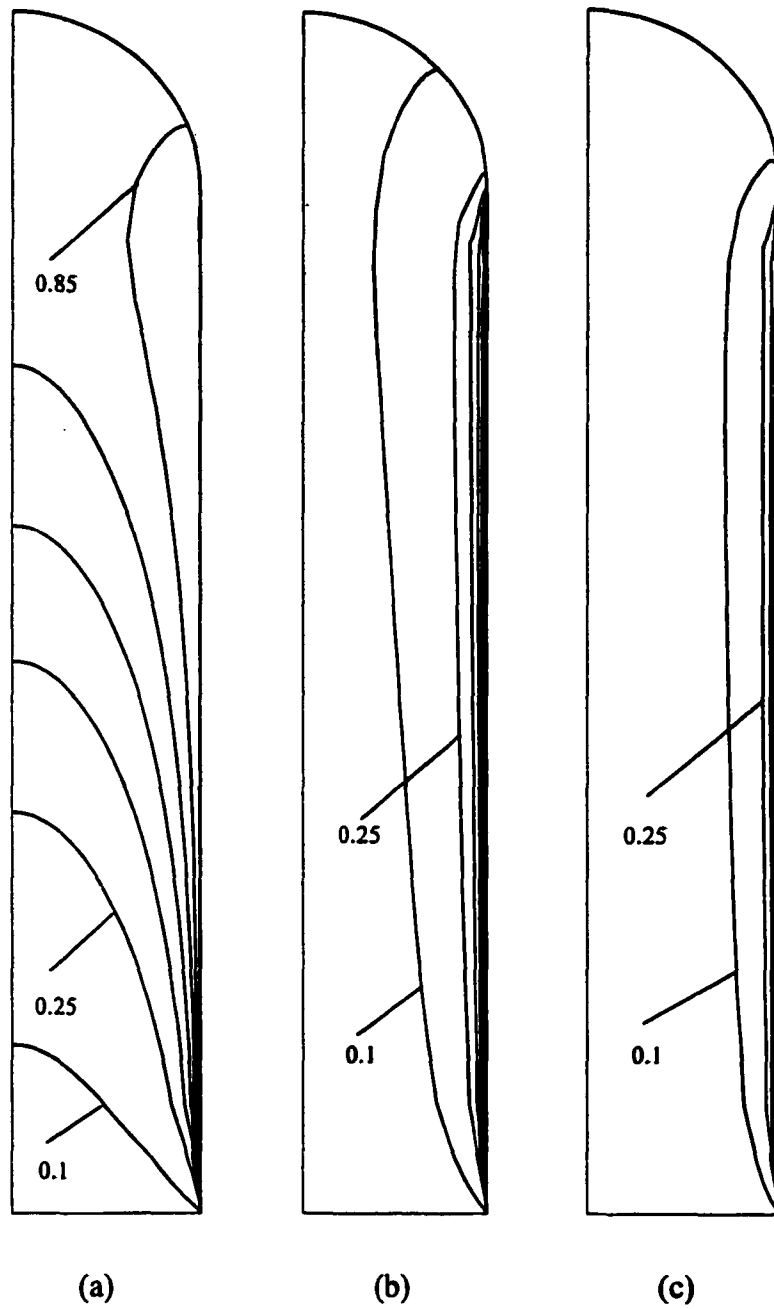


Figure 5.8 Viscosity contours for flow injection at various Peclet numbers ($St = 0$ and $Ca \rightarrow \infty$): (a) $Pe = 1$, (b) $Pe = 10$, and (c) $Pe = 50$ ($\Delta\mu = 0.15$).

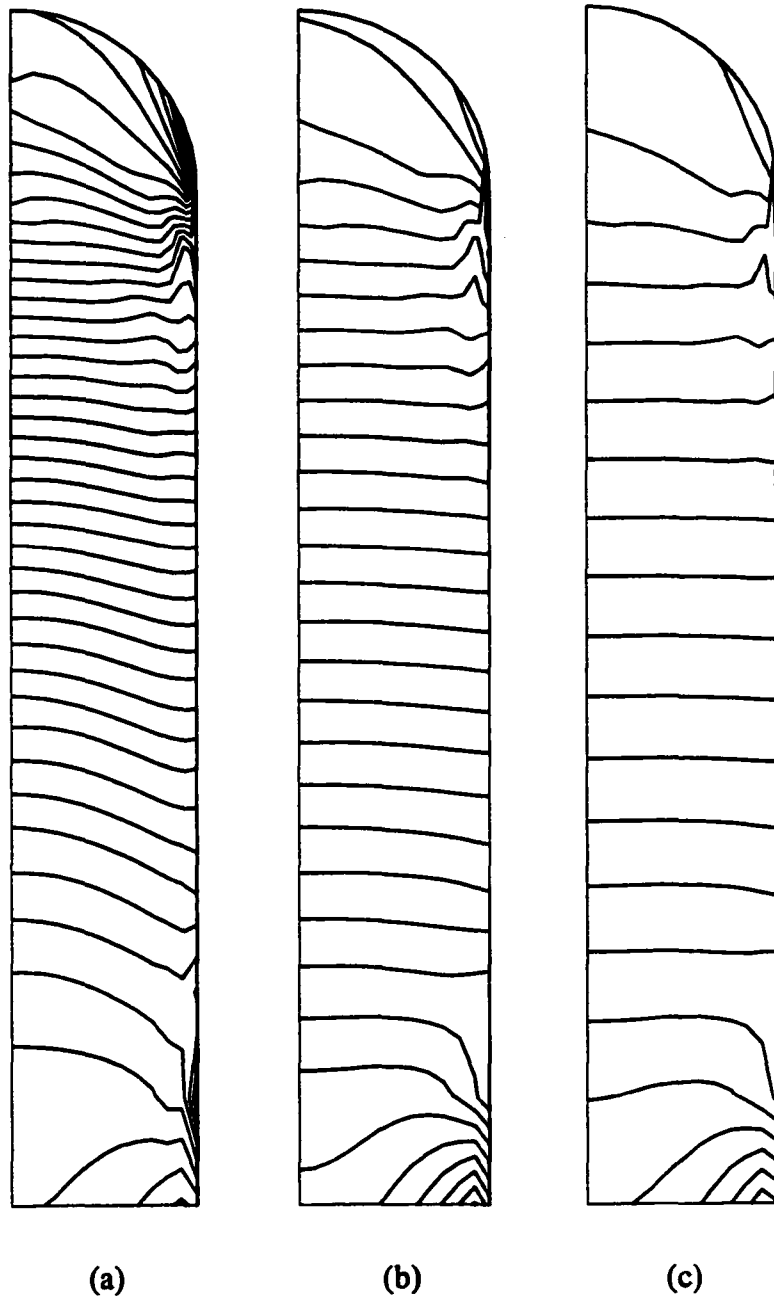


Figure 5.9 Pressure contours for flow injection at various Peclet numbers ($St = 0$ and $Ca \rightarrow \infty$): (a) $Pe = 1$ ($P_{max} = 185.33$, $P_{min} = -45.66$, and $\Delta P = 5$), (b) $Pe = 10$ ($P_{max} = 58.66$, $P_{min} = -5.68$ and $\Delta P = 2$), and (c) $Pe = 50$ ($P_{max} = 39.79$, $P_{min} = -3.60$, and $\Delta P = 2$).

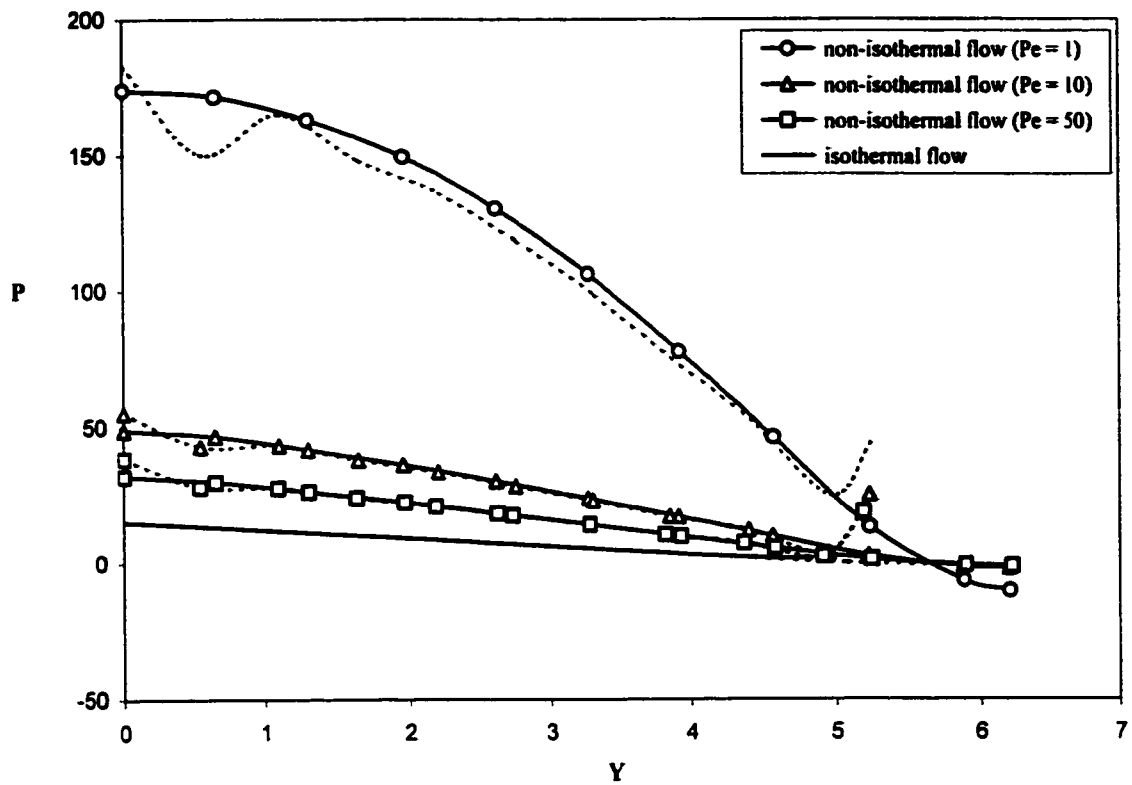
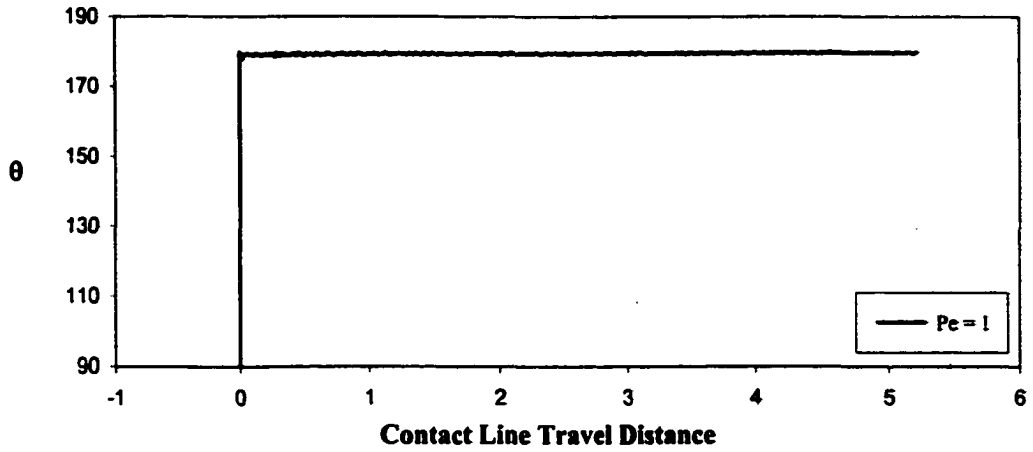
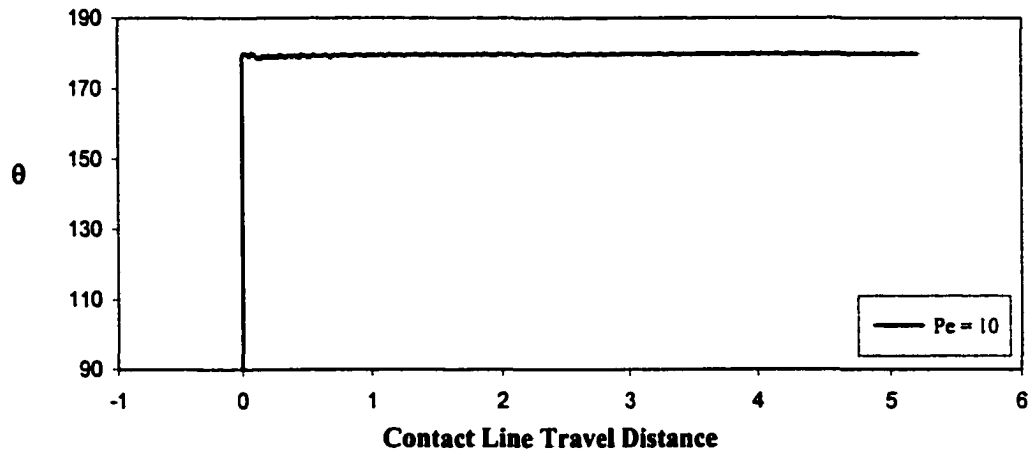


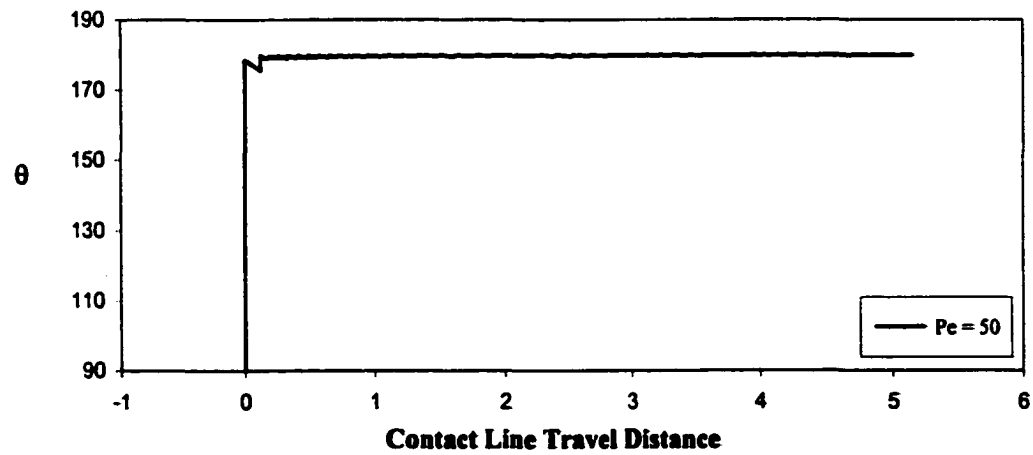
Figure 5.10 Thermal effects on the pressure distribution along the wall and centerline ($Ca \rightarrow \infty$ and $St = 0$): wall (---) and centerline (—○—).



(a)



(b)



(c)

Figure 5.11 Variation of contact angle at various Peclet numbers ($Ca \rightarrow \infty$ and $St = 0$): (a) $Pe = 1$, (b) $Pe = 10$, and (c) $Pe = 50$.

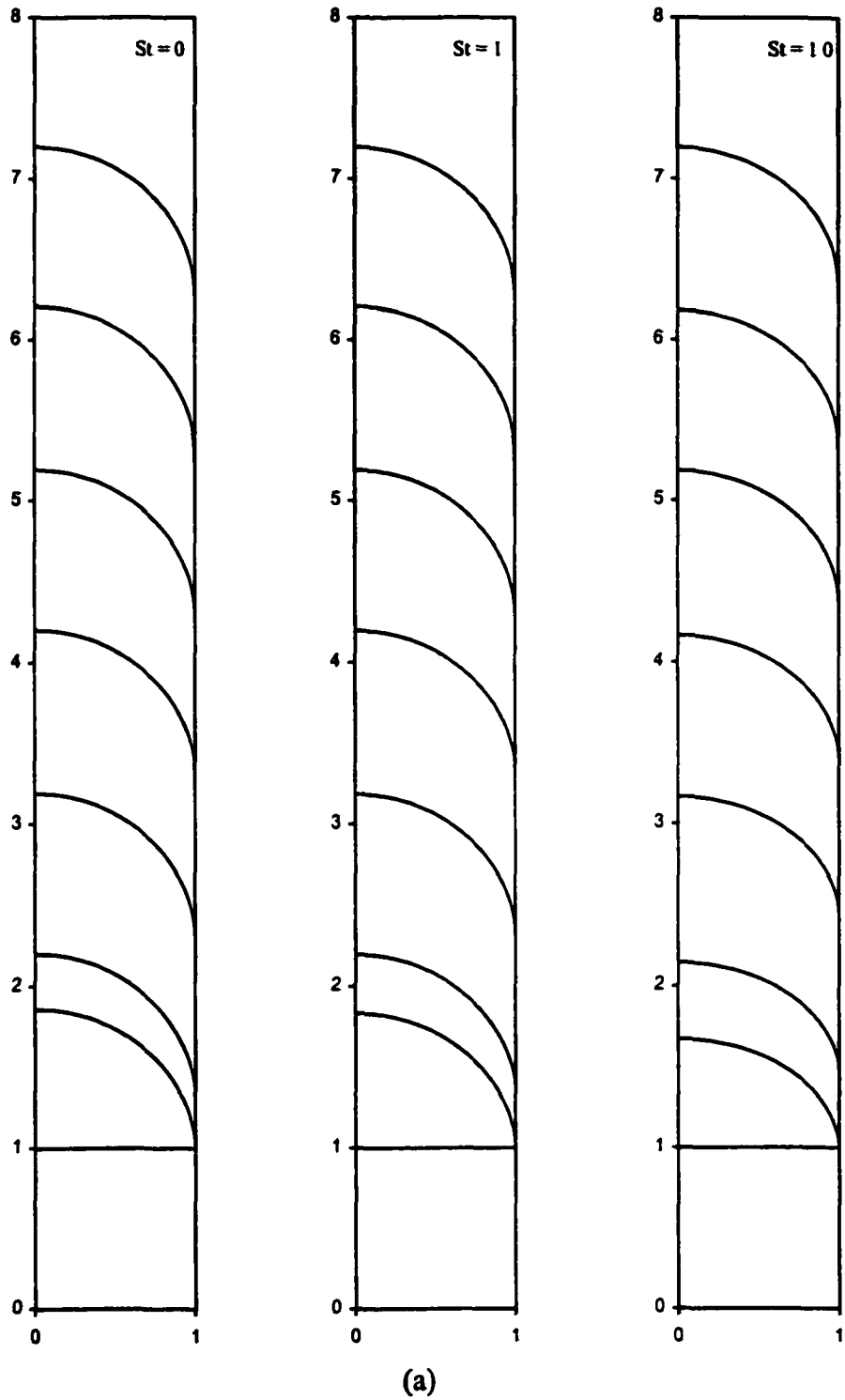


Figure 5.12 Development of flow front under various gravitational effects ($Ca = 1$): (a) $Pe = 1$, (b) $Pe = 10$, and (c) $Pe = 50$.

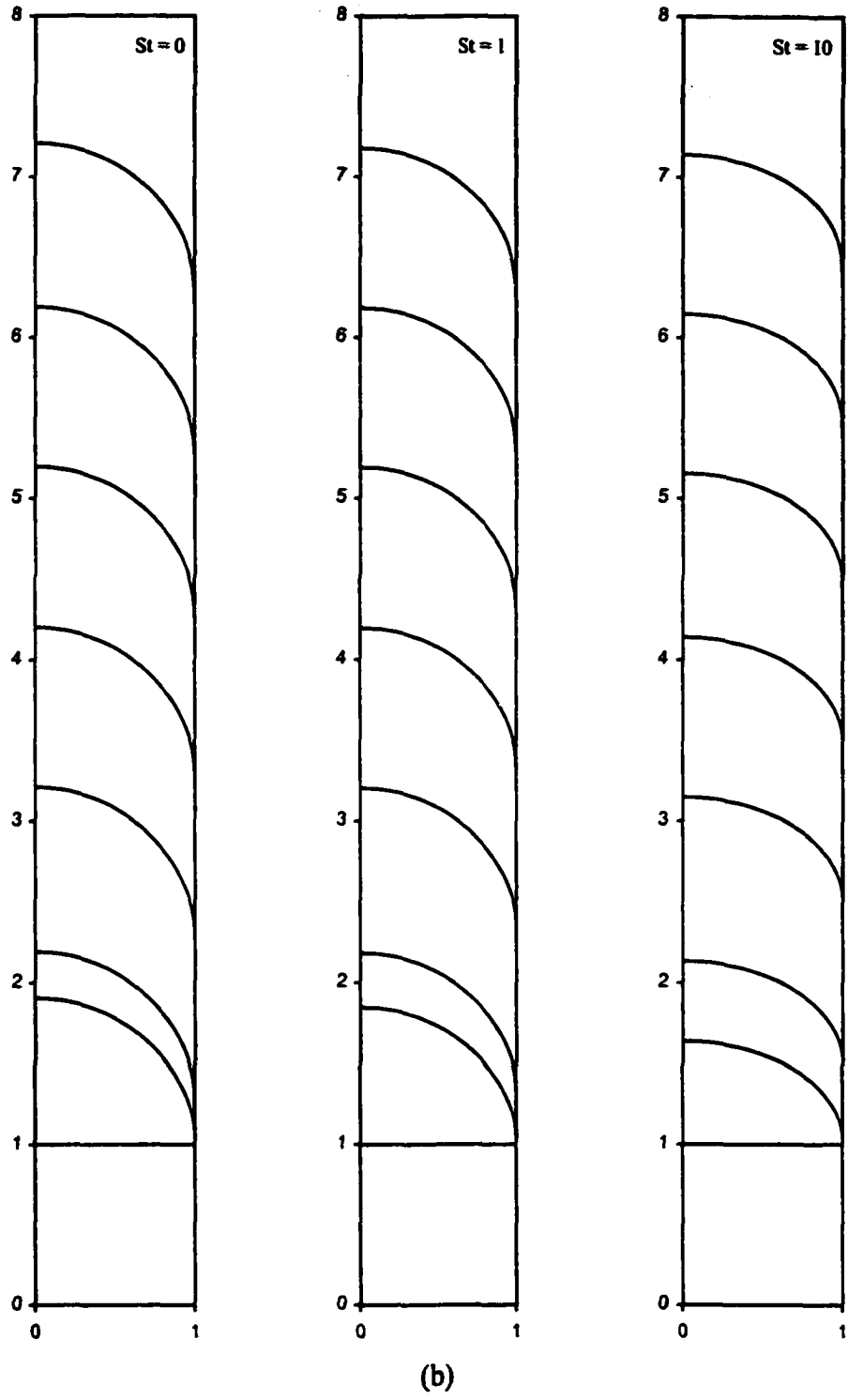
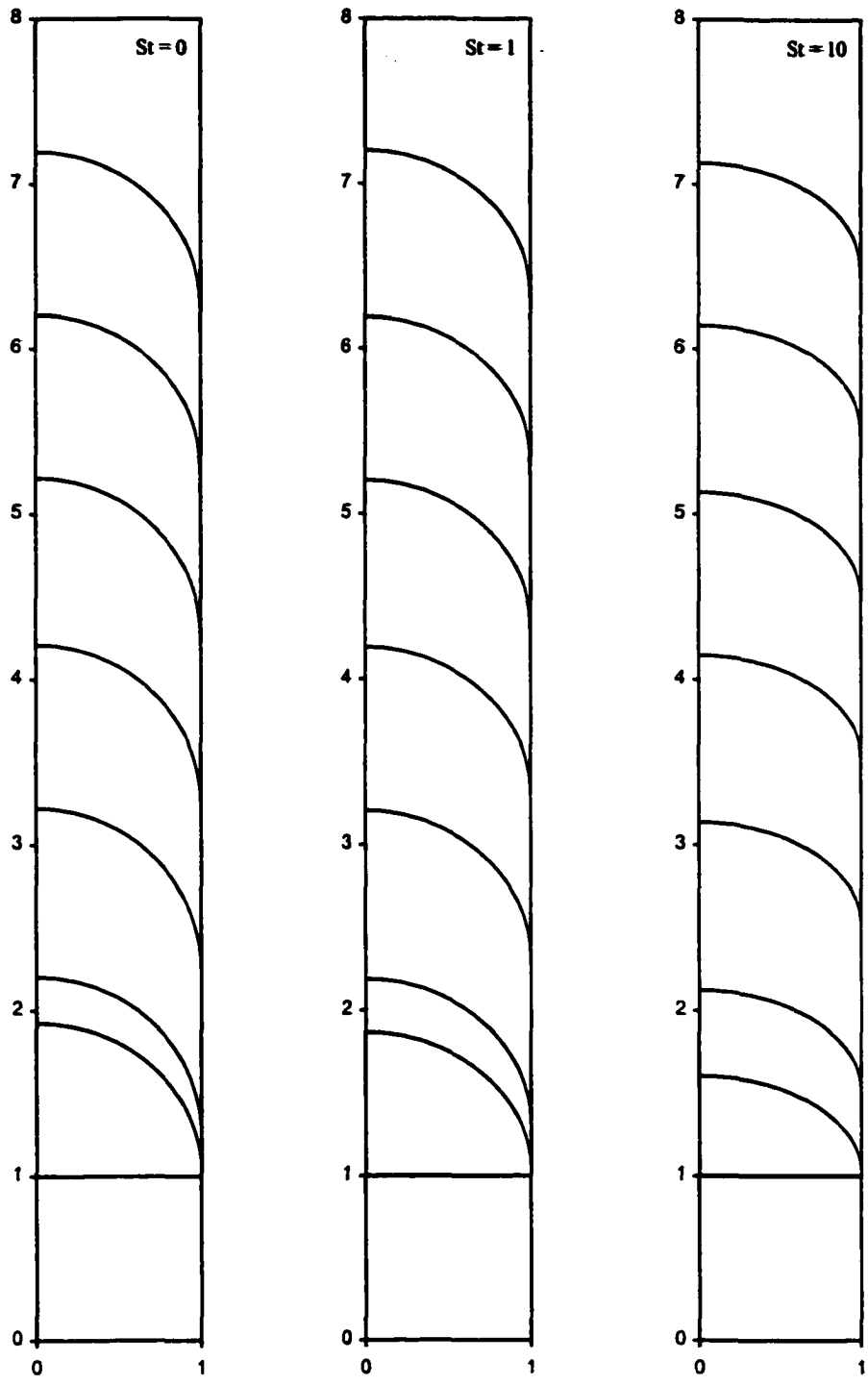


Figure 5.12 Continued.



(c)

Figure 5.12 Continued.

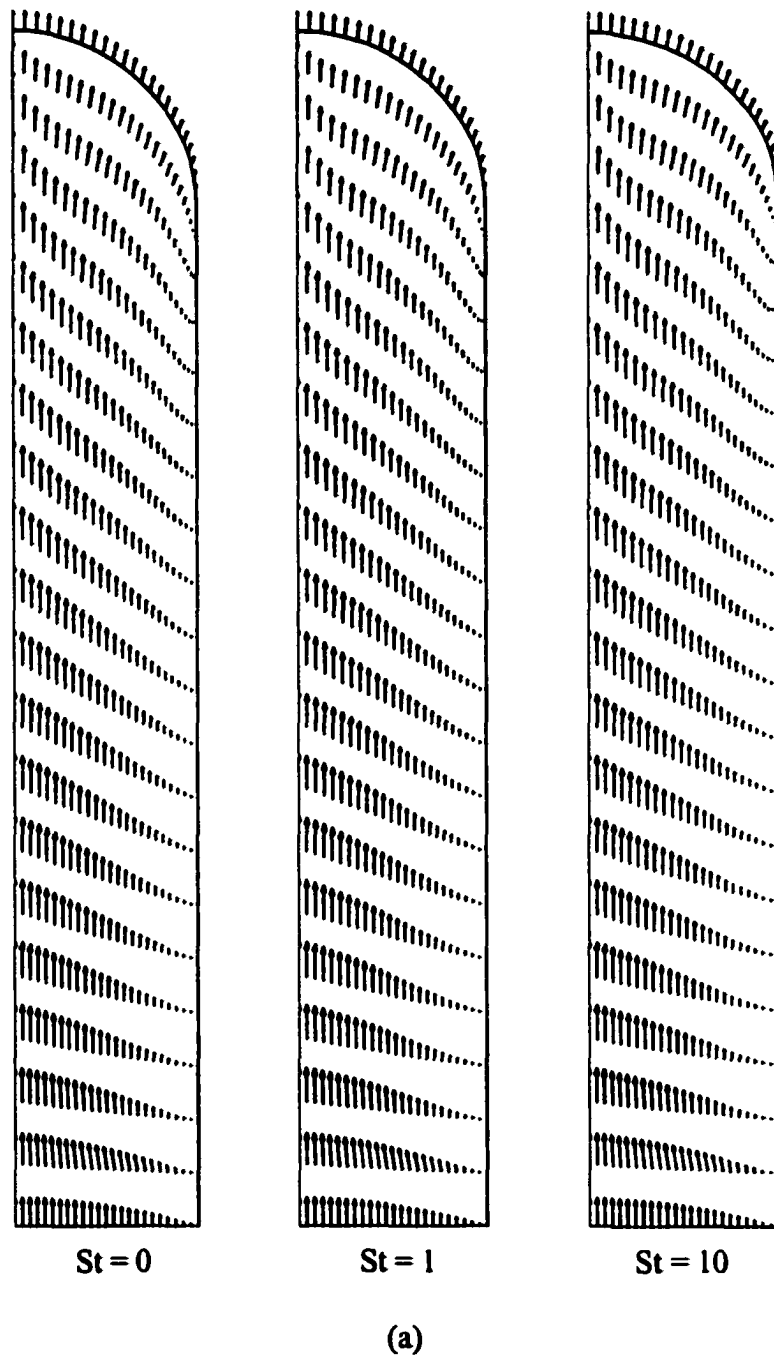
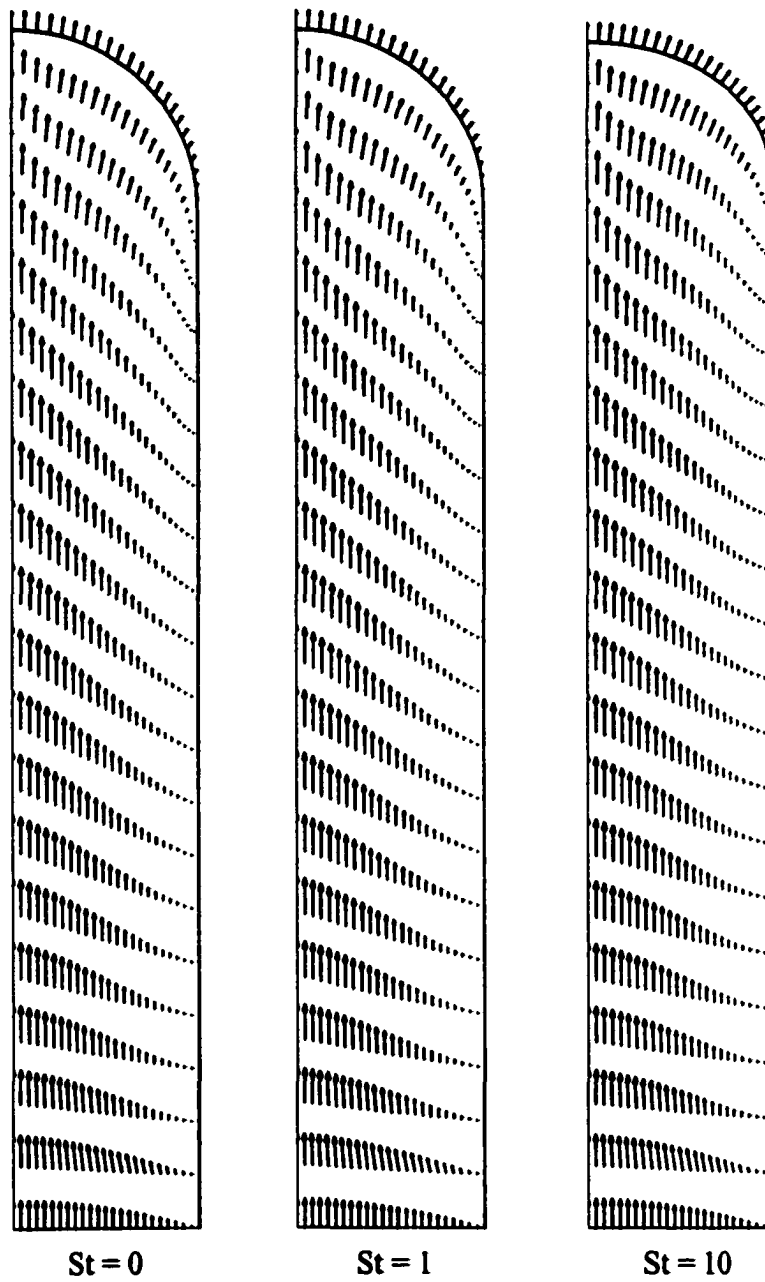
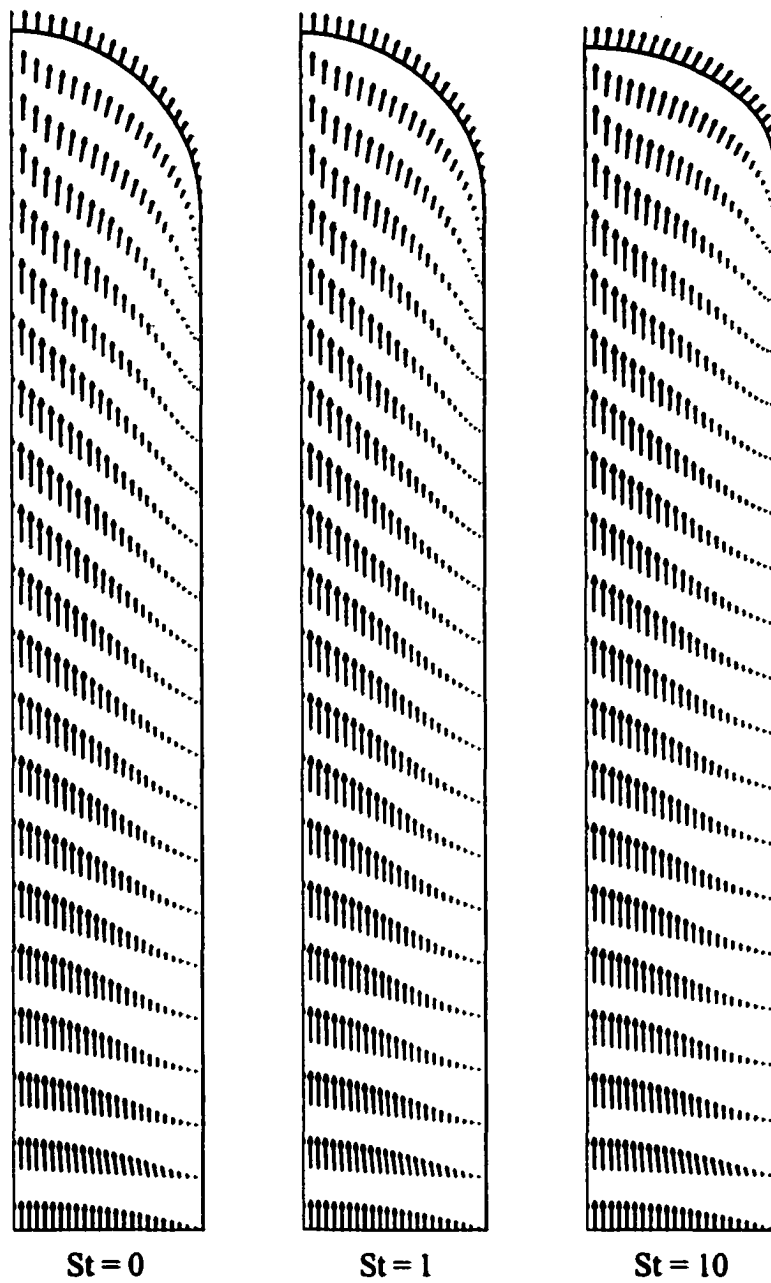


Figure 5.13 Velocity fields for flow injection in a vertical channel under various gravitational effects ($Ca = 1$): (a) $Pe = 1$, (b) $Pe = 10$, and (c) $Pe = 50$.



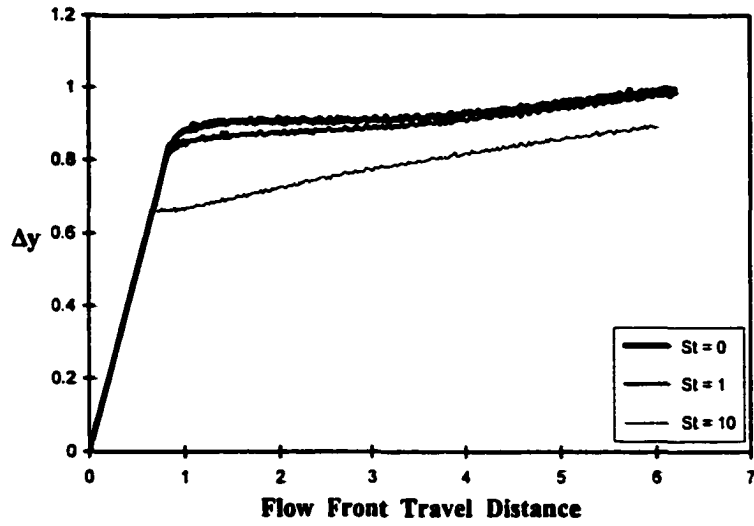
(b)

Figure 5.13 Continued

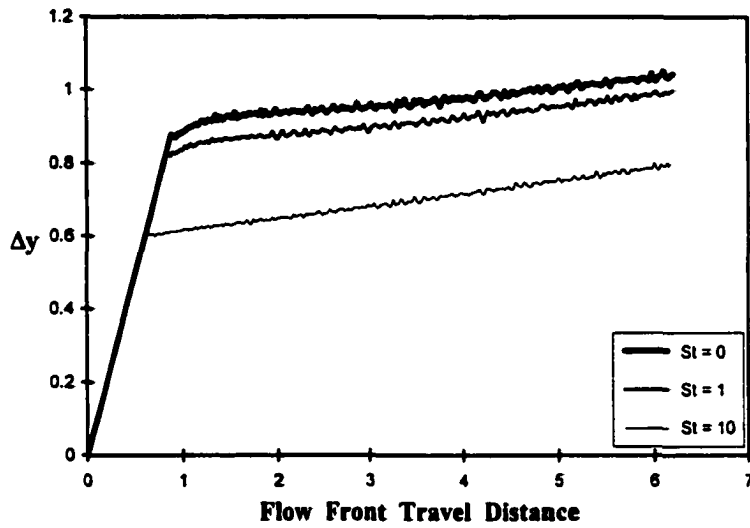


(c)

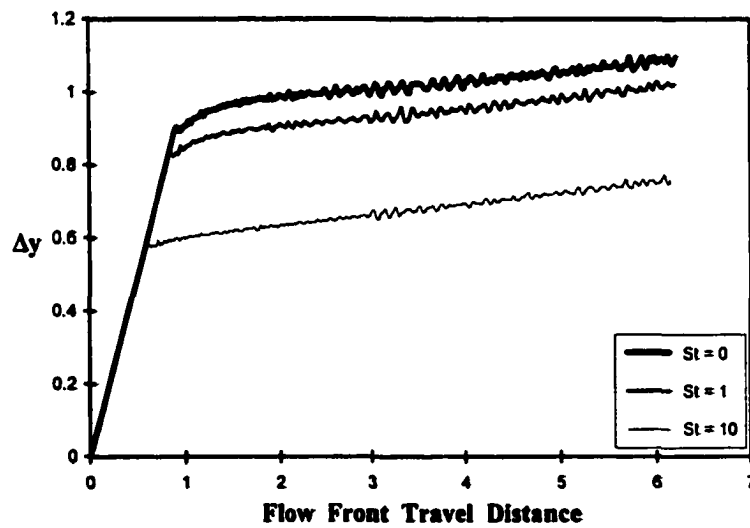
Figure 5.13 Continued



(a)



(b)



(c)

Figure 5.14 Relative flow front travel distance under various gravitational effects ($Ca = 1$): (a) $Pe = 1$, (b) $Pe = 10$, and (c) $Pe = 50$.

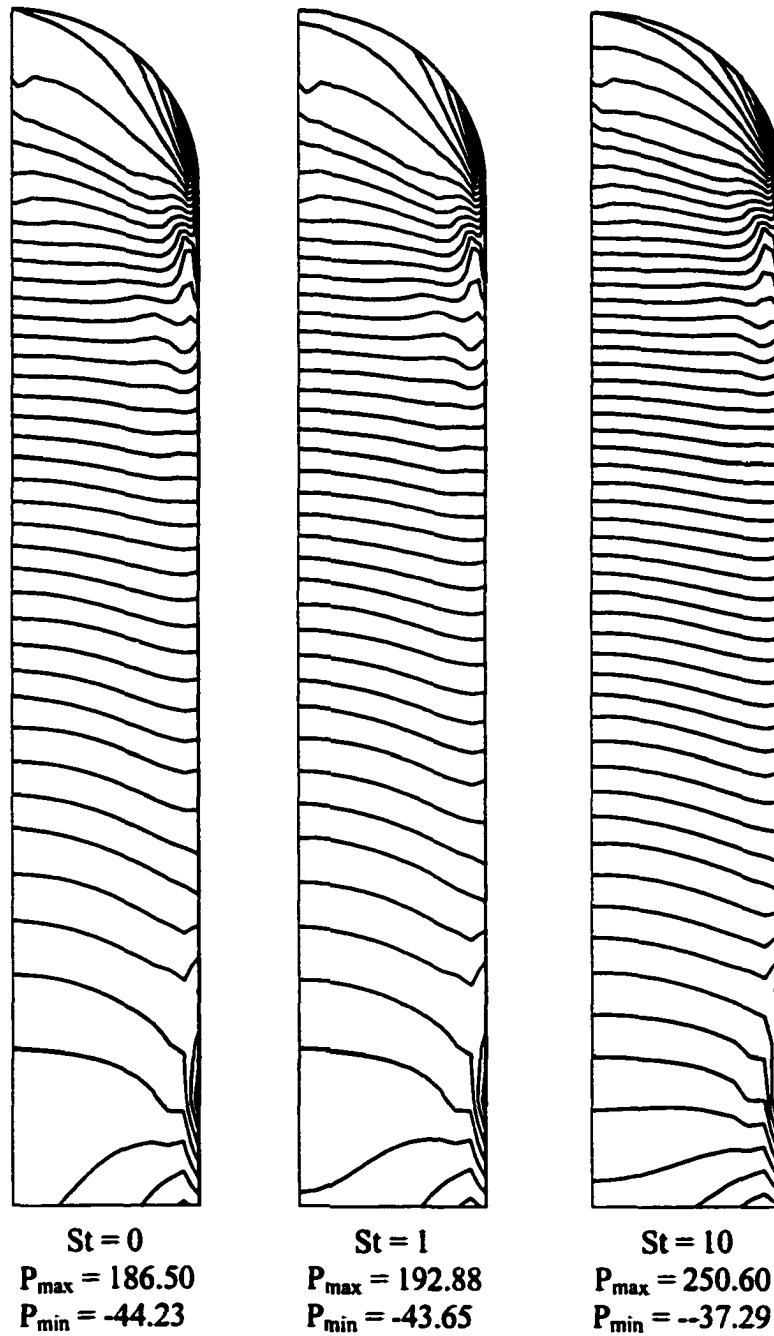


Figure 5.15a Pressure contours for flow injection under various gravitational effects ($Ca = 1$): $Pe = 1$ ($\Delta P = 5$).

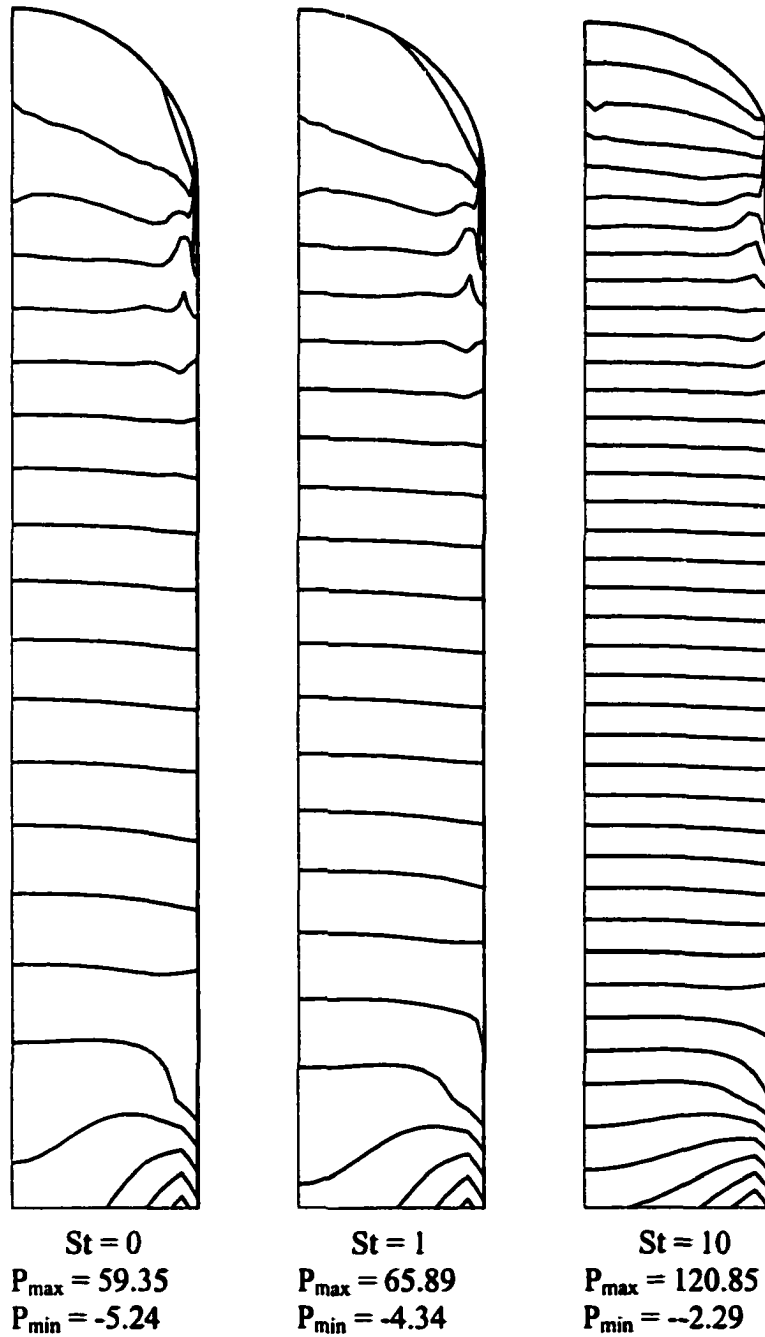


Figure 5.15b Pressure contours for flow injection under various gravitational effects ($Ca = 1$): $Pe = 10$ ($\Delta P = 3$).

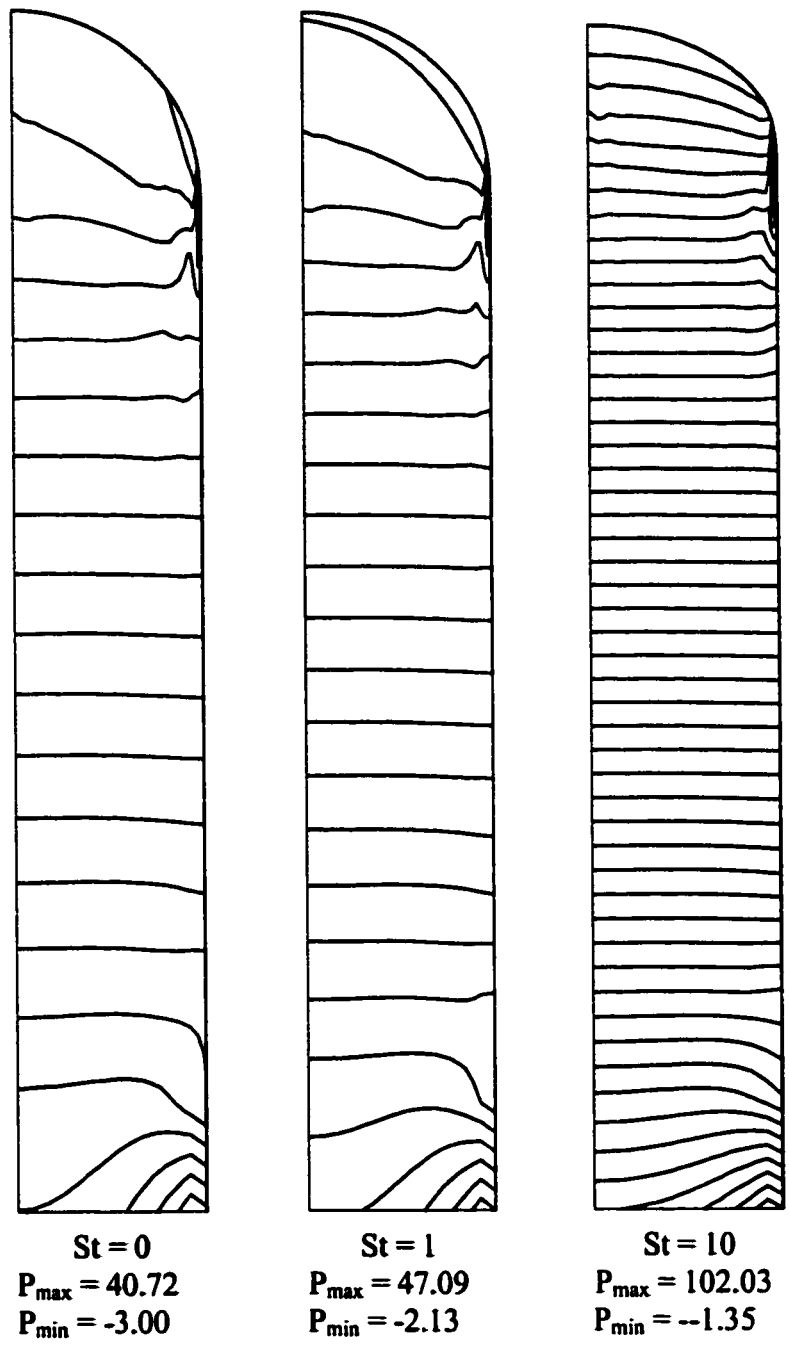


Figure 5.15c Pressure contours for flow injection under various gravitational effects ($Ca = 1$): $Pe = 50$ ($\Delta P = 2$).

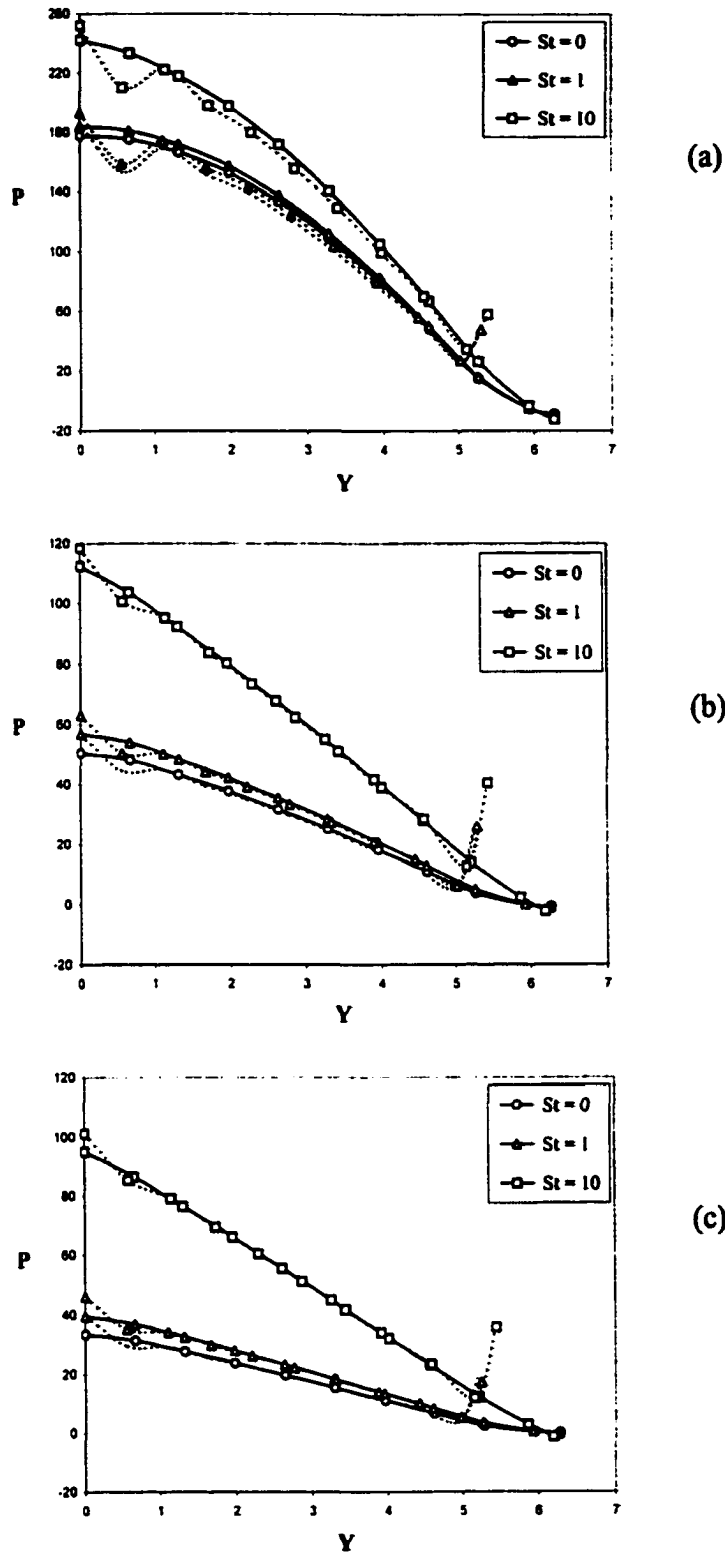


Figure 5.16 Gravitational effects on the pressure distribution along the wall and centerline for various Peclet numbers ($Ca = 1$): wall (---) and centerline (—).

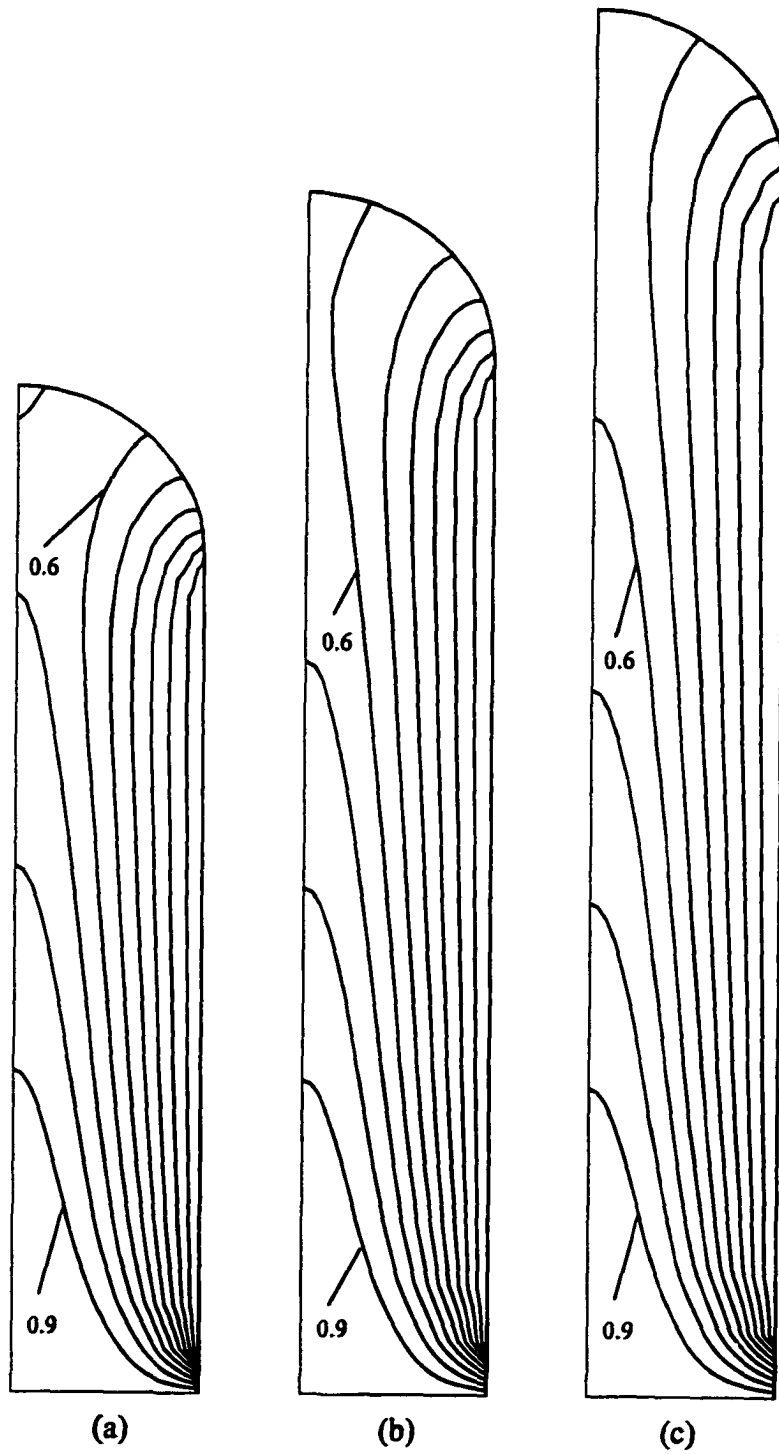


Figure 5.17 Temperature contours at various injection times for $St = 1$, $Ca = 1$, and $Pe = 10$ ($\Delta T = 0.1$): (a) $\tau = 4.02$, (b) $\tau = 5.04$, and (c) $\tau = 6.01$.

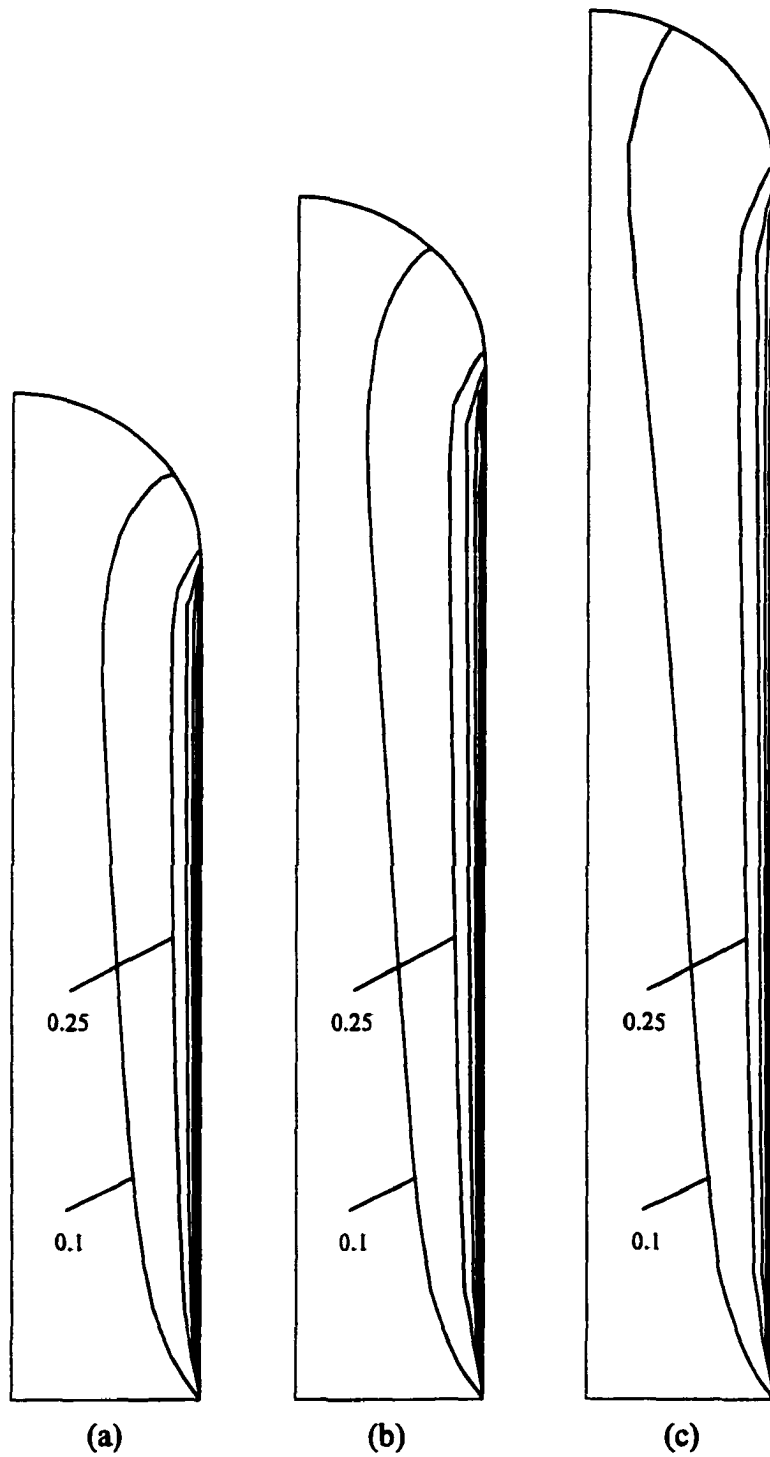


Figure 5.18 Viscosity contours at various injection times for $St = 1$, $Ca = 1$, and $Pe = 10$ ($\Delta\mu = 0.15$): (a) $\tau = 4.02$, (b) $\tau = 5.04$, and (c) $\tau = 6.01$.

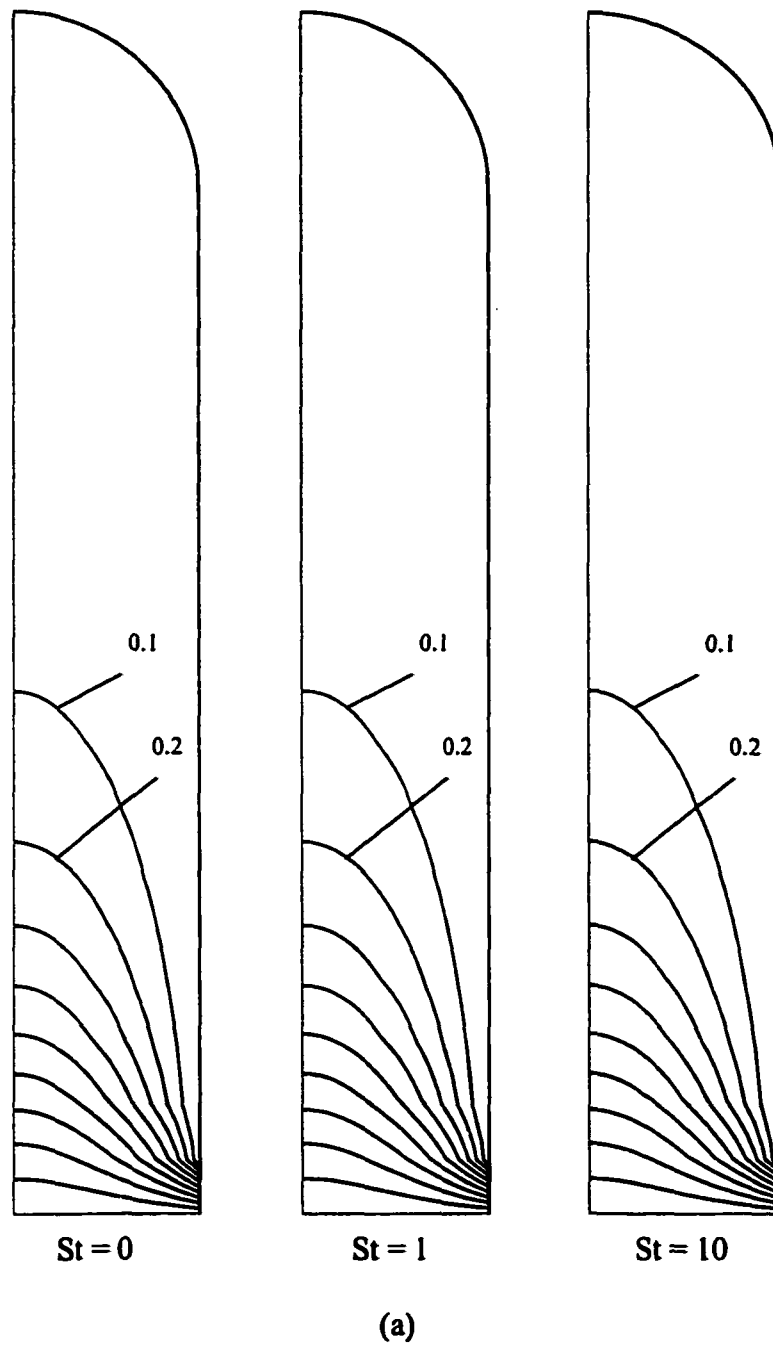
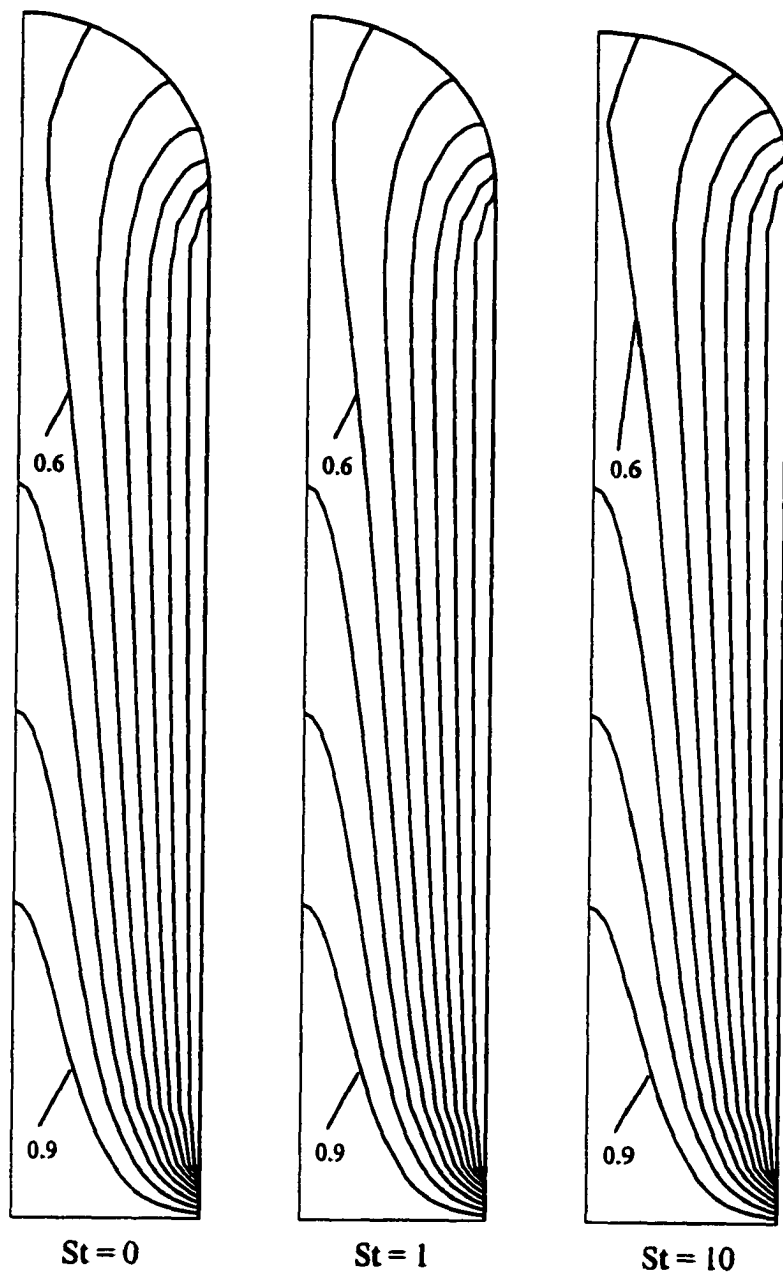


Figure 5.19 Temperature contours under various gravitational effects ($Ca = 1$): (a) $Pe = 1$, (b) $Pe = 10$, and (c) $Pe = 50$ ($\Delta T = 0.1$).



(b)

Figure 5.19 Continued

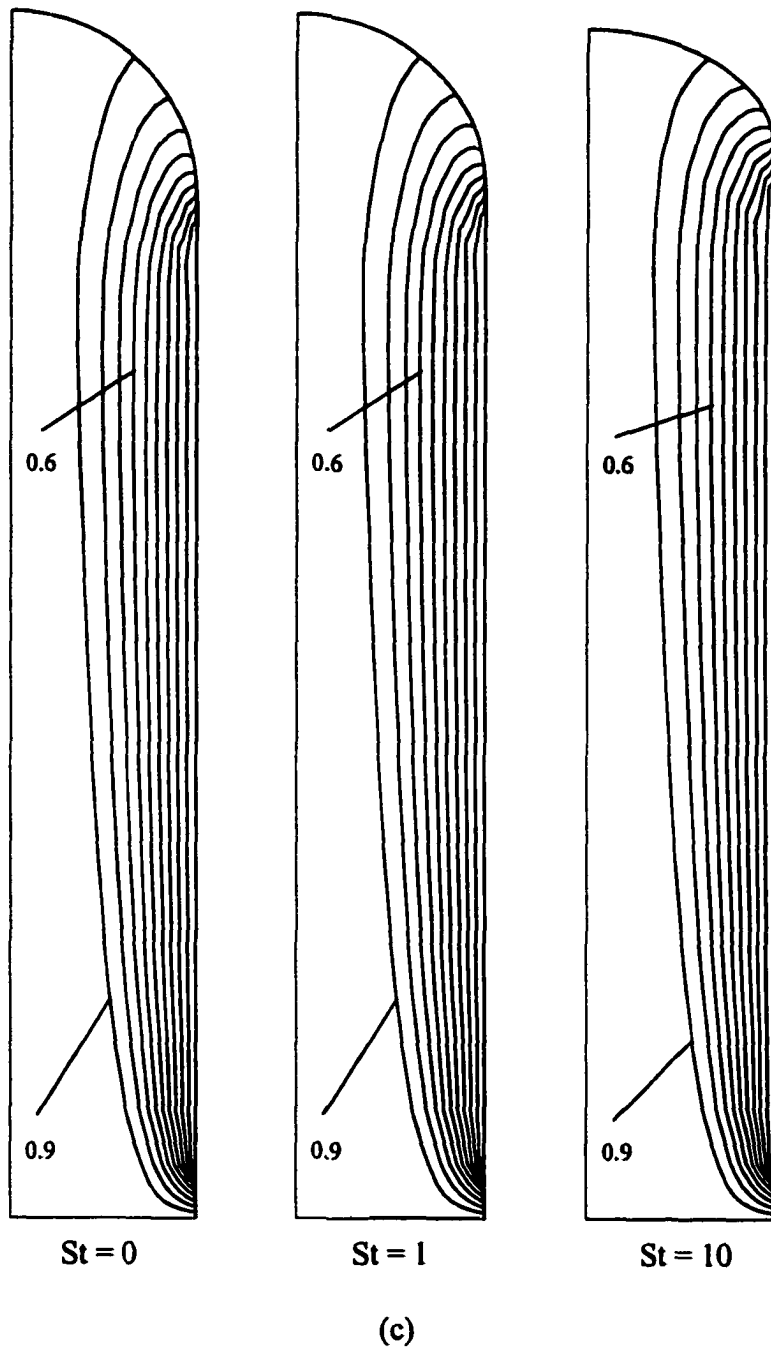


Figure 5.19 Continued

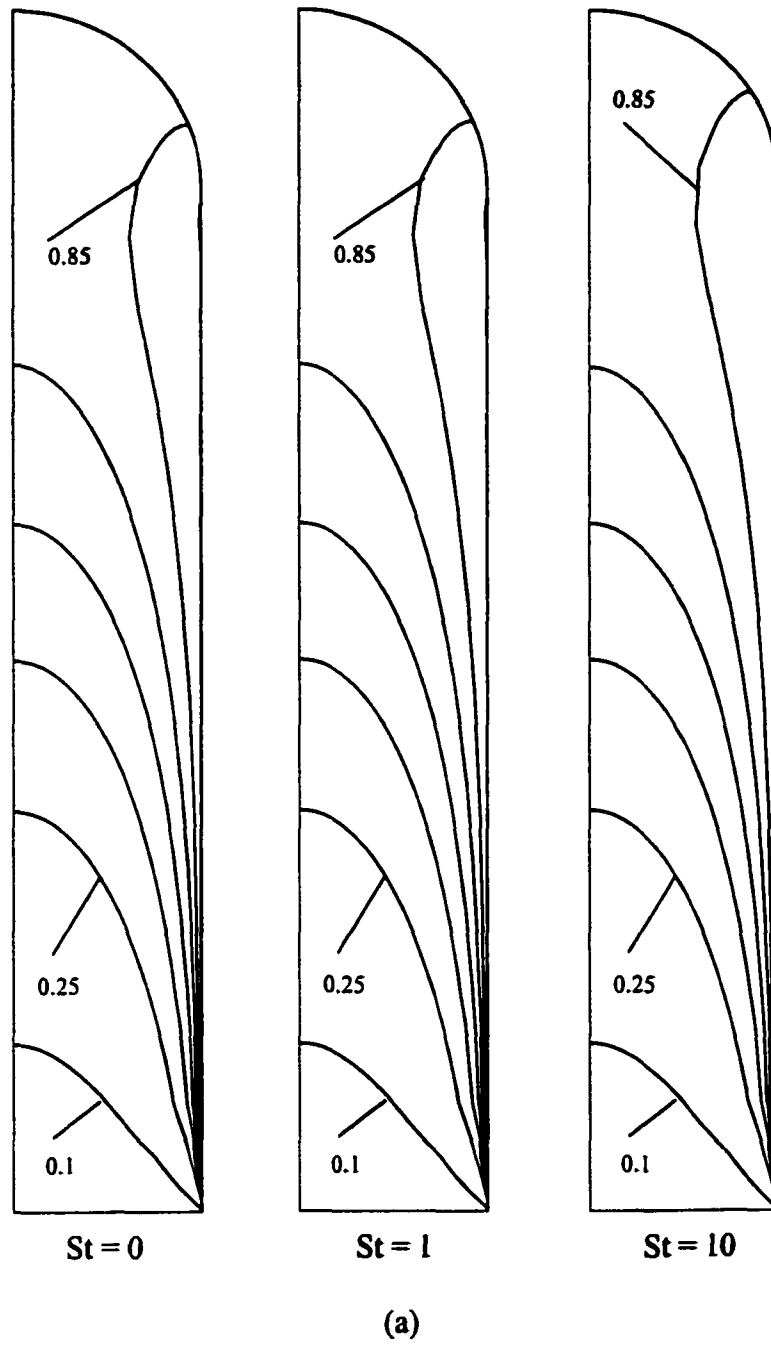
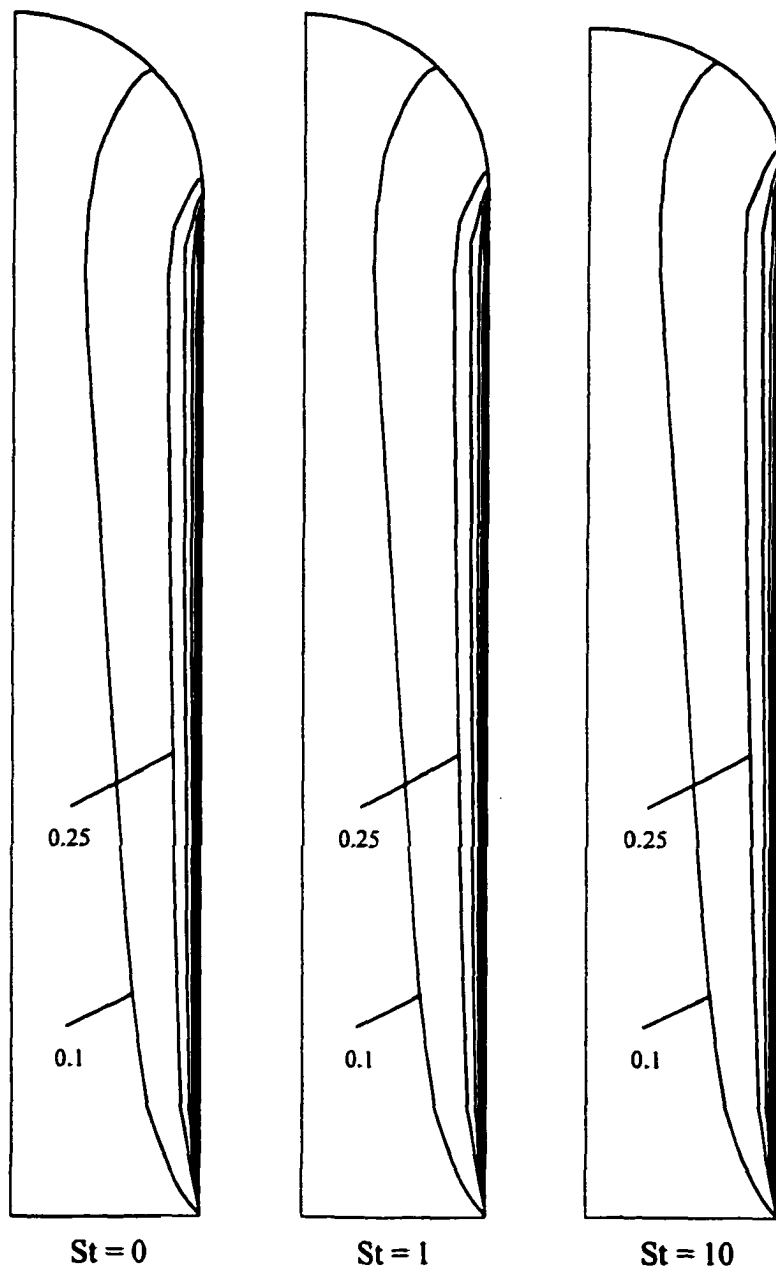
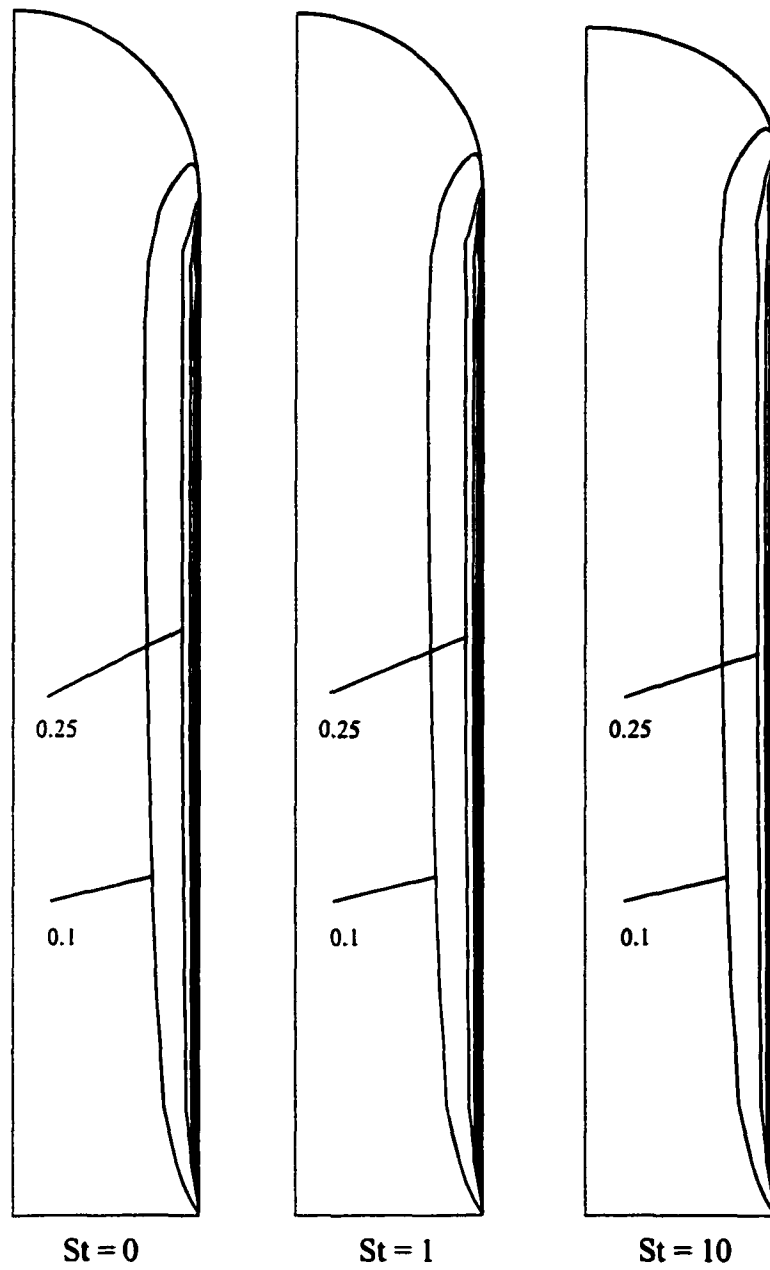


Figure 5.20 Viscosity contours under various gravitational effects ($Ca = 1$): (a) $Pe = 1$, (b) $Pe = 10$, and (c) $Pe = 50$ ($\Delta\mu = 0.15$).



(b)

Figure 5.20 Continued



(c)

Figure 5.20 Continued

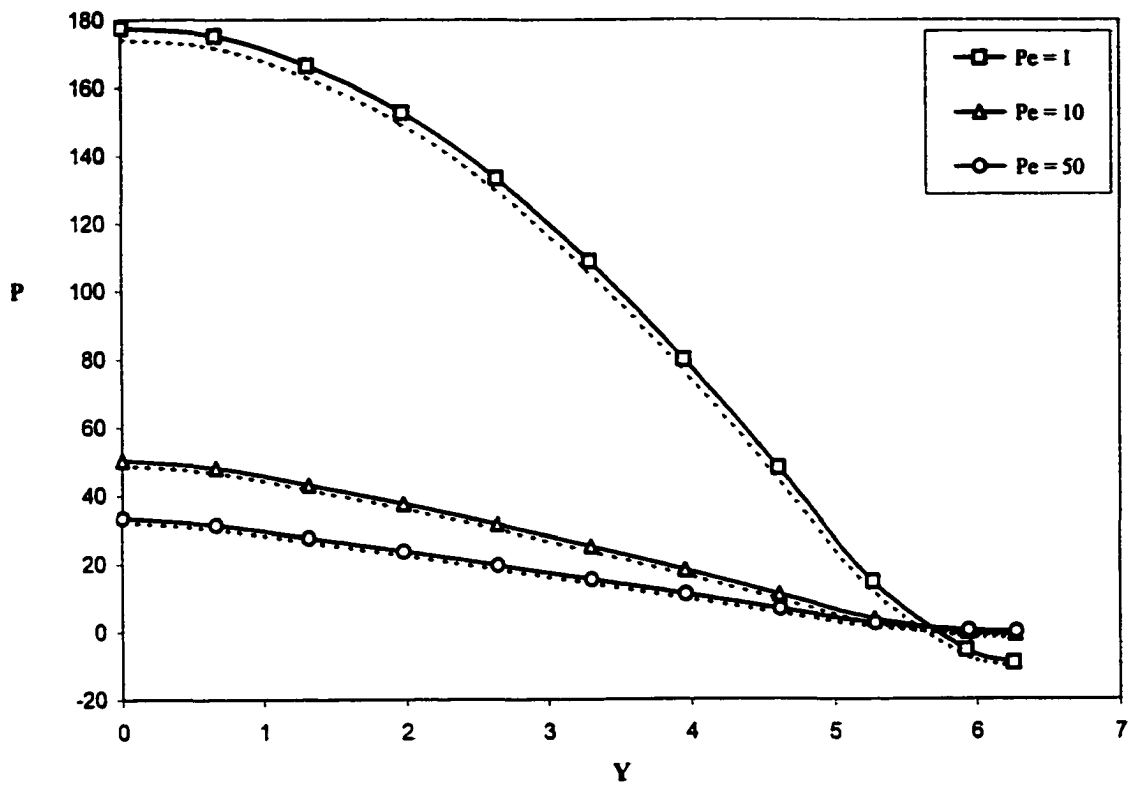


Figure 5.21 Pressure distribution along the centerline under various surface tension effect ($St = 0$): $Ca = 1$ (—) and $Ca \rightarrow \infty$ (---).

CHAPTER 6

CONCLUSIONS

The main objective of the present study is to evaluate the technical feasibility of producing high-performance composite materials using resin transfer molding under microgravity environment.

Since resin transfer molding involves the impregnation of fiber pre-form, the present study has served as a preliminary study to understand and to predict the gravitational and surface tension effects on the injection molding.

In this study, numerical simulations for isothermal and non-isothermal flow injection through planar gaps and center-gated disks have been successfully performed. The effects of gravitation, surface tension and temperature-dependent fluid viscosity on the development of the flow fields (flow front, velocity, pressure, temperature, and viscosity) have been systematically studied. Their effects on the fountain flow are also discussed.

From the present results, one can clearly observe that the fluid initially located near the centerline rolls out towards the wall due to the fountain flow effect. The fountain flow effect results in material restructuring near the flow front, especially in the vicinity of contact line. It can significantly affect the ultimate molecular structure and residual stress in the molded part. The results also show that the gravitational force can greatly modify the fountain flow region, especially for flow injection through an inclined channel. It leads to an asymmetric structure of the ultimate molded part and may reduce the material strength. If fibers were considered, the fiber orientation might become more

complicated and asymmetric, and which might reduce the material strength. For reaction injection moldings, it is even more critical to know the front location-time relation in order to find the temperature and conversion distribution throughout the mold.

The results obtained from the present study (for example, the development of the flow front and flow fields (velocity and pressure)) have provided the important information needed to design or improve the mold filling process, such as the required injection pressure, choice of material, fabrication of mold, and exit gate design. Since the major cost of a product cycle is usually spent on the initial design stage, it is important to have a completely understanding of the effects of the process variables (gravitation, surface tension, and temperature-dependent properties) on the factors (such as fountain flow , development of flow front, and fields variables distribution), which have ultimate influences on the product of quality.

REFERENCES

- Anturkar, N. R., "A Model of Advancing Flow Front in RIM," *Polymer Engineering and Science*, Vol. 34, pp. 1450-1454, 1994.
- Anturkar, N. R., "Petrov-Galerkin Finite Element Analysis for Advancing Flow Front in Reaction Injection Molding," *Computer and Fluids*, Vol. 24, pp. 55-62, 1995.
- Ballman, R. L., and Toor, H. L., "Injection Molding: a Rheological Interpretation Part I," *Modern Plastics*, Vol. 37, pp. 105-108, 1959a.
- Ballman, R. L., Shusman, T., and Toor, H. L., "Injection Molding: a Rheological Interpretation Part II," *Modern Plastics*, Vol. 37, pp. 115-106, 1959b.
- Behrens, R. A., "Transient Domain Free-Surface Flows and Their Applications to Mold Filling," Ph.D. Dissertation, University of Delaware, Newark, DE, 1983.
- Behrens, R. A., Crochet, M. J., Denson, C. D., and Metzner, A. B., "Transient Free-Surface Flows: Motion of a Fluid Advancing in a Tube," *AIChE Journal*, Vol. 33, pp. 1178-1186, 1987.
- Berger, I. T., and Gogos, C. G., "A Numerical Simulation of the Cavity Filling Process with PVC in Injection Molding," *Polymer Engineering and Science*, Vol. 13, pp. 102-112, 1973.
- Beris, A. N., "Fluid Elements Deformation behind an Advancing Flow Front," *Journal of Rheology*, Vol. 31, pp. 121-124, 1987.
- Bhattacharji, S., and Savic, P., "Real and Apparent Non-Newtonian Behavior in Viscous Pipe Flow of Suspensions Driven by a Fluid Piston," *Proceedings of the Heat Transfer and Fluid Mechanics Institute*, Vol. 15, pp. 248-262, 1965.
- Blake, J. W., "Studies in Reaction Injection Mold Filling," Ph.D. Dissertation, University of Minnesota, Minneapolis, MN, 1987.
- Blake, T. D., "Dynamic Contact Angles and Wetting Kinetics," *Wettability*, ed. by Berg, J. C., Marcel Dekker, New York, 1993.
- Boender, W., Chesters, A. K., and Van der Zanden, A. J. J., "An Approximate Analytical Solution of the Hydrodynamic Problem Associated with an Advancing Liquid-Gas Contact Line," *International Journal of Multiphase Flow*, Vol. 17, pp. 661-676, 1991.
- Brooks, A. N., and Hughes, T. J. R., "Streamline Upwind/Petrov-Galerkin Formulations for Convection Dominated Flows with Particular Emphasis on the Incompressible Navier-Stokes Equation," *Computer Methods in Applied Mechanics and Engineering*, Vol. 32, pp. 199-259, 1982.

Castro, J. M., and Macosko, C. W., "Studies of Mold Filling and Curing in the Reaction Injection Molding Process," *AICHE Journal*, Vol. 28, pp. 250-260, 1982.

Chen, Q., Rame, E., and Garoff, S., "The Breakdown of Asymptotic Hydrodynamic Models of Liquid Spreading at Increasing Capillary Number," *Physics of Fluids*, Vol. 7, pp. 2631-2639, 1995.

Chiang, H. H., Hieber, C. A., and Wang, K. K., "A Unified simulation of the Filling and Postfilling Stages in Injection Molding. Part I: Formulation," *Polymer Engineering and Science*, Vol. 31, pp. 116-124, 1991.

Coyle, D. J., Blake, J. W., and Macosko, C. W., "The Kinematics of Fountain Flow in Mold Filling," *AICHE Journal*, Vol. 33, pp. 1168-1177, 1987.

Cox, R. G., "The Dynamics of the Spreading of Liquids on a Solid Surface. Part 1. Viscous Flow," *Journal of Fluid Mechanics*, Vol. 168, pp. 169-192, 1986.

de Gennes, P. G., "Wetting: Statics and Dynamics," *Reviews of Modern Physics*, Vol. 57, pp. 827-863, 1985.

Donea, J., "A Taylor-Galerkin Method for Convective Transport Problems," *International Journal for Numerical Methods in Engineering*, Vol. 20, pp. 101-119, 1984.

Donea, J., Giuliani, S., Laval, H., and Quartapelle, L., "Time Accurate Solution of Advection-Diffusion Problems by Finite Elements," *Computer Methods in Applied Mechanics and Engineering*, Vol. 45, pp. 123-145, 1984.

Durbin, P. A., "Consideration on the Moving Contact-Line Singularity, with Application to Frictional Drag on a Slender Drop," *Journal of Fluid Mechanics*, Vol. 197, pp. 157-169, 1988.

Dussan V., E. B., "The Moving Contact Line: the Slip Boundary Condition," *Journal of Fluid Mechanics*, Vol. 77, pp. 665-684, 1976.

Dussan V., E. B., "Immiscible Liquid Displacement in a Capillary Tube: the Moving Contact Line," *AICHE Journal*, Vol. 23, pp. 131-133, 1977.

Dussan V., E. B., "On the Spreading of Liquids on Solid Surface: Static and Dynamic Contact Lines," *Annual Review of Fluid Mechanics*, Vol. 11, pp. 371-400, 1979.

Dussan V., E. B., and Davis, S. H., "On The Motion of a Fluid-Fluid Interface along a Solid Surface," *Journal of Fluid Mechanics*, Vol. 65, pp. 71-95, 1974.

- Dussan V., E. B., Rame, E., and Garoff, S., "On Identifying the Appropriate Boundary Conditions at a Moving Contact Line: an Experimental Investigation," *Journal of Fluid Mechanics*, Vol. 230, pp. 97-116, 1991.
- Elliott, G. E. P., and Riddiford, A. C., "Dynamic Contact Angle," *Journal of Colloid and Interface Science*, Vol. 23, pp. 389-398, 1967.
- Fauchon, D., Dannelongue, H. H., and Tanguy P. A., "Numerical Simulation of the Advancing Front in Injection Molding," *International Polymer Processing*, Vol. 6, pp.13-18, 1991.
- Friedrichs, B., and Guceri, S. I., "A Novel Hybrid Numerical Technique to Model 3-D Fountain Flow in Injection Molding Processes," *Journal of Non-Newtonian Fluid Mechanics*, Vol. 49, pp. 141-173, 1993.
- George, P. L., Automatic Mesh Generation – Application to Finite Element Methods, John Wiley & Sons, New York, 1991.
- Goldstein, S., Modern Developments in Fluid Dynamics, Oxford University Press, 1938.
- Gogos, C. G., Huang, C. F., and Schmidt, R. L., "The Process of Cavity Filling Including the Fountain Flow in Injection Molding," *Polymer Engineering and Science*, Vol. 26, pp. 1457-1466, 1986.
- Gong, H., "Fountain Flow in Injection Mold Filling An Analytical Solution," *Journal of Materials Processing and Manufacturing Science*, Vol. 2, pp. 247-260, 1994.
- Greenspan, H. P., "On the Motion of a Small Viscous Droplet That Wets a Surface," *Journal of Fluid Mechanics*, Vol. 84, pp. 125-143, 1978.
- Gresho, P. M., Lee, R. L., and Sani, R. L., "On the Time-Dependent Solution of the Incompressible Navier-Stokes Equations in Two and Three Dimensions," Recent Advances in Numerical Methods in Fluids, Vol. 1, ed. by Taylor, C. and Morgan, K., Pineridge Press, Swansea, U.K., 1979.
- Hansen R. J., and Toong, T. Y., "Interface Behavior as One Fluid Completely Displace Another from a Small-Diameter Tube," *Journal of Colloid and Interface Science*, Vol. 36, pp. 410-413, 1971.
- Hansen R. J., and Toong, T. Y., "Dynamic Contact Angle and Its Relationship to Forces of Hydrodynamic Origin," *Journal of Colloid and Interface Science*, Vol. 37, pp. 196-207, 1971.
- Harry, D. H., and Parrott, R. G., "Numerical Simulation of Injection Mold Filling," *Polymer Engineering and Science*, Vol. 10, pp. 209-214, 1970.

Heinrich, J. C., and Pepper, D. W., Intermediate Finite Element Method, Taylor & Francis, 1999.

Hieber, C. A., and Shen, S. F., "A Finite Element/Finite Difference Simulation of the Injection Molding Filling Process," *Journal of Non-Newtonian Fluid Mechanics*, Vol. 7, pp. 1-32, 1980.

Hieber, C. A., Socha, L. S., Shen, S. F., Wang, K. K., and Isayev, A. I., "Filling Thin Cavities of Variable Gap Thickness: a Numerical and Experimental Investigation," *Polymer Engineering and Science*, Vol. 23, pp. 20-26, 1983.

Hocking, L. M., "A Moving Fluid Interface on a Rough Surface," *Journal of Fluid Mechanics*, Vol. 76, pp. 801-817, 1976.

Hocking, L. M., "A Moving Fluid Interface. Part 2. The Removal of the Force Singularity," *Journal of Fluid Mechanics*, Vol. 79, pp. 209-229, 1977.

Hocking, L. M., and Rivers, A. D., "The Spreading of a Drop by Capillary Action," *Journal of Fluid Mechanics*, Vol. 121, pp. 425-442, 1982.

Hoffman, R. L., "A Study of the Advancing Interface I. Interface Shape in Liquid-Gas Systems," *Journal of Colloid and Interface Science*, Vol. 50, pp. 228-241, 1975.

Huang, C. F., "Simulation of the Cavity Filling Process with the Marker-and-Cell Method in Injection Molding," Ph.D. Dissertation, Stevens Institute of Technology, Hoboken, NJ, 1978.

Huh, C., and Mason, S. G., "The Steady Movement of a Liquid Meniscus in a Capillary Tube," *Journal of Fluid Mechanics*, Vol. 81, pp. 401-419, 1977.

Huh, C., and Scriven, L. E., "Hydrodynamic Model of Steady Movement of a Solid/Liquid/Fluid Contact Line," *Journal of Fluid Mechanics*, Vol. 35, pp. 85-101, 1971.

Jansons, K. M., "Determination of the Microscopic (Partial) Slip Boundary Condition for a Viscous Flow over a Randomly Rough Surface with a Perfect Slip Microscopic Boundary Condition," *Physics of Fluids*, Vol. 31, pp. 15-17, 1988.

Jiang, T. S., Oh, S. G., and Slattery, J. C., "Correlation for Contact Angle," *Journal of Colloid and Interface Science*, Vol. 69, pp. 74-77, 1979.

Jin, X., "Boundary Element Study on Particle Orientation Caused by the Fountain Flow in Injection Molding," *Polymer Engineering and Science*, Vol. 33, pp. 1238-1242, 1993.

Kafka, F. Y., and Dussan V., E. B., "On the Interpretation of Dynamic Contact Angle," *Journal of Fluid Mechanics*, Vol. 95, pp. 539-565, 1979.

Kamal, M. R., and Kenig, S., "The Injection Molding of Thermoplastics Part I: Theoretical Model," Polymer Engineering and Science, Vol. 12, pp. 294-301, 1972a.

Kamal, M. R., and Kenig, S., "The Injection Molding of Thermoplastics Part II: Experimental Test of the Model," Polymer Engineering and Science, Vol. 12, pp. 302-308, 1972b.

Kamal, M. R., Chu, E., and Lafleur, P. G., "Computer Simulation of Injection Mold Filling for Viscoelastic Melts with Fountain Flow," Polymer Engineering and Science, Vol. 26, pp.190-196, 1986.

Kamal, M. R., Goyal, K. S., and Chu, E., "Simulation of Injection Mold Filling of Viscoelastic Polymer with Fountain Flow," AIChE Journal, Vol. 34, pp. 94-106, 1988.

Kamal, M. R., and Lafleur, P. G., "A Structure-Oriented Computer Simulation of the Injection Molding of Viscoelastic Crystalline Polymers Part II: Model Predictions and Experimental Results," Polymer Engineering and Science, Vol. 26, pp. 103-110, 1986.

Keunings, R., "An Algorithm for the Simulation of Transient Viscoelastic Flows with Free Surface," Journal of Computational Physics, Vol. 62, pp. 199-220, 1986.

Kheshgi, H. S., and Scriven, L. E., "Penalty Finite Element Analysis of Unsteady Free Surface Flows," Finite Elements in Fluids, Vol. 5, ed. by Gallagher, R. H., Oden, J. T., Zienkiewicz, O. C., Kawai, T. and Kawahara, M., John Wiley & Sons, New York, 1984.

Kistler, S. F., "The Fluid Mechanics of Curtain Coating and Related Viscous Free Surface Flows with Contact Lines," Ph.D. Thesis, Univ. Minnesota, Minneapolis, 1984.

Kistler, S. F., "Hydrodynamics of Wetting," Wettability, ed. by Berg, J. C., Marcel Dekker, New York, 1993.

Koplik, J., Banavar, J. R., and Willemsen, J. F., "Molecular Dynamics of Poiseuille Flow and Moving Contact Lines," Physical Review Letters, Vol. 60, pp. 1282-1285, 1988.

Kuo, Y., and Kamal, M. R., "The Fluid Mechanics and Heat Transfer of Injection Mold Filling of Thermoplastic Materials," AIChE Journal, Vol. 22, pp. 661-669, 1976.

Lafleur, P. G., and Kamal, M. R., "A Structure-Oriented Computer Simulation of the Injection Molding of Viscoelastic Crystalline Polymers Part I: Model of Fountain Flow, Packing, Solidification," Polymer Engineering and Science, Vol. 26, pp. 92-102, 1986.

Lee, H. S., "Finite Element Analysis for the Flow Characteristics along the Thickness Direction in Injection Molding," Polymer Engineering and Science, Vol. 37, pp. 559-567, 1997.

Lekakou, C. N., and Richardson, S. M., "Simulation of Reacting Flow during Filling in Reaction Injection Molding (RIM)," *Polymer Engineering and Science*, Vol. 26, pp. 1264-1275, 1986.

Lord, H. A., and Williams, G., "Molding-Filling studies for the Injection Molding of thermoplastic Materials. Part II: the Transient Flow of Plastic Materials in the Cavities of Injection-Molding Dies," *Polymer Engineering and Science*, Vol. 15, pp. 569-582, 1975.

Lowndes, J., "The Numerical Simulation of the Steady Moving of a Fluid Meniscus in a Capillary Tube," *Journal of Fluid Mechanics*, Vol. 101, pp. 631-646, 1980.

Marsh, J. A., "Dynamic Contact Angles and Hydrodynamics near a Moving Contact Line," Ph.D. Dissertation, Carnegie Mellon University, Pittsburgh, PA, 1992.

Marsh, J. A., Garoff, S., and Dussan V., E. B., "Dynamic Contact Angles and Hydrodynamics Near a Moving Contact Line," *Physical Review Letters*, Vol. 70, pp. 2778-2781, 1993.

Mavridis, H., Hrymak, A. N., and Vlachopoulos, J., "Finite Element Simulation of Fountain Flow in Injection Molding," *Polymer Engineering and Science*, Vol. 26, pp. 449-454, 1986a.

Mavridis, H., Hrymak, A. N., and Vlachopoulos, J., "Deformation and Orientation of Fluid Elements behind an Advancing Flow Front," *Journal of Rheology*, Vol. 30, pp. 555-563, 1986b.

Mavridis, H., Hrymak, A. N., and Vlachopoulos, J., "Transient Free Surface Flows in Injection Mold Filling," *AIChE Journal*, Vol. 34, pp. 403-410, 1988.

Moffatt, H. K., "Viscous and Resistive Eddies near a Sharp Corner," *Journal of Fluid Mechanics*, Vol. 18, pp. 1-18, 1964.

Mues, W., Hens, J., and Boiy, L., "Observation of a Dynamic Wetting Process Using Laser-Doppler Velocimetry," *AIChE Journal*, Vol. 35, pp. 1521-1526, 1989.

Ngan, C. G., and Dussan V., E. B., "On The Nature of the Dynamic Contact Angle: an Experimental Study," *Journal of Fluid Mechanics*, Vol. 118, pp. 27-40, 1982.

Ngan, C. G., and Dussan V., E. B., "The Moving Contact Line with a 180° Advancing Contact Angle," *Physics of Fluids*, Vol. 27, pp. 2785-2787, 1984.

Ngan, C. G., and Dussan V., E. B., "On The Dynamics of Liquids Spreading on Solid Surface," *Journal of Fluid Mechanics*, Vol. 209, pp. 191-226, 1989.

- Perrett, F. J., Reible, D. D., and McIlhenny, R. C., "Modeling Fountain Flow and Filling Front Shape in Reaction Injection Molding," *Polymer Engineering and Science*, Vol. 33, pp. 716-720, 1993.
- Pismen, L. M., and Nir, A., "Motion of a Contact Line," *Physics of Fluids*, Vol. 25, pp. 3-7, 1982.
- Richardson, S., "On the No-Slip Boundary Condition," *Journal of Fluid Mechanics*, Vol. 59, pp. 707-719, 1973.
- Rose, W. R., "Fluid-Fluid Interfaces in Steady Motion," *Nature*, Vol. 191, pp. 242-243, 1961.
- Rose, W., and Heins, R. W., "Moving interfaces and Contact Angle Rate-Dependency," *Journal of Colloid and Interface Science*, Vol. 17, pp. 39-48, 1962.
- Sato, T., and Richardson, S. M., "Numerical Simulation of the Fountain Flow Problem for Viscoelastic Fluids," *Polymer Engineering and Science*, Vol. 35, pp. 805-812, 1995.
- Savelski, M. J., Shetty, S. A., Kolb, W. B., and Cerro, R. L., "Flow Pattern Associated with the Steady Movement of a Solid/Liquid/Fluid Contact Line," *Journal of Colloid and Interface Science*, Vol. 176, pp. 117-127, 1995.
- Schmidt, L. R., "A Special Mold and Tracer Technique for Studying Shear and Extensional Flows in a Mold Cavity during Injection Molding," *Polymer Engineering and Science*, Vol. 14, pp. 797-800, 1974.
- Shen, S. F., "Simulation of Polymeric Flows in the Injection Moulding Process," *International Journal for Numerical Methods in Fluids*, Vol. 4, pp. 171-183, 1984.
- Sheng, P., and Zhou, M., "Immiscible-Fluid Displacement: Control-Line Dynamics and the Velocity-Dependent Capillary Pressure," *Physical Review A*, Vol. 45, pp. 5694-5708, 1992.
- Shikhmurzaev, Y. D., "Mathematical Modeling of Wetting Hydrodynamics," *Fluid Dynamics Research*, Vol. 13, pp. 45-64, 1994.
- Shikhmurzaev, Y. D., "Dynamic Contact Angles and Flow in Vicinity of Moving Contact Line," *AIChE Journal*, Vol. 42, pp. 601-612, 1996.
- Shikhmurzaev, Y. D., "Moving Contact Lines in Liquid/Liquid/Solid Systems," *Journal of Fluid Mechanics*, Vol. 334, pp. 211-249, 1997.
- Shin, S., and Lee, W. I., "Analysis of the Non-Isothermal Mold Filling Process Using Finite Element Method," *Journal of Materials Processing and Manufacturing Science*, Vol. 3, pp. 333-356, 1995.

Slikkerveer, P. J., Van Lohuizen, E. P., and O'Brien, S. B., "An Implicit Surface Tension Algorithm for Picard Solvers of Surface-Tension-Dominated Free and Moving Boundary Problems," *International Journal for Numerical Methods in Fluids*, Vol. 22, pp. 851-865, 1996.

Spencer, R. S., and Gilmore, G. D., "Some Flow Phenomena in the Injection Molding of Polystyrene," *Journal of Colloid and Interface Science*, Vol. 6, pp. 118-132, 1951.

Tadmor, Z., "Molecular Orientation Injection Molding," *Journal of Applied Polymer Science*, Vol. 18, pp. 1753-1772, 1974.

Tadmor, Z., Broyer, E., and Gutfinger, C., "Flow Analysis Network (FAN) -A Method for Solving Flow Problems in Polymer Processing," *Polymer Engineering and Science*, Vol. 14, pp. 660-664, 1974.

Tanner, L. H., "The Spreading of Silicone Oil Drop on Horizontal Surfaces," *Journal of Physics D*, Vol. 12, pp. 1473-1484, 1979.

Thienel, P., and Menges, G., "Mathematical and Experimental Determination of Temperature, Velocity, and Pressure Fields in Flat Molds during the Filling Process in Injection Molding of Thermoplastics," *Polymer Engineering and Science*, Vol. 18, pp. 314-320, 1978.

Thompson, P. A., and Robbins, M. O., "Simulations of Contact-Line Motion: Slip and Dynamic Contact Angle," *Physical Review Letters*, Vol. 63, pp. 766-769, 1989.

Voinov, O. V., "Hydrodynamics of Wetting," *Fluid Dynamics*, Vol. 11, pp. 714-721, 1976.

Wang, K. K., Shen, S. F., Cohen, C., Hieber, C. A., and Jahanmir, S., "Computer-Aided Injection Molding System," Report 5, Cornell University, 1978.

Wang, K. K., Shen, S. F., Cohen, C., Hieber, C. A., Isayev, A. I., Jahanmir, S., and Tayler, A., "Computer-Aided Injection Molding System," Report 6, Cornell University, 1979.

Wu, P. C., Huang, C. F., and Gogos, C. G., "Simulation of the Mold-Filling Process," *Polymer Engineering and Science*, Vol. 14, pp. 223-230, 1974.

Yarnold, G. D., "The Motion of a Mercury Index in a Capillary Tube," *Proceedings of the Physical Society of London*, Vol. 50, pp. 540-552, 1938.

Zienkiewicz, O. C., Lohner, R., Morgan, K. and Nakazawa, S., "Finite Elements in Fluid Mechanics – a Decade of Progress," *Finite Elements in Fluids*, Vol. 5, ed. by Gallagher,

R. H., Oden, J. T., Zienkiewicz, O. C., Kawai, T. and Kawahara, M., John Wiley and Sons, New York, 1984.

Zienkiewicz, O. C., Lohner, R., Morgan, K. and Peraire, J., "High-Speed Compressible Flow and Other Advection Dominated Problems of Fluid Dynamics," Finite Elements in Fluids, Vol. 6, ed. by Gallagher, R. H., Carey, G., Oden, J. T. and Zienkiewicz, O. C., John Wiley and Sons, New York, 1985.

APPENDIX A

CHANGE IN SURFACE NORMAL VECTOR WITH TIME

Assume that a curve in a two-dimensional Cartesian or a three-dimensional axisymmetrical coordinate system can be described using a parameter ρ ,

$$\mathbf{X}(\rho) = x(\rho)\hat{i} + y(\rho)\hat{j}, \quad (\text{A.1})$$

where ρ is independent of time.

The tangent vector along the curve is defined as

$$\bar{\mathbf{r}} = \frac{d\mathbf{X}}{d\rho} = \frac{dx}{d\rho}\hat{i} + \frac{dy}{d\rho}\hat{j}. \quad (\text{A.2})$$

Then, the unit tangent vector is given by

$$\bar{\mathbf{t}} = \frac{\bar{\mathbf{r}}}{|\bar{\mathbf{r}}|} = \frac{\bar{\mathbf{r}}}{\sqrt{\bar{\mathbf{r}} \cdot \bar{\mathbf{r}}}} = \frac{\frac{dx}{d\rho}\hat{i} + \frac{dy}{d\rho}\hat{j}}{\sqrt{\bar{\mathbf{r}} \cdot \bar{\mathbf{r}}}} = t_x\hat{i} + t_y\hat{j} \quad (\text{A.3})$$

Accordingly, the unit outward normal vector can be expressed as

$$\bar{\mathbf{n}} = \frac{\frac{dy}{d\rho}\hat{i} - \frac{dx}{d\rho}\hat{j}}{\sqrt{\bar{\mathbf{r}} \cdot \bar{\mathbf{r}}}} = n_x\hat{i} + n_y\hat{j} = t_y\hat{i} - t_x\hat{j}. \quad (\text{A.4})$$

The change in the surface unit outward normal vector with time is obtained by differentiating Eq. (A.4).

$$\frac{d\bar{\mathbf{n}}}{d\tau} = \frac{d}{d\tau} \left(\frac{\frac{dy}{d\rho}\hat{i} - \frac{dx}{d\rho}\hat{j}}{\sqrt{\bar{\mathbf{r}} \cdot \bar{\mathbf{r}}}} \right) = \frac{d}{d\tau} \left(\frac{\frac{dy}{d\rho}\hat{i} - \frac{dx}{d\rho}\hat{j}}{\sqrt{\bar{\mathbf{r}} \cdot \bar{\mathbf{r}}}} \right) - \frac{\frac{dy}{d\rho}\hat{i} - \frac{dx}{d\rho}\hat{j}}{(\bar{\mathbf{r}} \cdot \bar{\mathbf{r}})^{3/2}} \left(\bar{\mathbf{r}} \cdot \frac{d\bar{\mathbf{r}}}{d\tau} \right). \quad (\text{A.5})$$

Since ρ is independent of time, the change in the tangent vector with respect to time is obtained as

$$d\bar{r} / d\tau = (du / d\rho)\hat{i} + (dv / d\rho)\hat{j}. \quad (\text{A.6})$$

With the aid of Eq. (A.6), Eq. (A.5) can be rewritten as

$$\frac{d\bar{n}}{d\tau} = \frac{\frac{dv}{d\rho}\hat{i} - \frac{du}{d\rho}\hat{j}}{\sqrt{\bar{r} \cdot \bar{r}}} - \frac{\frac{dy}{d\rho}\hat{i} - \frac{dx}{d\rho}\hat{j}}{(\bar{r} \cdot \bar{r})^{3/2}} \left(\bar{r} \cdot \left(\frac{du}{d\rho}\hat{i} + \frac{dv}{d\rho}\hat{j} \right) \right). \quad (\text{A.7})$$

The length of the vector \bar{r} can be expressed in terms of the length s along the curve as

$$|\bar{r}|^2 = \bar{r} \cdot \bar{r} = \left(\frac{ds}{d\rho} \right)^2. \quad (\text{A.8})$$

With the aid of Eq. (A.8) and the identity $t_x^2 + t_y^2 = 1$ (where $dx/ds = t_x$ and $dy/ds = t_y$),

one can take ρ to be equal to the curve distance s at time τ . Given $\bar{r} = \bar{t}$ and $\bar{r} \cdot \bar{r} = 1$,

Eq. (A.7) can be further simplified to give

$$\begin{aligned} \frac{d\bar{n}}{d\tau} &= \frac{dv}{ds}\hat{i} - \frac{du}{ds}\hat{j} - \left(\bar{t} \cdot \left(\frac{du}{ds}\hat{i} + \frac{dv}{ds}\hat{j} \right) \right) \left(\frac{dy}{ds}\hat{i} - \frac{dx}{ds}\hat{j} \right) \\ &= - \left(\frac{d\bar{U}}{ds} \cdot \bar{n} \right) \bar{t}. \end{aligned} \quad (\text{A.9})$$

where $\bar{U} = u\hat{i} + v\hat{j}$.